Study of microphytobenthos dynamics in temperate intertidal mudflats by using physical-biological coupled modelling and remote sensing data analysis

Raphaël Savelli

LA ROCHELLE UNIVERSITÉ

ÉCOLE DOCTORALE EUCLIDE

LABORATOIRE : LIttoral ENvironnement et Sociétés

THÈSE présentée par :

Raphaël SAVELLI

soutenance prévue le : 12 décembre 2019

pour obtenir le grade de : Docteur de La Rochelle Université

Discipline : Biologie de l'environnement, des populations, écologie

Étude de la dynamique du microphytobenthos des vasières intertidales aux latitudes tempérées

Approche combinée modélisation couplée physique-biologie et analyse de données satellitales

JURY :

Laurent BARILLÉ	Professeur, Université de Nantes
Ana BRITO	Chargée de recherche, MARE- Universidade de Lisboa
Christine DUPUY	Professeure, La Rochelle Université, Directrice de thèse
Virginie LAFON	Directrice associée, I-Sea
Sébastien LEFEBVRE	Professeur, Université de Lille 1, Rapporteur
Vincent LE FOUEST	Maître de conférences, La Rochelle Université, Responsable scientifique
Pierre POLSENAERE	Chargé de recherche, IFREMER LER-PC, Co-responsable scientifique
João SERÔDIO	Professeur, Universidade de Aveiro, Rapporteur
Graham UNDERWOOD	Professeur, University of Essex

STUDY OF MICROPHYTOBENTHOS DYNAMICS IN TEMPERATE INTERTIDAL MUDFLATS BY USING PHYSICAL-BIOLOGICAL COUPLED MODELLING AND REMOTE SENSING DATA ANALYSIS

RAPHAËL SAVELLI

Doctoral thesis for the degree of Doctor of Philosophy in Science
LIttoral ENvironnement et Sociétés
Faculté des Sciences et Technologies
La Rochelle Université

2019 – version 1

SUPERVISORS:
Vincent Le Fouest
Christine Dupuy
Pierre Polsenaere

ABSTRACT

Intertidal mudflats at temperate latitudes are among the most productive ecosystems on Earth. Their high primary production (PP) is mostly supported by microphytobenthos (MPB). MPB form a dense biofilm at the surface of the mudflats during daytime low tides. They fix a high quantity of inorganic carbon into organic carbon through photosynthesis, which supports both benthic and pelagic food webs. With a global annual primary production estimated to ~ 500 million tons of carbon, MPB also participate to the Blue Carbon. Recent methods using physical-biological coupled modelling or remote sensing improve our capacity to assess the MPB biomass and PP in response to highly variable environmental conditions.

In the present thesis, we use a physical-biological coupled model to investigate the spatial and temporal variability of MPB dynamics on a large temperate intertidal mudflat, the Brouage mudflat (French Atlantic coast). The model explicitly simulates the MPB biomass within the surface biofilm and the first centimetre of sediment and the grazer (*Peringia ulvae*) biomass and density at the sediment surface. It is constrained by realistic atmospheric and tidal forcings and simulated mud surface temperature (MST). The outputs of the physical-biological coupled model fairly compare to time-coincident remotely-sensed and *in situ* data and provide key findings on MPB dynamics. Light and MST mostly constrain the seasonal cycle of MPB biomass on the intertidal mudflat. In winter and early spring, optimal light and MST conditions for MPB growth lead to a MPB spring bloom. Light is the most limiting driver over the year. However, a high MST limits the MPB growth 40 % of the time during summer. The photoinhibition of MPB photosynthesis can potentially superimpose on thermo-inhibition in spring and summer. With more frequent and longer emersion periods, the upper shore of the mudflat receives higher amount of light and might experience stronger photoinhibition than the lower shore. However, the lower shore might be more sensitive to photoinhibition due to its low MPB biomass, PP and its emersion periods restricted to high light levels. Grazing and resuspension of MPB biomass also shape the dynamics of the photosynthetically active and competent MPB biomass. In late spring and summer, a moderate grazing pressure by *P. ulvae* combines with thermo-inhibition to lead to a summer depression of the MPB biomass. In addition, bioturbation by *P. ulvae* contributes to a chronic export of MPB biomass from the sediment to the water column in spring and summer. Waves substantially contribute to the MPB resuspension through massive resuspension events in winter, spring and fall. 50 % of the annual MPB PP is exported to the water column through chronic and massive resuspension events. During the thesis,

we also developed a new method that combines remote sensing data with outputs of the physical-biological coupled model into a single algorithm that can predict PP from satellite data. This algorithm provides the first PP estimates at the mudflat scale.

A next step would be the coupling of the physical-biological model into a 3D high resolution ocean-biogeochemical coupled model in order to monitor and predict the MPB PP at the seasonal, annual and inter-annual scales and, ultimately, to improve our knowledge on the fate of MPB carbon in the coastal ocean in response to contemporary climate change.

PUBLICATIONS

1. Savelli, R., Méléder, V., Barnett, A., Polsenaere, P., Lavaud, J., Dupuy, C., and Le Fouest, V., Sensitivity of MPB photosynthetic capacity parametrisation in MPB PP predictive models from synoptic to seasonal scales, in prep.

2. Méléder, V., Savelli, R., Barnett, A., Polsenaere, P., Le Fouest, V. and Lavaud, J.: Coupling multispectral remote sensing and modelling to map intertidal microphytobenthos Gross Primary Production, *Frontiers in Marine Sciences*, in prep.

3. Savelli, R., Cugier, P., Méléder, V., Lavaud., J, Barnett, A., Polsenaere, P., Dupuy, C., Le Fouest, V.: Potential impact of microphytobenthos photoinhibition on primary production of a temperate intertidal mudflat, in prep.

4. Savelli, R., Bertin, X., Orvain, F., Gernez, P., Dalle, A., Coulombier, T., Pineau, P., Lachaussée, N., Polsenaere, P., Dupuy, C., Le Fouest, V.: Impact of chronic and massive resuspension mechanisms on the microphytobenthos dynamics in a temperate intertidal mudflat, *Journal of Geophysical Research: Biogeosciences*, in press.

5. Savelli, R., Dupuy, C., Barillé, L., Lerouxel, A., Guizien, K., Philippe, A., Bocher, P., Polsenaere, P., Le Fouest, V.: On biotic and abiotic drivers of the microphytobenthos seasonal cycle in a temperate intertidal mudflat: a modelling study, *Biogeosciences*, 15.23:7243-7271, 2018.

ACKNOWLEDGEMENTS

The research conducted during the thesis was funded by the Centre national d'études spatiales (CNES), the Centre National de la Recherche Scientifique (CNRS, LEFE-EC2CO program), the Région Nouvelle-Aquitaine and the European Union (CPER/FEDER) and the Groupement d'Intérêt Public (GIP) Seine-Aval PHARESEE project. The thesis was supported by a PhD fellowship from the French Ministry of Higher Education, Research and Innovation. It was also made possible thanks to the collaboration with IFREMER, which allows the access to the MARS-3D code and a space allocation on the computational center DATARMOR.

I thank my supervisors Vincent, Christine and Pierre who were always available to guide me during the thesis. Vincent and Pierre, in addition to scientific conversations, your advice have been really important for me personally. It is a great pleasure to learn and collaborate with you.

I would like to especially highlight collaborations with Xavier, Francis, Pierre (Gernez), Laurent, Vona, Pierrick, which result in fruitful scientific development and progress.

In addition, the scientific developments during the thesis was made possible thanks to the help of Nicolas, Philippe and Thibault for instrumentation and field campaigns. I would like to thank also Olivier, Alizée and Garance for their implication and their work as interns in the framework of the thesis.

I would also like to thank Thierry for his contribution to graphics and conceptual schemes presented in the thesis and Fabrice for his great work concerning my MT 180 sec layout displayed in the title page.

A special dedication goes to my dear fellow Jean-Remy, which made this 3 years more styley. Thibault and Mederic are also responsible of my daily good mood. A special thought for Barnabé.

My family contributed a lot in the accomplishment of this thesis so I am very grateful for their support in my professional and personal choices. And I am glad to have seen the birth of my nieces Jeanne and Romane during the thesis.

I want to thank in particular Laura who has always supported me, even during the dark times of the end of the thesis.

CONTENTS

LIST OF FIGURES

LIST OF TABLES

CHAPTER I

INTRODUCTION

1

INTRODUCTION

Acronyms:
EPS: *Extracellular Polymeric Substances*
MPB: *Microphytobenthos*
MST: *Mud Surface Temperature*
PP: *Primary Production*

Coastal ecosystems are among the most productive ecosystems in the world and provide numerous services to the human society (Millennium Ecosystem Assessment, 2005). Within coastal areas, tidal flats are defined as sand, rocky or mud flats that undergo regular tidal immersion. Tidal flats are one of the most represented coastal ecosystems on Earth (Healy et al., 2002; Murray et al., 2019). They are present from equatorial to polar latitudes (Fig. 1; Deppe, 2000). They are of key importance as they contribute to storm protection, shoreline stabilisation and support a high biological production constituting food resources for the millions of people that live on littoral worldwide (Millennium Ecosystem Assessment, 2005; Nicholls and Wong, 2007). With a high autochthonous production combined with inputs of allochthonous organic matter and low decomposition rates of organic matter, tidal flats are carbon sinks corresponding to Blue Carbon (Duarte et al., 2004; Mcleod et al., 2011). In the era of climate change and growing human footprint, tidal flats and their services are threatened by coastal development (Millennium Ecosystem Assessment, 2005; Arkema et al., 2013), sea-level rise (Passeri et al., 2015; Lovelock et al., 2017), coastal erosion (Nicholls and Wong, 2007) and reduced riverine sediment inputs (Syvitski et al., 2005; Blum and Roberts, 2009). These natural and anthropic pressures make uncertain the ecological equilibrium of tidal flats whose high biological production is partly supported by the microphytobenthic biofilm that colonize their sediment surface (MacIntyre et al., 1996; Underwood and Kromkamp, 1999).

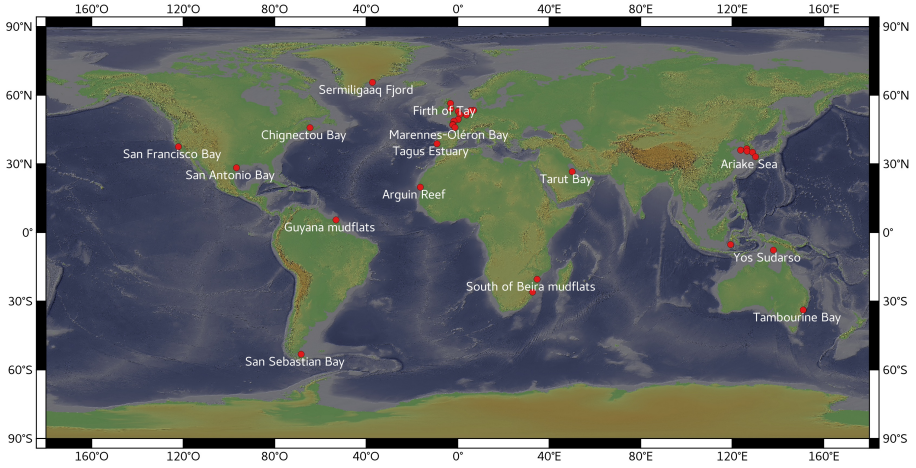

Figure 1: Examples of intertidal mudflats colonised by microphytobenthos (source: GEBCO and Lebreton et al., 2019).

WHAT ARE MICROPHYTOBENTHOS (MPB) OF INTERTIDAL MUDFLAT?

MPB is a generic term that regroups microalgae and photosynthetic bacteria that live in the upper millimetre of the sediment (*e.g.* diatoms, euglenids, dinoflagellates and cyanobacteria; MacIntyre et al., 1996; Paterson and Hagerthey, 2001). At temperate latitudes, MPB are dominated by diatoms (Admiraal, 1984; MacIntyre et al., 1996; Underwood and Kromkamp, 1999). In the present thesis, the further reference to MPB will refer to diatoms as considered dominant in MPB assemblages of the study site. MPB can be distinguished into three functional groups according to the nature of the sediment. Epipelic MPB are mainly composed by motile and free living diatoms. Epipsammic diatoms live in close association with sediment grains and their mobility is limited to the grain sphere. Finally, tychoplanktonic diatoms are able to grow both in the benthic and the pelagic compartment.

Epipelic diatoms dominate the MPB assemblage in very fine cohesive sediments where light is rapidly attenuated with depth in the sediment (see Box 1.1.1; Underwood, 2001). Epipelic diatoms can migrate up to the sediment surface during daytime low tides to receive sufficient light for photosynthesis. This vertical migration is made possible by excreting extracellular polymeric substances (EPS; Edgar and Pickett-Heaps, 1983). Consequently, their time window for photosynthesis is mainly restricted to low tides. The vertical motility in the sediment is therefore a way to remain in optimal conditions for growth and avoid harmful conditions related to tides, temperature, light, dessication, nutrients and grazing (Kingston, 2002; Saburova and Polikarpov, 2003; Consalvey et al., 2004). In addition to the tidal regime and photoperiods, this diel migration scheme is ruled by endogenous rythms that can be maintained over several days without any environmental change (Consalvey et al., 2004).

In contrast, epipsammic diatoms inhabit coarser and sandier sediments and live attached to sediment grain by a pad or short stalk of EPS (Underwood, 2001). Sandy sediments exhibit deeper light penetration (see Box 1.1.1). It results that, both during emersion and immersion, burried epipsammic MPB can maintain their photosynthetic activity if solar irradiance reaches the sea bottom and are therefore better adapted to subtidal area than epipelic MPB (Varela and Penas, 1985). Finally, tychoplanktonic cells live both at the surface of intertidal and subtidal sediments and in the water column (Vos and De Wolf, 1993). Depending on light conditions, they are photosynthetically active during low tides and during high tides if resuspended into the water column.

BOX 1.1.1

Light penetration in sediments and MPB biomass vertical distribution

In fine cohesive muddy sediments, the light penetrates up to 600 µm (Fig. 2; Cartaxana et al., 2011). The photic zone in sandy sediments is deeper (up to 3000 µm; Fig. 2; Cartaxana et al., 2011).

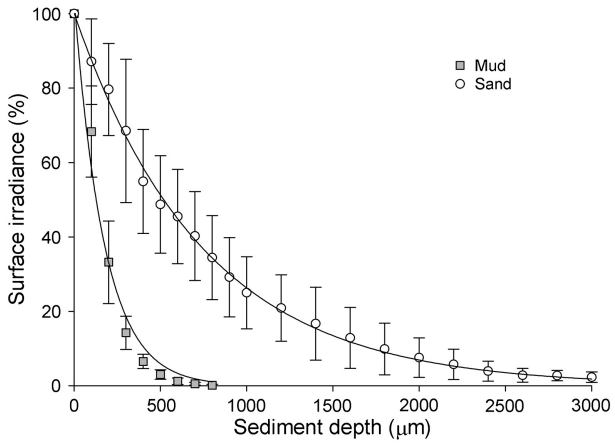

Figure 2: Percentage of surface irradiance (mean ± standard deviation) along depth profiles for intertidal muddy and sandy sediments (from Cartaxana et al., 2011).

Such vertical profile of light results in homogeneous 1-mm vertical profile of MPB biomass in sandy sediments, whereas the MPB biomass in muddy sediments is restricted to the upper hundred micrometers of the sediment (Cartaxana et al., 2011).

THE ENVIRONMENTAL DRIVERS OF MPB PHOTOSYNTHESIS

The spatial and temporal dynamics of MPB biomass and primary production (PP) is constrained by environmental factors that can be distinguished as abiotic or biotic divers.

Abiotic drivers

Light

Light is the major ecological factor driving the MPB photosynthesis (MacIntyre et al., 1996; Underwood, 2001). Considering both the light attenuation in the sediment and the full exposure of intertidal sediments, MPB have to adapt to

low and high light levels. Low light levels limit the MPB photosynthesis that does not exceed respiration losses. Consequently, light is a limiting factor for MPB photosynthesis deepward in muddy sediments and, in a lesser extent, in sandy sediments as it penetrates deeper (Kühl et al., 1995; MacIntyre et al., 1996; Kromkamp et al., 1998; Cartaxana et al., 2011). In addition, the attenuation of light in the sediment is accompanied by a variation of the spectral quality as infrared light penetrates deeper than the photosynthetically active visible light (Kühl and Jørgensen, 1992). Consequently, epipelic MPB inhabiting muddy sediments migrate at the sediment surface to meet their light requirements for photosynthesis. However, light levels reaching the sediment surface varies within an extremely wide range and on a short-term basis (Kühl et al., 1995). Irradiance at the mud surface can reach very high levels ($>$ 2000 µmol m^{-2} s^{-1}; Laviale et al., 2015). So that, MPB must develop adaptations to cope with such conditions.

Epipsammic diatoms use the Non-Photochemical Quenching of chlorophyll fluorescence (NPQ) to dissipate the excess of energy from light (XC; Lavaud and Goss, 2014). It corresponds to the de-epoxidation of xanthophyll pigments in the xanthophyll cycle (XC). In epipelic assemblages, low photoinhibition and low NPQ values indicate that the physiological photoprotection is not fully exploited and compensated by migration behavioural adaptations (Serôdio et al., 2001, 2012; Raven, 2011). In addition, "micro-migrations" within the sediment topmost layer ($\sim$ 250 µm) can be used by epipelic diatoms as a negative phototaxic short-term change of position (Kromkamp et al., 1998; Perkins et al., 2001; Cartaxana et al., 2011). While photoinhibition was successfully measured on MPB cells in laboratory experiments (Serôdio et al., 2012; Vieira et al., 2013), the MPB behavioural and physiological adaptations make scarce the observation of photoinhibition in the field (Serôdio et al., 2008).

BOX 1.2.1

Production-Irradiance curves for MPB photosynthesis

Several Production-Irradiance (P-I) models were used to study MPB photosynthesis as a function of light. The models of Platt and Jassby (1976), Webb et al. (1974), Chalker (1981) and Bannister (1979) that do not include photoinhibition was used (*e.g.* Barranguet et al., 1998; Uthicke and Klumpp, 1998; Dizon and Yap, 1999; Serôdio and Catarino, 2000; Guarini et al., 2000; Migné et al., 2004; Denis et al., 2012; Kwon et al., 2014, 2018; Rakotomalala et al., 2019).

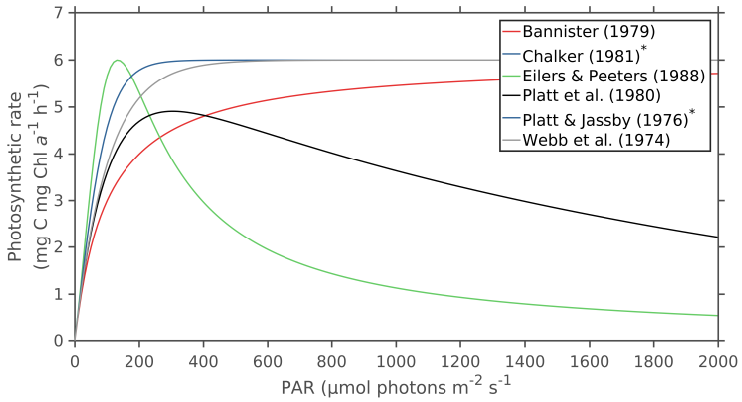

Figure 3: P-I models used in MPB studies (the asterisks indicate that P-I models use the same mathematical equation).

P-I models including photoinhibition of photosynthesis at saturating irradiance such as Eilers and Peeters (1988) and Platt et al. (1980) models were also used (*e.g.* Dodds et al., 1999; Goto et al., 2000; Herlory et al., 2007; Pniewski et al., 2015; Cartaxana et al., 2015; Vieira et al., 2016; Daggers et al., 2018).

Several P-I models are thus available for MPB studies. With or without photoinhibition, the choice must go to the model that exhibits the best adjustment to observations. Consequently, the use of P-I models in predictive models of MPB PP requires *in situ* or laboratory measurements to select the P-I model showing the best adjustment.

Temperature

The mud surface temperature (MST) significantly affects the MPB photosynthesis by changing the photosynthetic capacity (P^b_{max} in mg C mg Chl a^{-1} h^{-1}; Blanchard et al., 1996; Guarini et al., 1997). MPB at the sediment surface experience variations of MST on a short-term basis depending on prevailing

physical factors like solar irradiance, air temperature, wind, humidity and atmospheric pressure (Guarini et al., 1997). The short-term fluctuations of these factors depend on the time of the day, on the tidal cycle and on the meteorological conditions.

The hourly variations of the MPB photosynthetic capacity have been related to the fluctuation of the MST during low tides (Blanchard et al., 1996; Admiraal, 1984; Morris and Kromkamp, 2003; Salleh and McMinn, 2011). The photosynthetic capacity increases toward a temperature optimum and decreases beyond this optimum until any photosynthesis is precluded (Blanchard et al., 1996). The optimal and lethal temperature for MPB growth were reported to vary from 20 to 35 °C and from 30 to 40 °C, respectively (Blanchard et al., 1997a; Morris and Kromkamp, 2003; Hubas et al., 2006; Vieira et al., 2013; Rakotomalala et al., 2019). The seasonal variation of MST superimposes on the short-term fluctuations. In summer, the MST can be as high as 40 °C at midday and can alter the photosynthetic activity of MPB through thermoinhibition (Blanchard et al., 1996; Vieira et al., 2013). At extreme MST, the energy capture and electron transport for photosynthesis can be impeded (Vieira et al., 2013).

BOX 1.2.2

Seasonal adjustment of photosynthesis to temperature

Blanchard et al. (1997a) measured the variations of the photosynthetic capacity (P^b_{max} in mg C mg Chl a^{-1} h^{-1}) in response to changes of temperature on suspensions of MPB collected at each season on the Brouage mudflat (French Atlantic coast). They estimated the temperature-related parameters of the equation formulated by Blanchard et al. (1996):

$$P^b_{max} = P^b_{MAX} \times \left(\frac{T_{max} - T}{T_{max} - T_{opt}}\right)^{\beta} \times e^{\left(-\beta \times \left[\frac{T_{max}-T}{T_{max}-T_{opt}}-1\right]\right)}, \quad (1)$$

where T_{max} (°C) and T_{opt} (°C) are the maximum and optimal temperature for photosynthesis, respectively. β is a curvature coefficient that shapes the temperature-photosynthesis relationship. P^b_{MAX} (mg C mg Chl a^{-1} h^{-1}) is the maximum value that takes P^b_{max} at T_{opt}.

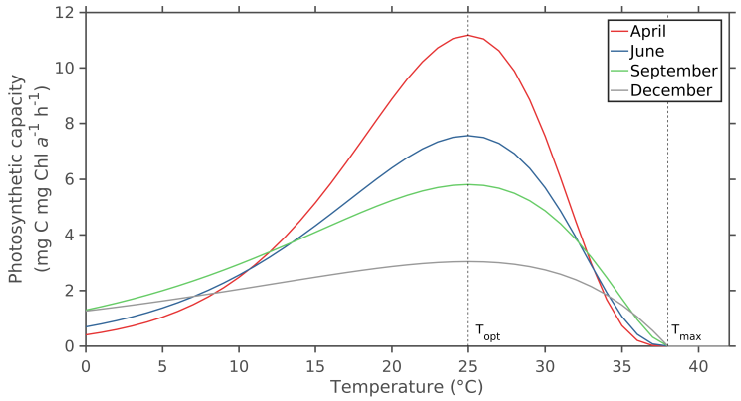

Figure 4: Relationship between P^b_{max} (mg C mg Chl a^{-1} h^{-1}) and temperature (°C) according to Blanchard et al. (1996).

Blanchard et al. (1997a) showed that P^b_{max} at T_{opt} was 3-fold higher in April than in December. No significant change was detected for T_{max} and T_{opt} over the year. The high P^b_{max} in spring coincides with the seasonal increase of the mud surface temperature and solar irradiance and is likely the driver of the spring bloom observed at their study site.

Salinity

The effect of changes in salinity in porewater on MPB photosynthesis is difficult to disentangle from the effect of other environmental factors as salinity can fluctuate with factors such as light, temperature and nutrients (Admiraal and Peletier, 1980; Underwood and Provot, 2000; Juneau et al., 2015). High solar irradiance and thus heating of the mud surface can lead to high salinity due to porewater evaporation in the upper layer of the sediment (Admiraal and Peletier, 1980). In addition, the increase of the riverine discharge in estuarine coastal waters decreases the salinity and increases nutrients concentrations in the water column (Ogilvie et al., 1997).

MPB diatoms were assumed to be highly tolerant to salinity changes (Admiraal, 1976; Admiraal and Peletier, 1980; Williams, 1964). The motility of epipelic diatoms is supposed to be a strategy to avoid harmful conditions at the surface of cohesive sediments (Consalvey et al., 2004). However, no significant negative effect of high salinity was detected on motility-deprived epipelic diatoms (Juneau et al., 2015). Their capacity to mitigate high-stress conditions through vertical migration depends on the rate of dessication of the sediment. In the study of Coelho et al. (2009), whereas the photosynthesis of the MPB biofilm was not affected by slow desiccation (reduction by 40 % of the porewater content in 4.5 h), it was reduced by fast desiccation (reduction by 40 % of the porewater content in 2 h). The resulting production of reactive oxygen can lead to the oxidation of the photosynthetic unit (Nishiyama et al., 2006). The excretion of EPS by epipelic diatoms is another protective mechanism that can dampen the effect of desiccation and high salinity (Steele et al., 2014).

pH

The pH reflects the inorganic carbon content within the sediment porewater. MPB exhibit high volume-specific rates of PP. The carbon dioxide (CO_2) assimilation within the photosynthetic layer of MPB results in a CO_2 depletion and a pH that can reach 9 (Revsbech and Jørgensen, 1986; de Jong et al., 1988). A high pH indicates a depletion in the concentration of dissolved inorganic carbon that might limit the MPB photosynthesis. Such a limitation is detailed in Section 1.2.2.1.

Tides and Hydrodynamics

Tidal regime is of key importance in determining the light and temperature levels at the sediment surface. The immersion-emersion cycle along with hydrodynamics also regulates the diffusive and advective transport of nutrients across the benthic boundary layer. In addition, the fortnightly tidal cycle drives longer and shorter emersion periods during spring and neap tides, respectively. It also drives the timing of emersion over the day, potentially leading to a high

light exposure during emersion occurring at noon. In contrast, emersion can occur early and late in the day and, as such, can lead to light limitation of the MPB photosynthesis. Therefore, a long emersion at noon (spring or neap condition depending on the geographical location) can be more optimal for MPB growth than a shorter emersion at low light levels early or late in the day (Kwon et al., 2014).

The variation of the seawater depth with tides is determinant for the waves-sea bottom interactions. The wave height and orbital velocity increase with the water depth until a critical depth is reached when orbital motions at the bottom start to decrease (Mariotti and Fagherazzi, 2013; Green and Coco, 2014; Li et al., 2019). Moreover, tidal current velocities over tidal flats are generally higher at mid-tide (Le Hir et al., 2000). The resulting combination of waves and tidal currents constrains the force exerted by the water movement on the sea bottom and drives MPB resuspension with or without any concomitant sediment resuspension (Mehta et al., 1989; Blanchard et al., 1997b; Wiltshire et al., 1998; Bassoullet et al., 2000; French et al., 2008; Dupuy et al., 2014; Orvain et al., 2014b). For example, de Jonge and van Beusekom (1995) associated the increase of resuspended benthic chlorophyll *a* with the increase of wind speed and resuspension of sediment in the Ems estuary (The Netherlands). Chlorophyll *a* pigments originating from MPB biofilms were also measured in the water column without any concomitant bed failure (Blanchard et al., 1997b; Wiltshire et al., 1998; Dupuy et al., 2014; Orvain et al., 2014b). The resuspended chlorophyll *a* pigments originating from the sediment in the absence of bed failure were associated to the resuspension of the biogenic fluff layer at the sediment surface. The fluff layer is formed through the action of bioturbation (grazing, crawling and egestion) by benthic deposit-feeders at the sediment surface. The fluff layer contains MPB cells and sediment grains and are more easily eroded than the sediment (Davis, 1993; Blanchard et al., 1997b; Willows et al., 1998; Andersen, 2001; Orvain et al., 2003; Le Hir et al., 2007).

While not directly affecting MPB photosynthesis, MPB resuspension acts on the MPB biomass within the sediment and thus on the photosynthetically competent biomass (MacIntyre and Cullen, 1995). Such synoptic variations of MPB biomass can impact locally the MPB PP. Finally, sediment resuspension along with MPB can alter indirectly the MPB photosynthesis through the increase of the water column turbidity. The increase of water turbidity was shown to decrease the light and temperature at the sediment surface with, as a result, the MPB photosynthesis in subtidal mudflats (Pivato et al., 2019).

Biotic drivers

Nutrients

In seawater, the diffusion of CO_2 from the water into phytoplankton cells is generally too low to match the rate of photosynthesis. However, microalgae are generally not limited by CO_2 as they develop carbon concentrating mechanisms in order to actively transport CO_2 and bicarbonate across the cell membrane and maintain efficient photosynthetic rates (Raven, 1997). Despite carbon concentrating mechanisms, the local depletion in dissolved inorganic carbon within dense photosynthetic biofilms due to CO_2 assimilation may result in the limitation of MPB photosynthesis. While no significant increase of MPB biomass with increasing air CO_2 concentration was detected by Hicks et al. (2011), enrichment experiments exhibited contrasting results. Torstensson et al. (2012) reported a negative effect of dissolved CO_2 enrichment on the biomass and growth rate of benthic diatoms in suspensions. In contrast, in the dissolved CO_2 enrichment experiment conducted by Cartaxana et al. (2015), low temperature microcosms exhibited a high MPB biomass at low pH (7.4). The bicarbonate enrichment of MPB suspensions by Vieira et al. (2016) caused an increase of the MPB photosynthetic rate, suggested a likely *in vitro* limitation by dissolved inorganic carbon.

In coastal estuarine waters, the nutrients load is high compared to open ocean waters. Anthropogenic sources in nitrogen and phosphorous add to the natural riverine nutrients inputs (Cloern, 2001). Inorganic nutrients can be exchanged between the water column and the sediment upper layer porewater by advective and diffusive transport (*e.g.* Zabel et al., 1998; Jahnke et al., 2003). The sediment porewater is particularly enriched by mineralisation of organic matter within the sediment (Deborde et al., 2008). The nutrients porewater content varies with the nutrients adsorption on organic or mineral compounds and the uptake by MPB (Mackin and Aller, 1984; Coelho et al., 2004). Nevertheless, the pool of nutrients in the sediment porewater is often considered as an inexhaustible source of nutrients (Cibic et al., 2008).

Epipelic diatoms are also able to locate nutrient- depleted and enriched zones by combining chemokinetic and chemotactic motility for dissolved silicate and phosphate (Bondoc et al., 2016, 2019b,a). In addition to the uptake of nutrients from the porewater, benthic diatoms can grow on the intracellularly-stored pool of ammonium, phosphate and silicate (Martin-Jézéquel et al., 2000; García-Robledo et al., 2010; Yamaguchi et al., 2015). The MPB affinity to ammonium is high due to its reduced molecular state and energetically-favourable assimilation (Feuillet-Girard et al., 1997; Sanz-Luque et al., 2015; Glibert et al., 2016). Motile epipelic MPB have the ability to access nutrients in deep sediment layers. Unbalanced C/N cell quota within the biofilm is an hypothesis for explaining the cells turnover at the sediment surface in order to re-equilibrate the C/N quota by taking up carbon in the photic zone and nitrogen in the aphotic zone

(Rakotomalala et al., 2019). In addition, in nutrient-depleted conditions, MPB can exudate carbon through EPS excretion (Staats et al., 2000; Rakotomalala et al., 2019).

The faunal activity in the upper layer of sediment can alter the nutrients availability at the sediment- water or air interface. The excretion of dissolved nutrients like ammonium (Prins et al., 1997; Martin et al., 2006; van Broekhoven et al., 2015) and the enhanced mineralisation of organic matter through biodeposition (*e.g.* by suspension-feeders) or bioturbation (Kristensen, 2000; Mermillod-Blondin and Rosenberg, 2006) by benthic fauna can enrich the sediment and promote directly or indirectly MPB growth (Chennu et al., 2015; Engel et al., 2017; Androuin et al., 2018; Echappé et al., 2018). Benthic fauna can potentially control MPB biomass directly through grazing and indirectly through mineralisation (Rakotomalala et al., 2019). High levels of MPB biomass were observed in presence of engineering species such as lugworms, oysters, mussels and slipper limpets (Chennu et al., 2015; Engel et al., 2017; Androuin et al., 2018; Echappé et al., 2018).

Grazing

Grazing pressure acts on MPB photosynthesis via the regulation of the photosynthetically active and competent biomass. Grazers can be benthic meiofauna (*e.g.* Blanchard, 1991; Lebreton et al., 2012) and macrofauna (*e.g.* Blanchard et al., 2000a; Peer et al., 2019), demersal fishes (*e.g.* Como et al., 2014), shorebirds (*e.g.* Jardine et al., 2015) and, once resuspended in the water column, suspensive feeders plankton (*e.g.* Perissinotto et al., 2003), fishes (*e.g.* Krumme et al., 2008) and sessile suspensive filter feeders (*e.g.* Smaal and Zurburg, 1997). The grazing pressure by benthic fauna on intertidal mudflats can be so high that it can drive local and potentially seasonal depletion of MPB biomass, especially in summer (Cadée and Hegeman, 1974; Cariou-Le Gall and Blanchard, 1995; Sahan et al., 2007; Orvain et al., 2014a). Morrisey (1988) reported a decrease by up to 30 % of the MPB cells abundance along with an increasing density of gastropod *Peringia ulvae* and amphipod *Corophium arenarium*. In the experiment conducted by Weerman et al. (2011), the addition of benthic fauna induced a strong decrease in MPB biomass driven by direct grazing and the absence of mud stabilisation due to bioturbation compared to treatments without fauna.

The potential of grazing to decrease the MPB biomass is also related to environmental factors such as light, MST, nutrients and hydrodynamics (Miller et al., 1996). Depending on the MPB growth conditions, the MPB PP could overcome the grazing pressure. Meanwhile, grazing intensity can also be promoted by external factors such as temperature. Thompson et al. (2000) suggested that the depression of the benthic microalgal biomass in summer resulted from the combination of light- and temperature- inhibited microalgal PP with temperature-promoted grazing. Locally, the grazing intensity can overcome the MPB growth and biomass accumulation supplemented by the deposi-

tion of resuspended MPB cells (Miller et al., 1996). However, the local depletion of MPB biomass through grazing can turn into an increase of the MPB growth rate due to a reduced MPB cells density (Admiraal et al., 1983).

ON THE NEED TO BETTER DECIPHER MPB DYNAMICS

The current intertidal and subtidal MPB dynamics results from the balance between the different environmental drivers. More importantly, such an equilibrium contributes to maintain the sustainability of ecosystem services provided by MPB.

Carbon storage

In shallow water areas such as subtidal and intertidal zones, MPB PP can be high and equal or exceed the phytoplankton PP (Underwood and Kromkamp, 1999). MPB exhibit high production rates ranging from 0 to 1.9 g C m^{-2} d^{-1} and from 29 to 314 g C m^{-2} yr^{-1} (Underwood and Kromkamp, 1999, and references within). In the Marennes-Oléron Bay (French Atlantic coast), the MPB annual PP was estimated equal to two-fold higher than that of phytoplankton (Leguerrier et al., 2003; Struski and Bacher, 2006). In the highly turbid Colne Estuary (UK), the phytoplankton annual PP was light-limited and estimated to 8.9 g C m^{-2} yr^{-1} (Kocum et al., 2002), which is 134-fold lower than the estimated range of MPB PP in the intertidal zone of the estuary (Thornton et al., 2002). In addition, once resuspended, MPB can contribute to the pelagic PP (Guarini et al., 2008b; Polsenaere et al., 2012).

With a global annual primary production estimated to ~ 500 million tons of carbon (Cahoon, 1999), MPB participate to the Blue Carbon (Otani and Endo, 2019). Guarini et al. (2008b) suggested that the high MPB PP was not accounted for in the global carbon cycle, making its contribution uncertain. The alteration of tidal flats under the effect of coastal development (Duraiappah et al., 2005; Arkema et al., 2013), sea-level rise (Passeri et al., 2015; Lovelock et al., 2017), coastal erosion (Nicholls and Wong, 2007) and reduced riverine sediment inputs (Syvitski et al., 2005; Blum and Roberts, 2009) might impact the carbon storage ensured by MPB PP. The loss of such an ecosystem service might have catastrophic consequences for natural and human systems as it contributes to the uptake of anthropogenic CO_2 emissions.

Trophic resource

In addition to carbon storage, MPB PP largely supports secondary production in shallow water systems (Daehnick et al., 1992; Moncreiff et al., 1992; Miller et al., 1996). Diet analysis underlined the importance of MPB in the diet of ben-

thic macrofauna (Herman et al., 2000) and meiofauna (van der Heijden et al., 2019). The high abundance and PP of MPB combined with its high nutritional quality (high nitrogen and phosphorus content, low refractory compounds) make MPB a reliable food resource (Moncreiff and Sullivan, 2001; Lebreton et al., 2009; van der Heijden et al., 2018).

Also, resuspended MPB supplement the pelagic food webs as it is consumed by suspensive feeders plankton (*e.g.* Perissinotto et al., 2003), fishes (*e.g.* Krumme et al., 2008) and sessile suspensive filter feeders (*e.g.* Smaal and Zurburg, 1997). For example, farmed bivalves such as oysters and mussels ingest MPB (Leroux, 1956; Paulmier, 1972; Newell et al., 1989). Riera and Richard (1996) highlighted the major contribution of MPB in the diet of oysters. Finally, an increase of the export of particulate organic carbon from the benthic compartment to the water column might fuel the pelagic carbon production (Saint-Béat et al., 2014). Any change in the current equilibrium between MPB and secondary producers is likely to upset the functioning of natural systems and ecosystem services such as the support of economical activities like shellfishes farming.

Nutrients exchanges

The presence of dense MPB biofilms at the sediment surface can modify the nutrients fluxes across the benthic boundary layer. MPB biofilms take up and assimilate nutrients from the overlying water column and from sediment porewater. The release of dioxygen in the photic sediment layer during MPB photosynthesis increases the depth of the oxic layer. The activity of aerobic decomposers is then stimulated and decreases the vertical export through diffusion of reduced forms of nutrients at the sediment-water interface (Underwood, 2001).

The assimilation of nutrients at the sediment surface by MPB is closely related to coupled bacterial nitrification-denitrification processes (Sundbäck et al., 2000; Risgaard-Petersen et al., 2004). Bacteria transform and remove available nitrogen into dinitrogen. The rate of denitrification relies on available nitrate and ammonium concentrations diffusing from the water column and from the sediment porewater to the sediment-water interface. Consequently, MPB alter the availability of ammonium and nitrate for nitrifying and denitrifying bacteria, respectively (Nils, 2003; Risgaard-Petersen et al., 2004). Finally, the increase of the oxic sediment surface layer due to MPB photosynthesis reduces the denitrification that is an anaerobic process (Rysgaard et al., 1995). MPB play therefore a role in the nutrients retention through their intracellular storage, growth and assimilation. Nutrients cycling within sediment upper layers is a bottom-up process. It controls the nutrients availability for MPB photosynthesis and thus the subtidal and intertidal PP, which sustains both benthic and pelagic food webs.

Morphodynamics of tidal flats

The excretion of EPS by benthic diatoms binds silt and clays. As a result, the presence of MPB decreases the probability of sediment erosion by stabilizing the sediment upper layer, which can turn into sediment accumulation through sediment deposition (Paterson, 1989; Madsen et al., 1993; Underwood and Paterson, 1993; Austen et al., 1999; Decho, 1990, 2000; Stal, 2010; Pierre et al., 2010, 2012). The biostabilisation by MPB was described as a positive feedback in which a high MPB biomass in the sediment leads to a higher resistance to erosion hence promoting MPB biomass accumulation in the sediment (Pivato et al., 2019). Such a feedback leads to the formation of spatial patterns of MPB colonisation as uncolonised spots may be hostile for MPB biomass establishment and accumulation.

The presence of ridges and runnels on intertidal mudflats is an example of a spatial self-organisation resulting from the biota-geomorphology interaction (Blanchard et al., 2000b). Runnels formed through the action of strong ebb currents correspond to channels that drain seawater seaward. Consequently, MPB preferentially colonise ridges and make them more resistant to erosion (Blanchard et al., 2000b). Therefore, tidal currents will erode the uncolonised runnels and will deposit sediment on the MPB-inhabited ridges, pending for consolidation. Such a process generates a regular self-organised pattern of MPB and geomorphological structures (van de Koppel et al., 2001). It results into a high stability of the mudflat system increasing the ecosystem biological production of organic matter but also its resistance and resilience to physical forcings like waves and currents (Stal, 2010; Pivato et al., 2019). The biostabilisation by plants such as halophytic vegetation and MPB biofilms is suggested to be a key component of tidal morphological equilibrium (Marani et al., 2010). In conclusion, even distributed in patchiness, MPB might drive the long and short term morphodynamic of the intertidal mudflats.

OBJECTIVES OF THE THESIS

In view of the physical and biological factors involved, the spatial and temporal dynamics of MPB is highly variable. Efforts to integrate the physical and biological linkage are therefore needed in order to better understand the MPB dynamics at the scale of intertidal mudflats. However, the large extent and composition made of fine cohesive sediments of intertidal mudflats make them difficult to study and monitor on the field at the appropriate spatial and temporal scales. The main objective of the present thesis is to investigate the drivers involved in the spatial and temporal dynamics of MPB and to quantify their relative contribution at the synoptic to seasonal time scale. To meet this goal, we used an approach that combines numerical modelling, remote sensing

and *in situ* data analysis. The approach was applied to the Brouage intertidal mudflat (French Atlantic coast; see Box 1.4.1).

- The first specific objective is to quantify the contribution of the main abiotic (light, temperature, tides, waves, currents, biostabilisation) and biotic (grazing, bioturbation) drivers in the spatial and temporal variability of the MPB primary production;
- The second objective is to assess the export of MPB biomass from the benthic to the pelagic compartment and its temporal variability;
- The third objective is to investigate the potential of coupling physical-biological modelling and remote sensing to monitor MPB PP at the mudflat scale.

In the present thesis, we first describe the MPB modelling approach and the model developed during the thesis to answer our 3 specific objectives (Chapter 2). In Chapter 3, we study the seasonal cycle of MPB in relation to environmental factors. In Chapter 4, we assess the role of chronic and massive resuspension on MPB temporal dynamics by introducing waves and current forcings. Then, in Chapter 5, we extend our comprehensive view of MPB dynamics by using a tri-dimensional model to assess over the whole Brouage mudflat the potential impact of photoinhibition on MPB PP. Finally, in Chapter 6, we propose a new monitoring tool that combines *in situ* and laboratory data, satellite and physical-biological modelling in order to map MPB PP at the whole mudflat scale. The thesis aims to bring new insights on the organic matter fluxes at the land-ocean continuum and to contribute to a more accurate assessment of the role of MPB in the coastal carbon cycle.

BOX 1.4.1

Les Pertuis Charentais: a relevant site for MPB studies

The Pertuis Charentais Sea is a coastal ecosystem under pressure that provides multiple services to people living in the littoral zone. It is a shallow semi-enclosed sea that hosts one of the biggest shellfish farming activities in Europe (Goulletquer, 1998). It receives riverine inputs originating from the agricultural watershed of the Sèvre, Charente and Seudre rivers (Fig. 5). The area also exhibits a high tourist attendance as it welcomes, especially during summer, a major part of the almost 10 millions overnights of the Charente-Maritime (source: Charentes Tourisme). In the southern part of the Pertuis Charentais, the Brouage mudflat is an 42-km^2 intertidal mudflat composed of fine cohesive sediments (Bocher et al., 2007).

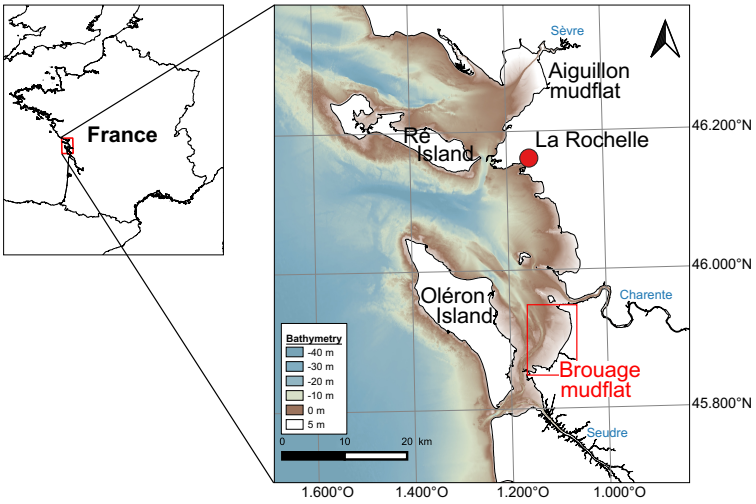

Figure 5: Bathymetry of the Pertuis Charentais Sea with its main intertidal mudflats (source: French marine service for hydrography and oceanography (SHOM)).

As in many mudflats along the northern European Atlantic coast, a dense biofilm of MPB develops at the sediment surface at low tide and reaches up to 25 mg Chl *a* m^{-2} (Herlory et al., 2004).

The Brouage mudflat was studied since the nineties and, the presence of a well-developed MPB makes it a relevant site for studying the spatial and temporal dynamics of MPB.

CHAPTER II

MICROPHYTOBENTHOS MODELLING

While first attempts to simulate phytoplankton dynamics date back to Fleming's work in 1939, efforts to simulate MPB dynamics are relatively new and the drivers involved are still in debate. In Chapter 2, we present a short state of the art of MPB modelling and how it all began with phytoplankton. The objective is to highlight the models ability to test hypotheses on MPB dynamics. We also give details about the mud surface temperature and MPB models developed during the thesis. They could serve as a framework for improvements and developments such as their coupling to high resolution tri-dimensional (3D) models.

2

MICROPHYTOBENTHOS MODELLING

The coupled physical-biological MPB model presented in this chapter was published in an article in the journal Biogeosciences (Savelli et al., 2018).

Acronyms:
EPS: *Extracellular Polymeric Substances*
MPB: *Microphytobenthos*
MST: *Mud Surface Temperature*
NDVI: *Normalised Difference Vegetation Index*
PP: *Primary Production*

Biological modelling is a relevant tool to understand complex biological systems and can extend the temporal and spatial coverage of observational data. Models are always based on observations. As such they can bring insights on the mechanisms in play behind the observations.

THE ORIGINS

Biological models were initially developed for demographic purposes when Graunt (1662) used mortality data to estimate human population density. A hundred years later, Malthus (1798) depicted growth of human population as an exponential growth. Verhulst (1845) introduced the notion of carrying capacity in the Malthus growth model, which tempers the exponential growth according to the maximal population size sustainable by the ecosystem. In the mid-1920s, Lotka and Volterra developed the prey-predator model to explain the relationships between prey and predator densities such in fish populations (Lotka, 1925; Volterra, 1926). The first plankton model was introduced by Fleming (1939) in order to describe the role of grazing on the phytoplankton temporal variability. Despite important simplifications and assumptions (negligible phytoplankton sinking, cell death and advection, no light and nutrient limitation and linear increase of grazing in time), the author obtained a relatively good agreement between model and *in situ* data. Fleming's approach highlighted the need to better understand zooplankton ingestion and growth to explain phytoplankton temporal dynamics. Based on the work of Fleming, Riley developed several phytoplankton models by improving the Fleming's assumptions (Riley, 1946). In addition to the grazing rate varying according observed zooplankton density, he introduced the variation of phytoplankton growth rate as a function of light intensity, water transparency, light penetration, nutrients, turbulence (mixed layer *vs.* euphotic zone depths) and respiration. Riley improved its first mass flux model by adding zooplankton and nutrient dynamics (phosphate; Riley, 1947, 1949). On the basis of Riley's model, Steele developed a nutrient-phytoplankton-zooplankton (NPZ) food chain model including nutrient and plankton dynamics within the oceans surface mixed layer enriched by nutrients fluxes from depth (Steele, 1958). Besides of estimating phytoplankton production and dynamics, Steele benefited the improvement in computation to perform sensitivity analysis on parameters values and mathematical formulations of his equations.

The models developed by Fleming (1939), Riley (1946) and (Steele, 1958) were pioneering works in mass flux ecosystem modelling of plankton. The principle of mass flux ecosystem models relies on the mass-balance between influxes and outfluxes of matter plus changes in biomass within a closed system where mass is conserved. Mass fluxes in these models are generally expressed in units of carbon, nitrogen or phosphorous. It will be some decades before mass flux ecosystem modelling spreads to MPB. In the 1960s, the first MPB modelling works consisted in the extrapolation of MPB PP measured at the synoptic hourly scale to daily and annual scales using a relationship with irradiance (Pomeroy, 1959; Leach, 1970; Marshall et al., 1971; Joint, 1978; Riznyk et al., 1978; Zedler et al., 1978; Zedler, 1980; Shaffer and Onuf, 1985). Using a model that accounted for tides and irradiance variations, Pinckney and Zingmark (1991) suggested that, because MPB PP varied too much at the hourly scale, such simple extrapolations were likely to result in large errors.

THE SHORT-TERM VARIABILITY OF MPB BIOMASS AND PRIMARY PRODUCTION

Pinckney and Zingmark (1993) developed the first MPB mathematical model to better assess the annual primary production (PP) of MPB without making extrapolations. The objective was to include the day-to-day variability of MPB PP related to light conditions, tides and MPB vertical migration. The simulated daily MPB PP was consistent with the monthly measurements in five different light-attenuated habitats. In addition, the authors used the model to test the sensitivity of the MPB PP to irradiance.

Brotas and Serôdio (1995) developed a model to describe the vertical distribution of MPB biomass from MPB biomass measured at the surface of muddy sediments. Their model was parametrised with a fixed degradation rate of chlorophyll *a* (*i.e.* senescence, grazing) and a burial rate representing the downward migration of MPB. The model estimates were in good agreement with the measured vertical profiles of MPB biomass. In contrast, the simulated decreasing exponential profile of MPB biomass was less satisfactory in sandy sediments.

The model of Pinckney and Zingmark (1991) and Pinckney and Zingmark (1993) was modified by Serôdio and Catarino (2000) to describe hourly variations of chlorophyll *a* fluorescence at the sediment surface. The authors assumed that the hourly variability of the MPB photosynthetic activity was caused by variations of the photosynthetically active biomass in the photic layer of the sediment due to MPB migration. They used the MPB biomass at the sediment surface expressed in fluorescence unit (F_0) to predict the short-term variations of the photosynthetic light response. The authors estimated F_0 as a function of tides and irradiance at the hourly scale. Then, they obtained photosynthetic parameters from hourly estimates of F_0 with empirical relationships and computed MPB production with a P-I model. From consistent hourly rates of MPB

production, they estimated MPB annual production in time and space at the scale of the Tagus Estuary (Portugal).

Guarini (1998) used the works of Blanchard et al. (1996), Blanchard et al. (1997a) and Guarini et al. (1997) to develop a discrete 2-layer mass flux model of intertidal MPB biomass accounting for light, mud surface temperature (MST), tides and MPB vertical migration at the mud surface. The model simulated the MPB biomass in the sediment first centimetre and in the surface biofilm. The total simulated MPB biomass compared with measurements made over 15 days at different tidal levels of an intertidal mudflat.

MPB IN MASS FLUX ECOSYSTEM MODELS

Subtidal MPB was first introduced as a benthic primary producer in an ecosystem model of Port Phillip Bay in Australia to study the effect of varying nitrogen load in this semi-enclosed area (Murray and Parslow, 1997). MPB PP was related to light, temperature, nutrients, biomass and maximum growth rate of MPB. MPB mortality was represented through a quadratic mortality rate to represent an increased predation rate at higher MPB densities. The authors suggested that the ammonium uptake by MPB limited the coupled nitrification-denitrification process. The consideration of different primary producers (MPB, seagrass, macroalgae) in the bay tempered the response of the system to increasing nitrogen load, because the capacity of the system to cope with high nitrogen loads varied in space.

Blackford (2002) introduced a MPB module in the European Regional Seas Ecosystem Model (ERSEM; Baretta et al., 1995). They inferred on the role of subtidal MPB in an one-dimensional (1D) ecosystem model of the Northern Adriatic Sea. They parametrised the MPB compartment as they did for the phytoplankton compartment but with specific parameters that related its response to light, temperature and nutrients (nitrogen, phosphorous, silica) limitation, respiration, senescence and grazing. The authors highlighted the substantial contribution of MPB to the total PP in shallow waters. In addition, the presence of MPB affected the benthic compartment by increasing benthic carbon fixation through photosynthesis, by enhancing higher detritus uptake by benthic grazers and by promoting the activity of aerobic decomposers in the surface layer of the sediment. However, the authors did not detect any effect of MPB on the dynamics of the phytoplankton community.

In their study, Hochard et al. (2010) introduced subtidal MPB activity in the biogeochemical model OMEXDIA (Soetaert et al., 1996) run in a 1D configuration for the Florida Bay, a semi-enclosed, shallow, sub-tropical estuary in southern Florida (USA). The MPB growth was related to light, temperature and nutrients as well as EPS exudation. The MPB PP was simulated with the phytoplankton cell quota model of Geider et al. (1998). Cell quota models allow for a variable chlorophyll a/C mass ratio and account for a dynamic carbon/ni-

trogen molar ratio in phytoplankton cells. The model suggested that MPB enhanced mineralisation at the sediment surface due to the production of EPS and inhibited the coupled nitrification-denitrification bacteria that reduced the export of nutrients from the sediment to the water column. By adding physical forcings (waves and currents) in a similar biogeochemical model, Hochard et al. (2012) showed that the physical forcings can overcome the nutrient retention capacity of MPB at the sediment surface by light-limiting MPB PP through sediment resuspension and by increasing the rate of nutrients exchanges from porewater to the water column.

In the modelling work of Brito et al. (2011) applied to a Portuguese lagoon, subtidal MPB growth depended on light, temperature and on the uptake of nutrients flux from the sediment and of nutrients supply from the water column. The MPB photosynthetic rate as a function of light was modulated by MPB vertical migration. The authors succeeded to simulate the MPB biomass within the range of variability of observations (Brito et al., 2010). In contrary to Blackford (2002) but similarly to Hochard et al. (2012), the study of Brito et al. (2011) highlighted the role of MPB in nutrients retention at the seawater-sediment interface.

Recently, Rakotomalala et al. (2019) developed a model based on the modelling approach of Guarini (1998) and on the phytoplankton cell quota model of Geider et al. (1998). The objective was to analyse the biogeochemical functioning of an intertidal benthic system including epipelic MPB, associated EPS, bacteria and nutrients dynamics. The model accounted for the vertical migration of MPB as a function of light and tides but also of the carbon and nitrogen cell requirements. They remained at the surface until carbon exceeded nitrogen cell content. In the aphotic sediment layer, if nitrogen exceeded the carbon cell content, MPB migrated upward at the sediment surface during daytime low tides. Such a parametrisation of MPB migration gave satisfactory results compared to observations in tidal mesocosms. In the model, nutrients depletion was shown to limit the MPB growth in the absence of faunal-enhanced nutrients diffusion and availability (bioturbation, bioirrigation, secretion). Subsequent sensitivity analysis revealed that the diffusion of nutrients within the sediment was enhanced by faunal activity.

THE COUPLED PHYSICAL-BIOLOGICAL MPB MODEL

The coupled model consisted of a mud temperature model coupled to a biological model. In order to quantify the contribution of the abiotic and biotic drivers in the MPB spatial and temporal dynamics, we extended the work of Guarini (1998) which represented the dynamics of MPB biomass within the sediment and at the surface of the intertidal mudflat in a 2-layer mass flux model. We added a third layer that accounted for the dynamics of *P. ulvae* at the sediment surface, a very abundant MPB grazer on the intertidal mudflats of the Pertuis

Charentais (Sauriau et al., 1989). The model used realistic meteorological and tidal forcings in order to simulate the MST and the MPB biomass and PP.

Mud temperature model

The original version of the mud temperature model of Guarini et al. (1997) is simplified by only resolving the MST (K) which is governed by the following equation during emersion periods:

$$\rho_M C_{P_M} \frac{\partial T_M(z_0,t)}{\partial t} = f(T_M(z_0,t)), \tag{2}$$

where $f(T_M(z_0,t))$ is the heat energy balance (HEB, W m^{-2}) at the sediment surface z_0 (m) at time t (s). This sediment surface layer is 1-cm deep. The temperature (K) is assumed to be homogeneous within the layer and is governed by the HEB (Harrison and Phizacklea, 1987; Piccolo et al., 1993). ρ_M is the volumetric mass of mud (kg m^{-3}) *i.e.* the sum of the water and dry sediment fractions ($\rho_M = \rho_W \xi + \rho_S(1-\xi)$ where ρ_W and ξ are the water volumetric mass (kg m^{-3}) and the porosity (%), respectively. C_{P_M} is the specific heat capacity of mud at constant pressure (J kg^{-1} K^{-1}):

$$C_{P_M} = \frac{\eta}{\mu \rho M}, \tag{3}$$

where η is the heat conductivity (W m^{-1} K^{-1}) and μ the thermal diffusivity (m^2 s^{-1}). Heat exchange fluxes at the sediment surface are different according to the emersion-immersion cycle. During low tide, the HEB is governed by fluxes of radiation from the sun (R_S, W m^{-2}), the atmosphere (R_{Atm}, W m^{-2}), the mud surface (R_M, W m^{-2}), by conductive sensible heat fluxes due to mud-air temperature differences ($S_{Mud \to Air}$, W m^{-2}) and by evaporative heat flux (V_M, W m^{-2})(Fig. 6):

$$f(T_M(z_0,t)) = R_S + R_{Atm} - R_M - S_{Mud \to Air} - V_M \text{ with } V_M = \xi V_W, \tag{4}$$

where ξ is the mud porosity ($\xi \in [0,1]$, %) and V_W is the seawater evaporative heat flux (W m^{-2}). Details about equations and parameters governing fluxes during emersion are given in Tables 1 and 2.

During immersion periods, Guarini et al. (1997) and Harrison and Phizacklea (1987) suggested a rapid equilibrium between MST and the temperature of the overlying water layer. The simulated MST is therefore set to water temperature during immersion periods:

$$T_M(z_0,t) = T_W(t), \tag{5}$$

The simulated seawater temperature of the whole water column (T_W) results from the mixing of the surface layer (z_{top}, *i.e.* the mixed layer) with the bottom

Table 1: Equations of the processes involved in the sediment temperature model

Process	Symbol meaning
Atmospheric and solar radiation	
$R_{sth} = R_0 sin(h)(1 - A)$	R_{sth} : cloudless sky theoritical solar radiation
formulated by Brock (1981)	R_0 : solar constant
	h : sun height
	A : albedo
$R_{Atm} = \varepsilon_A \sigma T_A^4 (\zeta - k)$	ε_A: emissivity of air
	σ: Stephan-Boltzman constant
	T_A : measured air temperature
	ζ: constant ($2 \geqslant \zeta \geqslant 1$)
	k: attenuation coefficient imposed to 1 if greater than 1. During night periods, k is an average of the values 2 h before the night.
$\varepsilon_A = 0.937 \times 10^{-5} T_A^2$	
$k = \frac{R_S}{R_{sth}}$	R_S: solar radiation
$sin(h) = sin(\delta)sin(\phi) + cos(\delta)cos(\phi)cos(AH)$	δ: declination of the sun
	ϕ: latitude of the area
	AH: true horary angle
Mud and Water radiation	
$R_M = \varepsilon_M \sigma T_M^4(z_0, t)$	ε_M: emissivity of mud
$R_W = \sigma T_W^4(t)$	
Conduction	
$S_{Mud \to Air} = \rho_A C_{P_A} C_{h_{M \to A}} \left(1 + \frac{U}{10}\right) (T_M(z_0, t) - T_A)$	ρ_A: air volumetric mass
	C_{P_A}: specific heat of air at constant pressure
	$C_{h_{M \to A}}$: bulk transfer coefficient for conduction between mud and air
	U: wind speed measured at 10 m
$S_{Air \to Water} = \rho_A C_{P_A} C_{h_{A \to W}} (1 + U) (T_W(t) - T_A)$	$C_{h_{A \to W}}$: bulk transfer coefficient for conduction between air and water
Evaporation	
$V_W = \rho_A L_V C_V (1 + U) \left[q_S \left(1 - \frac{q_A}{q_S}\right)\right]$	L_V: latent heat evaporation
	C_V: bulk transfer coefficient for evaporation
	q_S: specific humidity of saturated air at water temperature
$q_A = q_S H_r$	q_A: absolute air humidity
$L_V = [2500.84 - 2.35 (T_E - 273.15)] \times 10^3$	H_r: relative air humidity
formulated by van Bavel and Hillel (1976)	T_E: temperature of interstitial water (in equilibrium with mud temperature)
$q_S = \frac{\lambda p_{sat}^V}{p_{Atm} - (1-\lambda) p_{sat}^V}$	λ: ratio between mass constant for dry air and mass constant for the vapour
	p_{sat}^V: vapour pressure in saturation at interstitial water temperature
$p_{sat}^V = exp\{2.3 \left[\frac{7.5(T_E - 273.15)}{237.3 + (T_E - 273.15)} + 0.76\right]\}$	p_{Atm}: atmospheric pressure

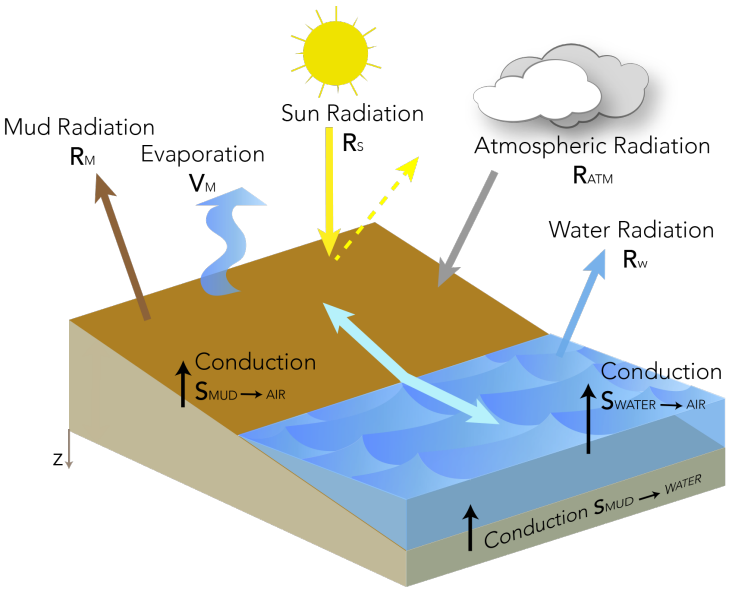

Figure 6: Conceptual scheme of heat exchange at the mud surface in the intertidal zone. Fluxes contributing to heat energy balance are represented by arrows during emersion and immersion periods (modified from Guarini et al., 1997).

layer (z_{bot}), which conserves the seawater temperature computed at the previous time step. The seawater temperature in z_{top} is governed by the HEB at the air-water interface:

$$\rho_W C_{P_W} \frac{\partial T_W(z_{top}, t)}{\partial t} = f\left(T_W(z_{top}, t)\right), \tag{6}$$

$$\text{with } f\left(T_W(z_{top}, t)\right) = R_S + R_{Atm} - R_W - S_{Air \rightarrow Water}, \tag{7}$$

where ρ_W is the volumetric mass of water (kg m^{-3}). C_{P_W} is the specific heat capacity of seawater at constant pressure (J kg^{-1} K^{-1}). $T_W(z_{top}, t)$ is the water temperature (K) in the surface mixed layer. The term $S_{Air \rightarrow Water}$ is the sensible heat flux (W m^{-2}) mediated by the air-water thermal conduction. R_W (W m^{-2}) is the seawater upward radiation.

The upper fraction of the water column influenced by atmospheric forcings is defined by the coefficient α_{top}:

$$\alpha_{top} = 0.15\left(1 + \frac{U}{3}\right), \tag{8}$$

where U is the wind speed (m s^{-1}). Consequently, the simulated seawater temperature of the whole water column (T_W) results from the mixing between the fraction α_{top} and the remaining fraction of the water column ($1 - \alpha_{top}$):

$$T_W(t) = \alpha_{top} T_W(z_{top}, t) + (1 - \alpha_{top})\, T_W(z_{bot}, t) \text{ with } T_W(z_{bot}, t) = T_W(t-1) \tag{9}$$

T_W (K) is initialised by the following equation:

$$T_W(t) = 18.5 + 5\cos\left(2\pi\frac{day - 230}{year\ length}\right) + 273.15, \quad (10)$$

where day is the day of the year and the year length is in days. Details on parameters and constants are given in Tables 1 and 2.

Table 2: Parameters of the MST model

Parameter	Description	Value	Unit
General equations			
η	Conductivity	0.8	W m^{-1} K^{-1}
ρ_S	Soil volumetric mass	2650	kg m^{-3}
ρ_W	Water volumetric mass	1000	kg m^{-3}
ξ	Mud porosity	0.62	%
μ	Thermal diffusivity	0.48×10^{-6}	m^2 s^{-1}
Solar radiation			
R_0	Solar constant	1353	W m^{-2}
A	Albedo	0.08	-
Atmospheric radiation			
σ	Stephan-Boltzman	5.67×10^{-8}	W m^{-2} K^{-4}
ζ	Constant	Radiation on water : 1.7	-
		Radiation on mud : 1	-
Mud radiation			
ε_M	Mud emissivity	0.96	-
Conduction			
ρ_A	Air volumetric mass	1.2929	kg m^{-3}
C_{P_A}	Air specific heat	1003	J kg^{-1} K^{-1}
C_{P_W}	Water specific heat	4180	J kg^{-1} K^{-1}
$C_{h_{M\to A}}$	Mud-air bulk coefficient	5	-
$C_{h_{A\to W}}$	Air-water bulk coefficient	0.014	-
Evaporation			
C_V	Bulk coefficient	0.0014	-
λ	Constant ratio	0.621	-

Biological model

MPB migration scheme

A system of three partial differential equations describes the temporal dynamics of MPB biomass within the surface biofilm (S), MPB biomass within the first cm of sediment (F), and biomass of MPB grazer *P. ulvae* (Z). The system drives the MPB migration scheme according to the diurnal and tidal cycles that

constrain the biological-physical coupled model (see Box 2.4.1). During the daytime emersion periods:

$$\text{if } \gamma* > 0 \begin{cases} \frac{dS}{dt} = \left(r_F F + P^b S\right)\left(1 - \frac{S}{S_{max}}\right) - m_S S - \left[IR\left(\frac{Z}{W_Z^{mean}}\right)\right] \times H\left(S, S_{mini}\right) \\ \frac{dF}{dt} = -r_F F\left(1 - \frac{S}{S_{max}}\right) + P^b S\left(\frac{S}{S_{max}}\right) - m_F F \\ \frac{dZ}{dt} = \theta \times \left[IR\left(\frac{Z}{W_Z^{mean}}\right)\right] \times H\left(S, S_{mini}\right) - m_Z Z \\ \frac{d\gamma*}{dt} = -1 \end{cases} \tag{11}$$

$$\text{if } \gamma* \leqslant 0 \begin{cases} \frac{dS}{dt} = -r_S S - m_S S - \left[IR\left(\frac{Z}{W_Z^{mean}}\right)\right] \times H\left(S, S_{mini}\right) \\ \frac{dF}{dt} = r_S S - m_F F \\ \frac{dZ}{dt} = \theta \times \left[IR\left(\frac{Z}{W_Z^{mean}}\right)\right] \times H\left(S, S_{mini}\right) - m_Z Z \\ \frac{d\gamma*}{dt} = -1 \end{cases} \tag{12}$$

where $\gamma*$ (h) corresponds to the potential duration of the biofilm at the sediment surface. It is computed at the end of each night-time emersion and immersion periods for the next daytime emersion period (Eq. 14 and 15). According to Guarini et al. (2006) and Guarini et al. (2008a), $\gamma*$ is set by dividing the MPB biomass in F into fractions of biofilm ($S_{max} = 25$ mg Chl *a* m^{-2}) that spend 1 h in average at the sediment surface (γ). The higher is the biomass in F, the longer is $\gamma*$. This potential time is independent of the duration of the daytime emersion periods, which can be shorter or longer.

When $\gamma* > 0$, the MPB cells migrate upward in the sediment from F to S compartment at a transfer rate of r_F (h^{-1}). MPB stop migration when S reaches saturation at S_{max} (mg Chl *a* m^{-2}). PP within the S compartment regulated by the biomass-specific photosynthetic rate P^b (µg C (µg Chl *a*)$^{-1}$ h^{-1}) is set to zero when $S = S_{max}$ according to the term $\left(1 - \frac{S}{S_{max}}\right)$, which represents the MPB space-limitation in the S compartment. The MPB biomass produced is therefore transferred from S to F according to the term $P^b S\left(\frac{S}{S_{max}}\right)$ in the F time derivative. The dynamics of the biomass in the MPB biofilm and its associated PP is represented by the $S*$ time derivative:

$$\frac{dS*}{dt} = \frac{dS}{dt} + \mathbf{P^b S}\left(\frac{\mathbf{S}}{\mathbf{S_{max}}}\right). \tag{13}$$

When $\gamma* \leqslant 0$, the MPB cells migrate downward in the sediment from the S to F compartment at a transfer rate of r_S (h^{-1}). The terms m_S and m_F are loss rates (h^{-1}) representing MPB senescence and grazing by surface deposit feeders (on

S) and subsurface deposit feeders (on F). m_Z is a loss rate (h^{-1}) representing *P. ulvae* mortality (see section 2.4.2).

BOX 2.4.1

Conceptual scheme of MPB migration

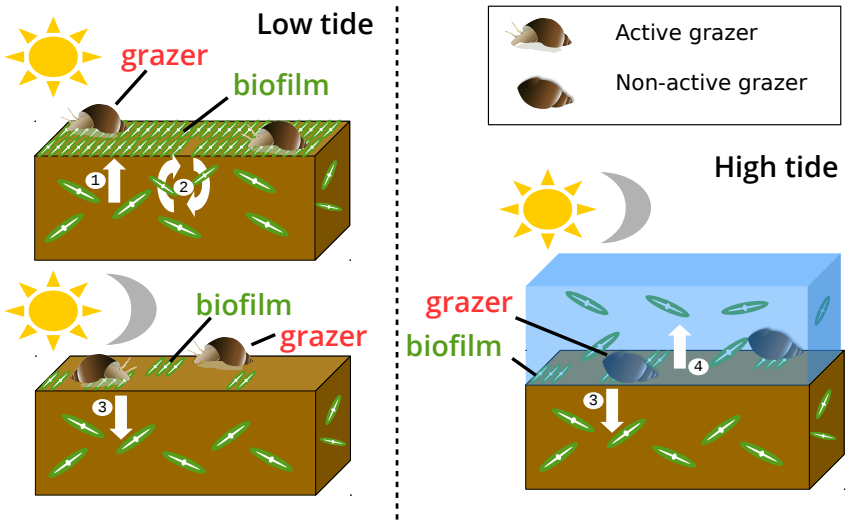

Figure 7: Conceptual scheme of MPB migration (modified from Guarini et al., 2008a).

During daytime emersion periods, MPB cells migrate at the sediment surface (1) to produce and transfer biomass to the sediment first centimetre (2). Before the end of daytime emersion periods or during night-time emersion periods, MPB cells migrate down to the sediment first centimetre (3). During immersion periods, MPB cells are chronically resuspended from the sediment first centimetre to the water column (4) and the persisting MPB cells within the biofilm finish their downward migration (3). *P. ulvae* grazing is only active during emersion periods (modified from Guarini et al., 2008a).

During night emersion periods, the MPB cells migrate downward into the sediment from S to F. *P. ulvae* grazes on MPB cells remaining in the biofilm (S):

$$\begin{cases} \frac{dS}{dt} = -r_S S - m_S S - \left[IR \left(\frac{Z}{W_Z^{mean}} \right) \right] \times H(S, S_{mini}) \\ \frac{dF}{dt} = r_S S - m_F F \\ \frac{dZ}{dt} = \theta \times \left[IR \left(\frac{Z}{W_Z^{mean}} \right) \right] \times H(S, S_{mini}) - m_Z Z \\ \gamma* = \left(\frac{F}{S_{max}} + 1 \right) \times \gamma \end{cases} \quad (14)$$

During immersion periods, MPB cells remaining in the biofilm finish their downward migration from S to F and *P. ulvae* does not exert any grazing pressure any more:

$$\begin{cases} \frac{dS}{dt} = -r_S S - m_S S \\ \frac{dF}{dt} = r_S S - \nu_F F \\ \frac{dZ}{dt} = -m_Z Z \\ \gamma* = \left(\frac{F}{S_{max}} + 1\right) \times \gamma \end{cases} \tag{15}$$

In the model, we assumed a constant rate of MPB cells resuspended during immersion periods. During immersion periods, the generic loss term (ν_F, 0.003 h^{-1}) includes the chronic resuspension, MPB senescence processes and the grazing by subsurface deposit feeders. During emersion periods, the loss term is lower (m_F, 0.001 h^{-1}) as it only represents the MPB senescence and the grazing by subsurface deposit feeders. Parameter values are given in Table 3.

MPB primary production

The biomass-specific photosynthetic rate P^b (µg C (µg Chl *a*)$^{-1}$ h^{-1}) is regulated by temperature (T, °C) and by photosynthetically active radiation (I, W m^{-2}), which corresponds to 44 % of downward short-wave radiation (Britton and Dodd, 1976). The model of Platt and Jassby (1976) is used to compute the production rate as a function of I:

$$P^b = P^b_{max} \times \tanh\left(\frac{I}{I_k}\right), \tag{16}$$

where P^b_{max} is the photosynthetic capacity (µg C (µg Chl *a*)$^{-1}$ h^{-1}) and I_k is the light saturation parameter (W m^{-2}). P^b_{max} depends on the MST (T) according to the relationship of Blanchard et al. (1996):

$$P^b_{max} = P^b_{MAX} \times \left(\frac{T_{max} - T}{T_{max} - T_{opt}}\right)^{\beta} \times e^{\left(-\beta \times \left[\frac{T_{max}-T}{T_{max}-T_{opt}} - 1\right]\right)}, \tag{17}$$

where T_{max} (°C) and T_{opt} (°C) are the maximum and optimal temperature for MPB photosynthesis, respectively. β is a curvature coefficient that shapes the temperature-photosynthesis relationship. P^b_{MAX} is the maximum value that takes P^b_{max} at T_{opt}.

The biomass-specific photosynthetic rate P^b is expressed in µg C (µg Chl *a*)$^{-1}$ h^{-1}. It is therefore necessary to convert it in terms of produced Chl *a* to obtain a gross growth rate in h^{-1}. In that respect, we used a variable C:Chl *a* ratio (g C g Chl a^{-1}). The ratio is computed according the formulation of Cloern et al. (1995) adapted for coastal pelagic diatoms (Sibert et al., 2010, 2011; Le Fouest et al., 2013):

$$\frac{Chla}{C} = \left(\frac{Chla}{C}\right)_{min} \times \left(1 + 4 \times e^{-0.5 \times \frac{I}{K_E}}\right), \tag{18}$$

where $\left(\frac{Chl\,a}{C}\right)_{min}$ is the minimum Chl *a*:C ratio (g Chl *a* g C^{-1}) and K_E, the half-saturation constant for light use (Ein m^{-2} d^{-1}).

The MPB PP (µg C m^{-2} h^{-1}) corresponds to the sum of the space-dependant production at the surface of the biofilm (*i.e.* the $P^bS\left[1-\frac{S}{S_{max}}\right]$ term) and of the biomass produced and directly transferred from S to F (*i.e.* the $P^bS\left[\frac{S}{S_{max}}\right]$ term). Consequently, it can be simplified by:

$$production = P^bS\left(1-\frac{S}{S_{max}}\right)+P^bS\left(\frac{S}{S_{max}}\right)=P^bS \tag{19}$$

The constants are given in Table 3.

Grazer P. ulvae

S is explicitly grazed by the mud snail *Peringia ulvae* (Z, mg C m^{-2}). The grazing rate is regulated by the individual ingestion rate of snails (IR, ng Chl *a* ind^{-1} h^{-1}) and by Z expressed in terms of density (ind m^{-2}). Density is computed as the ratio of Z (mg C m^{-2}) over the mean individual weight (W_Z^{mean}, mg C) linearly interpolated (Table 4). An Heaviside function limits the grazing to a feeding threshold (S_{mini}, mg Chl *a* m^{-2}). Only a fraction (θ, %) of the MPB biomass grazed by Z is assimilated into new Z biomass. The individual ingestion rate (ng Chl *a* ind^{-1} h^{-1}) by *P. ulvae* is calculated using a sigmoid mathematical function accounting for the effect of MST (T, °C):

$$IR = IR_{max}\times\frac{T^{\alpha_Z}}{T^{\alpha_Z}+(\frac{T_{opt_Z}+10}{2})^{\alpha_Z}}, \tag{20}$$

where T_{opt_Z} (°C) is the optimal temperature for grazing. IR_{max} is the maximal observed individual ingestion rate. α_Z (no unit) is a curvature parameter. The maximal individual ingestion rate IR_{max} (ng Chl *a* ind^{-1} h^{-1}) is calculated according the formulation of Haubois et al. (2005) for adult snails. IR_{max} depends on the total MPB biomass:

$$IR_{max} = 0.015\times(F+S)^{1.72} \tag{21}$$

The Chl *a* uptake rate is converted into carbon unit according to the C:Chl *a* ratio described previously. The term $(F+S)$ is expressed in µg Chl *a* g dry sed^{-1}. The biomass expressed in mg Chl *a* m^{-2} is converted into µg Chl *a* g dry sed^{-1} as follows:

$$[Chl\,a](\mu g\ Chl\ a\ g\ dry\ sed^{-1}) = \frac{[Chl\,a]^{1.2605}(mg\ Chl\ a\ m^{-2})}{\rho_S}\times thickness_{sed}, \tag{22}$$

where ρ_S is the sediment bulk density in g l^{-1} and $thickness_{sed}$ is the sediment thickness *i.e.* 1 cm. The Chl *a* concentration is scaled by the exponent

Table 3: Biological model parameters

Symbol	Description	Value	Unit	Source
MPB				
r_S	Transfer rate of biomass from S to F	10	h^{-1}	Guarini et al. (2008a)
r_F	Transfer rate of biomass from F to S	1	h^{-1}	Guarini et al. (2008a)
m_S	Loss rate of biomass of S	0.001	h^{-1}	Guarini et al. (2008a)
m_F	Loss rate of biomass of F during emersion periods	0.001	h^{-1}	Guarini et al. (2008a)
ν_F	Loss rate of biomass of F during immersion periods	0.003	h^{-1}	Present study
S_{max}	Maximum biomass of S	25	mg Chl *a* m^{-2}	Guarini et al. (2000)
S_{mini}	Minimum biomass of S for grazing	0.5	mg Chl *a* m^{-2}	Present study
γ	Average time spent by a unit of S_{max} at the surface	1	h	Blanchard et al. (2004)
I_k	Light saturation parameter	100	W m^{-2}	Guarini et al. (2000)
P^b_{MAX}	Maximum photosynthetic capacity in April	11.18	µg C (µg Chl *a*)$^{-1}$ h^{-1}	Blanchard et al. (1997a)
	Maximum photosynthetic capacity in June	7.56	µg C (µg Chl *a*)$^{-1}$ h^{-1}	Blanchard et al. (1997a)
	Maximum photosynthetic capacity in September	5.81	µg C (µg Chl *a*)$^{-1}$ h^{-1}	Blanchard et al. (1997a)
	Maximum photosynthetic capacity in December	3.04	µg C (µg Chl *a*)$^{-1}$ h^{-1}	Blanchard et al. (1997a)
T_{opt}	Optimum temperature for photosynthesis	18	°C	Present study
T_{max}	Maximum temperature for photosynthesis	38	°C	Blanchard et al. (1997a)
β	Shape parameter of the P-T relationship in April	3.90	-	Blanchard et al. (1997a)
	Shape parameter of the P-T relationship in June	2.80	-	Blanchard et al. (1997a)
	Shape parameter of the P-T relationship in September	1.76	-	Blanchard et al. (1997a)
	Shape parameter of the P-T relationship in December	1.03	-	Blanchard et al. (1997a)
K_E	Half-saturation constant for light use	20	Ein m^{-2} d^{-1}	Present study
$\left(\frac{Chl a}{C}\right)_{min}$	Minimum Chl *a*: C ratio	0.0125	g Chl *a* g C^{-1}	Present study
Grazer *P . ulvae*				
α_Z	Shape parameter of the temperature related grazing	15	-	Present study
T_{opt_Z}	Optimum temperature for grazing	20	°C	Pascual and Drake (2008)
m_Z^{min}	Minimum mortality rate of *P. ulvae*	1×10^{-6}	h^{-1}	Present study
θ	Assimilation rate	0.55	%	Kofoed (1975)
Sediment				
φ	Mean bulk density of sediment	520	g l^{-1}	Present study

1.2605 in order to reach a maximal observed ingestion rate of 385 ng Chl *a* ind^{-1} h^{-1} (Coelho et al., 2011) when the Chl *a* concentration converges towards a maximal observed value (300 mg Chl *a* m^{-2}, Guarini, 1998).

Finally, the mortality rate of Z is a quadratic density-dependant mortality rate:

$$m_Z = m_Z^{min} Z, \tag{23}$$

where m_Z^{min} is the minimum mortality rate (h^{-1}). The constants are given in Table 3.

Table 4: Observed mean individual weight of *P. ulvae* (mg C).

Month	J	F	M	A	M	J	J	A	S	O	N	S
Weight	0.21	0.13	0.11	0.11	0.15	0.22	0.26	0.23	0.10	0.23	0.19	0.15

CONCLUSIONS

Eighty years ago, Fleming developed the first phytoplankton model. New developments on mass flux marine ecosystem models along with increasing computational capacity never stop ever since. Modelling efforts on MPB are limited and much remained to be done. Nevertheless, any further developments will be conditioned by a better understanding of the MPB dynamics made possible from *in situ* and laboratory observations. In the following chapters, we combine MPB modelling with *in situ* and remotely-sensed data analysis to investigate the spatial and temporal variability of MPB dynamics on a large temperate intertidal mudflat (see Box 2.5.1).

BOX 2.5.1

Remote sensing of MPB

The first use of remote sensing to measure MPB biomass dates back to 1979 (Zingmark, 1979). Ever since, remote sensing for studying MPB spread in the MPB scientific community (*e.g.* Méléder et al., 2003a; Brito et al., 2013; Benyoucef et al., 2014; Daggers et al., 2018). Remote sensing covers large spatial scales (~ from one to few hundred meters) and is useful to map MPB biomass with the Normalised Difference Vegetation Index (NDVI; Tucker, 1979). The NDVI is calculated from surface reflectance (ρ) in the red (R) and near-infrared (NIR) bands following Eq. (24) to estimate the horizontal distribution of the MPB biomass (*e.g.* Méléder et al., 2003a)

$$\mathrm{NDVI} = \frac{\rho(\mathrm{NIR}) - \rho(\mathrm{R})}{\rho(\mathrm{NIR}) + \rho(\mathrm{R})} \tag{24}$$

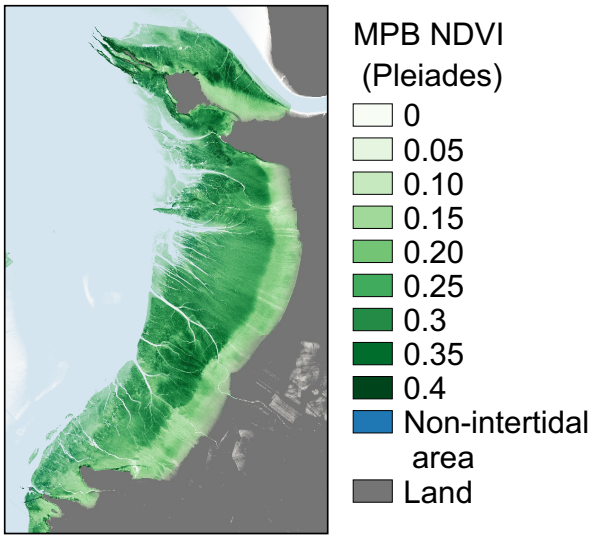

Figure 8: MPB normalised-difference vegetation index on 3 March 2018 on the Brouage mudflat.

Remotely-sensed NDVI maps inform about the horizontal distribution of MPB biomass at the sediment surface. In addition, time series of MPB remotely-sensed products can be extracted from remotely-sensed data at a daily frequency depending on the revisit time of the satellite and the meteorological conditions.

CHAPTER III

ON BIOTIC AND ABIOTIC DRIVERS OF THE MICROPHYTOBENTHOS SEASONAL CYCLE IN A TEMPERATE INTERTIDAL MUDFLAT: A MODELLING STUDY

Uncertainties on the likely key factors driving the MPB dynamics (nutrients, photoinhibition, thermoinhibition, grazing) are a challenge for MPB mass flux modelling. They impede our ability to accurately represent the mechanistic processes involved in the MPB primary production. In Chapter 3, the objective is to infer on the factors that shape the MPB seasonal cycle. For this purpose, we use the MPB model to test hypotheses on the potential factors controlling the MPB primary production and biomass at low tide over a seasonal cycle on the Brouage mudflat in 2008. The model explicitly simulates MPB and its main grazer (*P. ulvae*) over and within the first centimetre of sediment. It is forced by realistic seasonal cycles of irradiance and mud surface temperature. *In situ* and remote sensing time series based on the Normalised Difference Vegetation Index (NDVI) are used to calibrate the model and assess its predictive capacity. The simulated seasonal cycle of MPB biomass is characterised by a spring bloom, a summer depression and a moderate fall bloom. It is consistent with the reported seasonal cycle at the study site. Light is the most limiting factor over the year. In summer, the high mud surface temperature limits the MPB growth. In addition, grazing by *P. ulvae* individuals contributes to decrease PP already thermoinhibited. Regarding the high variability of abiotic and biotic factors in play on the Brouage mudflat, the model was relevant to disentangle the relative contribution of all the factors considered.

3

ON BIOTIC AND ABIOTIC DRIVERS OF THE MICROPHYTOBENTHOS SEASONAL CYCLE IN A TEMPERATE INTERTIDAL MUDFLAT: A MODELLING STUDY

ABSTRACT

Microphytobenthos (MPB) from intertidal mudflats are key primary producers at the land-ocean interface. MPB can be more productive than phytoplankton and sustain both benthic and pelagic higher trophic levels. The objective of this study is to assess the contribution of light, mud temperature, and gastropod *Peringia ulvae* grazing pressure in shaping the seasonal MPB dynamics on the Brouage mudflat (NW France). We use a physical-biological coupled model applied to the sediment first centimeter for the year 2008. The simulated data compare to observations including time-coincident remotely sensed and *in situ* data. The model suggests a MPB annual cycle characterised by a main spring bloom, a biomass depression in summer, and a moderate fall bloom. In early spring, simulated photosynthetic rates are high due to mud surface temperature (MST) values close to the MPB temperature optimum for photosynthesis and because increasing solar irradiance triggers the onset of the MPB spring bloom. Simulated peaks of high *P. ulvae* grazing (11 days during which ingestion rates exceed primary production rate) mostly contribute to the decline of the MPB bloom along with the temperature limitation for MPB growth. In late spring-summer, the MPB biomass depression is due to the combined effect of thermoinhibition and a moderate but sustained grazing pressure. The model ability to infer on biotic and abiotic mechanisms driving the seasonal MPB dynamics could open the door to a new assessment of the export flux of biogenic matter from the coast to the open ocean and, more generally, of the contribution of productive intertidal biofilms to the coastal carbon cycle.

This chapter was published as an article in the journal Biogeosciences (Savelli et al., 2018).

Acronyms:
EPS: *Extracellular Polymeric Substances*
MPB: *Microphytobenthos*
MST: *Mud Surface Temperature*
NDVI: *Normalised Difference Vegetation Index*
PAR: *Photosynthetically Active Radiation*
PP: *Primary Production*

INTRODUCTION

Coastal and nearshore waters receive large amounts of organic matter and inorganic nutrients from land that support a high biological productivity (Mann, 1982; Admiraal, 1984; Hopkinson and Smith, 2005). However, the high turbidity of estuarine influenced coastal waters limits the penetration of downward solar irradiance in the water column and, as such, phytoplankton production (Cloern, 1987; Struski and Bacher, 2006). In subtidal and intertidal zones, primary production (PP) sustained by benthic microalgae, or microphytobenthos

(MPB), can exceed that of phytoplankton (Underwood and Kromkamp, 1999; Struski and Bacher, 2006). MPB are mostly composed of free motile epipelic diatoms and of epipsammic diatoms that live in close association (attached or free-living) with sediment grains (Round, 1971). Epipelic MPB are associated with fine cohesive intertidal sediments and develop within the top few millimetres (Underwood, 2001). During daytime exposure, they migrate toward the sediment surface constituting a dense biofilm of a few hundred micrometers (Herlory et al., 2004). They are fully exposed to solar irradiance at low tide promoting PP that can reach values as high as 1.9 g C m^{-2} d^{-1} (Underwood and Kromkamp, 1999). During the flood, epipelic MPB move downward within the sediment but can be resuspended into the water column (Demers et al., 1987; de Jonge and van Beusekom, 1992, 1995; Lucas et al., 2001; Orvain et al., 2004; Ubertini et al., 2012). Both epipelic and epipsammic MPB are a key resource for higher trophic levels from benthic fauna to birds on bare mudflats (Herman et al., 2000; Kang et al., 2006; Jardine et al., 2015), but also for pelagic organisms such as zooplankton and planktivorous fishes (Perissinotto et al., 2003; Krumme et al., 2008).

On intertidal mudflats, MPB PP rates are mainly constrained by solar irradiance and temperature (Barranguet et al., 1998). The MPB biofilm faces strong daily and seasonal variations of mud surface temperature (MST) caused by heating through solar irradiance during low tide emersion periods (Harrison and Phizacklea, 1985; Harrison, 1985; Guarini et al., 1997) and develops phenological adaptations. Blanchard and Cariou-Le Gall (1994), Barranguet et al. (1998) and Pniewski et al. (2015) showed a light-related seasonal adjustment of photosynthetic parameters (the photosynthetic capacity P^b_{max} and the light saturation parameter I_k) from Production-Irradiance (P-I) curves fitted to the model of Platt and Jassby (1976). Photo-inhibition was rarely observed in the field since epipelic diatoms can achieve "micro-migrations", *i.e.* a negative phototaxic short-term change of position in the sediment (Kromkamp et al., 1998; Perkins et al., 2001; Cartaxana et al., 2011). With respect to mud temperature, Blanchard et al. (1996) related mathematically P^b_{max} to temperature. Using this relationship, Blanchard et al. (1997a) showed that P^b_{max} varies according to seasons suggesting a thermoinhibition process in response to high mud temperature ($>$ 25 °C). de Jonge (1980) also showed seasonal variations of the carbon (C) to chlorophyll *a* (Chl *a*) ratio, which is a proxy of the physiological state of autotrophic cells, as a function of air temperature (de Jonge et al., 2012). Regarding nutrients, their limiting role on the MPB growth and photosynthetic rate is not evidenced in fine cohesive sediments naturally enriched both from within the sediment and the water column (Underwood, 2001; Cadée and Hegeman, 1974; Admiraal, 1984). Vieira et al. (2016) suggested a likely *in vitro* limitation by dissolved inorganic carbon within biofilms. Benthic diatoms were shown to store ammonium and phosphate within the intracellular matrix (García-Robledo et al., 2010; Yamaguchi et al., 2015) potentially usable for as-

similation and growth (Garcia-Robledo et al., 2016). The nutrient limitation of MPB is still in debate.

At temperate latitudes, the seasonal cycle of MPB is shaped by the prevailing environmental conditions. Seasonal blooms are reported to occur throughout the year, *i.e.* in spring (de Jong and de Jonge, 1995; Sahan et al., 2007; Brito et al., 2013), summer (Cadée and Hegeman, 1977) and fall (Hubas et al., 2006; Garcia-Robledo et al., 2016). Along the French Atlantic coast, the spring bloom and summer depression observed in the Brouage mudflat in the Marennes-Oléron Bay are explained by optimal temperature conditions and thermoinhibition, respectively (Blanchard et al., 1997a). Reported differences in the observed MPB seasonal cycles are also attributed to the benthic diatom assemblage (Underwood, 1994). In terms of biomass, epipelic diatoms associated with muddy sediments show a higher seasonality caused by a marked exposure to stressful environmental conditions (*e.g.* cycle of deposition/erosion, desiccation, grazing) than less motile epipsammic species in coarser sandy sediments (Underwood, 1994). In summer, thermoinhibition and a high grazing pressure by deposit feeders are suggested to dampen the MPB biomass (Cadée and Hegeman, 1974; Cariou-Le Gall and Blanchard, 1995; Sahan et al., 2007). On intertidal mudflats, the prosobranch gastropod *Peringia ulvae* can reach densities up to 30 000 snails m^{-2} (Sauriau et al., 1989) with a reported maximal ingestion rate of 385 ng Chl *a* $snail^{-1}$ h^{-1} (Coelho et al., 2011). Such grazing activity may translate into a theoretical uptake of 12 g C m^{-2} d^{-1} for a C:Chl *a* ratio of 45 g C g Chl a^{-1} (Guarini, 1998), which is 6-fold more than the daily maximum MPB PP rate reported for MPB (Underwood and Kromkamp, 1999).

The role of each individual abiotic or biotic factor involved in the MPB short-term dynamics is well documented (*e.g.* Admiraal, 1977; Admiraal et al., 1983; Blanchard and Cariou-Le Gall, 1994; Montagna et al., 1995; Blanchard et al., 1997a; Feuillet-Girard et al., 1997; Barranguet et al., 1998; Light and Beardall, 2001; Blanchard et al., 2002; Pinckney et al., 2003; Coelho et al., 2009; Weerman et al., 2011; Dupuy et al., 2014; Pniewski et al., 2015; Barnett et al., 2015; Cartaxana et al., 2015; Vieira et al., 2016). However, and in light of the current knowledge, the quantitative contribution of combined factors in the seasonal MPB dynamics remains uncertain. This impedes any future assessment on how global change might impact the MPB dynamics and carbon cycle in the land-ocean continuum. The goal of this study is to quantify the relative contribution of light, temperature and grazing on the MPB seasonal cycle and production on an intertidal mudflat (Marennes-Oléron Bay) of the French Atlantic coast. For this purpose, we use a two-layer physical-biological model representing the MPB and *P. ulvae* compartments to assess the contribution of the three drivers over an annual cycle. In the paper, we describe first the physical-biological coupled model and the *in situ* and remotely-sensed data used to investigate the MPB seasonal cycle. Second, we assess the relative contribution of light, MST and *P. ulvae* grazing on the MPB dynamics and PP, and we analyse the

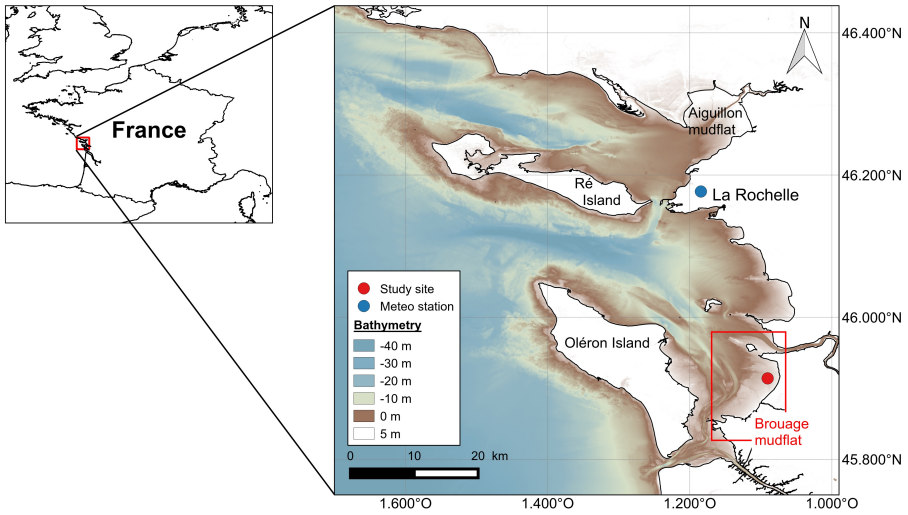

Figure 9: Bathymetry of the Pertuis Charentais (source: SHOM) and location of the main intertidal mudflats. The study site is represented by a red full point and the Meteo France weather station is represented by a blue full point.

model sensitivity to key biological constants. Finally, we discuss the role of light, temperature and grazing in the MPB seasonal cycle and the future challenges of modelling the MPB contribution to the carbon cycle at the land-ocean continuum.

MATERIAL AND METHODS

The study area is the Pertuis Charentais sea on the French Atlantic coast. It is a shallow semi-enclosed sea characterised by semi-diurnal tides and a macrotidal regime. The tidal range is ~ 6 m during spring tides. The intertidal zone has two main mudflats composed of fine cohesive sediments, *i.e.* the Brouage mudflat (42 km^2) and the Aiguillon mudflat (28.7 km^2) (Fig. 22). The study site (45°54′50″N, 01°05′25″W) is located on the Brouage mudflat (Fig. 22). It is composed of fine cohesive sediments (median grain size of 17 µm and 85 % of grain with a diameter lower than 63 µm; Bocher et al., 2007) and sheltered from Atlantic swells by the Oléron Island (Pascal et al., 2009).

Observations

A large multiparametric dataset of physical and biological measurements collected in the Pertuis Charentais was used to constrain the model and to compare with the model outputs. We provide here a summary of the data used along with their respective references, where a detailed methodology of each set of measurements can be found.

In situ data

Atmospheric and hydrological forcings were required to set the temperature and light environment that constrained the physical-biological model. Atmospheric forcings (Fig. 10a-e) consisted of meteorological observations (shortwave radiation, air temperature in the shade, atmospheric pressure above the sea, wind speed and relative humidity) acquired at the Meteo France weather station located near the airport of La Rochelle (46°10'36"N, 1°11'3"W; data available online: https://publitheque.meteo.fr; Fig. 22). Hydrology was represented by the absence or presence of seawater at the study site of the Brouage mudflat. Emersion/immersion periods were determined by the observed water height at the tide gauge of La Rochelle-La Pallice (46°9'30"N, 1°13'14"W, data Service Hydrographique et Océanographique de la Marine (SHOM) / Grand Port Maritime La Rochelle-La Pallice; data available: http://data.shom.fr/) corrected by the bed elevation at the study site. The bed elevation (3.204 m above chart datum) was extracted from a digital elevation model (Litto3D® 2010 Charente Maritime by the Institut National de l'Information Géographique et Forestière (IGN) and the SHOM) at pixels corresponding to the study site (Fig. 22). The weather and tide gauge stations were located ~ 30 km away from the study site. Atmospheric and hydrological forcings were one hour frequency from January 1, 2008 (00:00 AM) to December 31, 2008 (11:00 PM). They were linearly interpolated at the time step of the model (6 min).

In order to validate the model, we used daily measurements of MST (first cm of sediment), Chl *a* concentration (first cm of sediment) and *Peringia ulvae* biomass and density from a multiparametric dataset collected in February 16-24 and July 13-26, 2008 at the study site where the model was run (45°54'50"N, 01°05'25"W, Fig. 22). The sampling protocol is fully detailed in Orvain et al. (2014a). In addition to the 2008 dataset, we used data of *in situ* MPB Chl *a* concentration collected within the first cm of sediment at the same station in April 19-22, 2012, July 05, 2012, November 14, 2012, February 11, 2013 and April 10, 2013. The sampling protocol is fully detailed in Lavergne et al. (2017). Monthly data of *P. ulvae* abundance and biomass sampled monthly from April, 2014 to July, 2015 over the Aiguillon mudflat were used to estimate a monthly-averaged individual weight. The monthly-averaged individual weight was used to convert the simulated biomass per unit of surface into density per unit of surface. The sampling protocol is given in Bocher et al. (2007). We spatially averaged the *P. ulvae* abundance and biomass data to obtain a monthly mean value for the entire mudflat. Ash-free dry mass (AFDM) was converted to carbon using the relationship derived from Jansson and Wulff (1977) and Remmert (2013) and used by Asmus (1994) for benthic deposit feeders (1 g AFDM = 0.58 g C). When the individual weight was not available, the individual height was used to estimate the AFDM (mg) using the formulation of Santos et al. (2005):

$$\mathrm{AFDM} = 0.0154\mathrm{H}^{2.61}, \tag{25}$$

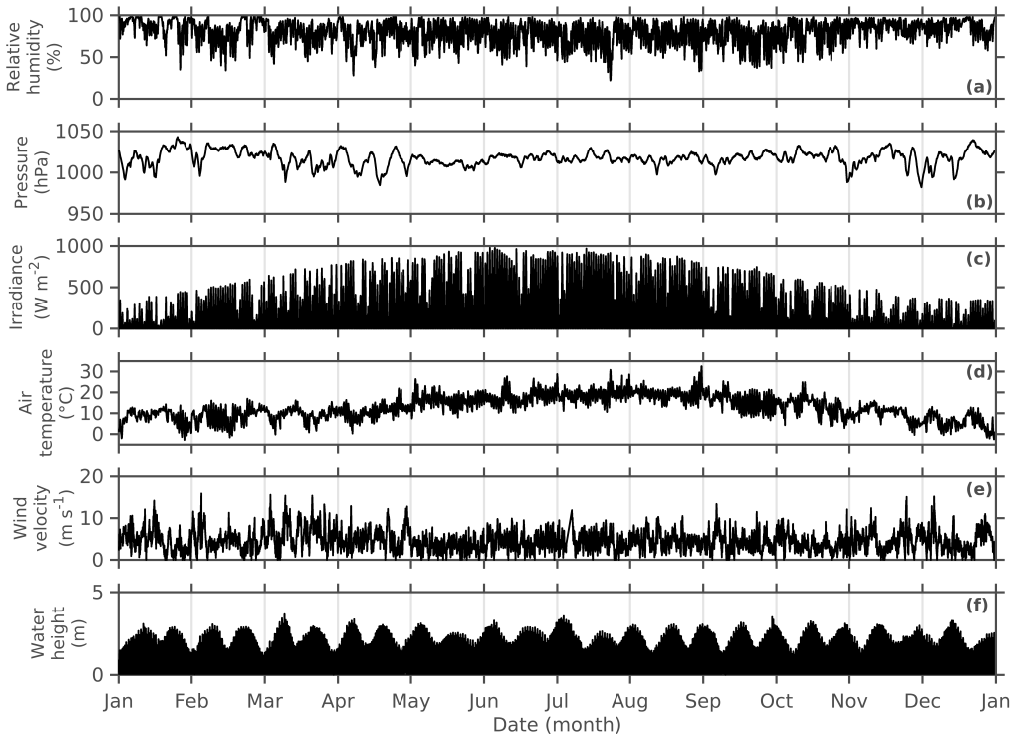

Figure 10: Annual cycle of the 2008 **(a)** relative humidity, **(b)** atmospheric pressure above the sea, **(c)** global irradiance, **(d)** air temperature in the shade, **(e)** wind velocity, and **(f)** water height at the study site. Meteorological data comes from the weather station located near the airport of La Rochelle and the water height was measured at the tide gauge of La Rochelle-La Pallice corrected by the bed elevation at the study site.

where H is the total individual height (mm).

Remote sensing data

Moderate Resolution Imaging Spectroradiometer (MODIS) images from the Terra satellite were downloaded from the USGS Earth Resources Observation and Science Center (http://earthexplorer.usgs.gov/). The Terra MODIS Surface Reflectance Daily L2G Global 250m SIN Grid product (MOD09GQ) contains 250-m surface reflectance in a red band (620-670 nm, band center at 645 nm) and a near-infrared band (841-876 nm, band center at 859 nm). Terra data were used because the morning-pass (10-11 h Universal Time) is better adapted than Aqua MODIS data to observe spring low tides at our study site. The data were corrected for atmospheric effects (aerosol, water vapor) and each image was checked for clouds/cirrus and cloud shadows. Cloud-free low-tide scenes were selected to apply a vegetation index. Images were reprojected to UTM/WGS84 coordinate system. The Normalised Difference Vegetation Index

(NDVI; Tucker, 1979) was calculated with the reflectance (ρ) in the red (R) and near-infrared (NIR) bands :

$$\mathrm{NDVI} = \frac{\rho(\mathrm{NIR}) - \rho(\mathrm{R})}{\rho(\mathrm{NIR}) + \rho(\mathrm{R})} \tag{26}$$

The NDVI thresholds proposed by Méléder et al. (2003a) to identify MPB with SPOT images was adapted for MODIS data and a range of 0 to 0.35 was used in this study. Negative NDVI values were associated with water and null values to bare sediment, while values higher than 0.35 corresponded to macrophytes (macroalgae and seagrass). For the present study, a NDVI time-series was extracted for 2008 (47 scene images) at pixels corresponding to the study site (Fig. 22). Scene images were processed with the ENVI® software.

The coupled physical-biological one-dimensional model

The coupled model consisted of a mud temperature model coupled to a 3-compartment biological model. The mud temperature model was a thermodynamic model developed by Guarini et al. (1997) resolving heat fluxes at the surface in a 1-cm thick sediment layer. Equations are given in Chapter 2 (section 2.4.1) and Table 1. It was calibrated and validated on the Brouage mudflat by Guarini et al. (1997). During exposure periods, the simulated MST resulted from heat exchanges between the sun, the atmosphere, the sediment surface, from the conduction between mud and air and from evaporation (Fig. 11). The MST was set to the temperature of the overlying seawater during immersion periods. The seawater temperature was simulated according to heat fluxes resulting from thermal conduction between air and seawater, from upward seawater radiation, and from downward solar and atmospheric radiation. The simulated mud temperature was considered homogeneous at the horizontal scale. The heat fluxes were determined according equations given in Table 1 (Chapter 2, section 2.4.1). The MST differential equation (Eq. 2 in Chapter 2, section 2.4.1) was solved with an Euler Cauchy algorithm at a 30-sec time step.

The mud temperature model constrained a 3-compartment biological model, which was modified from Guarini (1998) and Guarini et al. (2000). It is fully detailed in Chapter 2 (section 2.4.2). MPB was represented by two compartments including the Chl *a* concentration in the first cm sediment (F, mg Chl *a* m^{-2}) and the Chl *a* concentration within the surface biofilm (S, mg Chl *a* m^{-2}). The variable S$*$ represented the S compartment that incorporated the S instantaneous production of biomass (mg Chl *a* m^{-2}), which is directly transferred to F. The model assumed no sediment erosion nor deposition and no horizontal movement of MPB within the sediment. It included a scheme of MPB vertical migration between the S and F compartments (Guarini, 1998; Guarini et al., 2000). The migration scheme is summarised in Table 5. The MPB growth rate was constrained by the photosynthetically active radiation (PAR) intensity,

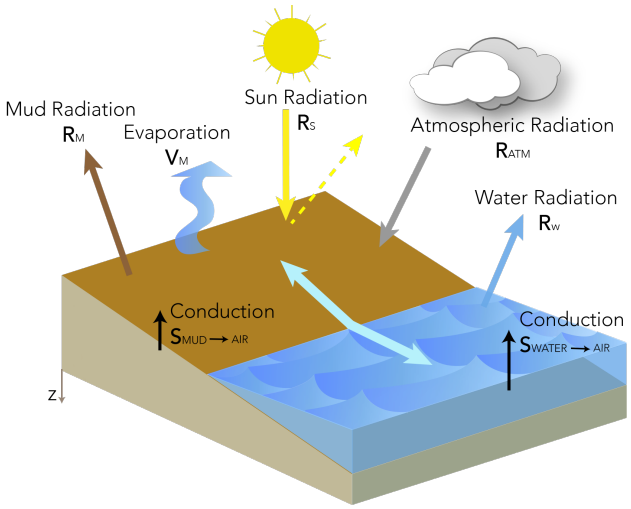

Figure 11: Conceptual scheme of heat exchange at the mud surface in the intertidal zone. Fluxes contributing to heat energy balance are represented by arrows during emersion and immersion periods. Modified from Guarini et al. (1997).

the simulated MST, and the grazing pressure. The grazing pressure was represented through a new scalar, Z, representing the *P. ulvae* biomass (mg C m^{-2}). *P. ulvae* is a very abundant MPB grazer on the Pertuis Charentais intertidal mudflats (Sauriau et al., 1989). The *P. ulvae* growth rate was constrained by the simulated MPB biomass and the MST. The fourth-order Runge-Kutta method was used to solve the biological differential equations with a 6-min time step.

The coupled physical-biological model was run at the study site (Fig. 22) from 1 January to 30 December, 2008. Initial conditions were 100 mg Chl *a* m^{-2} for F and 1000 mg C m^{-2} for Z. No biomass was set for S at the beginning of the simulation as it started at midnight (*i.e.* no light). The initial MST was initialised at the seawater temperature (see Eq. 6-10 in Chapter 2, section 2.4.1) at the first period of immersion. A 2008 10-year spin-up was performed before the analysis of the model outputs. The spin-ups and initial biomass conditions allowed for the convergence towards similar values of biomass at the end of each run.

We performed a sensitivity analysis to quantify how simultaneous variations of key biological constants might impact the simulated MPB production. A Monte-Carlo fixed sampling method (Hammersley and Handscomb, 1964) was used to randomly select values of the temperature optimum for photosynthesis (T_{opt}), the temperature maximum for photosynthesis (T_{max}), the optimal temperature for grazing (T_{opt_Z}), the shape parameter of the temperature related grazing (α_Z), the light saturation parameter (I_k) and the half-saturation constant for light use (K_E) within observed ranges (Table 6). A total of 10,000 model runs was performed with the same previous initial conditions. Statistical

Table 5: Conceptual schemes and differential equations of the biological model including the MPB biomass within the sediment first cm (F), the MPB biomass within the biofilm (S) and the biomass of *P. ulvae* (Z). The upper case corresponds to daytime emersion periods, when MPB cells migrate at the sediment surface (1) to produce and transfer biomass to the sediment first cm (2). The middle case corresponds to day or night time emersion period when MPB cells migrate down to the sediment first cm (3). The lower case corresponds to immersion periods, when MPB cells are chronically resuspended from the first cm to the water column (4) and the remaining MPB cells within the biofilm finish their downward migration (3). *P. ulvae* grazing is only active during emersion periods (right side up on schemes)(modified from Guarini et al., 2008a).

Scheme	Cases	Equations
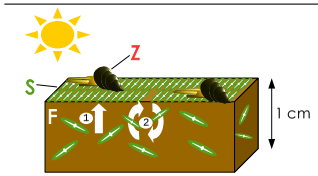	Day	$\frac{dS}{dt} = \left(r_F F + P^b S\right)\left(1 - \frac{S}{S_{max}}\right) - m_S S - \left[IR\left(\frac{Z}{W_Z^{mean}}\right)\right] \times H(S, S_{mini})$
	Low tide	$\frac{dF}{dt} = -r_F F\left(1 - \frac{S}{S_{max}}\right) + P^b S\left(\frac{S}{S_{max}}\right) - m_F F$
	$\gamma* > 0$	$\frac{dZ}{dt} = \theta \times \left[IR\left(\frac{Z}{W_Z^{mean}}\right)\right] \times H(S, S_{mini}) - m_Z Z$
		$\frac{d\gamma*}{dt} = -1$
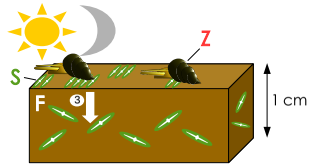	Day	$\frac{dS}{dt} = -r_S S - m_S S - \left[IR\left(\frac{Z}{W_Z^{mean}}\right)\right] \times H(S, S_{mini})$
	Low tide	$\frac{dF}{dt} = r_S S - m_F F$
	$\gamma* \leqslant 0$	$\frac{dZ}{dt} = \theta \times \left[IR\left(\frac{Z}{W_Z^{mean}}\right)\right] \times H(S, S_{mini}) - m_Z Z$
		$\frac{d\gamma*}{dt} = -1$
		$\frac{dS}{dt} = -r_S S - m_S S - \left[IR\left(\frac{Z}{W_Z^{mean}}\right)\right] \times H(S, S_{mini})$
	Night	$\frac{dF}{dt} = r_S S - m_F F$
	Low tide	$\frac{dZ}{dt} = \theta \times \left[IR\left(\frac{Z}{W_Z^{mean}}\right)\right] \times H(S, S_{mini}) - m_Z Z$
		$\gamma* = \left(\frac{F}{S_{max}} + 1\right) \times \gamma$
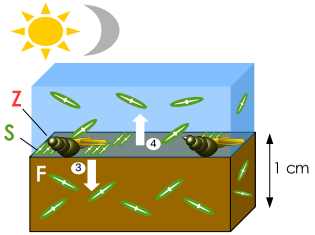	High tide	$\frac{dS}{dt} = -r_S S - m_S S$
		$\frac{dF}{dt} = r_S S - v_F F$
		$\frac{dZ}{dt} = -m_Z Z$
		$\gamma* = \left(\frac{F}{S_{max}} + 1\right) \times \gamma$

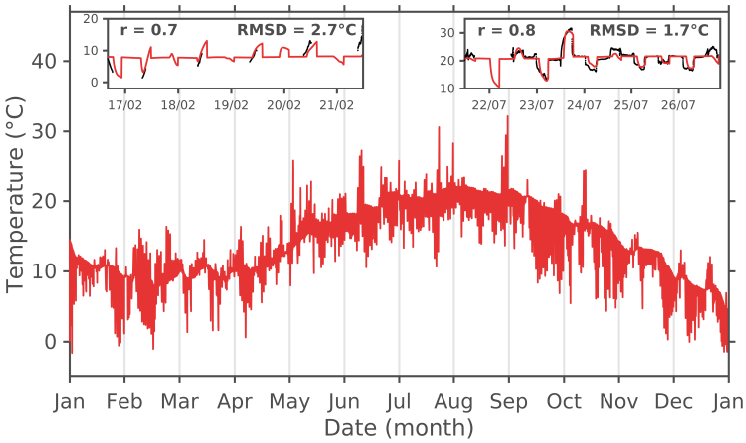

Figure 12: Measured (black points) and simulated (red lines) mud surface temperature in 2008. r is the Pearson's correlation coefficient. RMSD is the root mean square deviation (°C).

metrics on simulated annual PP according to parameters values and variations (Spearman's correlation coefficient and parameters average, normalised standard deviation, minimum and maximum) were computed. In addition to the simultaneous variations of parameters, the effect of a gradual variation of each single parameter on the MPB production was investigated. Each single parameter varied while the others were fixed at the value set by default in the model ($T_{opt} = 18$ °C, $T_{max} = 38$ °C, $I_k = 100$ W m^{-2}, $K_E = 20$ Ein m^{-2} d^{-1}, $T_{optz} = 20$ °C, $\alpha_Z = 15$).

RESULTS

Mud surface temperature

The simulated MST followed the seasonal cycle of air temperature (Pearson's r = 0.85, *p-value* < 0.05; Fig. 10d and Fig. 12). From November to April, the simulated mud temperature was 9.7 ± 2.6 °C in average. The simulated average temperature was twice from May to October reaching 18.3 ± 3 °C. The amplitude (*i.e.* the difference between the seasonal maximum and the minimum value) of the simulated mud temperature was higher from May to October (32.1 °C) than from November to April (18.1 °C). At the synoptic scale, the model reasonably simulated the high frequency (1 min) variations of MST measured at the study site in February and July 2008 (RMSD = 2.7 and 1.7 °C, respectively; Fig. 12).

Table 6: Range of values for the random selection of the model constants used in the Monte-Carlo sensitivity analysis.

Model constant	Unit	Range	References
T_{opt} (temperature optimum for photosynthesis)	°C	[15; 40]	Blanchard et al. (1997a); Hubas et al. (2006); Morris and Kromkamp (2003)
T_{max} (temperature maximum for photosynthesis)	°C	[T_{opt}+1; 40]	Same as T_{opt}
I_k (light saturation parameter)	W m^{-2}	[2.5; 180]	Blanchard and Cariou-Le Gall (1994); Barranguet et al. (1998); Light and Beardall (2001); Pniewski et al. (2015); Barnett et al. (2015) and references within
K_E (half-saturation constant for light use)	Ein m^{-2} d^{-1}	[1; 20]	Sibert et al. (2011); Le Fouest et al. (2013)
T_{opt_Z} (optimal temperature for grazing)	°C	[18; 38]	Present study
α_Z (shape parameter of the temperature related grazing)	-	[1; 30]	Present study

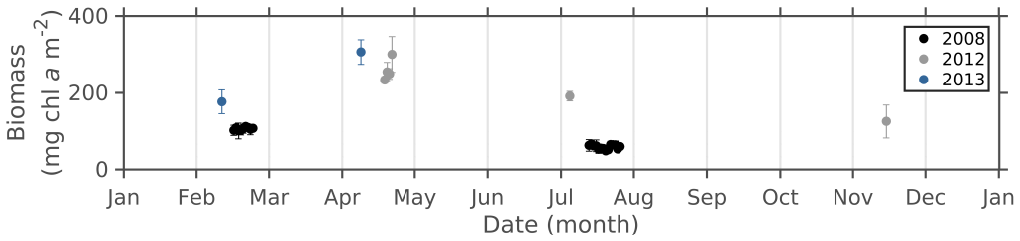

Figure 13: Daily-averaged *in situ* MPB biomass (mg Chl *a* m^{-2}) sampled in the sediment first cm at the study station on the Brouage mudflat in 2008 (black full dots), 2012 (grey full dots) and 2013 (blue full dots). Error bars correspond to the standard deviation.

MPB dynamics

Based on *in situ* Chl *a* measurements sampled in the sediment first cm in 2008 and 2012-2013, the observed seasonal cycle of Chl *a* was characterised by concentrations increasing from February to April, when the values were the highest (234-306 mg C m^{-2}; Fig. 13). Then the Chl *a* concentration decreased to reach a seasonal minimum in July (48-191 mg C m^{-2}; Fig. 13).

The total MPB biomass ($S + F$) simulated by the model within the first cm sediment was the lowest in January and September ($\sim$ 30 and 40 mg Chl *a* m^{-2}, respectively) and reached a seasonal maximum in March ($\sim$ 266 mg Chl *a* m^{-2}, Fig. 14a). The simulated seasonal maximum and minimum of MPB biomass during spring and summer were consistent with the observations of 2008 and 2012-2013 (Fig. 13). The model reproduced the fortnightly tidal cycle with maximum values of MPB biomass simulated in spring tides (Fig. 14a). The simulated values of biomass of MPB were compared to 2008 time coincident observations (Fig. 14a). In February 2008, the simulated biomass was about 140.7 ± 27.7 mg Chl *a* m^{-2}, which was close but significantly higher compared to the measured total MPB biomass (106.5 ± 11.3 mg Chl *a* m^{-2}; Mann Whitney test: *p-value* < 0.05). In July 2008, the model also overestimated (68.1 ± 4.5 mg Chl *a* m^{-2}) the observed (58.6 ± 10.3 mg Chl *a* m^{-2}) MPB biomass (Mann Whitney test: *p-value* < 0.05). Nevertheless, the simulated values reasonably compared, on average, with match-up measurements gathered. The simulated daily biomass-specific photosynthetic rate followed a seasonal pattern similar to that of the simulated Chl *a* with values higher in late winter-spring (0.56 ± 0.1 mg C (mg Chl *a*)$^{-1}$ h^{-1}) than in summer (0.41 ± 0.06 mg C (mg Chl *a*)$^{-1}$ h^{-1}) and fall-early winter (0.29 ± 0.14 mg C (mg Chl *a*)$^{-1}$ h^{-1}) (Fig. 14b).

The observed seasonal cycle of MPB retrieved from NDVI time series was compared to the biomass simulated in the biofilm ($S*$). The daily maximum values of $S*$ simulated by the model for 2008 were subsampled to match the 2008 NDVI time series data (Fig. 15). Three distinct seasonal phases were identified in both time series using the amplitude of sign change of the $S*$ and

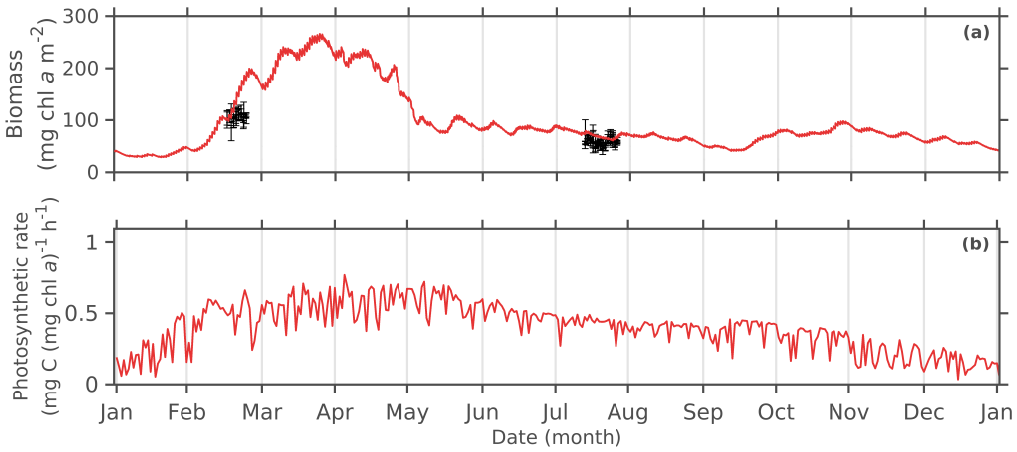

Figure 14: Seasonal cycle of the 2008 **(a)** simulated total MPB biomass (mg Chl *a* m^{-2}), and **(b)** simulated biomass-specific photosynthetic rate (mg C (mg Chl *a*)$^{-1}$ h^{-1}) averaged during daytime low tides. Black dots and error bars correspond to the mean and standard deviation of the Chl *a* (mg Chl *a* m^{-2}) measured *in situ*.

NDVI second order time derivatives (Fig. 15). The phase 1 corresponded to the spring bloom during which the biomass in the biofilm and the NDVI data reached their seasonal maximum value (day 1 to 144 and day 1 to 158 in the NDVI and model data, respectively). The phase 2 coincided with a summer depression in the simulated MPB biomass and NDVI data (day 145 to 270 and day 159 to 263 in the NDVI and model data, respectively). Finally, the phase 3 showed an increase of both the simulated biomass and NDVI values suggesting a fall bloom (day 271 to 365 and day 264 to 365 in the NDVI and model data, respectively). With respect to the NDVI data, the model showed a 14 days and 7 days longer spring and fall bloom, respectively, and a 21 days shorter summer depression (Fig. 15). Overall, the seasonal cycle of the simulated MPB biofilm compared reasonably to that depicted by the remotely-sensed NDVI data.

Biological parameters simulated by the model were compared to observed ranges reported in the literature (Table 7). The yearly-averaged value of $S*$ simulated by the model (27.2 $\pm$ 3.6 mg Chl *a* m^{-2}) was in agreement with the value given by Herlory et al. (24 $\pm$ 5 mg Chl *a* m^{-2}; 2004). The yearly-averaged MPB gross growth rate (μ) simulated within the biofilm was 0.25 $\pm$ 0.07 d^{-1} with values ranging between 0.05 d^{-1} and 0.41 d^{-1}, which compared to the observed growth rate (0.035-0.86 d^{-1}; Table 7). In the model, the MPB growth rate was related to the C:Chl *a* ratio (see Eq. 18 Chapter 2, section 2.4.2). The simulated C:Chl *a* ratio (16 and 75.5 g C g Chl a^{-1} varied between the observed range (18.7-80 g C g Chl a^{-1}; Table 7). The simulated annual and daily MPB PP rates (127 g C m^{-2} yr^{-1} and 369 $\pm$ 281 mg C m^{-2} d^{-1}, respectively) were

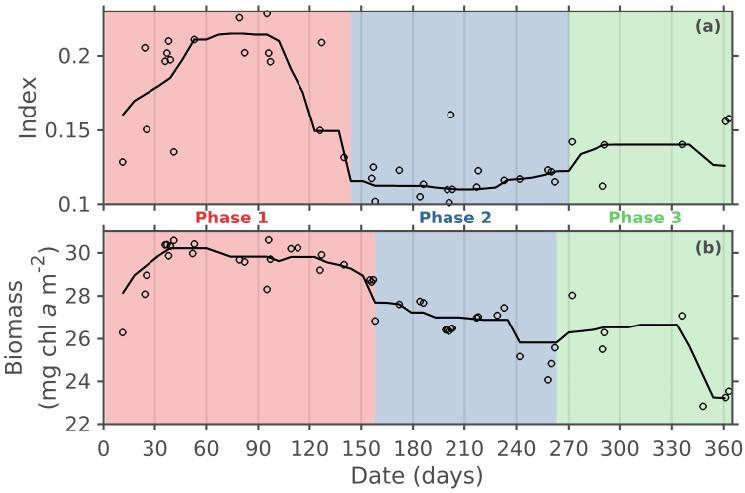

Figure 15: Seasonal cycle of the 2008 **(a)** Normalised difference vegetation index (NDVI), and **(b)** simulated daily maximum of the MPB biomass (mg Chl *a* m^{-2}) in the biofilm. Original extracted data (black circles) are overlaid. The black full lines represent the original extracted data regularised and filtered with running medians (window size = 7). The NDVI was calculated at the pixel corresponding to the study site. Phases were determined according to the amplitude of the sign change of the second order derivative.

also consistent with the reported *in situ* estimates (142 ± 82 g C m^{-2} yr^{-1} and 690 ± 682 mg C m^{-2} d^{-1}, respectively).

In the model, a linear loss term representing the resuspension process was applied to the MPB biomass simulated within the first cm of sediment (F compartment; see Appendix B1). In average over a high tide, 1.7 ± 0.3 % of the simulated MPB biomass was resuspended. With respect to primary production, 25 % of the MPB primary production simulated during low tides was resuspended, which corresponded in the model to a total annual resuspension of 31.6 g C m^{-2}.

P. ulvae dynamics

The MPB biomass simulated by the model was also constrained by the grazing pressure from the gastropod *P. ulvae*. The simulated density and biomass of *P. ulvae* increased in late winter with a first seasonal peak of ingestion on February 22 (Fig. 16c). A seasonal maximum of simulated density (25135 ind m^{-2}) and biomass (4 g C m^{-2}) was reached on May 2 (Fig. 16ab). The simulated density and biomass of *P. ulvae* were compared to 2008 time coincident observations (Fig. 16ab). In February, 2008 the simulated density (2616 ± 371 ind m^{-2}) was significantly lower than the measured density (5766 ± 2985 ind m^{-2}; Mann Whitney test: *p-value* < 0.05). In July, 2008 an average density of 9020 ±

Table 7: Range of values of simulated and observed biological variables.

Compartments	Variables	Units	Present study	Literature	References
MPB	S*	mg Chl *a* m^{-2}	27.2 ± 3.6	24 ± 5	Herlory et al. (2004)
	μ	d^{-1}	0.05 - 0.41	0.035 - 0.86	Gould and Gallagher (1990) Underwood and Smith (1998) Scholz and Liebezeit (2012)
	$\frac{C}{Chla}$	g g^{-1}	16 - 75.6	18.7 - 80	Guarini (1998) de Jonge et al. (2012) Gould and Gallagher (1990)
	Annual PP	g C m^{-2} yr^{-1}	127.23	142 ± 82	Underwood and Kromkamp (1999)
	Daily PP	mg C m^{-2} d^{-1}	369 ± 281	690 ± 682	
P. ulvae	Ingestion rate	ng Chl *a* ind^{-1} h^{-1}	0 - 87	0.75 - 385	Blanchard et al. (2000a) Haubois et al. (2005) Pascal et al. (2008) Coelho et al. (2011)

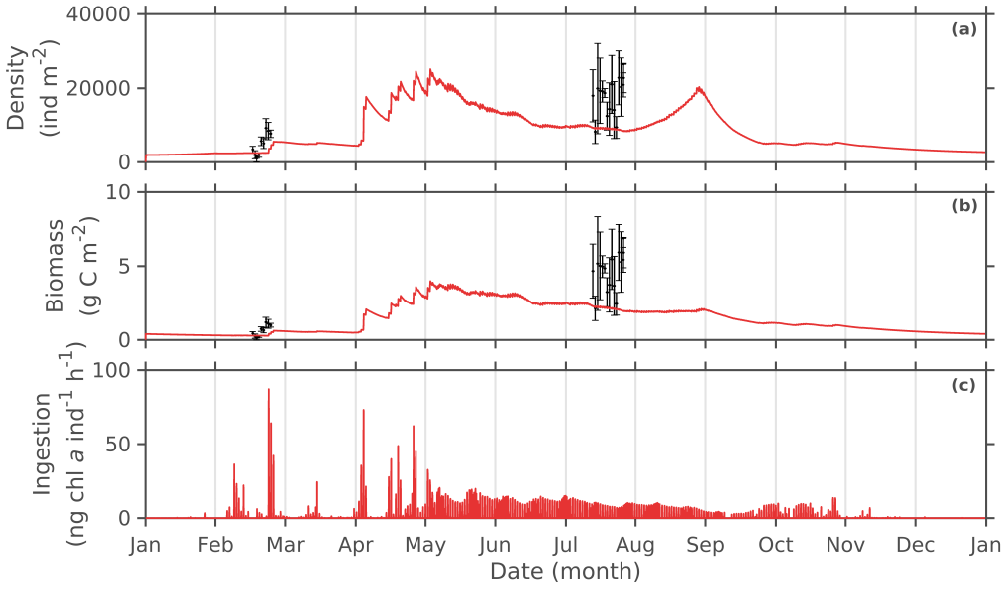

Figure 16: Seasonal cycle of the 2008 **(a)** simulated *P. ulvae* density (ind m^{-2}), **(b)** simulated *P. ulvae* biomass (g C m^{-2}), and **(c)** simulated individual ingestion rate by *P. ulvae* (ng Chl *a* ind^{-1} h^{-1}). Black dots (mean) and error bars (standard deviation) correspond to *in situ* observations.

227 ind m^{-2} was simulated by the model while a significantly higher average density of 17191 $\pm$ 7084 ind m^{-2} was measured (Mann Whitney test: *p-value* $<$ 0.05). In February, 2008 the simulated biomass of *P. ulvae* was 303.8 $\pm$ 40 mg C m^{-2}, which was significantly lower (Mann Whitney test: *p-value* $<$ 0.05) than the observed biomass (749.5 $\pm$ 388 mg C m^{-2}). In July, 2008 the model underestimated biomass (2157.2 $\pm$ 85 mg C m^{-2}) whereas the measured biomass was 4469.8 $\pm$ 1841.9 mg C m^{-2} (Mann Whitney test: *p-value* $<$ 0.05). The *P. ulvae* gross secondary production simulated by the model was 27 g C m^{-2} yr^{-1}. Overall, the model reasonably captured the seasonal features depicted by the match-up observations.

Contribution of light, temperature and grazing to the MPB seasonal cycle

In the model, bottom-up (MST and solar irradiance) and top-down (grazing by *P. ulvae*) processes constrained the simulated MPB growth rate. Light and temperature limitation terms (see Eq. 16 and 17 in Chapter 2, section 2.4.2) varied between 0 and 1. At each time step, the lowest value was set as the most limiting term constraining the computation of the MPB photosynthetic rate. Over each daytime exposure period, the most limiting bottom-up factor was defined as the factor whose limitation was the longest.

In phase 1, MST and light limited MPB growth 30 % and 70 % of the time, respectively, because PAR and simulated MST values were lower than the light

Table 8: Simulated contribution of light and temperature limitation during the three phases of the MPB seasonal cycle.

Phase	Temperature	Light
Phase 1	30 %	70 %
Phase 2	40 %	60 %
Phase 3	1 %	99 %

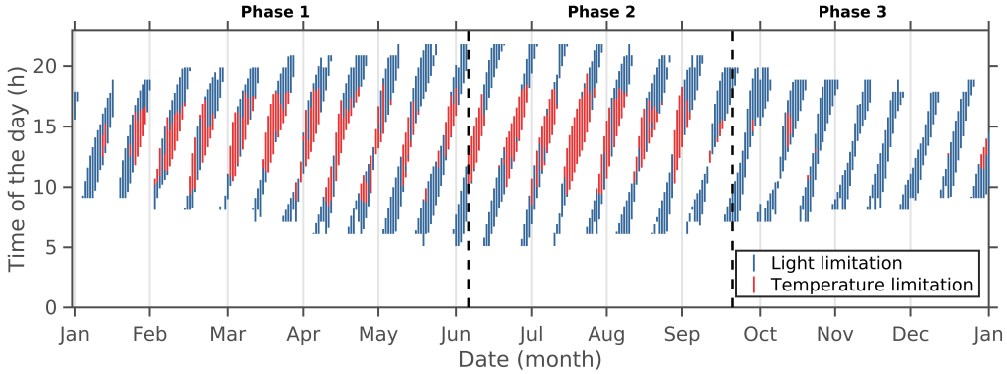

Figure 17: Simulated time occurrence of the light or temperature limitation of the MPB growth rate over daytime emersion periods in 2008.

saturation parameter (I_k, 100 W m^{-2}) and the temperature optimum for photosynthesis (T_{opt}, 18 °C), respectively (Table 8). In phase 2, light was the most limiting factor (60 %, Table 8). The increasing daytime duration allowed MPB to grow on two daytime emersion periods at the beginning and at the end of the daytime period during neap tides (Fig. 17). However, the simulated MPB was exposed to relatively low light levels during dawn and dusk compared to spring tides conditions, when the emersion periods occurred in the middle of the day and at relatively high light levels (Fig. 17). With respect to temperature, the MPB growth was more limited by MST in phase 2 (40 %) than in phase 1 (30 % Table 8). The high summer air temperature and solar irradiance heated the mud surface (Fig. 10cd and 12), especially when daytime exposure periods occurred in the middle of the day (10 AM - 16 PM) in spring tides (Fig. 17) with, as a consequence, simulated MST higher in average than the MPB T_{opt} value (Fig. 18a). In phase 3, the MPB growth rate was almost limited only by downward irradiance (99 %, Table 8). In fall, the average solar irradiance in daytime exposure periods decreased faster (slope = - 2.34 W m^{-2} d^{-1}, *p-value* < 0.05, corresponding to a deviation from I_k of - 2.3 % d^{-1}) than the MST (slope = - 0.13 °C d^{-1}, *p-value* < 0.05, corresponding to a deviation from T_{opt} of - 0.7 % d^{-1}).

Figure 18a shows the daily occurrence of MPB limitation by the simulated MST over 2008. In phase 1, the simulated MST increased towards T_{opt} and,

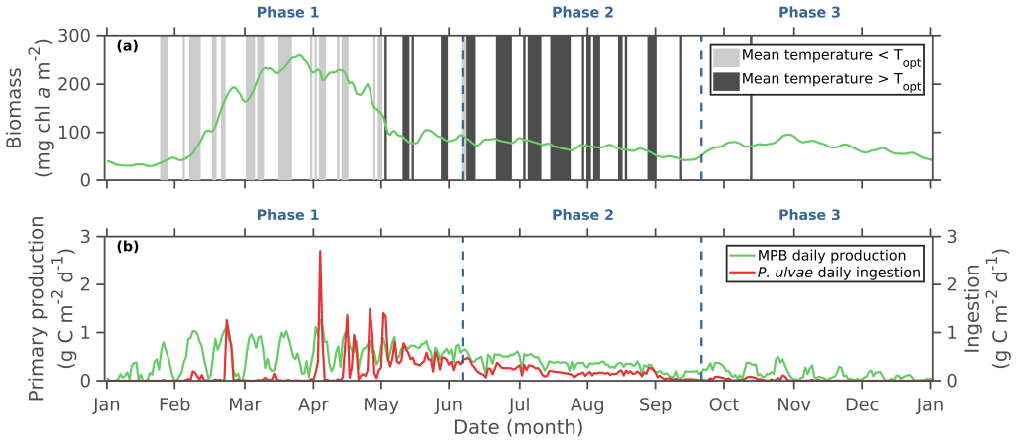

Figure 18: Seasonal cycle of the 2008 **(a)** simulated MPB biomass (mg Chl *a* m^{-2}, green full line) with time occurrence and duration (days) of the simulated temperature limitation term when daily-averaged mud surface temperature during emersion periods was lower (grey vertical bars) or higher (black vertical bars) than the optimal temperature for MPB growth (T_{opt}), and **(b)** simulated daily primary production rate (mg C m^{-2} d^{-1}) and *P. ulvae* ingestion rate (mg C m^{-2} d^{-1}). The dashed vertical lines delimit the 3 phases shown in Fig. 15.

combined with increasing irradiance, led to a seasonal maximum of the biomass-specific photosynthetic rate (Fig. 14b). It resulted in a seasonal maximum of MPB biomass in late March (Fig. 18a). In May (phase 1), the biomass-specific photosynthetic rate started to decrease due to thermoinhibition as soon as the MST exceeded T_{opt} (Fig. 14b and Fig. 18a). In phase 2, the simulated MST was always higher than T_{opt} when temperature limitation occurred (Fig. 18a).

With respect to grazing, the simulated biomass grazed by *P. ulvae* was compared to the simulated MPB biomass produced over the daytime emersion period (Fig. 18b). During phase 1, the ingested MPB biomass exceeded the MPB PP during 11 days (Fig. 18b). The simulated peaks of ingestion rate during these days varied between ~ 20 and 90 ng Chl *a* ind^{-1} h^{-1} (Fig. 16c), which was consistent with the reported values from laboratory measurements (0.75-385 ng Chl *a* ind^{-1} h^{-1}; Table 7). The daily-averaged *P. ulvae* ingestion:MPB production ratio was lower but more variable in phase 1 (0.31 ± 0.45) than in phase 2 (0.47 ± 0.18) (Fig. 18b). Phase 1 was characterised by a marked and synoptic impact of grazing at high MPB biomass levels. By contrast, grazing was moderate but more sustained in phase 2. Grazing contributed with thermoinhibition to maintain relatively low levels of MPB biomass (Fig. 18). As the ingestion rate of *P. ulvae* was related to the MPB biomass and to the MST, the peaks of grazing simulated in spring resulted from both the high MPB biomass accumulated during the bloom and the MST close to the temperature optimum for grazing by *P. ulvae* (T_{opt_Z}).

In the model, the occurrence of temperature or light limitation resulted from the coupling of the fortnightly tidal cycle with the seasonal solar irradiance and air temperature cycles. Over 2008, light was the most limiting factor because of low light levels in fall-winter and the occurrence of early and late daytime exposure periods during neap tides in spring-summer. During summer spring tides, the exposure periods occurred in the middle of the day and led to high simulated MST value (> 20 °C), hence limiting the MPB growth rate (T_{opt} = 18 °C). Consequently, the high grazing by *P. ulvae* in spring driven by the high MPB biomass simulated during the bloom was followed by a low MPB PP due to thermoinhibition along with a moderate but sustained grazing by *P. ulvae* in summer. It resulted into a marked depression of the simulated MPB biomass in summer.

Annual MPB production sensitivity

A total of 10,000 model runs (N) was performed, in which a set of biological constants (T_{opt}, T_{max}, T_{opt_Z}, α_Z, I_k and K_E) was randomly selected within the reported observed ranges (Table 6). These biological constants were chosen, because they were direct inputs in the mathematical functions used in the calculation of the simulated MPB production rate and *P. ulvae* ingestion rate. The sensitivity analysis resulted in two kinds of model runs according to the sustainability of the MPB PP over the year. Model runs in which PP was sustained (SPP runs, PP > 40 g C m^{-2} yr^{-1}, N = 1632) were distinguished from runs characterised by vanishing PP (VPP runs, PP ⩽ 40 g C m^{-2} yr^{-1}, N = 8368) according to a graphical representation of the annual PP as a function of the number of runs (Fig. 19). Figure 20 shows the 10,000 parameters combinations and the resulting MPB annual PP. The VPP runs are represented by the dark blueish lines (PP < 40 g C m^{-2} yr^{-1}) while the light blueish to reddish color gradient represent the SPP runs (PP > 40 g C m^{-2} yr^{-1}). In addition to SPP and VPP runs where all six biological constants varied simultaneously, simulations were run for which only one of the six constants varied at a time (Fig. 21).

Figures 20 and 21ab show that either a T_{opt} value greater than 24 °C or a MPB temperature maximum (T_{max}) lower than 26 °C induced the reduction of the annual MPB PP. The annual MPB PP was significantly negatively and positively correlated with T_{opt} and T_{max}, respectively (Fig. 21ab). In SPP runs, the annual PP was negatively but not significantly correlated with T_{opt} (Spearman's r = -0.04, *p-value* > 0.05; Table 9) because T_{opt} slightly varied within a range (18 ± 2.34 °C) corresponding to the T_{opt} threshold shown in Figure 21a. Moreover, the annual PP simulated in the SPP runs reflected the combined effect of the variation of T_{opt} with the other biological constants (Fig. 20). The annual PP simulated in SPP runs was positively and significantly correlated with T_{max} (Spearman's r = 0.15, *p-value* < 0.05; Table 9). In SPP runs, the

Table 9: Metrics obtained from the Monte-Carlo sensitivity analysis on the simulated annual primary production of MPB. r is the Spearman's correlation coefficient between annual production values from the different runs with the parameters values associated (the asterisk indicates that *p-value* < 0.05). T_{amp} corresponds to the difference between T_{max} and T_{opt}. σ_{norm} is the normalised standard deviation, *i.e.* the standard deviation divided by the mean.

	Sustainable primary production runs							Vanishing primary production runs						
	T_{opt}	T_{max}	T_{opt_Z}	α_Z	I_k	K_E	T_{amp}	T_{opt}	T_{max}	T_{opt_Z}	α_Z	I_k	K_E	T_{amp}
r	-0.04	0.15*	0.17*	-0.03	-0.71*	0.20*	0.21*	-0.83*	-0.44*	0.01	0.01	0.03	-0.06*	0.93*
Mean	18.00	34.00	28.00	15.00	77.00	12.00	15.00	29.00	34.00	28.00	15.00	94.00	10.00	5.10
σ_{norm}	0.13	0.13	0.21	0.57	0.64	0.43	0.27	0.22	0.16	0.21	0.56	0.55	0.54	0.73
Min	15.00	20.00	18.00	1.00	2.50	1.00	4.50	15.00	16.00	18.00	1.00	2.50	1.00	0.051
Max	27.00	40.00	38.00	29.00	180.00	20.00	25.00	40.00	41.00	38.00	29.00	180.00	20.00	22.00

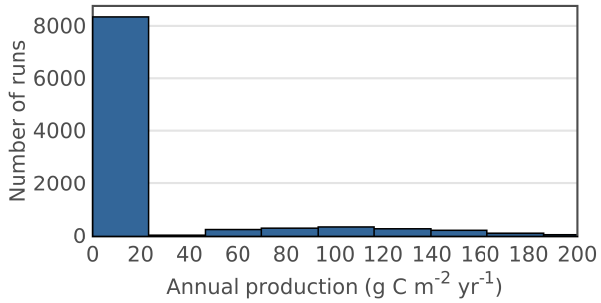

Figure 19: Frequency histogram of the annual primary production (g C m^{-2} yr^{-1}) simulated in the Monte-Carlo sensitivity analysis.

correlation between the annual PP and the MPB temperature amplitude (T_{amp}, the difference between T_{opt} and T_{max}) was even higher than the correlation between PP and T_{opt} and T_{max} (Spearman's $r = 0.21$, *p-value* < 0.05; Table 9). Figure 20 showed indeed that an increase of T_{amp} (*i.e.* a decrease of T_{opt} concomitant with an increase of T_{max}) led to an increase of PP. The positive effect of an increase of T_{amp} on the annual PP is also shown in Figure 21ab as either T_{opt} or T_{max} varied while the other was fixed ($T_{opt} = 18$ °C, $T_{max} = 38$ °C). The mean values of T_{amp}, T_{opt} and T_{max} were 15 °C, 18 °C and 34 °C, respectively, with relatively low variations of T_{opt} and T_{max} ($\sigma_{norm} \approx 0.13$) in SPP runs (Table 9). With respect to temperature, the use of such a set of values promoted PP in the model. In the contrary, runs with combinations which included a T_{opt} above 27 °C or a T_{max} below 20 °C resulted in the vanishing of PP over 2008 (dark blueish lines on Fig. 20). In VPP runs, the mean value of T_{amp} was 10.1 °C lower than in SPP runs, because the mean T_{opt} value (29 °C) was higher than in SPP runs (18 °C). The maximum value of T_{opt} was 13 °C higher in VPP runs than in SPP runs. The resulting wider range of T_{opt} values led to higher variations in T_{amp} in VPP runs ($\sigma_{norm} = 0.73$). However, SPP runs were also characterised by a T_{amp} minimum of 4.5 °C, which was ~ 3-fold lower than the T_{amp} mean value (15 °C).

PP was negatively correlated with I_k in SPP runs (Spearman's $r = -0.71$, *p-value* < 0.05) and induced large variations of annual MPB PP (Fig. 21c). Runs in which the simulated annual PP was high were characterised by I_k values in the lower part (from 2.5 to 100 W m^{-2}) of the full tested range (Fig. 20). In SPP runs, the mean value of I_k (77 m^{-2}) was lower than in VPP runs (94 W m^{-2}). However, I_k variations were comparable ($0.55 < \sigma_{norm} < 0.64$) and the minimum (2.5 W m^{-2}) and maximum values (180 W m^{-2}) were same in both the SPP and VPP runs. Consequently, annual PP is less sensitive to variations of I_k than to variations of T_{opt} and T_{max} and in SPP runs, a low value of I_k could sustain PP if T_{amp} was lower than 15 °C. Annual PP was sensitive to the half-saturation constant for light use (K_E) but to a lesser extent as a high annual PP was simulated using a K_E value spanning within the full tested range (Fig. 20).

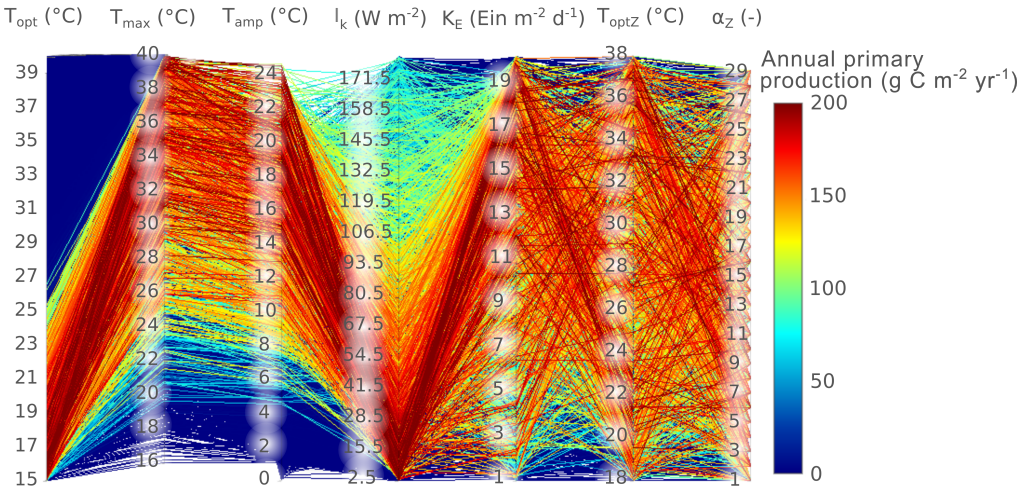

Figure 20: Parallel coordinates of the MPB annual primary production (g C m^{-2} yr^{-1}) according to the temperature optimum for MPB growth (T_{opt}), the temperature maximum for MPB growth (T_{max}), the light saturation parameter (I_k), the half saturation constant for light use (K_E), the temperature optimum for grazing by *P. ulvae* (T_{optz}), and the shape parameter of the temperature grazing function (α_Z) 10,000 combinations tested in the Monte-Carlo sensitivity analysis.

The annual PP in SPP runs was positively correlated with the half-saturation constant for light use (K_E; Spearman's $r = 0.2$, *p-value* < 0.05; Table 9 and Fig. 21d). Parameters combinations including high K_E values (15-20 Ein m^{-2} d^{-1}) resulted into highest annual PP.

When either T_{optz} or the shape parameter of the temperature grazing function (α_Z) varied individually in the model, it induced only small variations of the simulated annual PP (Fig. 21ef). In SPP runs, PP showed a low but significant correlation with T_{optz} (Spearman's $r = 0.17$, *p-value* < 0.05) suggesting that high T_{optz} values resulted in high levels of annual PP. PP was not correlated with α_Z in SPP runs (Spearman's r = -0.03, *p-value* > 0.05). However, T_{optz} and α_Z variations were high and of the same extent in both the SPP and VPP runs ($\sigma_{norm} = 0.21$ and $\sigma_{norm} \approx 0.57$, respectively). The mean, maximum and minimum value of T_{optz} and α_Z were also very similar in both SPP and VPP runs (Table 9). Compared to other parameters, annual PP was less sensitive to the *P. ulvae* grazing parameters as SPP runs took place in all the regions of the tested ranges (Fig. 20). Overall, the simulated annual PP was most sensitive to the MPB light- and temperature-related constants. The specific set of biological constants used in the study promoted realistic levels of MPB primary production. A specific set of these temperature and light related parameters allowed for a sustainable level of MPB production and biomass, which resulted in a significant effect of grazing on the MPB annual production.

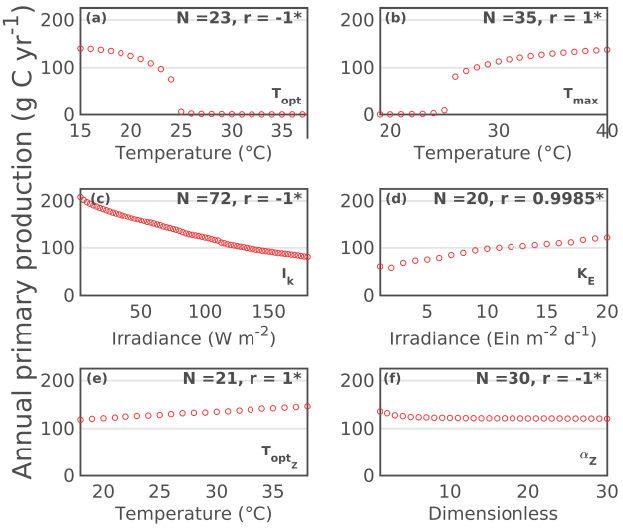

Figure 21: Sensitivity analysis of the 2008 simulated annual primary production of MPB according to **(a)** the temperature optimum for MPB growth (T_{opt}), **(b)** the temperature maximum for MPB growth (T_{max}), **(c)** the light saturation parameter (I_k), **(d)** the half saturation constant for light use (K_E), **(e)** the temperature optimum for grazing by *P. ulvae* (T_{opt_Z}), and **(f)** the shape parameter of the temperature grazing function (α_Z). N is the number of tested values and r is the Spearman's correlation coefficient (the asterisk indicates that *p-value* < 0.05).

DISCUSSION

The MPB seasonal cycle

Our study suggests a MPB seasonal cycle on the Brouage mudflat characterised by three phases in 2008, *i.e.* a bloom in winter-spring, low biomass levels in summer, and a peak of moderate intensity in fall. Cariou-Le Gall and Blanchard (1995) sampled monthly from March 1992 to February 1993 the MPB Chl *a* concentration within the top 0.5 cm sediment on the Brouage mudflat. Their measurements suggest a bloom in winter-spring and low Chl *a* concentrations in summer, which is consistent with the 2008 NDVI data, the observed MPB biomass (2008, 2012-2013) and MPB biomass simulated by the model. Cariou-Le Gall and Blanchard (1995) did not report any peak of MPB biomass in fall, which may be modulated by the inter-annual variability driven by the meteorological conditions. In Northern (de Jong and de Jonge, 1995; Sahan et al., 2007) and Southern (Brito et al., 2013) European mudflats, MPB spring blooms are also observed. However, the contribution of underlying abiotic (*e.g.* air temperature, irradiance, rain, wind) and biotic (*e.g.* autotrophic species community, predators) factors are likely to be different in shaping the seasonal MPB cycle at such contrasted latitudes.

In the Brouage mudflat, the simulated seasonal cycle of MPB at the sediment surface compares to that depicted by the remotely sensed NDVI data and measurements made in 2008 and 2012-2013. The simulated MPB biomass in the biofilm and its instantaneous PP are close to maximum values of biomass previously measured in biofilms developing at the surface of very fine sediments of the Brouage mudflat (Herlory et al., 2004). Once at the surface, the simulated MPB growth is regulated by the mass-specific photosynthetic rate in μg C (μg Chl *a*)$^{-1}$ h^{-1} converted into a growth rate (h^{-1}) using a variable C:Chl *a* ratio. The resulting MPB growth rates simulated by the model were consistent with observations made on epipelic diatoms (Gould and Gallagher, 1990; Underwood and Smith, 1998; Scholz and Liebezeit, 2012). With respect to the simulated C:Chl *a* ratio, it varies within the range of observed values in mudflats (Guarini, 1998; Gould and Gallagher, 1990; de Jonge et al., 2012).

Contrary to Chl *a* measurements, there were no PP measurements made in 2008 on the Brouage mudflat. For comparison, we use averages of biomass-specific photosynthetic rates computed from previous measurements at different locations on the Brouage mudflat for different years (using CO_2 fluxes data measured in benthic chambers). Despite the year-to-year variability, the mean biomass-specific photosynthetic rates simulated by the model during spring tides (0.66 ± 0.04 mg C (mg Chl *a*)$^{-1}$ h^{-1} in April, 0.52 ± 0.03 mg C (mg Chl *a*)$^{-1}$ h^{-1} in May and 0.44 ± 0.04 mg C (mg Chl *a*)$^{-1}$ h^{-1} in July) were in the range of measurements for the same months (1.6 ± 1.1 mg C (mg Chl *a*)$^{-1}$ h^{-1} in April 2012, 0.28 ± 0.11 mg C (mg Chl *a*)$^{-1}$ h^{-1} in May 2015 and 0.32 ± 0.13 mg C (mg Chl *a*)$^{-1}$ h^{-1} in July 2015; pers.comm. from J. Lavaud). Moreover, simulated daily and yearly PP rates compared to measurements made across other European intertidal mudflats (Underwood and Kromkamp, 1999). The model-data comparison suggests that the model can resolve with confidence the main patterns of the MPB seasonal cycle.

The relative contribution of light, MST and grazing to the simulated MPB seasonal cycle resulted from the coupling of the fortnightly tidal cycle and seasonal solar irradiance and air temperature cycles. Such a coupling is reported in intertidal sediments in the Tagus estuary, Portugal (Serodio and Catarino, 1999). In the model, an emersion period takes place in the middle of the day during spring tides exposing the mud surface to a daily solar irradiance and temperature maximum. In summer, when the seasonal maximum of daily solar irradiance and temperature is reached, the high simulated MST values translate into an enhanced thermoinhibition of MPB growth and *P. ulvae* grazing pressure. The highest MPB thermoinhibition in summer spring tides was also highlighted by Guarini et al. (1997) in the Brouage mudflat. During neap tides, light limits the MPB growth when exposure periods occur early in the morning and late in the afternoon at low daily light levels. The reduced PP of MPB at low light levels and MST values during neap tides compared to spring tides was also observed by Kwon et al. (2014) on the Hwaseong mudflat, South Korea.

In the model, we do not consider any MPB limitation by inorganic nutrients. In the Brouage mudflat, Feuillet-Girard et al. (1997) highlighted the greater affinity of MPB to ammonium compared to nitrate. They suggest a higher availability of ammonium released from the sediment in summer, making unlikely that the nutrient limitation is responsible of the summer depression of MPB biomass. The high nutrient availability in the sediment in summer can be attributed to faunal activities (bioturbation, bio-irrigation, excretion; Feuillet-Girard et al., 1997; Heilskov et al., 2006; Laverock et al., 2011).

The short-term daily dynamics of MPB is also regulated by resuspension events (Blanchard et al., 2002). The intensity of resuspension of MPB into the water column can be either chronic or catastrophic according to the flow velocity and the sediment stabilisation (Mariotti and Fagherazzi, 2012). Catastrophic events can locally resuspend all the MPB biomass as the resuspended sediment layer is thicker than the vertical distribution of MPB biomass (Mariotti and Fagherazzi, 2012). The repeated occurrences of such events over several days could contribute to shape the seasonal cycle of MPB by lowering the biomass of photosynthetically competent MPB. In their model, Guarini et al. (2008a) introduced a chronic resuspension of all the MPB biomass remaining in the biofilm when tidal floods occurred. In their parametrisation, the MPB biomass remains at the sediment surface according to a mean time spent at the surface (equivalent to τ_s in our study). In our study, the chronic resuspension of MPB biomass is formulated by a linear loss term of the MPB biomass within the first cm (0.002 h^{-1}). In the absence of MPB biomass deposition, the total simulated MPB biomass that is resuspended into the water column represents 25 % of the simulated benthic MPB annual production. Such a value suggests that the benthic MPB production contributes significantly to the pelagic food web (Perissinotto et al., 2003; Krumme et al., 2008). In the light of the work of Mariotti and Fagherazzi (2013), resuspension and deposition are key mechanisms that need to be related to fauna bioturbation, sediment characteristics (*e.g.* nature and stabilisation) and hydrodynamics (Mariotti and Fagherazzi, 2013). Such an approach requires the availability of waves and current data to estimate the bed shear stress and modulate the intensity of resuspension (from chronic to catastrophic events), which are not available at our study site for 2008.

Role of mud surface temperature on the MPB and P. ulvae activity

On the Brouage mudflat, the simulated MST plays a major role in the MPB seasonal cycle. In spring, the simulated MST increases towards the MPB temperature optimum for photosynthesis. Along with increasing light levels, it contributes to increase the mass-specific photosynthetic rate and triggers the onset of the MPB spring bloom. As soon as the simulated MST exceeds the MPB temperature optimum for photosynthesis, the MPB PP starts to decrease

due to thermoinhibition, particularly during spring tides. In fall, the average solar irradiance during daytime exposure periods decreased faster than the simulated MST. The simulated MST departs slower from the temperature optimum for photosynthesis than does the downward irradiance from the light saturation parameter. Despite decreasing solar irradiance in fall, the simulated MPB PP increases until November, when the simulated MPB growth rate is limited by low light levels and MST values with respect to the MPB light saturation parameter (100 W m^{-2}) and temperature optimum for photosynthesis (18 °C), respectively.

Using the Production-Temperature (P-T) model from Blanchard et al. (1996), Blanchard et al. (1997a) and Guarini et al. (2006) also suggested that the MPB PP was temperature-limited in summer on the Brouage mudflat. On a southern intertidal mudflat (Tagus Estuary, Portugal), Brito et al. (2013) suggested that thermoinhibition was responsible for the summer MPB depression observed in NDVI times series in conditions of high sediment temperature (30 °C). In addition, the detrimental effect of MST ranging between 18 °C and 24 °C was shown in microcosms using fluorescence (Cartaxana et al., 2015).

In the model, the production is related to temperature according the P-T relationship of Blanchard et al. (1996). As a result, the occurrence and intensity of MPB thermoinhibition depends on the MPB temperature optimum and maximum for photosynthesis used in the relationship. The set of parameters determines the thermal threshold and interval at which thermoinhibition occurs. The sensitivity analysis shows that the annual PP is very sensitive to the temperature amplitude between the two parameters. The annual PP increases as the amplitude increases. On the Brouage mudflat, the MPB temperature optimum and maximum for photosynthesis were estimated to 25 °C and 38 °C, respectively, and assumed to be constant over the year (Blanchard et al., 1997b). In our study, a lower MPB temperature optimum for photosynthesis value of 18 °C is required to simulate a spring bloom that compares to the NDVI time series. Such a temperature optimum also implies a more rapid onset and a higher MPB thermoinhibition as the simulated MST increases in summer. Values of both MPB temperature optimum and maximum for photosynthesis are reported to vary by up to 10 °C (Table 10). In that respect, the MPB temperature optimum for photosynthesis is a key parameter in the model, because it constrains the onset of the MPB spring bloom and the thermoinhibition span and intensity.

In addition, the strong heating and wind exposure of the mud surface is accompanied by pore water evaporation that results into desiccation and increased salinity (Coelho et al., 2009). A decrease of pore water content can induce even more detrimental effects within the cells through production of reactive oxygen species (Rijstenbil, 2003; Roncarati et al., 2008) potentially leading to the oxidation of the photosynthetic unit (Nishiyama et al., 2006). The motility of epipelic diatoms is supposed to be a strategy to avoid harmful con-

Table 10: Temperature optimum and maximum for photosynthesis (T_{opt} and T_{max}, respectively; °C).

Location	T_{opt}	T_{max}	Reference
Marennes-Oléron (France)	25	38	Blanchard et al. (1997a)
Roscoff (France)	21	32.5	Hubas et al. (2006)
Ems Dollard (Netherlands)	30	40	Morris and Kromkamp (2003)
Marennes-Oléron (France)	18	38	Present study

ditions at the surface of cohesive sediments (Admiraal, 1984). However, Juneau et al. (2015) showed no significant negative effect of salt stress on the photosynthesis of immobile epipelic diatoms. Coelho et al. (2009) highlighted the role of the rate of pore water content decrease in the field. While slow desiccation (reduction by 40% of the pore water content in 4.5 h) had no significant negative effect on the photosynthesis of microphytobenthic cells within the biofilm, fast desiccation (reduction by 40% of the pore water content in 2 h) resulted in desiccation and decreased the photosynthetic activity of MPB (Coelho et al., 2009). In addition to micro-migrations, epipelic diatoms produce extracellular polymeric substances (EPS) to temper the effect of desiccation and high salinity (Steele et al., 2014). High sediment temperature (> 35 °C) is also known to reduce the motility of MPB diatoms and so their capacity to avoid harmful conditions at the sediment surface (Cohn et al., 2003; Laviale et al., 2015). The detrimental effects of high salinity levels are not explicitly accounted for in the model. The underlying processes could be accounted for in the model in an implicit way by adjusting the MPB temperature-related growth parameters to accentuate the PP reduction, in simulated conditions when high evaporation is associated to high MST. The detrimental effects of desiccation on MPB cells motility could also be implicitly represented in the model through more photoinhibition.

The simulated MST also governs the ingestion rate of MPB by the grazer *P. ulvae* in the model. Simulated PP rates increase as the value of the optimal temperature for grazing increases, because the grazing optimum is not often reached in the model. In the model, the ingestion rate increases when the MST tends towards the optimal temperature for grazing (fixed at 20 °C ; Pascual and Drake, 2008). A high metabolism of benthic grazers promoted by high temperature conditions (up to 22 °C) and the resulting increase of the grazing pressure on benthic diatoms was observed by Sahan et al. (2007) on a mudflat in Netherlands.

Effect of light on MPB photosynthesis

In the model, light is the most limiting factor throughout the year. The low irradiance during fall and winter limits the MPB photosynthesis as the irradiance is in average lower than the light saturation parameter. In spring, the increasing irradiance and MST translate into higher biomass-specific photosynthetic rates than in fall-winter leading to the onset of the simulated MPB spring bloom. In summer, photo-inhibition is not accounted for in the model as the simulated mean time spent by a MPB cells at the surface is lower than the time required to induce photo-inhibition at saturating light levels (Blanchard et al., 2004). As a consequence, light limits the simulated MPB growth only during neap tides, when the sediment exposure occurs at low light levels early and late in the day.

Photosynthesis is represented in the model by the Production-Irradiance (P-I) model of Platt and Jassby (1976). It relies on the photosynthetic capacity (P^b_{max}), the light saturation parameter (I_k) and the maximum light utilisation coefficient ($\alpha = \frac{P^b_{max}}{I_k}$, Talling, 1957). Irradiance has no influence on the photosynthetic capacity and maximum light utilisation coefficient (MacIntyre et al., 2002) in our study. Based on the work of Blanchard et al. (1996), the photosynthetic capacity and maximum light utilisation coefficient vary in the model with the simulated MST. Therefore, the seasonal adjustment of photosynthesis to irradiance depends mainly on the photoacclimation status of MPB cells, which can be related to the light saturation parameter (Sakshaug et al., 1997). The light saturation parameter corresponds to the irradiance at which photosynthesis switches from light reactions (light absorption and photochemical energy conversion) to dark reactions (reductant utilisation) (Sakshaug et al., 1997). It has been reported to vary seasonally in benthic microalgae (Blanchard and Cariou-Le Gall, 1994; Barranguet et al., 1998; Light and Beardall, 2001; Pniewski et al., 2015; Barnett et al., 2015). Cells increase their light saturation parameter at high irradiance (summer) and reduce it with decreasing light levels (Sakshaug et al., 1997). In our study, as the light saturation parameter is set as constant throughout the year (100 W m^{-2}), photoacclimation is simulated by the way of a variable C:Chl *a* ratio.

During winter, low light acclimated cells have a lower C:Chl *a* ratio due to an increase of the Chl *a* content (MacIntyre et al., 2002; Brunet et al., 2011). In summer, with the increasing irradiance and day length, high light-acclimated cells reduce their Chl *a* content leading to a higher C:Chl *a* ratio (MacIntyre et al., 2002; Brunet et al., 2011). In the model, solar irradiance shapes the simulated C:Chl a ratio (Eq. 18 in Chapter 2, section 2.4.2). The C:Chl *a* ratio reaches a seasonal maximum value (75.5 g C g Chl a^{-1} in summer when solar irradiance is the highest. Such a result is consistent with estimate (80 g C g Chl a^{-1} reported in summer by de Jonge et al. (2012). In the model, given that the biomass-specific photosynthetic rate (µg C (µg Chl *a*)$^{-1}$ h^{-1}) and the C:Chl *a* ratio are related to the growth rate (h^{-1}), the growth rate increases as the

C:Chl *a* ratio decreases (low light acclimated cells). The seasonal variation of the simulated growth rate results from the combination of the variation of the photosynthetic capacity and maximum light utilisation coefficient driven by the simulated MST and the variation of the C:Chl *a* ratio with irradiance.

Finally, photoinhibition at high irradiance is not accounted for in the P-I model of Platt and Jassby (1976) used in the model. Epipelic diatoms achieve "micro-migrations" within the sediment to avoid harmful light conditions prevailing at the sediment surface (Kromkamp et al., 1998; Perkins et al., 2001; Cartaxana et al., 2011). However, combined with high temperature conditions (> 35 °C) at the sediment surface potentially leading to reduced cell motility (Cohn et al., 2003), epipelic diatoms can be photoinhibited (Laviale et al., 2015). In temperate intertidal mudflats, high light and temperature conditions occur during summer and their combined effect on MPB photosynthetic rate may explain the depression of MPB biomass observed in summer.

Top-down regulation of MPB dynamics

Grazing by meio- and macrobenthos is often suggested as the main driver of the MPB biomass depression observed in summer on intertidal mudflats (Cadée and Hegeman, 1974; Cariou-Le Gall and Blanchard, 1995; Sahan et al., 2007; Orvain et al., 2014a). Weerman et al. (2011) showed experimentally a strong decrease of MPB biomass in the presence of macrofauna driven by direct grazing and by the absence of surface mud stabilisation due to bioturbation by deposit feeders.

In the model, *P. ulvae* grazing exceeds the MPB PP mainly in spring (11 days of MPB biomass removal). *P. ulvae* depletes a substantial part of the MPB biomass accumulated during the spring bloom. After the bloom, a moderate but sustained grazing by *P. ulvae* adds to the effect of thermoinhibition on the MPB dynamics. The simulated gain terms promoting the growth rate of MPB limited by thermoinhibition do not compensate the loss terms dominated by the grazing pressure, which leads to a decrease of the MPB biomass. In a conceptual model, Thompson et al. (2000) showed such a seasonal uncoupling between the grazing intensity by intertidal grazing molluscs and the microalgae abundance from observations made on a rocky shore of the Isle of Mann (UK). The authors conceptualised the role played by the light and temperature stress on the microalgae productivity and by the temperature-promoted grazing in the depression of the microalgal standing stocks in summer.

The simulated annual *P. ulvae* gross secondary production is 27 g C m^{-2} yr^{-1}, which represents 21 % of the simulated annual MPB PP (127 g C m^{-2} yr^{-1}). This fraction of PP transferred to *P. ulvae* secondary production is consistent with the average fraction reported by Asmus and Asmus (15 ± 12 %; 1985) on intertidal sand bottom communities of the Island of Sylt in the North Sea. In July, the simulated density of *P. ulvae* lies in the lower range of time-coincident

measurements. As the simulated MST fairly agrees with time-coincident measurements, other factors may explain the likely underestimation by the model of the density and ingestion of *P. ulvae*. First, there may be a bias resulting from the monthly-averaged weight estimates used to simulate the *P. ulvae* density (see Chapter 2, section 2.4.2). The monthly-averaged weights are based on samples gathered in 2014-2015 on the Aiguillon mudflat, in the vicinity of the Brouage mudflat (Fig. 22). Nevertheless, the seasonality of the *P. ulvae* density is similar on the two mudflats with a peak of density in late summer (Haubois et al., 2002), which suggests that such a bias is likely limited. In addition, the simulated ingestion rates (20 - 90 ng Chl *a* ind^{-1} h^{-1}) are consistent with ingestion rates measured in experiments with *P. ulvae* and benthic diatoms collected in our study area and performed at a temperature close to the optimal temperature for grazing in the model (15 - 20 °C; 0.75 - 52 ng Chl *a* ind^{-1} h^{-1}; Blanchard et al., 2000a; Haubois et al., 2005; Pascal et al., 2008). Second, the *P. ulvae* density on the mudflat can change horizontally as a result of the foraging activity of the individuals and transport mediated by the wave- and tidal-induced shear stress on the bottom sediment. Such a process is not accounted for in the model and may lead to an underestimation of the *P. ulvae* biomass and density. Finally, potential MPB grazing by fauna other than *P. ulvae* is represented in a simple way by a linear and generic loss term in the model whereas it might be a non-linear process that can vary seasonally (Pinckney et al., 2003). This closure term may be underestimated in the model.

With respect to meiofauna, Pinckney et al. (2003) suggested a more intense grazing by meiofauna in summer than in winter in the Terrebonne Bay estuary (USA). Admiraal et al. (1983) estimated the meiofauna grazing at 300 mg C m^{-2} d^{-1} on a mudflat of the Ems Dollard estuary (Netherlands). Comparable rates of meiofauna ingestion (58 - 189 mg C m^{-2} d^{-1}) are reported for the Brouage mudflat (Montagna et al., 1995). Admiraal et al. (1983) observed a non-significant effect of meiofauna grazing relative to the MPB production rates. Nevertheless, their estimated grazing rate exceeds our simulated daily MPB production rates for 36 days in summer *i.e.* 34% of the time of the second phase in the model, suggesting that meiofauna grazing could impact MPB. In addition, Pascal et al. (2008) compared ingestion rates by *P. ulvae* and a nematode community from the Brouage mudflat in experimental conditions. According to the abundance of organisms selected for the experiment of Pascal et al. (2008) and a constant C:Chl *a* ratio of 45 g C g Chl a^{-1} (Guarini, 1998), the amount of Chl *a* ingested by nematodes per hour was only 1.5 % of the Chl *a* ingested by *P. ulvae* per hour in their experiment. However, in regard to the observed abundances on the field and without density-dependant effect on grazing rates, this theoretical amount of Chl *a* ingested by nematodes increases to almost 50% of the Chl *a* ingested by *P. ulvae* in the study of Pascal et al. (2008). According to the measured biomass uptake by meiofauna (Montagna et al., 1995) and nematodes (Pascal et al., 2008) for the Brouage mudflat, an

explicit representation of meiofauna ingestion in the model might magnify the simulated depletion of MPB biomass in summer months. The representation of grazing in the model can be improved. Nevertheless, the fair agreement between the simulated *P. ulvae* densities and biomass levels with time-limited but time-coincident observations suggests that overall the model simulates with some confidence the grazing pressure on MPB.

Physical setting of the coupled model

The predictive ability of the physical-biological coupled model depends on the accuracy of the oceanic and meteorological forcings. The frequency of the water height and meteorological time series used to constrain the model is hourly while the model time step 6 minutes. The lower frequency of the model forcings over a day partly explains the model-data discrepancies. In addition, the weather station where meteorological data were acquired is located 30 km away from the Brouage study site. Local weather conditions may differ between the two sites, especially the global irradiance and wind speed used to simulate the MST and MPB growth rate. Global irradiance can be impacted by local cloud cover and the wind regime can be different due to local thermal winds. In the model, the timing of the emersion-immersion cycle is constrained by the observed water heights and bathymetric level. The bathymetric level used to compute the water height above the Brouage study site originates from a digital elevation model with a 1-m horizontal resolution and a 15-cm vertical precision. Even if the Brouage mudflat is relatively flat (1:1000), ridges and runnels are present near the study site (Gouleau et al., 2000) and the topography is highly variable at a meter scale. Inaccuracies in the bathymetric level relative to the study site may translate into model-data discrepancies in terms of timing of the emersion-immersion cycle in the model. Given that the mud temperature model is constrained by the water height and meteorological data, it is sensitive to possible inaccuracies in the forcings that may impact the simulated hourly dynamics of MPB and *P. ulvae*. Nevertheless, at the seasonal scale, the impact on the biological compartments of such inaccuracies in the forcings may be limited.

CONCLUSIONS

This study is a first attempt to simulate the MPB seasonal cycle observed on a temperate intertidal mudflat and to quantify the relative contribution of both biotic and abiotic factors on the seasonal MPB dynamics. The physical-biological coupled model fairly compares to time-coincident remotely sensed and *in situ* data and provides key findings about the seasonality of MPB on the Brouage mudflat (French Atlantic coast):

- The 2008 MPB seasonal cycle consists in 3 phases: a spring bloom, a summer depression of the biomass levels, and a moderate peak of biomass in fall;
- In winter and early spring, the seasonal mass-specific maximum photosynthetic rate mainly driven by the simulated MST and the seasonal low C:Chl *a* ratios lead to a seasonal maximum of MPB growth rate and to a MPB spring bloom;
- *P. ulvae* grazing has a marked and synoptic impact on the MPB biomass accumulated during the spring bloom;
- In late spring-summer, grazing is moderate but more sustained. Both grazing and thermoinhibition, which is limiting for MPB growth 40 % of time in summer, contribute to maintain relatively low levels of MPB biomass;
- The model is sensitive to MPB temperature parameters (temperature optimum and maximum for photosynthesis), to the MPB light saturation parameter and, to a lesser extent, to grazing parameters (the optimal temperature for grazing and the shape parameter of the temperature-related grazing function).

The seasonal MPB dynamics simulated by the model compares to time coincident times series of remotely sensed NDVI data hence providing a qualitative assessment of the model predictive ability. A next step would be to extend such a model-satellite data comparison to a more quantitative assessment to validate the simulated levels of MPB Chl *a* concentration and PP. The recent advance of multispectral and hyperspectral remote sensing allows for the development of new algorithms to retrieve products of ecological interest for MPB. Brito et al. (2013) developed local empirical relationships relating synchronised NDVI data to *in situ* Chl *a* concentrations to retrieve from space estimates of Chl *a* concentration on a Portuguese intertidal mudflat. Efforts are also focused in using remote sensing reflectance from airborne hyperspectral data to assess MPB PP rates (Méléder et al., 2018). Recently, and in light of the work of Brito et al. (2013), Daggers et al. (2018) combined biomass derived from NDVI data with simulated photosynthetic capacity from environmental conditions (irradiance and air temperature) to map MPB PP on intertidal mudflats in Netherlands. Other promising methods in the estimation of PP in intertidal mudflat at the ecosystem scale are the non-invasive atmospheric and aquatic Eddy Covariance (EC) techniques. The atmospheric EC provides continuous and direct CO_2 flux measurements at the air-water and air-sediment interfaces during high and low tides, respectively, across different time scales from hours to years (Baldocchi et al., 1988; Aubinet et al., 1999; Zemmelink et al., 2009; Polsenaere et al., 2012). Similarly, the aquatic EC measures benthic O_2 fluxes

at the sediment/water interface (Berg et al., 2003). Quantifying the MPB PP and biomass on intertidal mudflats is a prerequisite for further estimating the flux of biogenic carbon from the benthos to the pelagos. During the immersion period, MPB can be resuspended (9.7 mg C per high tide, i.e 3 % of the mean simulated production during low tides, Dupuy et al., 2014) and highly disturb the functioning of the benthic-pelagic ecosystem (Saint-Béat et al., 2014). The study of air-water and sediment-water exchanges through simultaneous atmospheric and aquatic EC measurements could allow quantifying the importance of metabolic fluxes during immersion and exposure periods but also the coupled processes between the benthic and pelagic compartments such as MPB resuspension. Microphythobenthic community resuspension can significantly contribute to planktonic gross PP and, in turn, explain lower CO_2 fluxes from the water column to the atmosphere at high tide during the day than at night (Guarini et al., 2008a; Polsenaere et al., 2012). To date, the modelling effort put on the physically-driven (tides and waves) resuspension processes of MPB is still limited (see Mariotti and Fagherazzi, 2012). Accounting in models for sediment bottom shear stress mediated by hydrological forcings (current and waves) along with bioturbation processes could lead to more realistic predictions of the inter-annual MPB dynamics. Such a representation of the biologically and physically-driven benthic-pelagic interactions would be fully apprehended by the coupling of biological MPB models to high resolution ocean models. Such an approach would open the door to an accurate assessment of the vertical and horizontal export flux of biogenic matter at the land-ocean interface and, more generally, of the contribution of productive biofilms in mudflats in the carbon cycle of the global coastal ocean.

CHAPTER IV

IMPACT OF CHRONIC AND MASSIVE RESUSPENSION MECHANISMS ON THE MICROPHYTOBENTHOS DYNAMICS IN A TEMPERATE INTERTIDAL MUDFLAT

In Chapter 3, we used the MPB one-dimensional (1D) model to test hypotheses on the factors likely controlling the seasonal cycle of MPB biomass on the Brouage mudflat. We identified the key role played by light, mud surface temperature and grazing in shaping the MPB seasonality. However, we assumed a constant and linear resuspension of MPB during high tides. To date, the modelling effort put on the physically- (tides and waves) and biologically- (biostabilisation, bioturbation) driven resuspension processes of MPB is limited. In Chapter 4, we constrain the MPB 1D model with hydrodynamical forcings for the year 2012 to test hypotheses on the factors controlling MPB resuspension on the Brouage mudflat. The model is constrained by bed shear stress data computed from realistic waves, tidal currents simulated by the SCHISM two-dimensional (2D) model and sediment characteristics. The effect of physically-induced bed shear stress, bioturbation and MPB biomass in the sediment on the quantity and frequency of MPB resuspended in the water column is highlighted. At the tidal scale, the MPB resuspension is the highest at the flood beginning and at the end of ebb, and during spring tides due to high current velocities and low water heights that promote waves-sea bottom interactions and sediment erosion. In 2012, the simulated MPB resuspension is the highest in spring and the lowest in summer. The seasonal dynamics of MPB resuspension results from the MPB biomass in the sediment, physical disturbances and the grazer activity at the mud surface that remobilised and facilitated the MPB resuspension through bioturbation. The explicit representation of bed shear stress mediated by oceanic forcings along with the bioturbation and biostabilisation processes promoted realistic MPB dynamics and consistent benthopelagic fluxes of MPB biomass.

4

IMPACT OF CHRONIC AND MASSIVE RESUSPENSION MECHANISMS ON THE MICROPHYTOBENTHOS DYNAMICS IN A TEMPERATE INTERTIDAL MUDFLAT

ABSTRACT

Microphytobenthos (MPB) resuspension is a key mechanism in the transfer of organic matter from productive intertidal mudflats to terrestrial and marine systems. In this study, we infer on the contribution of physical and biological factors involved in the MPB resuspension. We use a physical-biological coupled model forced by realistic meteorological and hydrodynamical forcings to simulate chronic (without any concomitant sediment resuspension) and massive (driven by bed failure) resuspension over a year. The model simulates mud surface temperature, MPB growth and grazing by the gastropod *Peringia ulvae*. The model suggests that MPB resuspension is the highest in spring tides and at the flood beginning due to high current velocity and low water heights that promote waves-sea bottom interactions. The seasonal export of MPB biomass is the highest in spring, up to 3-fold higher than in summer when the export is the lowest. The simulated seasonal dynamics of MPB resuspension results from the MPB biomass concentration in the sediment, physical disturbances and the bioturbation activity by *P. ulvae*. Annually, 43 % of the simulated MPB primary production is resuspended. The MPB resuspension (60.8 g C m^{-2} yr^{-1}) exceeds the loss by *P. ulvae* grazing (41.1 g C m^{-2} yr^{-1}). The model suggests that chronic and massive resuspension events are important in the synoptic to seasonal MPB dynamics in temperate intertidal mudflats. Accounting for such processes in the carbon budget assessment in the land-ocean interface could bring new insights to our understanding of the role played by MPB in the coastal carbon cycle.

This chapter was accepted on 15 October 2019 as an article in the journal Journal of Geophysical Research: Biogeosciences (Savelli et al., in press).

Acronyms:
BSS: *Bed shear stress*
EPS: *Extracellular Polymeric Substances*
MPB: *Microphytobenthos*
MST: *Mud surface temperature*
PAR: *Photosynthetically Active Radiation*
PHY $_{\mathrm{run}}$ *Run with wave- and tidal-induced MPB resuspension and fluff layer erosion*
PP: *Primary Production*
REF $_{\mathrm{run}}$***:*** *Run with a constant rate of resuspension*

INTRODUCTION

Tidal flats play a key role in the structure and functioning of coastal areas (Healy et al., 2002, Millennium Ecosystem Assessment, 2005). Benthic microalgae or microphytobenthos (MPB) living in intertidal and shallow sediments significantly contribute to the high biological production of coastal ecosystems (MacIntyre et al., 1996; Underwood and Kromkamp, 1999). MPB assemblages consist mainly of diatoms, cyanobacteria, euglenophyta and chlorophyta, which vary with sediment properties (Underwood, 2001). In sandy, coarse and non-cohesive sediments, MPB are composed by epipsammic taxa that live in close

association with sediment grains (Underwood, 2001). In very fine cohesive sediments, MPB consist mainly of free motile epipelic cells that bury in the first centimetre of sediment during high tides and migrate up to the sediment surface during daytime low tides (Underwood, 2001). At the sediment surface, the MPB photosynthetic rate is driven by mud surface temperature (MST) and solar irradiance (Barranguet et al., 1998; Perkins et al., 2010; Vieira et al., 2013; Cartaxana et al., 2013, 2015). At optimal levels, they drive a high MPB primary production (PP) up to 1.9 g C m^{-2} d^{-1} (Underwood and Kromkamp, 1999). The MPB production is transferred to adjacent terrestrial and marine zones through trophic export (Carlton and Hodder, 2003; Perissinotto et al., 2003; Galván et al., 2008; Saint-Béat et al., 2013; Jardine et al., 2015) and hydrodynamics (Ubertini et al., 2012). During the rising tide, MPB cells are susceptible to be resuspended in the water column (de Jonge and van Beusekom, 1992, 1995). Therefore, in addition to the direct export to benthic food webs through grazing (Herman et al., 2000; Lucas et al., 2001; Kang et al., 2006; Jardine et al., 2015), MPB also sustain pelagic suspensive and filter feeders, such as herbivorous fishes and zooplankton, as well as wild or farmed shellfishes (Leroux, 1956; Paulmier, 1972; Newell et al., 1989; Perissinotto et al., 2003; Krumme et al., 2008).

The MPB resuspension consists of chronic resuspension of MPB cells without any concomitant sediment resuspension and of episodic massive resuspension driven by bed failure. As MPB are associated with sediment, MPB resuspension can be driven by the same hydrodynamical mechanisms that govern sediment resuspension. In intertidal mudflats, tidal currents can be strong enough to induce the resuspension of unconsolidated sediment (Mehta et al., 1989). However, only high bed shear stress (BSS) driven by waves, combined or not with tidal currents, can resuspend consolidated sediment (Bassoullet et al., 2000; French et al., 2008). Episodes of strong waves and tidal currents can therefore remobilise a sediment surface layer deeper than 1 cm (Andersen et al., 2007; Christie et al., 1999) and export a high quantity of MPB biomass to the water column, identified as massive resuspension (Mariotti and Fagherazzi, 2013). Moreover, MPB control the bed failure probability by stabilising the sediment upper layer. The excretion of extracellular polymeric substances (EPS) mainly by MPB, increases the sediment consolidation and its resistance to hydrodynamical disturbances by binding the sediment particles together (Paterson, 1989; Madsen et al., 1993; Underwood and Paterson, 1993; Austen et al., 1999; Decho, 1990, 2000; Pierre et al., 2010, 2012).

In conditions without any bed failure, chlorophyll pigments originating from MPB biofilms were measured in the water column and were related to the fluff layer erosion (Blanchard et al., 1997b; Wiltshire et al., 1998; Dupuy et al., 2014; Orvain et al., 2014b). This biogenic fluff layer is formed by the tracks, mucus and pellets generated by grazing, crawling and egestion of benthic deposit-feeders at the sediment surface containing MPB cells and sediment grains (Willows et al., 1998; Le Hir et al., 2007). The fluff layer formed through the action

of bioturbation is not bounded to the sediment bed and can be eroded more easily (Davis, 1993; Blanchard et al., 1997b; Willows et al., 1998; Andersen, 2001; Orvain et al., 2003). Consequently, normal hydrodynamical conditions can promote fluff layer erosion and associated MPB more frequently. Such a process can be considered as chronic resuspension (Orvain et al., 2014b).

The *in situ* monitoring of the MPB export from the sediment to the water column is not trivial. This is due to the highly responsive behaviour of MPB when exposed to the highly variable physical (light, temperature, tide, waves) and biological (MPB dynamics, bacteria and grazers) conditions. Remotely-sensed data of MPB cover a wide range of spatial scales (~ from one to few hundred meters) but their limited number of products and their limited time resolution (~ from one to several days and 1 hour for geostationary satellites) impede our capacity to investigate the underlying processes of the retrieved state of MPB (*e.g.* Brito et al., 2013; Benyoucef et al., 2014; Gernez et al., 2017; Daggers et al., 2018; Méléder et al., 2018).

Physical-biological coupled modelling is a complementary tool to field and remote sensing studies to better understand physical and biogeochemical processes prevailing in these complex intertidal systems. Our study aims to estimate the chronic and massive MPB resuspension and to infer on its role on the seasonal MPB dynamics over one of the largest intertidal mudflat of the French Atlantic coast, in the Bay of Marennes-Oléron. We used a physical-biological coupled model that simulated the seasonal pattern of MPB growth and grazing by gastropod deposit-feeder *Peringia ulvae*. In the paper, we first describe the coupled physical-biological modelling approach. Then, we assess the role and the temporal variability of each resuspension type (chronic *vs.* massive) on the MPB dynamics. Finally, we discuss the importance of considering MPB resuspension to better understand the coastal food webs functioning and the seasonal export to the water column of organic matter mediated by MPB.

MATERIAL AND METHODS

Study site

The study area is the Pertuis Charentais Sea, a shallow semi-enclosed sea on the French Atlantic coast (Fig. 22). It is characterised by a semi-diurnal macrotidal regime (tidal range ~ 6 m at spring tides). In the southern part of the domain, the Bay of Marennes-Oléron covers 170 km^2 including 60 km^2 of intertidal mudflats. The study site (45°54'50"N, 01°05'25"W) is located in the Bay, on the Brouage mudflat (Fig. 22). It is a 42 km^2 intertidal mudflat made of fine cohesive sediments (median grain size 17 µm and 85 % of grains with a diameter < 63 µm; Bocher et al., 2007) and characterised by a gentle slope (~ 1/1000; Le Hir et al., 2000). The concentration of total suspended matter over the mudflat lies in the range 50-80 mg l^{-1} at neap tides and can reach 500 mg l^{-1} at spring

tides (Kervella, 2009). North of the Brouage mudflat, the turbidity usually takes values between 4 ± 1 NTU and 12 ± 8 NTU in summer and winter, respectively (Luna-Acosta et al., 2015). South of the mudflat, it varies between 10 ± 8 NTU and 14 ± 12 NTU in summer and winter, respectively (Luna-Acosta et al., 2015). The highest current velocity reached at neap and spring tides is ~ 0.2 m s^{-1} and 0.5 m s^{-1}, respectively (Le Hir et al., 2000). On the Brouage mudflat, the wave height was measured as up to 0.7 m (Bassoullet et al., 2000). As in many mudflats along the northern European Atlantic coast, a dense biofilm of epipelic MPB develops at the surface of the mudflat at low tide and can reach up to 25 mg Chl *a* m^{-2} (Herlory et al., 2004). When resuspended by waves and tidal currents, MPB can contribute significantly to in-water Chl *a* measured in the area (from 4 to 16 mg Chl *a* m^{-3}; Soletchnik et al., 1998; Guarini et al., 2004; Struski and Bacher, 2006; Soletchnik et al., 2017).

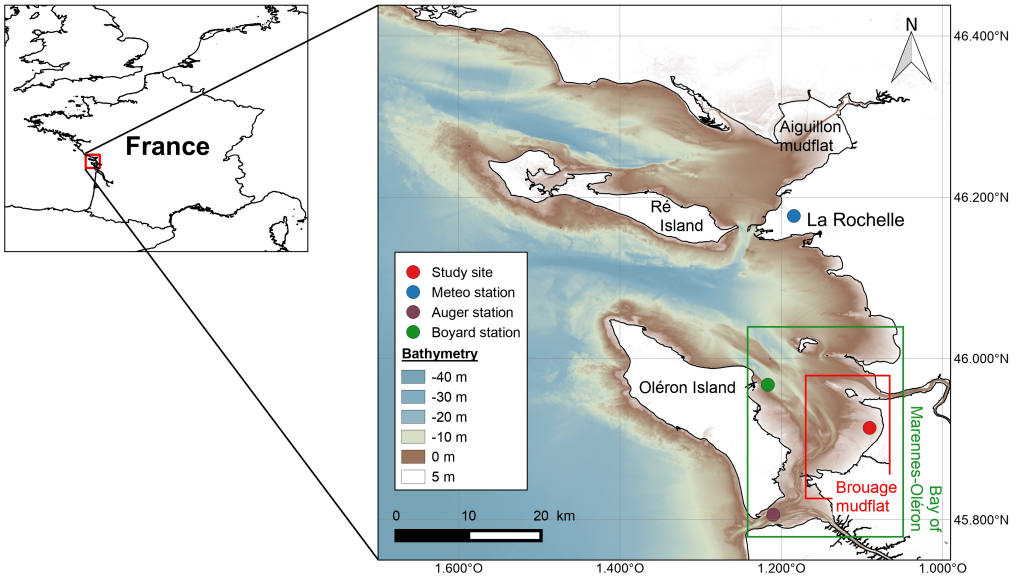

Figure 22: Bathymetric map of the Pertuis Charentais Sea (source: SHOM) and location of the main intertidal mudflats. The study site and the Meteo France weather station are represented by a red and a blue full point, respectively. The two REPHY monitoring stations are represented by the purple and green full points.

Observations

A large multiparametric dataset of physical and biological measurements collected in the Pertuis Charentais Sea was used to constrain the model and to compare with the model outputs. We provide here a summary of the data used along with their respective references, within which a detailed methodology of each set of measurements can be found.

In situ data

We used 2012 atmospheric forcings to constrain the MST model and the MPB model. Atmospheric forcings consisted of hourly meteorological observations (shortwave radiations, air temperature in the shade, and relative humidity) acquired at the Meteo France weather station located near the La Rochelle airport (46°10'36" N, 1°11'3" W; data available online at https://publitheque.meteo.fr; Fig. 23). They were complemented by hourly sea level atmospheric pressure and wind velocity extracted from the atmospheric reanalysis CFSR (NCEP Climate Forecast System Version 2 (CFSv2) selected hourly time-series products, https://rda.ucar.edu/datasets/ds094.1) at the study site (Fig. 23). Atmospheric forcings span from 1 September 2011 (03:00 UTC) to 31 December 2012 (23:00 UTC).

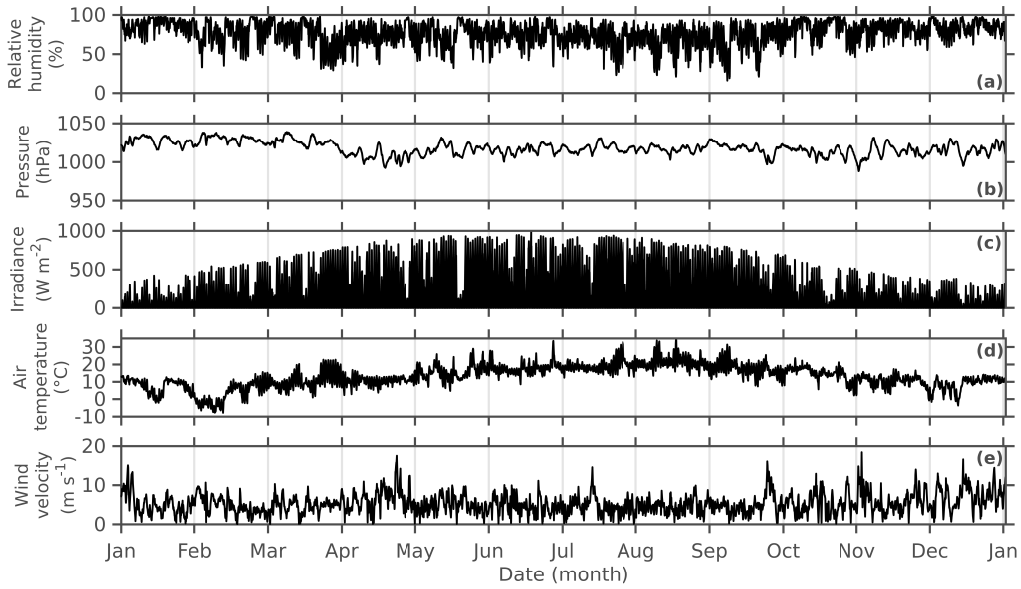

Figure 23: Time series of the 2012 **(a)** relative humidity, **(b)** atmospheric pressure above the sea, **(c)** global irradiance, **(d)** air temperature in the shade, and **(e)** wind velocity at the study site.

An acoustic Doppler current profiler mounted with a pressure transducer (ADCP; Aquadopp Profiler 2MHz, Nortek AS) was deployed on the sea bottom from 19 April 2012 (12:00 UTC) to 22 April 2012 (12:00 UTC). The ADCP data were used to compare with the water depth, the current velocity and the wave parameters simulated by the SCHISM model and used to constrain the coupled physical-biological model. The ADCP was set to measure 1 minute-mean velocity profiles with a 0.1 m vertical resolution followed by 10 minutes continuous measurements at 2 Hz, where current velocities were averaged in a 0.5 m-thick cell. Power spectral density (PSD) estimates were computed using 5 overlapping and hanning-windowed segments, which results in 10 degrees

of freedom and a frequency resolution of 0.0196 Hz. Pressure attenuation with depth was corrected using linear wave theory. The spectral significant wave height Hm_0 and the mean wave period Tm_{02} were computed integrating the corrected PSD from 0.05 to 0.44 Hz.

The overall consistency of the MPB compartment was assessed using both field and satellite-derived data of chlorophyll concentration. We compared the simulated resuspended MPB biomass (mg Chl *a* m^{-3}) with the in-water Chl *a* concentration (mg Chl *a* m^{-3}) measured at two sampling stations of the French Phytoplankton and Phycotoxin Monitoring Network (REPHY; Belin and Raffin, 1990; French Observation and Monitoring program for Phytoplankton and Hydrology in coastal waters, 2017) in the Pertuis Charentais Sea. The samples were collected twice a month at a sub-surface depth (between 0 and 1 m) with a HYDROBIOS sampling bottle (2.5 L). The first station is the Boyard station located at the East of Oléron Island (Fig. 22). The second station is the Auger station located to the South of the Bay of Marennes-Oléron (Fig. 22; Soletchnik et al., 2017, 2018). In addition to Chl *a* concentration, we also used the phytoplankton cells taxonomic identification from the same samples, in order to differentiate the contribution of resuspended benthic species to the total microalgae cell counts. Taxonomic identification was performed at the class to species level. Class and species were associated to a full or partial benthic growth and pelagic growth form according to the classification given in Hernández Fariñas et al. (2017). Counts (number of cells per liter) were used to determine the contribution of each forms. Only Chl *a* measurements from samples in which the contribution of benthic form exceed 50 % were used.

Remote sensing data

In addition to *in situ* REPHY data, we compared the simulated Chl *a* data with space and time coincident cloud-free satellite data from the Medium Resolution Imaging Spectrometer (MERIS) on-board the polar-orbiting environmental research satellite (ENVISAT) of the European Space Agency (ESA). MERIS has a global coverage of 3 days and a horizontal resolution of 300 m in Full-resolution mode (Rast et al., 1999). Level2 data of spectral marine reflectance were downloaded from the ESA's MERCI server (`https://merisfrs-merci-ds.eo.esa.int/`). The Chl *a* concentration was computed using a semi-analytical inversion algorithm specifically developed for coastal and inland waters (Gons, 1999; Gons et al., 2005). The algorithm used the spectral bands at 665, 705, and 775 nm, and the Chl *a* retrieval was performed in three steps.

The backscattering coefficient (b_b) was first estimated from the water reflectance (ρ_w) at 775 nm:

$$b_b(775) = \frac{1.61\rho_w(775)}{0.082 - 0.6\rho_w(775)} \tag{27}$$

Then, a NIR/red band ratio was used to compute the phytoplankton absorption at 665 nm:

$$a_{phy}(665) = \frac{(0.70 + b_b)\rho_w(705)}{\rho_w(665)} - 0.40 - b_b^p, \tag{28}$$

where p is a constant set to 1.02 (Gernez et al., 2017). Finally, Chl *a* concentration (mg Chl *a* m^{-3}) was obtained by dividing the phytoplankton absorption by the chlorophyll-specific absorption coefficient at 665 nm (a^*_{phy}):

$$[\text{Chl a}] = \frac{a_{phy}(665)}{a^*_{phy}(665)} \tag{29}$$

The value of a^*_{phy} (0.014 m^2 (mg Chl *a*)$^{-1}$) was set up from Gons results, which correspond to the average computed from a large variety of inland and coastal water samples. As communication with ENVISAT-1 was lost on 8 April 2012, 6 cloud-free high tide scene images were extracted from 4 January to 1 April 2012. Chl *a* concentration was estimated at the pixels corresponding to the study site (Fig. 22).

The coupled physical-biological one-dimensional model

The mud surface temperature model

A mud temperature model was coupled to a two-layer biological model and run for the year 2012. The model is not horizontally-resolved. Heat fluxes were simulated in a 1-cm deep sediment layer through a set of thermo-dynamic equations detailed in Savelli et al. (2018). The simulated temperature of exposed mud resulted from heat exchanges between the Sun, the atmosphere, the sediment surface, from the heat conduction between mud and air, and from mud evaporation. The simulated surface (1 cm) temperature of immersed mud was set to the temperature of the overlying seawater, which resulted from thermal conduction between air and seawater, upward seawater radiation, and downward solar and atmospheric radiation. The MST simulated by the model was successfully compared to 2008 *in situ* 1-min data at the same study site (see Savelli et al., 2018). The differential equation was solved with a 30-s Euler-Cauchy scheme.

The MPB model

The biological model explicitly represented the MPB biomass concentration in the surface biofilm compartment (S, mg Chl *a* m^{-2}) and in the sediment first centimetre (F, mg Chl *a* m^{-2}). The MPB model was developed and calibrated for epipelic diatoms. Exchanges of MPB biomass between the biofilm and the underlying sediment were ruled by a vertical MPB migration scheme according to the diurnal and tidal cycles (Guarini, 1998). During the daytime emersion

periods, the MPB cells migrated upward in the sediment from F to the S compartment until the biofilm saturation. In the biofilm, the MPB growth rate depended on the photosynthetically active radiation (PAR), the simulated MST and the grazing pressure. The potential time spent by the MPB at the surface was calculated before each low tide by the parameter γ^* (h):

$$\gamma* = (\frac{F}{S_{max}} + 1) \times \gamma, \tag{30}$$

where S_{max} is the saturation value of the surface biofilm (25 mg Chl *a* m^{-2}) and γ is the mean time spent by a MPB cells at the surface (1 h; Blanchard et al., 2004). The formula sets the potential duration of MPB biofilm at the sediment surface during daytime emersion periods by dividing the MPB biomass in F into fractions of biofilm (S_{max} = 25 mg Chl *a* m^{-2}) that spend 1 h in average at the sediment surface. The higher is the biomass in F, the longer is γ^*. This potential time is independent of the duration of the daytime emersion periods, which can be shorter or longer. As soon as MPB exceeded their potential duration at the surface, they migrated downward from S to the F compartment. MPB migrated downward also at nightfall and during immersion if hydrodynamical conditions were calm (*i.e.* when $\tau_{max} < \tau_{crit_{mass}}$, see Section 4.3.3.5). The grazing pressure was simulated through the *Peringia ulvae* biomass (Z, mg C m^{-2}) grazing on MPB at the sediment surface. The *P. ulvae* growth rate was related to the MST and the simulated MPB biomass.

The crawling activity of *P. ulvae* generates at the sediment surface a fluff layer composed by a mineral and organic matrix including MPB cells. Consequently we introduced a new compartment that represented the dynamics of MPB biomass in the fluff layer. Such a compartment was not taken into account in Savelli et al. (2018). The fluff layer was represented by the B compartment (mg Chl *a* m^{-2}), supplemented by a flux of MPB biomass from the biofilm to the fluff layer:

$$\frac{dB}{dt} = min\left[S \times (1 - \frac{B}{B_{max}}) \times \nu Z, \frac{S}{dt}\right], \tag{31}$$

where B_{max} is the saturation of Chl *a* concentration in the fluff layer. Considering a mean Chl *a* concentration in the sediment of 500 µg Chl *a* g^{-1} of dry sediment and a maximal resuspended mass of sediment of 23 g of dry sediment m^{-2} (Orvain et al., 2007), B_{max} was set to 11.5 mg Chl *a* m^{-2}. Here, Z was expressed in density of individuals (ind m^{-2}) using the same *P. ulvae* monthly-averaged individual weight estimated in Savelli et al. (2018). Therefore, the higher is the MPB biomass in the biofilm (S), the higher is the flux of MPB biomass from the biofilm to the fluff layer. This flux was also modulated by the density of *P. ulvae* individuals (Z) and their crawling rate υ (m^2 s^{-1} ind^{-1}).

The SCHISM modelling system

The SCHISM modelling system (Zhang et al., 2016) was used to obtain the 2012 10-min time series of water height (m), East-West and North-South depth-integrated velocity (m s^{-1}), significant wave height (m), mean wave period (s) and direction (°) and wave orbital velocity (m s^{-1}) used to compute the BSS and emersion-immersion periods used to constrain the physical-biological model. SCHISM fully couples several modules to simulate *e.g.* hydrodynamic circulation, short waves, sediment transport and that all share the same unstructured grid and domain decomposition. In the present application, the two-dimensional horizontal (2DH) circulation model was fully coupled with the spectral wave model Wind Wave Model II (hereafter WWM-II; Roland et al., 2012), which were implemented over the study area using an unstructured grid with a spatial resolution ranging from ~ 2 km along the open boundaries and ~ 100 m in the Bay of Marennes-Oléron. The circulation model uses the combination of an Eulerian-Lagrangian Method with a semi-implicit scheme, which relaxes the CFL condition associated with the advection of momentum and allows for stable and accurate numerical results, even using large time steps. Along its open boundary, the circulation model was forced with amplitudes and phases of the 19 main tidal constituents, linearly interpolated from the regional model of Bertin et al. (2012). Over the whole domain, the circulation model was forced by wind and sea-level pressure fields at 10 m above the sea surface originating from the CFSR reanalysis, with spatial resolutions of 0.20° and 0.5°, respectively. SCHISM was fully coupled with WWM-II using a radiation stress formalism (Longuet-Higgins and Stewart, 1964). WWM-II simulates short wave generation and propagation by solving the wave action equation (Komen et al., 1996) using a four-step fractional method. In the present application, the source terms included wave growth and dissipation by whitecapping according to Bidlot et al. (2007), non-linear wave interactions computed using the Discrete Interaction Approximation of Hasselmann et al. (1985), bottom friction using the JONSWAP approach (Hasselmann et al., 1973) and depth-induced breaking using the model of Battjes and Janssen (1978). The fields were extracted at the node corresponding to the study site.

BSS computation

The current BSS (τ_c, Pa) was calculated assuming a logarithmic velocity profile in the first layer above the sea bottom (Schlichting and Gersten, 2016):

$$\tau_c = \rho u_*^2, \quad \text{with} \quad u_* = \frac{\kappa u(z)}{\ln\left(\frac{z}{z_0}\right)}, \tag{32}$$

where u_* is the current friction velocity (m s^{-1}), ρ is the seawater density (kg m^{-3}) and κ is the Von Karman constant (0.4). z is the water height (m) and

$u(z)$ is the associated depth-integrated current velocity (m s^{-1}). We applied a Nikuradse roughness (k_s) of 0.01 m previously applied by Le Hir et al. (2000) on the Brouage mudflat. The bottom roughness z_0 was equal to $\frac{k_s}{30}$. The wave BSS (τ_w, Pa) was calculated according to the formula of Soulsby (1997):

$$\tau_w = 0.5\rho f_w U_b^2, \tag{33}$$

where U_b is the wave orbital velocity (m s^{-1}) and f_w is the wave friction coefficient. f_w was calculated according to the formula of Swart (1974):

$$f_w = 0.3, \quad \text{if} \quad r \leqslant 1.57, \tag{34}$$

$$f_w = 0.00251 exp\left(5.21 r^{-0.19}\right), \quad \text{if} \quad r > 1.57, \tag{35}$$

where r is the relative roughness related to the wave excursion A (m) and the Nikuradse roughness:

$$r = \frac{A}{k_s}, \quad \text{with} \quad A = \frac{U_b T}{2\pi}, \tag{36}$$

where T is the wave period (s). The average BSS (τ_m) and the maximum BSS (τ_{max}) were calculated according to the formulation of Soulsby (1997), which takes into account non-linear interactions between waves and currents:

$$\tau_m = \tau_c \left[1 + 1.2\left(\frac{\tau_w}{\tau_c + \tau_w}\right)^{3.2}\right], \quad \text{and} \tag{37}$$

$$\tau_{max} = \left[(\tau_m + \tau_w cos\phi)^2 + (\tau_w sin\phi)^2\right]^{\frac{1}{2}}, \tag{38}$$

where ϕ is the angle (°) between waves and currents direction.

The MPB resuspension

The model previously used in Savelli et al. (2018) was modified to take into account the explicit representation of the hydrodynamically and wave driven MPB resuspension mechanisms. We set the loss rate of MPB biomass in the sediment to 0.001 h^{-1} during high tides. The constant represents MPB senescence and the grazing by subsurface deposit feeders. We related the resuspension of MPB biomass to the simulated τ_{max}, which combined τ_w and τ_c. During high tides, three different resuspension scenarios were modulated by BSS thresholds. First, the critical BSS for fluff layer resuspension ($\tau_{crit_{fluff}}$) was set at 0.015 Pa (Orvain et al., 2004). Second, the critical BSS for massive resuspension ($\tau_{crit_{mass}}$) was set according to the critical BSS for bare sediment ($\tau_{baresed}$), consolidated by the total MPB biomass (mg Chl *a* m^{-2}; Mariotti and Fagherazzi, 2012):

$$\tau_{crit_{mass}} = \tau_{baresed} + [\omega \times (F + S)], \quad (39)$$

where ω is the consolidation coefficient of the bare sediment by the MPB biomass (Pa(mg Chl *a* m^{-2})$^{-1}$).

During immersion periods,

- if $\tau_{max} < \tau_{crit_{fluff}}$, no resuspension occurred. Immersed MPB cells achieved the downward migration from S to F and *P. ulvae* individuals were still active (grazing and bioturbating);
- if $\tau_{crit_{fluff}} < \tau_{max} < \tau_{crit_{mass}}$, *P. ulvae* individuals were not grazing and bioturbating any more and only the fluff layer was eroded at the rate:

$$\frac{dB}{dt} = -\phi B \times \left[\frac{\tau_{max}}{\tau_{crit_{mass}}} - 1\right], \quad (40)$$

  where ϕ is the erosion coefficient of the fluff layer (s^{-1}) and $\left[\frac{\tau_{max}}{\tau_{crit_{mass}}} - 1\right]$ represents the intensity of the resuspension.

- if $\tau_{max} > \tau_{crit_{mass}}$, the resuspension was considered massive and all the MPB compartments (sediment, biofilm and fluff layer) were impacted by resuspension. *P. ulvae* individuals were inactive. Both the surface biofilm and the fluff layer were fully resuspended. The Partheniades-Ariathurai law (Partheniades, 1962; Ariathurai and Krone, 1976) for mud erosion was used to determined the MPB biomass resuspension from the sediment:

$$E = E_0 \times \left[\frac{\tau_{max}}{\tau_{crit_{mass}}} - 1\right]^n, \quad (41)$$

  where E and E_0 are the sediment erosion rate (kg m^{-2} s^{-1}) and the erosion constant (kg m^{-2} s^{-1}), respectively. n is a power function of the sediment composition (for mud, $n = 1$). The MPB biomass in the sediment (mg Chl *a* m^{-2}) was converted into Chl *a* concentration per mass of sediment (F^*, mg Chl *a* kg^{-1} dry sediment) using a constant bulk density of sediment (520 g l^{-1}). The resulting MPB erosion rate (E_{MPB}, mg Chl *a* m^{-2} s^{-1}) is as follows:

$$E_{MPB} = E_0 \times F^* \times \left[\frac{\tau_{max}}{\tau_{crit_{mass}}} - 1\right]^n, \quad (42)$$

  The occurrence of the massive resuspension events also depended on the MPB biomass remaining in the sediment first centimetre. In case of a massive resuspension event, a background of MPB biomass (F_{mini}, mg Chl *a* m^{-2}) was always kept in the sediment to allow the biomass recovery after the event. If $F > F_{mini}$, E_{MPB} and all the surface biofilm and fluff layer were eroded. Otherwise, only the fluff layer was integrally resuspended.

BOX 4.3.1

Conceptual scheme of the MPB resuspension

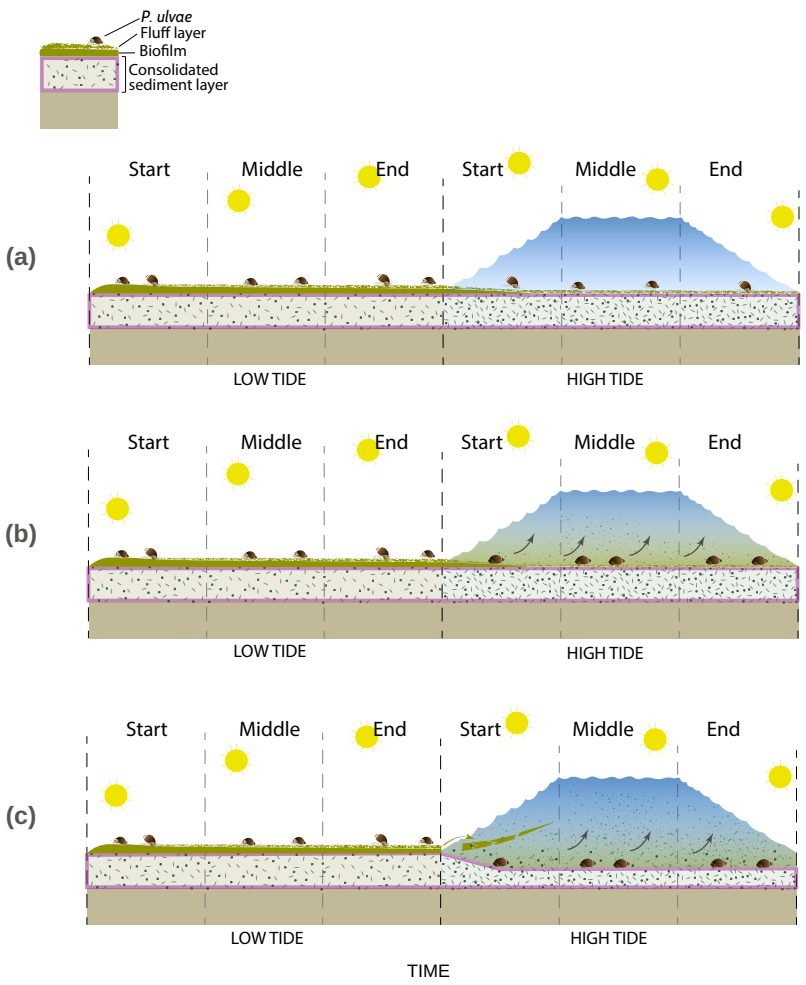

Figure 24: Conceptual scheme of the MPB resuspension. **(a)** $\tau_{max} < \tau_{crit_{fluff}}$, no resuspension occurs. Immersed MPB cells achieve the downward migration from S to F and *P. ulvae* individuals are still active (grazing and bioturbating). **(b)** $\tau_{crit_{fluff}} < \tau_{max} < \tau_{crit_{mass}}$, *P. ulvae* individuals are not grazing and bioturbating any more and only the fluff layer is eroded. **(c)** $\tau_{max} > \tau_{crit_{mass}}$, the resuspension is considered massive and all the MPB compartments (sediment, biofilm and fluff layer) are impacted by resuspension. *P. ulvae* individuals are inactive. Both the surface biofilm and the fluff layer are fully resuspended. The MPB biomass in the sediment is resuspended according to the Partheniades-Ariathurai law (Partheniades, 1962; Ariathurai and Krone, 1976) for mud erosion.

The physical and biological constants used in this study are given in Table 11. The differential equations of the biological model without wave- and tidal-induced MPB resuspension are fully detailed in Savelli et al. (2018). The physical-biological coupled model was run at the study site from 1 September 2011 to 31 December 2011 for the spin-up, and from 1 January 2012 to 31 December 2012 for the analysis. F and Z were initially set to 100 mg Chl *a* m^{-2} and 500 mg C m^{-2}, respectively. The differential equations were solved with the fourth-order Runge-Kutta method with a 6-min time step. The model run with the explicit representation of wave- and tidal-induced MPB resuspension (PHY_{run}) was compared to a reference run (REF_{run}) with a constant rate of MPB resuspension during high tides without any parametrisation of biologically-consolidated sediment. The setup of the REF_{run} is detailed in Savelli et al. (2018).

Finally, we tested the sensitivity of the simulated MPB PP and instantaneous resuspension to simultaneous variations of key biological and physical constants. Random values of the bed roughness length (z_0), critical BSS for resuspension of bare sediment ($\tau_{baresed}$), consolidation factor (ω), erosion constant of pure mud (E_0), minimum MPB biomass in the sediment (F_{mini}) and mean time spent by a MPB cell at the sediment surface (γ) were selected within the observed ranges (Table 12) by a Monte Carlo fixed sampling method (Hammersley and Handscomb, 1964). The method aims to quantify how simultaneous variations of key biological and physical constants might impact the simulated MPB production and instantaneous resuspension (see Chapter 3). A total of 10,000 model runs was performed using the same set of initial conditions.

RESULTS

Physical conditions

In situ water height and current velocity derived from ADCP measurements in April 2012 were used to compute the 10-min mean significant wave height and mean wave period that were compared to the model data (Fig. 25). The model simulated well the high-frequency (10 min) variations of the water height (RMSD = 0.14 m, NRMSD = 9%) and current velocity components. The RMSD was 0.087 m s^{-1} for the East-West component and 0.06 m s^{-1} for the North-South component (Fig. 25). With respect to the wave height and mean wave period, the RMSD was 0.057 m and 0.337 s, respectively (Fig. 25). It corresponded to NRMSD of 19 % and 10 %, respectively.

The water height and depth-integrated velocity simulated by the model in 2012 varied fortnightly with the tidal cycle (Fig. 26). During neap tides, the simulated water height and current velocity reached 1.42 m and 0.41 m s^{-1}, respectively. During spring tides, they were higher and reached 3.24 m and 0.83 m s^{-1}, respectively.

Table 11: Physical and biological model parameters related to the MPB resuspension

Symbol	Description	Value	Unit	Source
Physics				
$\tau_{baresed}$	Critical BSS for bare sediment	0.3	Pa	Present study
$\tau_{crit_{fluff}}$	Critical BSS for fluff layer erosion	0.015	Pa	Orvain et al. (2004)
k_s	Nikuradse roughness	0.01	m	Le Hir et al. (2000)
E_0	Mud erosion constant	2×10^{-5}	kg m^{-2} s^{-1}	Present study
ω	Consolidation factor by MPB biomass	0.006	Pa (mg Chl *a* m^{-2})$^{-1}$	Present study
Biology				
γ	Mean time spent by a MPB cell at the surface	1	h	Blanchard et al. (2004)
F_{mini}	Background MPB biomass	73	mg Chl *a* m^{-2}	Present study
υ	*P. ulvae* crawling rate	1.2×10^{-9}	m^2 s^{-1} ind^{-1}	Present study
B_{max}	Saturation of Chl *a* concentration in the fluff layer	11.5	mg Chl *a* m^{-2}	Orvain et al. (2007)

Table 12: Range of values for the random selection of the model constants used in the Monte Carlo sensitivity analysis.

Parameters	Units	Range	Source
z_0	m	$[2 \times 10^{-4}; 1.65 \times 10^{-2}]$	Ke et al. (1994)
			Le Hir et al. (2000)
			Verney et al. (2006)
E_0	kg m^{-2} s^{-1}	$[1 \times 10^{-5}; 1 \times 10^{-3}]$	Mengual et al. (2017) and references within
$\tau_{baresed}$	Pa	[0.05; 1]	Mariotti and Fagherazzi (2012) and references within
ω	Pa (mg Chl *a* $m^{-2})^{-1}$	[0.001; 0.02]	Mariotti and Fagherazzi (2012) and references within
F_{mini}	mg Chl *a* m^{-2}	[35; 100]	Guarini et al. (2000)
			Blanchard et al. (2002)
			Herlory et al. (2004)
			Blanchard et al. (2006)
			Orvain et al. (2014a)
γ	h	[0.25; 1.5]	Blanchard et al. (2004)

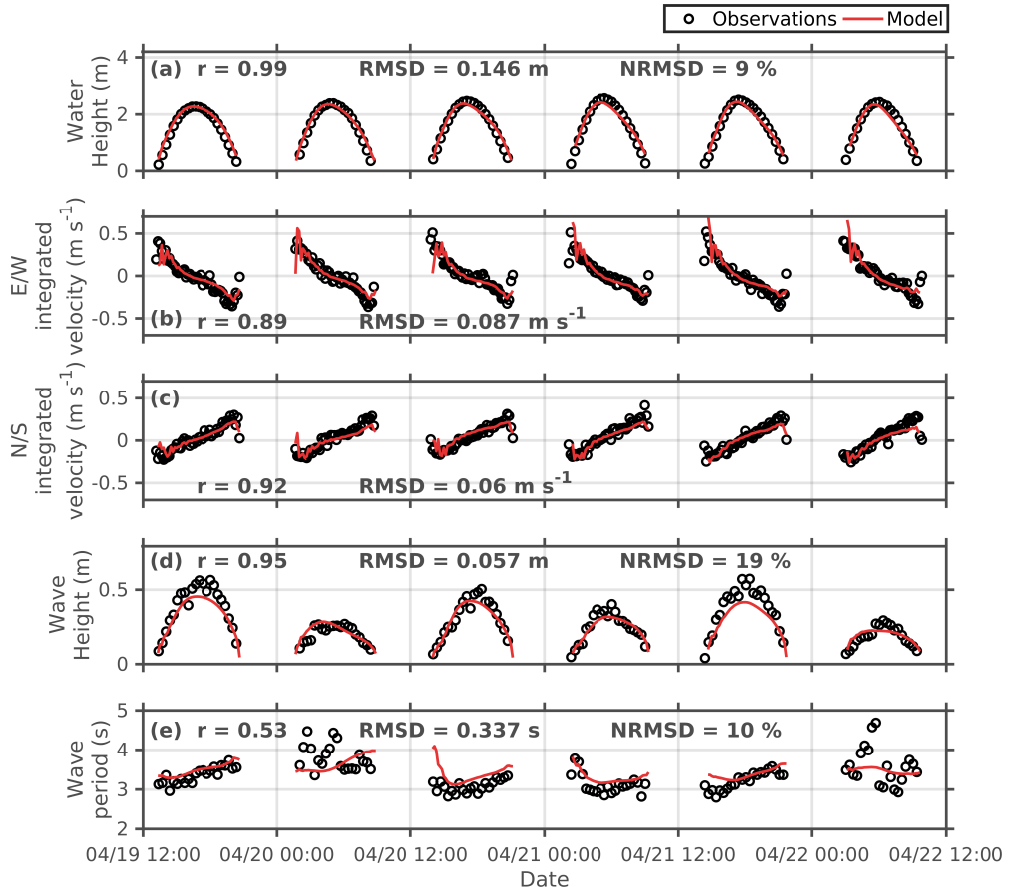

Figure 25: Measured and simulated **(a)** water height, **(b)** East-West current velocity component, **(c)** North-South current velocity component, **(d)** significant wave height, and **(e)** wave period of the 2nd moment at the study site between 19 April 2012 and 22 April 2012. r is the Pearson's correlation coefficient. RMSD and NRMSD are the root mean square deviation and the normalised root mean square deviation.

The simulated wave period ranged from 3 to 15.5 s (Fig. 26). The simulated wave height and orbital velocity varied by several orders of magnitude, ranging between 2×10^{-3} m and 0.61 m and between 5×10^{-3} m s^{-1} and 0.62 m s^{-1}, respectively (Fig. 26). The median wave orbital velocity was 0.14 m s^{-1}. High values of wave orbital velocity (*i.e.* higher than the median) were more frequently reached during winter and fall compared to spring and summer (Fig. 27).

During winter, the simulated MST was 6.2 $\pm$ 4.3 °C in average (Fig. 28). The simulated mean MST was more than twice in summer reaching 20.4 $\pm$ 2.8 °C (Fig. 28). It was comparable in spring and fall with 14.2 $\pm$ 3.5 °C and 12.4 $\pm$ 3.8 °C, respectively (Fig. 28).

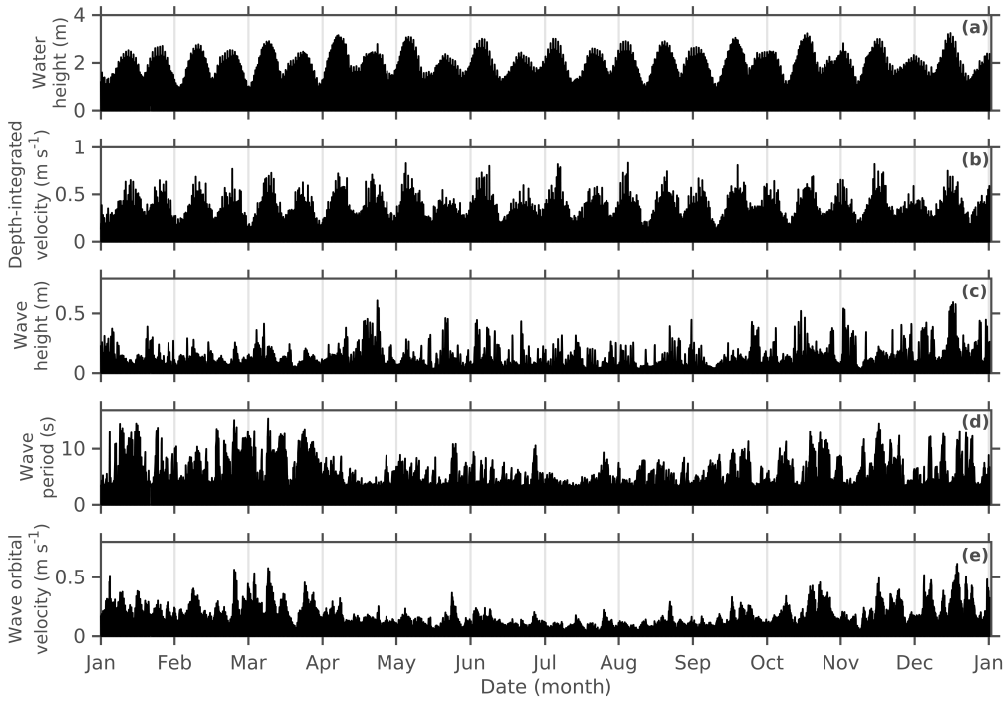

Figure 26: Time series of the 2012 simulated **(a)** water height, **(b)** depth-integrated current velocity, **(c)** significant wave height, **(d)** wave period of the 2nd moment, and **(e)** wave orbital velocity

MPB and P. ulvae dynamics

The total simulated MPB biomass (MPB biomass in the biofilm and the MPB biomass in the sediment) reached a seasonal maximum on May 1 (252 mg Chl *a* m^{-2} ; Fig. 29a). This peak is preceded by three peaks of simulated MPB biomass around 150 mg Chl *a* m^{-2} on January 30, February 29 and March 23 (Fig. 29a). In summer, the simulated MPB biomass decreased below 100 mg Chl *a* m^{-2}. In fall, one peak of MPB biomass of moderate intensity (137 mg Chl *a* m^{-2}) occurred on November 14 (Fig. 29a). The peaks of MPB biomass simulated in March and April were tightly followed by two seasonal peaks of simulated *P. ulvae* density (~ 20,100 and 37,000 ind m^{-2}, respectively; Fig. 29b) during which the simulated MST (19.5 °C and 17.6 °C) was close to the optimal temperature for *P. ulvae* grazing (20 °C). In fall, the simulated *P. ulvae* density was low (~ 3,500 ind m^{-2} ; Fig. 29b).

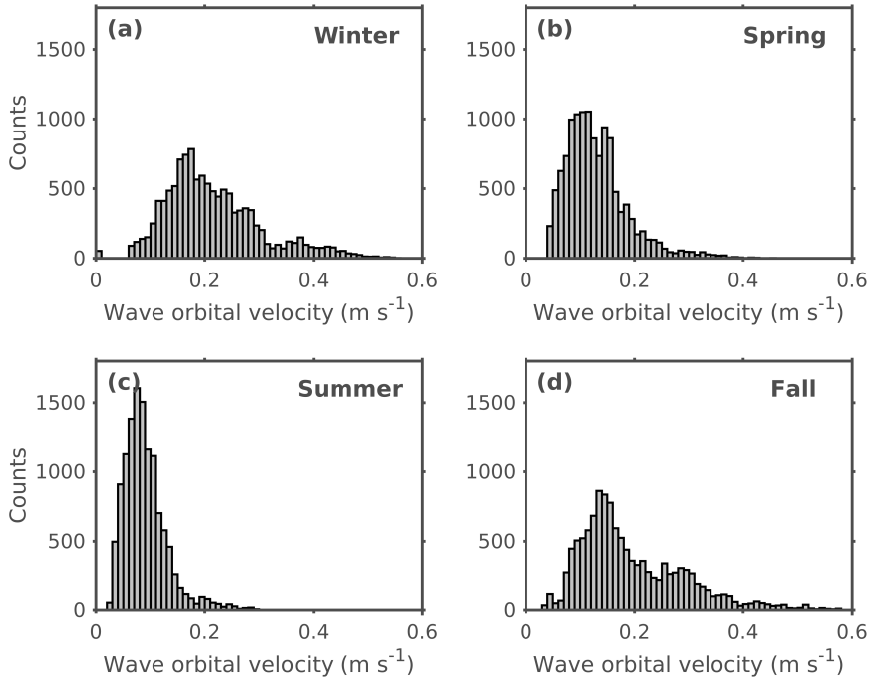

Figure 27: Histograms of the 2012 simulated wave orbital velocity in **(a)** winter, **(b)** spring, **(c)** summer, and **(d)** fall.

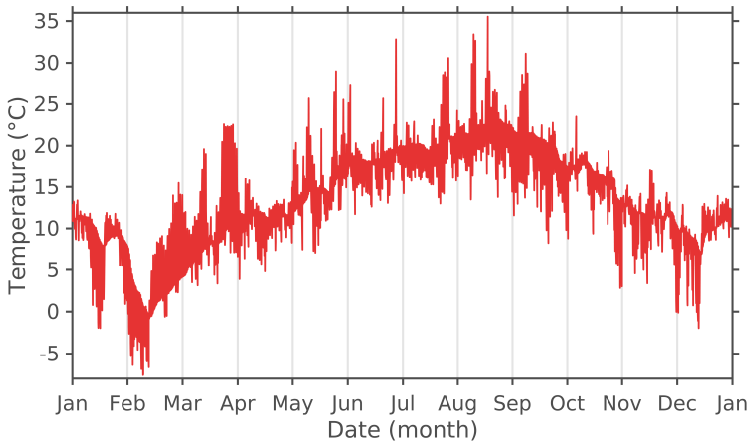

Figure 28: Simulated mud surface temperature (°C) in 2012.

MPB biomass resuspension

Model validation

The modelled resuspended MPB Chl *a* was normalised by the water height and compared to the time-coincident in-water Chl *a* concentration provided by remote sensing and *in situ* water samples from two monitoring stations (Figs.

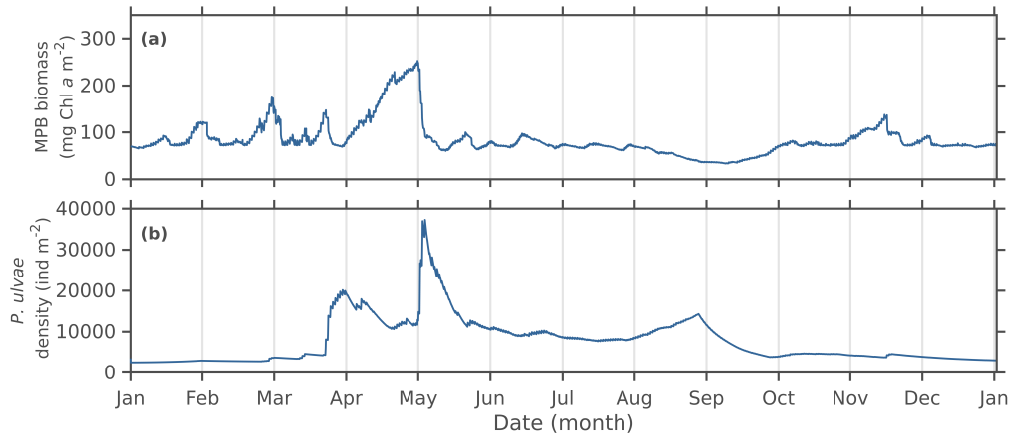

Figure 29: Time series of the 2012 simulated **(a)** total MPB biomass (mg Chl *a* m^{-2}), and **(b)** *P. ulvae* density (ind m^{-2}).

22 and 30). Both *in situ* and satellite observations favourably compared with the simulated resuspended Chl *a*. Whatever the source of data (model output, *in situ* sampling or remote sensing), the in-water Chl *a* concentration exhibited a consistent seasonal variability with higher value in winter-spring than in summer-fall. The simulated maximum peaks of resuspended MPB (from 5 - 45 mg Chl *a* m^{-3}) generally compared to satellite estimates (1.4 - 35.4 mg Chl *a* m^{-3}). In particular, the height of peaks occurring from late February - early March was consistent with satellite observations (30 ± 18 mg Chl *a* m^{-3}, February 28; Fig. 30). In fall and winter, the lower concentration of resuspended MPB (2.44 ± 7 mg Chl *a* m^{-3}) was in agreement with *in situ* measurements (2.1 ± 1 mg Chl *a* m^{-3}; Fig. 30). All together, the reasonable agreement between simulation outputs, satellite estimates, and *in situ* observations is very encouraging. In order to better understand the temporal dynamics of MPB resuspension, we now analyse in more details the time-series of MPB resuspension using high frequency simulations.

Temporal variability

MPB resuspension was highly variable in terms of seasonal occurrence and quantity and did not systematically occur during each tidal cycle (Fig. 31). The instantaneous resuspended biomass was in average 0.04 ± 0.45 mg Chl *a* m^{-2}. The instantaneously resuspended MPB water column-normalised concentration peaked to 110 mg Chl *a* m^{-3} on February 1. Over a high tide, the rate of MPB erosion averaged 0.4 ± 0.85 mg Chl *a* m^{-2} h^{-1} with a maximum of 8.93 mg Chl *a* m^{-2} h^{-1} on November 12.

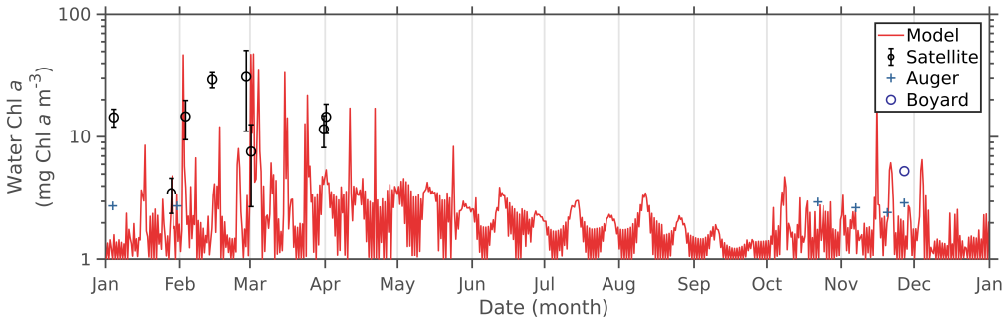

Figure 30: Time series of the 2012 simulated and observed remotely-sensed and measured *in situ* in-water Chl *a* concentration (mg Chl *a* m^{-3}). The simulated resuspended MPB biomass was cumulated over each high tide and normalised over the corresponding maximal water depth.

Massive resuspension

Interestingly, the seasonal variation of the MPB resuspension was mainly driven by massive resuspension events. Massive resuspension represented 70 % of the MPB biomass resuspended annually, which was exported to the water column in 37 days only (Tables 13 and 14). Massive resuspension mostly occurred during winter and fall, as evidenced by a mean contribution of 80 % to total resuspended MPB biomass (Fig. 31b). The contribution of such events relative to total resuspension was the highest during winter (613 mg Chl *a* m^{-2}, Table 13). In winter, 18 days (457 events) of massive resuspension were responsible of the export to the water column of 32 % of the total annually resuspended MPB biomass (Table 13). The same trend was also observed during spring, when 5.8 days (363 events) of massive resuspension contributed to 20 % of the total annually resuspended MPB biomass (Table 13). On the contrary, massive resuspension was rare during summer (only 192 events), and did not substantially contribute to the total annual export of MPB to the water column (Table 13). In the model, spring tides were isolated by considering tides with a maximal water depth > 1.8 m. Beside the above-mentioned seasonal pattern, it is noteworthy to report that 60 % of the annual MPB export from the sediment to the water column occurred during spring tides.

Chronic resuspension

In contrast, the MPB biomass resuspended in the model through bioturbation contributed to only 30 % of the total annual water column export (Table 13). Resuspension through bioturbation mainly occurred from late March to September (Fig. 31b and Table 13), when *P. ulvae* individuals were active and abundant in the model (Fig. 29b). Fluff layer mediated export of MPB corresponded to 46 days of resuspension and 392 events (Table 13). In spring, fluff layer MPB resuspension (337 mg Chl *a* m^{-2}) compared to that of massive resuspension

(381 mg Chl a m-2) but was 3-fold more frequent. In summer, the fluff layer resuspension (157 mg Chl *a* m^{-2}) was higher than massive resuspension (78 mg Chl *a* m^{-2}), which was only episodic (< 2 days). Annually, the number of fluff layer resuspension events (392 events) were lower than the massive resuspension events (1504 events; Table 13). However, the fluff layer resuspension events were longer (46.2 days) than the synoptic and shorter massive resuspension events (37 days; Table 13).

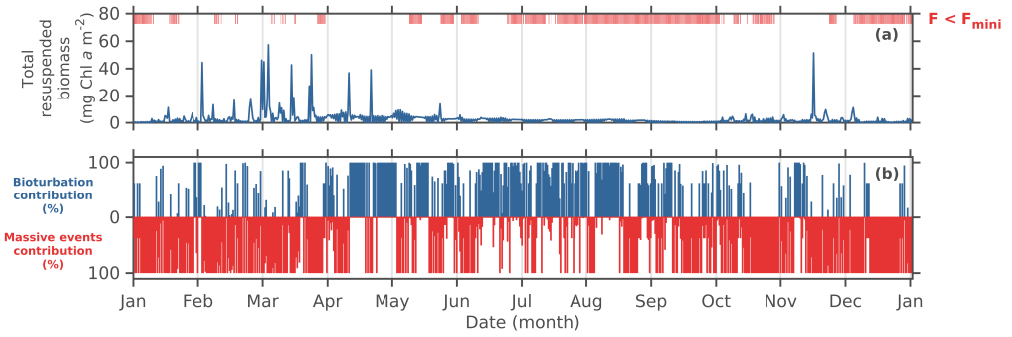

Figure 31: Time series of the 2012 simulated **(a)** total resuspended MPB biomass (mg Chl *a* m^{-2}), **(b)** relative contribution (%) of resuspended MPB biomass through bioturbation (blue) and massive events (red). The simulated resuspended MPB biomass was cumulated over each high tide.

Resuspended MPB biomass and MPB PP

In order to assess the impact of wave- and tidal-induced resuspension on MPB dynamics, we compared the time-integrated total resuspended MPB biomass and MPB PP simulated in 2012 (PHY_{run}) with the reference run where the rate of MPB resuspension is constant during high tides (REF_{run}). The total resuspended MPB biomass was twice in the PHY_{run} (60.8 g C m^{-2}) than in the REF_{run} (30.2 g C m^{-2}; Table 14). The seasonal variability also differs between the two series of simulations. In the PHY_{run}, the resuspended MPB biomass was the highest in spring (27.9 g C m^{-2}) and the lowest in fall (7.38 g C m^{-2}; Table 14). On the contrary, in the REF_{run}, the resuspended MPB biomass was the highest in winter (10.3 g C m^{-2}) and the lowest in summer (5.6 g C m^{-2}; Table 14), and the amplitude of the seasonal difference was twice lower than in the PHY_{run}. In the REF_{run}, the frequency (53 - 56 %) and duration (48.6 - 51.4 d) of MPB resuspension events were similar throughout all the seasons (Table 14). By contrast, in the PHY_{run}, summer and fall were characterised by the lowest seasonal MPB resuspension frequency (20 % and 16.6 %, respectively) and duration (18.8 d and 15.1 d, respectively; Table 14), whereas the frequency and duration of resuspension events were both higher during spring (respectively 29 % and 26.6 d).

Table 13: Simulated total resuspended MPB biomass ($\sum_{RES}$) in 2012 through bioturbation and massive events, and frequency ($Freq_{RES}$), duration (Dur_{RES}), and number (N) of the simulated events.

	Massive resuspension				Fluff layer resuspension			
	$\sum_{RES}$ (mg Chl *a* m^{-2})	$Freq_{RES}$ (%)	Dur_{RES} (d)	N	$\sum_{RES}$ (mg Chl *a* m^{-2})	$Freq_{RES}$ (%)	Dur_{RES} (d)	N
Winter	613.1	20	18	457	34.4	5	4.6	73
Spring	381.3	6.3	5.8	363	337.7	22.6	20.8	120
Summer	78.4	1.7	1.54	192	157.6	19	17.3	129
Fall	283.7	12.7	11.6	492	41.7	4	3.5	70
Annual	1355.5	10	37	1504	571.3	12.6	46.2	392

With respect to MPB PP, the annual rate was close both in the PHY_{run} (140.5 g C m^{-2}) and the REF_{run} (151.5 g C m^{-2}; Table 14). In both runs, PP was the highest in spring (47.2 g C m^{-2} in the REF_{run} and 67.6 g C m^{-2} in the PHY_{run}). PP simulated in spring departed more from the other seasons in the PHY_{run} than in the REF_{run}. In the PHY_{run}, the spring PP was 2.3-fold to 3.6-fold higher than in other seasons (Table 14). At the annual scale, 43.3 % (PHY_{run}) and 19.9 % (REF_{run}) of the PP was resuspended (Table 14). At the seasonal scale, PP was resuspended the most in winter and the least in summer in both runs (Table 14). In winter, PP was relatively low while the resuspended biomass was high. In the PHY_{run}, high resuspended MPB biomass resulted from more frequent intense hydrodynamical disturbances combined with moderate MPB biomass in winter (Fig. 31a). Such a pattern led to a moderate consolidation of the sediment (0.82 ± 0.13 Pa; Fig. 32). In contrast, in summer, PP was slightly lower than in winter but the level of resuspended biomass was much lower due to less frequent intense hydrodynamic disturbances and lower MPB biomass in the sediment than in winter. This pattern was simulated although the sediment was relatively unconsolidated (0.64 ± 0.08 Pa; Fig. 32).

Table 14: Simulated total resuspended MPB biomass ($\sum_{RES}$), frequency ($Freq_{RES}$) and duration (Dur_{RES}) of the resuspension events, and MPB PP in the REF_{run} and the PHY_{run} in 2012.

	$\sum_{RES}$ (g C m^{-2})	$Freq_{RES}$ (%)	Dur_{RES} (d)	PP (g C m^{-2})	$\sum_{RES}$:PP (%)
REF_{run}					
Winter	10.3	53	48.6	34	30.3
Spring	8.1	56	51.4	47.2	17.2
Summer	5.6	55	50.6	41	13.7
Fall	6.2	56	51	29.3	21.7
Annual	30.2	55	201.6	151.5	19.9
PHY_{run}					
Winter	15.9	25	22.6	28.4	56
Spring	27.9	29	26.6	67.6	41.3
Summer	9.61	20	18.8	26	37
Fall	7.38	16.6	15.1	18.6	39.7
Annual	60.8	22	83.2	140.5	43.3

Drivers of MPB resuspension

Waves and currents bed shear stress

The critical BSS for massive resuspension ($\tau_{crit_{mass}}$) was compared to the wave BSS (τ_w) and, current BSS (τ_c) and to the maximal BSS (τ_{max}) which combined both current and wave BSS. As MPB had a consolidating effect on the sediment, $\tau_{crit_{mass}}$ was set to co-vary with MPB biomass in the model. As a result, $\tau_{crit_{mass}}$ displayed a seasonal variation similar to that of MPB biomass (Fig. 29 and 32): winter-spring maximum (with 4 peaks from 1 to 1.8 Pa) and summer minimum (0.64 $\pm$ 0.08 Pa). Overall, τ_{max} exceeded $\tau_{crit_{mass}}$ at a similar frequency than τ_w.

In contrast to the massive resuspension BSS, τ_w was more variable and exhibited more peaks in winter (1.15 $\pm$ 0.6 Pa) and fall (1.1 $\pm$ 0.75 Pa) than in spring (0.65 $\pm$ 0.34 Pa) and summer (0.43 $\pm$ 0.25 Pa; Fig. 32a). During the studied year, τ_w exceeded $\tau_{crit_{mass}}$ during 84 days. The dominance of τ_w was higher in winter (36 %) and fall (34 %) than during summer (10 %; Table 4). The current BSS was generally lower (annual average of 0.1 $\pm$ 0.13 Pa) than τ_w (annual average of 0.8 $\pm$ 0.6 Pa), and displayed values similar to that of $\tau_{crit_{mass}}$ during each season (Table 15). As τ_c was driven by tidal dynamics, it reached a maximum and was as high as $\tau_{crit_{mass}}$ during spring tides (Fig. 32b).

Resuspension intensity

In order to relate MPB dynamics with BSS, the highest MPB resuspension events (corresponding to the last percentile of the resuspended MPB biomass simulated time series, *i.e.* higher than 40.6 mg Chl *a* m^{-2}) were highlighted in Fig. 32c by dark circles. All the seven highest resuspension events occurred during November or February-March. Three of them were responsible for the export to the water column of $\sim$ 150 mg Chl *a* m^{-2} in early-March (Fig. 32c). They were followed by a drop in $\tau_{crit_{mass}}$, which was due to a decrease in MPB biomass within the sediment. Though the decrease in MPB biomass contributes to lessen the sediment consolidation (Fig. 29), strong resuspension events did not occur during summer (Fig. 32c). The lowest maximal value reached by τ_{max} during high tides of 2012 was 0.29 Pa (Fig. 32b). $\tau_{crit_{fluff}}$ (0.015 Pa) was therefore exceeded at each high tide. The simulated fluff layer was therefore always eroded at least one time during immersion periods.

Over a tidal cycle, most of the simulated resuspension events occurred at the flood beginning (14 %) and at the end of ebb (10 %; Fig. 33). These moments correspond to low water height when τ_w was maximised until around 1 - 1.25 m of seawater depth (Fig. 34). Most of the simulated total resuspended MPB biomass (76 %) was exported at the flood beginning (Fig. 33).

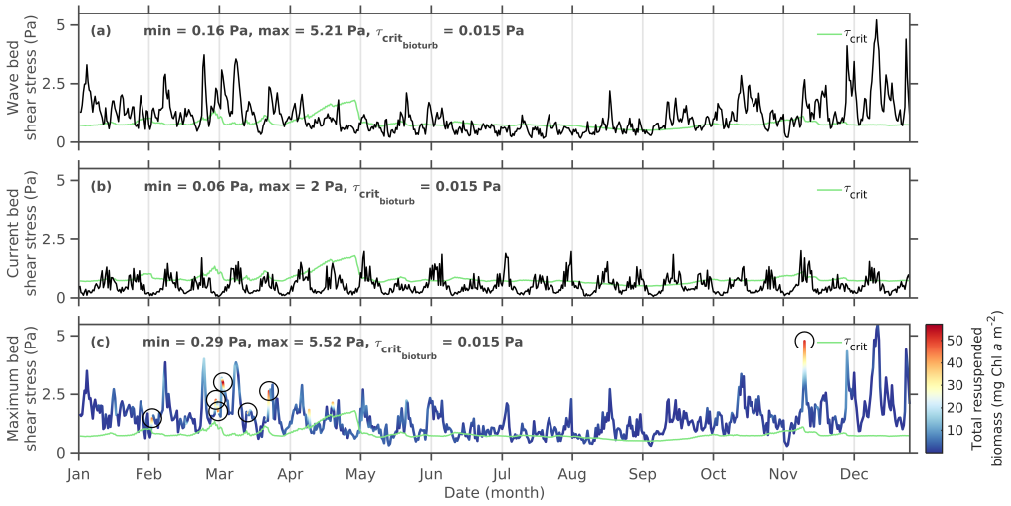

Figure 32: Time series of the 2012 simulated **(a)** wave BSS, **(b)** current BSS, and **(c)** maximum BSS along with the total resuspended MPB biomass. The green line represents the critical BSS for massive resuspension events. Dark circles indicate resuspended biomass higher than the last percentile of the resuspended MPB biomass simulated in 2012 (40.6 mg Chl *a* m^{-2}). Note that only maximum values of BSS per tidal cycle are shown.

Table 15: Simulated frequency of waves BSS, tidal current BSS and combined waves and current maximal BSS higher than the critical BSS in 2012.

	Waves (%)	Current (%)	Combined waves and current (%)
Winter	36	0.22	36.2
Spring	13	0.18	13.4
Summer	10	0.5	11.5
Fall	34	0.28	34.6
Annual	23	0.30	23.7

MPB PP and resuspension, P. ulvae ingestion

In order to relate the resuspended MPB biomass with the MPB growth conditions, the simulated daily MPB resuspension was compared to the simulated daily MPB PP and to the simulated daily *P. ulvae* ingestion (Fig. 35b). PP increased during winter-spring and reached a maximum in late-March (~ 1.6 g C m^{-2} d^{-1}; Fig. 35). It resulted into an increase of MPB biomass in the sediment (Fig. 35a). The simulated decreases of the MPB biomass in early-March, late-March and early-May were driven by strong resuspension and/or by *P. ulvae* ingestion events (Fig. 35). Seven peaks of daily resuspension (1 - 2.2 g C m^{-2} d^{-1}) occurred in winter, spring and fall (Fig. 35b). By comparison, the daily *P. ulvae* ingestion exhibited two peaks, one of them reaching a maximum of 4.1

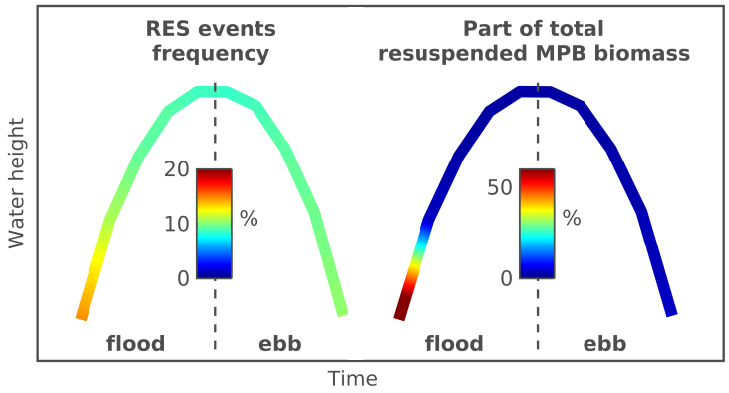

Figure 33: Frequency of the resuspension events simulated in 2012 and the relative distribution of the total resuspended MPB biomass over a high tide.

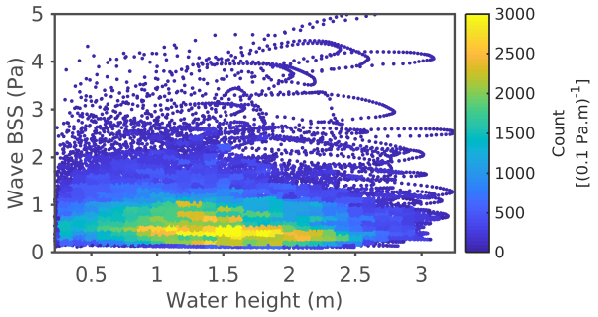

Figure 34: Relationship between the simulated wave BSS and the water depth.

g C m^{-2} d^{-1} in early-May (Fig. 35b). The yearly-integrated resuspension of MPB (60.8 g C m^{-2} yr^{-1}) was 1.3-fold higher than the yearly-integrated *P. ulvae* ingestion (41.1 g C m^{-2} yr^{-1}). The loss of MPB biomass by resuspension was therefore higher than the loss by grazing by *P. ulvae*.

Sensitivity analysis

A total of 10,000 simulations were run using random sets of biological (F_{mini}, γ) and physical (ω, $\tau_{baresed}$, E_0, z_0) constants varying within the reported observed ranges (Table 12). This approach was used in Savelli et al. (2018). The constants were chosen as they shape the simulated MPB production and the occurrence and rate of MPB resuspension. Figures 36 and 37 show the 10,000 parameters combinations and the resulting simulated MPB annual PP and maximal instantaneous resuspension.

Except for γ, a high annual MPB PP was simulated in all regions of the tested ranges of F_{mini}, ω, $\tau_{baresed}$, E_0 and z_0 (Fig. 36). The annual PP was the most sensitive to γ (Fig. 36). This constant set the duration of the time spent by the

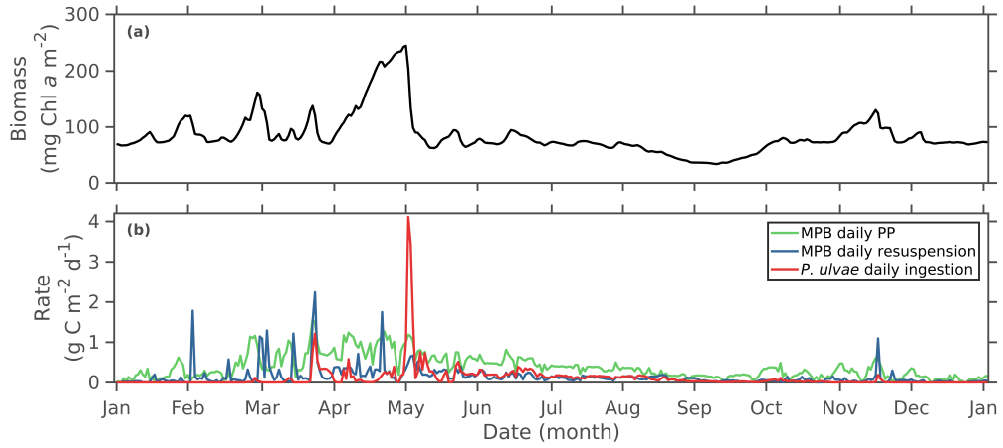

Figure 35: Time series of the 2012 simulated **(a)** MPB biomass in the first centimetre of sediment (mg Chl *a* m^{-2}), **(b)** daily PP rate (g C m^{-2} d^{-1}), daily resuspension of MPB biomass (g C m^{-2} d^{-1}), and daily ingestion of *P. ulvae* (g C m^{-2} d^{-1}).

MPB biofilm at the sediment surface for the next low tide. The higher was γ, the higher was the annual PP. Below 25 min spent at the sediment surface, the annual PP reached critical values (PP $<$ 50 g C m^{-2} yr^{-1}; Fig. 36).

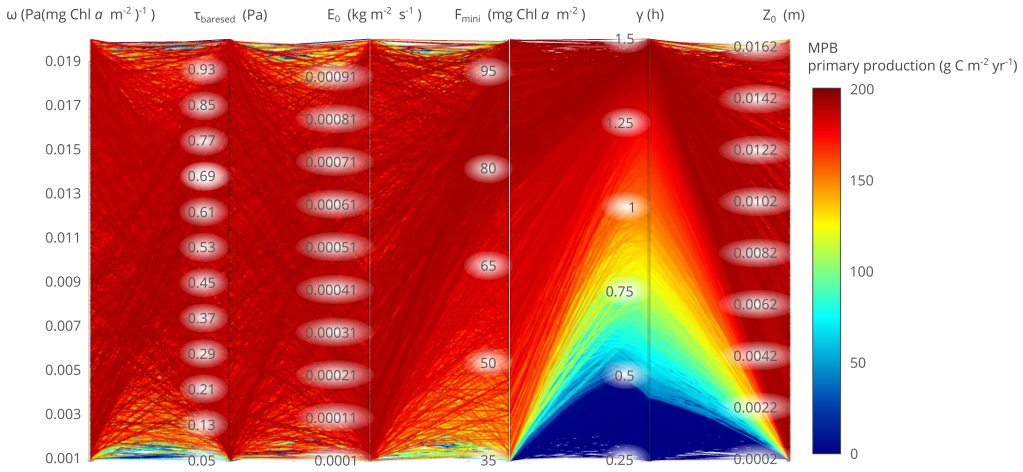

Figure 36: Parallel coordinates of the simulated MPB primary production (g C m^{-2} yr^{-1}) according to the consolidation factor of sediment by the MPB biomass (ω), the critical BSS for the resuspension of bare sediment ($\tau_{baresed}$), the erosion constant (E_0), the background MPB biomass (F_{mini}), the average time spent by MPB cells at the surface (γ), and the bed roughness (z_0) for 10,000 combinations run in the Monte Carlo sensitivity analysis.

The instantaneous rate of MPB biomass resuspension was also sensitive to γ when it took values lower than 25 min (Fig. 37). A low PP resulting from a low γ value led to the decline of the MPB biomass in the sediment and resuspended

MPB biomass. When γ was higher than 25 min, the MPB resuspension was sensitive to ω, E_0 and $\tau_{baresed}$ (Fig. 37).

An increase of ω and E_0 combined with a decrease of $\tau_{baresed}$ resulted into a higher maximal instantaneous resuspension of MPB (Fig. 37). The strongest resuspension events ($>$ 200 mg Chl *a* m^{-3}) occurred for ω, E_0 and $\tau_{baresed}$ values ranging between 0.001 and 0.005 Pa(mg Chl *a* m^{-2}), 5.5×10^{-4} to 1×10^{-3} kg m^{-2} s^{-1} and 0.4 and 1 Pa, respectively (Fig. 37).

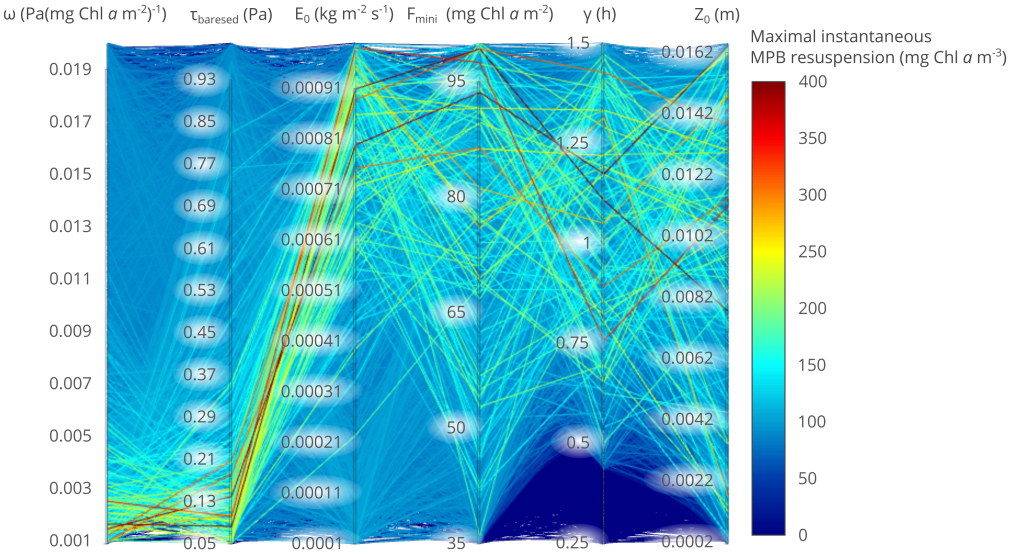

Figure 37: Parallel coordinates of the maximal simulated instantaneous resuspension of MPB biomass (mg Chl *a* m^{-3}) according to the consolidation factor of sediment by the MPB biomass (ω), the critical BSS for the resuspension of bare sediment ($\tau_{baresed}$), the erosion constant (E_0), the background MPB biomass (F_{mini}), the average time spent by MPB cells at the surface (γ), and the bed roughness (z_0) for 10,000 combinations run in the Monte Carlo sensitivity analysis.

Overall, the simulated annual MPB PP was mainly sensitive to γ. When PP was relatively high ($\gamma > 25$ min), the MPB resuspension was mostly sensitive to the sediment erodibility constants ω, E_0 and $\tau_{baresed}$, as they constrained the occurrence and rate of MPB resuspension.

DISCUSSION

The seasonal cycle of MPB resuspension

The dynamics of the simulated MPB resuspension relies on the seasonal cycle of MPB biomass in the sediment. Here, we used the model of Savelli et al. (2018), which reasonably simulates the MPB dynamics in the sediment for the year 2008. The simulated seasonal cycle of MPB biomass is characterised by a

spring bloom, a summer depression and a moderate fall bloom. According to Savelli et al. (2018), the spring bloom of MPB biomass was driven by a high PP triggered by MST close to the MPB temperature optimum for photosynthesis and an increasing solar irradiance from late winter to the end of spring. In summer, the combined effect of a low thermoinhibited MPB PP and a moderate but sustained grazing pressure was responsible for a low MPB PP and biomass (Savelli et al., 2018). In fall, the absence of grazing and a lower simulated MST than in summer led to a moderate bloom of biomass that declined rapidly due to decreasing light levels (Savelli et al., 2018). The total MPB biomass simulated within the first centimetre of sediment exhibited a seasonal pattern consistent with that previously observed in other northern European mudflats (*i.e.* van der Wal et al., 2010; Echappé et al., 2018). The simulated synoptic events of MPB resuspension superimposed on the MPB intrinsec seasonal cycle of MPB biomass and PP.

The model suggests a high seasonal MPB resuspension during winter and spring. In their study on the South Korean Nanaura mudflat, Koh et al. (2007) sampled the MPB Chl *a* concentration in the sediment and the suspended particulate matter to derive resuspended benthic Chl *a* concentration in seawater from July 2002 to February 2003. The measured Chl *a* concentration in the sediment and the resuspended benthic Chl *a* were higher during winter than in summer and fall in line with our results. On the same study site, Koh et al. (2006) estimated the highest concentrations of resuspended Chl *a* during spring tides, which is consistent with the high MPB export from the sediment to the water column simulated during spring tides (60 % of the annual export). The simulated resuspended MPB biomass is also higher during flood than ebb. 76 % of the annual export of MPB biomass from the sediment to the water column occurs during flood in the model. In the Bay of Bourgneuf (NW France), Gernez et al. (2017) also retrieved higher benthic Chl *a* resuspension in flood than in ebb using the remote sensing algorithm used in our study.

We compared the resuspended Chl *a* concentrations simulated for year 2012 with 2012 seawater Chl *a* concentrations remotely-sensed above the mudflat and measured *in situ* at water quality monitoring stations in the vicinity of the Brouage mudflat. The simulated seasonal cycle of the resuspended MPB biomass is consistent with the winter, spring and fall observations. The model suggests a higher contribution of benthic micro-algae in winter-spring than in summer. Guarini et al. (2004) and Hernández Fariñas et al. (2017) analysed the phytoplankton community in seawater sampled at water quality monitoring stations in the Bay of Marennes-Oléron and the Bay of Bourgneuf (160-km north of the Brouage mudflat), respectively. Both studies suggest a similar seasonal pattern with a higher contribution of benthic microalgae in seawater in winter-spring than in summer. Nevertheless, we remain cautious on the reasonable agreement between the model and *in situ* data as the number of *in situ* samples we used was defined by a threshold we set for benthic cells resuspen-

sion representativeness. Below 50 % of benthic cells in the sample, the sample was discarded in the analysis. Such a threshold implies that, in summer, all the samples are discarded so no model-data comparison is possible. In addition, ~ 15 km separate the study site from the monitoring stations. Such a distance may involve some model-data discrepancies caused by grazing, MPB deposition and resuspension occurring between sites.

The horizontal transport of the MPB cells within the water column may impact the biomass of resuspended MPB. Guarini et al. (2004) and Guarini et al. (2008a) report an horizontal transport of resuspended MPB cells in the Bay of Marennes-Oléron and over the Brouage mudflat. In our modelling approach, there is no horizontal transport in seawater or deposition on the sea floor of the resuspended MPB biomass. Such a parametrisation implies that once resuspended, all the MPB biomass is definitely transported away from the study site. Similarly, the model precludes any incoming flux of MPB biomass produced in other areas and transported to the study site. Waves and current BSS can also shape the spatial distribution of *P. ulvae* individuals on the mudflat (Armonies and Hartke, 1995) and so the local grazing pressure on MPB developing in the sediment. In the model, the lack of grazing pressure on MPB cells resuspended in the water column may result into an overestimation of the simulated resuspended MPB biomass (Guizien et al., 2014). The intensive oyster farming in the Brouage mudflat vicinity can result into a substantial removal of the resuspended MPB biomass (Smaal and Zurburg, 1997). Such a process is not considered in the model. To that respect, an explicit benthopelagic coupling would be required to fully account for the complex biogeochemical processes controlling the planktonic activity within the water column (Hochard et al., 2012).

With respect to the rate and amplitude of the MPB resuspension, the simulated values compare with the values reported in the literature. The instantaneous resuspended MPB biomass simulated by the model reaches 110 mg Chl *a* m^{-3}, in the range of observations (~ 45 mg Chl *a* m^{-3} measured by Baillie and Welsh (1980); 320 mg Chl *a* m^{-3}, derived from suspended particulate matter measurements by Koh et al. (2007); 52.5 mg Chl *a* m^{-3} retrieved from remote sensing data by Gernez et al. (2017)). The maximum erosion rate of Chl *a* in the sediment simulated during massive resuspension events (8.93 mg Chl *a* m^{-2} h^{-1} or 2.48 µg Chl *a* m^{-2} s^{-1}) is consistent with measurements (1.72 µg Chl *a* m^{-2} s^{-1}) made by Orvain et al. (2014b) in July, 2008 in an erosion flume with sediment samples gathered in the Brouage mudflat. In the model, the MPB biomass export to the water column through the fluff layer erosion corresponds to MPB resuspension without any concomitant sediment erosion. The chronic events of fluff layer erosion led to instantaneous resuspended Chl *a* concentrations between 0 and 5.51 mg Chl *a* m^{-2}. On the Brouage mudflat, Guarini et al. (2008a) estimated the chronic resuspension to up to 11 mg Chl *a* m^{-3} in 1.5 m of seawater height (*i.e.* corresponding to 16.5 mg Chl *a* m^{-2}). They related it to a full resuspension of a well-established biofilm (~ 25 mg Chl

a m^{-2}) rather than erosion of the fluff layer only. In the model, the export of the entire biofilm is represented through the massive resuspension.

Physical and biological controls on MPB resuspension

Waves and tides

On the annual scale, the simulated export of MPB biomass to the water column is partly driven by wave-related massive resuspension events. These events occur mostly in winter and, to a lesser extent, in fall. In the model, the high bottom wave orbital velocity in winter and fall results in high simulated values of τ_w and τ_{max}. On mudflats of the Ems estuary in The Netherlands, de Jonge and van Beusekom (1995) related the MPB resuspension to wind waves. They showed a concomitant increase of resuspended benthic Chl *a* concentration with an increase of wind speed. The Bay of Marennes-Oléron extends over 170 km^2 and, regarding the geometry of the Bay, the highest fetch in the area can established from the North-West or the South-West (Fig. 22). This fetch configuration is promoted by dominant winds from the oceanic sector (SW to NW) especially during winter-fall (source: Meteo France 1961-1990). Such fetches drive wind waves with a short period and orbital motions that reach easily the shallow sea bottom with, as a result, the resuspension of the sediment including MPB biomass (Green and Coco, 2014). At the highest water depth simulated at our study site (3.24 m), orbital motions of waves with periods higher than 2 s start to interact with the sea bottom. Waves with periods higher than 2 s occur 55 % of the time in 2012. As a consequence, orbital motions often reach the sea bottom in the model. Moreover, wave-related MPB resuspension in the Brouage mudflat is not only dominated by waves generated locally but also by swells entering in the Bay from the ocean (Bertin et al., 2005). As a result, and contrarily to de Jonge and van Beusekom (1995), the sediment and MPB resuspension is not related to local winds only as peaks of wave orbital velocity are not always associated to strong local winds. The low wave orbital velocity simulated in spring and summer results in a much lower contribution of massive resuspension events to MPB resuspension at these seasons.

With respect to tides, the tidal currents contribute to massive MPB resuspension events during spring tides. Only the highest current velocities reached during spring tides can overpass $\tau_{crit_{mass}}$. The high contribution of spring tides current velocity on sediment resuspension was suggested by Toublanc et al. (2016) in their tri-dimensional (3D) modelling study in the Charente estuary in close vicinity of the Brouage mudflat. They suggest a higher concentration of resuspended sediment in spring tides than in neap tides, because the current velocity and τ_c were lower in neap tides.

14 % and 10 % of the simulated events of MPB resuspension occurs at the flood beginning and at the end of ebb, respectively. The action of waves on sea

bottom are limited by the water height (Fig. 25). The wave height and orbital velocity increase with the water level until a critical depth when orbital motions at the bottom start to decrease (Mariotti and Fagherazzi, 2013; Green and Coco, 2014; Li et al., 2019). In the model, the average critical depth is about 1 - 1.25 m. Such a water height is reached mainly at the beginning and at the end of high tides, which explains the high simulated impact of average wave conditions on MPB resuspension at the beginning of flood and at the end of ebb. Moreover, the high current velocity and τ_c at the flood beginning and at the end of ebb, combine to high τ_w at this moment of the tide, which increases τ_{max}. Using a 2D model, Le Hir et al. (2000) also simulated higher current velocities at the beginning of flood and at the end of ebb on the Brouage mudflat. Overall, the model reasonably simulates the process of MPB resuspension at both the tidal and seasonal scale.

MPB behaviour

The seasonal cycle of the MPB biomass in the sediment also plays a role in the seasonality of the massive MPB resuspension. Waves drive more frequent massive resuspension events in winter and fall. However, most of the high resuspension events (events identified when resuspended MPB biomass is higher than the last percentile of the resuspended MPB biomass simulated time series in 2012) are simulated in late winter-early spring. The occurrence from March to June of the simulated spring bloom of MPB biomass in the sediment explains this pattern. Because of the high MPB biomass in the sediment, the sediment erosion driven by strong-moderate hydrodynamical conditions leads to an important export of MPB biomass in the water column.

The mean time spent by MPB cells at the surface (γ) is a key parameter in the model that controls both the simulated MPB PP and resuspension. The highest value of instantaneous MPB resuspension is simulated when MPB cells remain longer at the sediment surface. The longer is the stay of the cells at the sediment surface, the higher is their PP. The MPB biomass accumulates in the sediment and leads to a high export of MPB biomass to the water column. In the model, the mean time spent by the MPB cells at the sediment surface is set according to the time required to induce photoinhibition (Blanchard et al., 2004). Combined with the MPB biomass in the sediment before the emersion period, γ sets the potential duration of the biofilm or the potential duration of the production period named γ^* (h) in the model. The longer is γ^*, the higher is the PP and the more likely are the cells remaining at the surface resuspended during the rising tide.

Resuspension events also contribute to shape the dynamics of the MPB biomass in the sediment. For example, in early February and early and late March, the simulated MPB biomass in the sediment decreases in response to massive resuspension events. In the model, a minimum threshold of MPB biomass in the sediment (73 mg Chl a m^{-2}) is set when massive resuspension events occur.

Such a threshold dampens the resuspension intensity when the MPB biomass is lower than this value. In their modelling study, Mariotti and Fagherazzi (2012) also set a constant background of MPB biomass during massive resuspension events to prevent any non resilient behavior of the simulated MPB. In addition, the laboratory erosion flume experiments made by Valentine et al. (2014) suggest that only a small biofilm can build up when repeated erosion events occur.

In response to massive resuspension events, MPB inhabiting the sediment first centimetre can develop resilience strategies to maintain a background of active biomass in the sediment. Larson and Sundbäck (2008) suggested that MPB cells in anoxic stressful conditions could migrate down in the sediment and go into a dormant state and keep respiration demands to a minimum. The survival capacity of non-resting benthic diatoms can be due to heterotrophy on organic substrates present in the sediment (Tuchman et al., 2006). Veuger and van Oevelen (2011) suggested that non-resting benthic diatoms can remain in dark sediment for a year and remain fully photosynthetically active. Once the sediment uppermost layer is eroded, buried MPB cells from deeper sediment layers newly exposed to favourable growth conditions can get active and productive. MPB cells newly deposited on the eroded sediment can also initiate recolonisation. In their field experiment, Pan et al. (2017) suggest that benthic diatoms are able to recolonise the sediment. By removing the top 2-cm of the microbial mat present at the sediment surface, the authors observed a rapid (4 - 7 days) recolonisation by diatoms corresponding to epipelic groups triggered by the horizontal advection and redistribution of cells over the mudflat during high tides

Fauna

The chronic erosion of the fluff layer simulated by the model is responsible for a substantial export of the MPB biomass from the sediment to the water column in spring and summer. The Chl *a* content in the fluff layer is fueled by the crawling activity of *P. ulvae* individuals, which increases the transfer of MPB biomass from the biofilm to the fluff layer. The high contribution of fluff layer erosion to total resuspended MPB biomass in spring and summer is driven by the relatively high *P. ulvae* density at these seasons. At the annual scale, the fluff layer erosion is more frequent than massive resuspension (31.3 % and 24 %, respectively). However, it contributes less to the total resuspended MPB biomass (36.7 %) than massive resuspension events (63.3 %). In our study, we considered the bioturbation by *P. ulvae* only but other fauna species can also contribute to bioturbation. On the upper Brouage mudflat, bivalve *Scrobicularia plana* individuals exhibit high densities ($\sim$ 1,000 ind m^{-2}) and play an important role in the bioturbation process in this part of the mudflat (Orvain et al., 2007). Other abundant species of macrofauna and meiofauna (*e.g.* the homogeneously spatially distributed nematodes on the Brouage mudflat) can also bioturbate

substantially the sediment (Rzeznik-Orignac et al., 2003; Passarelli et al., 2014). As we only explicitly account for the dominant MPB grazer at our study station, the model may underestimate bioturbation and the fluff layer erosion compared to the massive resuspension process.

The presence and grazing-crawling activity of *P. ulvae* can also impact the sediment bed roughness as the gastropod is able to cope with strong currents. Blanchard et al. (1997b) and Orvain et al. (2003) suggest that the *P. ulvae* shell can increase the bed roughness, which results into an increase of the BSS. Such an effect is not represented in the model. However, the bed roughness variations driven by *P. ulvae* individuals might have a limited effect in the model as the simulated annual MPB PP and instantaneous resuspension show a low sensitivity to bed roughness.

Sediment

The instantaneous MPB resuspension and annual MPB PP simulated by the model are not sensitive to the bed roughness. The model is run with the same constant value used in Le Hir et al. (2000) in their 2D hydrodynamical modelling study on the Brouage mudflat. Nevertheless, the Brouage mudflat is characterised by the presence of ridges and runnels (Gouleau et al., 2000), by the settlement of a sheet flow (*i.e.* a fluid sediment layer moving along the bottom) and the presence of biogenic structures. Consequently, the bed roughness is likely to vary in space and time. The horizontal resolution of the SCHISM physical model is ~ 100 m on the Brouage mudflat, which is too coarse for resolving ridges and runnels. These morphological sea bed structures are important in the sediment erosion-deposition-consolidation mechanisms. Average wave conditions and tidal currents remobilise the sediment mainly in runnels (Carling et al., 2009). In contrast, strong wind waves and spring tides current and associated high BSS can induce sediment resuspension both in runnels and ridges (Carling et al., 2009; Fagherazzi and Mariotti, 2012). Blanchard et al. (2000b) suggest that MPB colonise and consolidate preferentially ridges compared to runnels, which are more drainage structures. Consequently, ridges are more consolidated than runnels due to a high MPB and EPS content (Blanchard et al., 2000b). Marani et al. (2010) showed that biostabilisation processes by halophytic vegetation and microbial biofilm is a key component of tidal morphological equilibrium. Therefore, even spatially distributed in patchiness, MPB might play a key role on the long and short term morphodynamic of the intertidal mudflat. The current and waves simulated by the SCHISM physical model compare with the ADCP measurements deployed in 2012 on a ridge of the Brouage mudflat, which suggests that the physical-biological model can reproduce the MPB dynamics prevailing on ridge-like structures.

In the model, the physical properties of the sediment are impacted by the biology. The sediment is consolidated by biota as the erosion threshold increases along with the MPB biomass in the sediment first centimetre. Such a mecha-

nism represents the sediment consolidation by EPS excreted mainly by MPB (Pierre et al., 2010, 2012). EPS increase the adhesion of fine sediment grains (Decho, 1990, 2000) and decrease the sediment permeability, which results into a increase of the sediment consolidation (Zetsche et al., 2011). Consequently, the higher is the simulated MPB biomass in the sediment, the higher is simulated $\tau_{crit_{mass}}$. $\tau_{crit_{mass}}$ reaches a seasonal maximum in early-May when the MPB biomass in the sediment is the highest. Pivato et al. (2019) described the relationship between the biostabilisation effect and the seasonal cycle of MPB biomass as a positive feedback. The high MPB PP in spring promotes the fast recovery of MPB biomass in the sediment hence leading to a higher resistance to erosion through biostabilisation. In that sense, MPB create their own favourable conditions for MPB biomass accumulation in the sediment in spring. On a mudflat in the Westerscheldt in The Netherlands, Stal (2010) reports the highest erosion threshold right after the MPB biomass maximum in the biofilm during one low tide. On a mudflat at Kjelst in the Danish Wadden Sea, Andersen (2001) also suggests a good correspondence between a well-established MPB biofilm and a high erosion threshold in spring and late summer-early winter. In our study, the simulated seasonal maximum of $\tau_{crit_{mass}}$ (1.8 Pa) is 6-fold higher than the critical BSS constant for bare cohesive sediment. This is consistent with the laboratory flume experiment of Neumeier et al. (2006) that suggests that biofilm-inhabited sediments exhibit a critical BSS 4- to 10-fold higher than in bare sediments without any established biofilm. On the Kapellebank mudflat of the Western Scheldt Estuary (the Netherlands), Zhu et al. (2019) also report a critical BSS 5-fold higher in a sediment inhabited by diatoms than in sediments without diatoms. The erosion threshold commonly follows the Chl *a* content in sediment. However, a stronger correlation is found between sediment consolidation and EPS production (Underwood and Paterson, 1993) by both benthic diatoms and bacterial assemblages (Chen et al., 2017), the latter process being not simulated by the model. Accounting for bacteria and EPS production might improve the model ability to simulate the sediment consolidation.

MPB-driven benthic-pelagic flux

At the annual scale, 43 % of the simulated PP is resuspended. In winter, the ratio between MPB resuspension and PP is the highest due to a moderate resuspension and a low PP. In contrast, in spring, the ratio decreases as resuspension reaches its seasonal maximum and PP is higher than in winter. With respect to secondary production, the simulated annual resuspension (60.8 g C m^{-2} yr^{-1}) is 1.3-fold higher than the annually-integrated MPB ingestion by *P. ulvae* (41.1 g C m^{-2} yr^{-1}). It suggests that the export of MPB biomass to the water column is higher than the MPB grazing that builds up secondary production. Moreover, the simulated annual resuspension represents 33 % of the phytoplankton PP estimated in the same study area (Struski and Bacher, 2006). Such a result high-

lights the key role played by MPB in the benthopelagic coupling. Using inverse modelling based on data from the Brouage mudflat, Saint-Béat et al. (2014) suggest that the export of particulate organic carbon from the benthic compartment fuels the pelagic carbon production when biofilm resuspension is considered in summer. MPB resuspension varies seasonally in response to contrasting hydrodynamical conditions. The coupled physical-biological model simulates such a seasonal dynamics that impacts the seasonal benthopelagic flux of organic carbon. This is not the case in Savelli et al. (2018), where MPB resuspension is formulated as a continuous and linear MPB loss term at high tide. Such a formulation in Savelli et al. (2018) results in a seasonality of resuspension that only varies according to the MPB biomass in the sediment without considering any physical forcing. It then implies that the higher is the MPB biomass in the sediment, the higher is the resuspension of the MPB biomass. Such a parametrisation is not realistic considering the increase of sediment consolidation with the MPB biomass. In addition, this formulation might overestimate and underestimate the MPB resuspension during calm physical conditions and intense physical conditions, respectively.

CONCLUSIONS

We used a physical-biological model to assess the role of chronic and massive resuspension events on the MPB dynamics in a very productive temperate intertidal mudflat. The model reasonably simulates the seasonal pattern of MPB resuspension and gives some insights to our understanding of the contribution of the physical and biological mechanisms controlling the MPB export from the sediment to the water column:

- At the tidal scale, MPB resuspension is the highest in spring tides due to strong tidal currents. Over the year, 76 % of the resuspended MPB biomass is exported to the water column at the flood beginning due to high velocity currents and low water heights that promote wave orbital motions-sea bottom interactions;
- In winter and fall, waves are the main driver for massive MPB resuspension events;
- During the spring bloom, MPB biomass accumulates and consolidates the sediment first centimetre. The simulated critical BSS is 6-fold higher than the critical BSS constant for bare sediment;
- In spring, the density of *P. ulvae* individuals increases and so the bioturbation, which promotes MPB in the chronically eroded fluff layer at the sediment surface;
- When the MPB biomass in the sediment reaches its seasonal maximum in spring, massive resuspension events driven by the wave- and tidal-

induced BSS and chronic fluff layer erosion events lead to the highest seasonal export of MPB biomass to the water column (from 1.1 to 3-fold higher than in other seasons in terms of Chl *a*). In terms of Chl *a*, massive and chronic resuspension events in spring represent 20 % and 17.5 % of the MPB biomass resuspended annually;

- In summer, MPB resuspension is the lowest (1.3 to 3-fold lower than in other seasons in terms of Chl *a*) due to calm hydrodynamical conditions and low MPB biomass in the sediment;
- At the annual scale, 43.3 % of the MPB PP is resuspended to the water column and this export (60.8 g C m^{-2} yr^{-1}) exceeds the *P. ulvae* grazing pressure on MPB (41.1 g C m^{-2} yr^{-1}).

Accounting for the physically (tides and waves) and biologically (biostabilisation and bioturbation) driven resuspension processes of MPB in predictive physical-biological coupled models is an important step in assessing the export of biogenic matter at the land-ocean interface. These processes could be represented into 3D ocean-biogeochemical coupled models that resolve the 3D fields of advection and diffusion in the water column required to simulate the spatial and temporal dynamics of MPB over a whole mudflat. 3D models would hence allow the assessment of benthopelagic MPB fluxes driven by the action of waves and tidal currents. Once in the water column, MPB can turn into a planktonic life forms whose growth rate can depend on seawater nutrients, light availability and temperature (MacIntyre et al., 1996). According to the prevailing environmental conditions, MPB can be grazed, contribute to pelagic PP (Guarini et al., 2008a; Polsenaere et al., 2012), remain into the water column until senescence or can sink and return to a benthic life form (MacIntyre et al., 1996; Miller et al., 1996; Guizien et al., 2014). Such processes could be inferred by coupling MPB models that include the resuspension mechanisms with high-resolution regional models that simulate the interactions between the coastal ocean and the planktonic ecosystem dynamics. Accounting for such processes in the carbon budget of the land-ocean interface would improve our understanding and assessment of the benthopelagic fluxes of organic matter, and bring new insights on the role played by MPB in the carbon cycle of the global coastal ocean.

CHAPTER V

POTENTIAL IMPACT OF MICROPHYTOBENTHOS PHOTOINHIBITION ON PRIMARY PRODUCTION OF A TEMPERATE INTERTIDAL MUDFLAT

In the previous chapters, the MPB model was not resolved spatially on a tri-dimensional (3D) framework. In Chapter 5, we use a regional and high-resolution 3D hydrodynamical model (MARS-3D) in which we couple the MPB model to investigate the spatial and temporal variability of MPB dynamics on the Brouage mudflat in 2015. The objective is to infer on the potential effect of photoinhibition on MPB primary production over the mudflat. The model suggests that the light exposure on the upper shore is higher than on the lower parts of the mudflat due to more frequent and longer emersions. Consequently, the annual MPB primary production is higher on the upper shore than on the middle and lower shores. As the upper shore emerges more frequently and longer than the lower shore, the quantitative difference of MPB PP under the effect of photoinhibition is higher on the upper shore than on the lower shore. However, the lower shore might be more sensitive to photoinhibition due to its low MPB biomass, PP and its emersion periods restricted to high light levels. Photoinhibition over the whole mudflat is stronger in spring and summer than in fall and winter. It results into a decrease by 50 % of MPB primary production in spring and summer.

5

POTENTIAL IMPACT OF MICROPHYTOBENTHOS PHOTOINHIBITION ON PRIMARY PRODUCTION OF A TEMPERATE INTERTIDAL MUDFLAT

This chapter will be submitted as an article in a journal, which has not yet been determined.

Acronyms:

MPB: *Microphytobenthos*

MST: *Mud surface temperature*

NoPhoto run: *Run without photoinhibition*

PAR: *Photosynthetically Active Radiation*

Photo run: *Run with photoinhibition*

PP: *Primary Production*

ABSTRACT

The benthic microalgae or microphytobenthos (MPB) biofilm formed at the surface of intertidal mudflats during low tides faces strong daily to seasonal variations of solar irradiance. Despite photoacclimation and photoprotective mechanisms, MPB cells can be subject to photoinhibition. The objective of this study is to estimate and map the potential impact of photoinhibition on MPB primary production (PP) over the whole Brouage mudflat (NW France). We use a regional and high-resolution tri-dimensional (3D) hydrodynamical model (MARS-3D) in which we couple the MPB model with and without photoinhibition. The model suggests that photosynthetically active radiation (PAR) reaching the mud surface of the upper shore is higher than on the lower parts of the mudflat due to more frequent (almost twice a day) and longer (6.8 $\pm$ 2.6 h in average) emersion periods on the upper shore. The amount of PAR reaching the mud surface of the whole mudflat is the highest during spring-summer when it represents 70 % of the total annual PAR reaching the surface of the mudflat. As a result, with or without photoinhibition, annual MPB PP on the upper shore represents 50 % of the annual MPB PP over the whole mudflat and half of the annual MPB PP is attributed to spring-summer MPB PP. As the upper shore emerges more frequently and longer than the lower shore, the quantitative difference of MPB PP under the effect of photoinhibition is higher on the upper shore (-0.9 Gg C yr^{-1}) than on the lower shore (-0.3 Gg C yr^{-1}). However, the lower shore might be more sensitive to photoinhibition due to its low MPB biomass, PP and its emersion periods restricted to high light levels. Photoinhibition over the whole mudflat is stronger in spring and summer than in fall and winter. It results into a decrease by 50 % of MPB primary production in spring and summer. The accurate estimation of the photosynthetic response of MPB to its highly variable environment is a challenge in a perspective of quantifying MPB PP over large mudflats from a synoptic to inter-annual time scale.

INTRODUCTION

The primary production (PP) of benthic microalgae or microphytobenthos (MPB) sustains the high biological productivity of intertidal mudflats (MacIntyre et al.,

1996; Underwood and Kromkamp, 1999). Despite highly variable physical conditions, intertidal mudflats constitute one of the most productive natural ecosystems on Earth (Cahoon, 1999). MPB cells can be exposed to high light levels at the sediment surface (> 2000 µmol m^{-2} s^{-1}; Laviale et al., 2015). In response, MPB develop physiological and behavioural photoprotective mechanisms which vary with MPB growth forms (Jesus et al., 2009; Cartaxana et al., 2011; Barnett et al., 2015; Pniewski et al., 2015; Cartaxana et al., 2016). In sandy sediments, light penetrates up to 3000 µm (Cartaxana et al., 2011) and MPB are mostly composed of epipsammic diatoms that live in close association with sediment grains (Underwood, 2001). Epipsammic diatoms exhibit high physiological photoprotection and low behavioural adaptations as their motility is restricted to the sphere of the sediment grains (van Leeuwe et al., 2008; Jesus et al., 2009; Cartaxana et al., 2011; Barnett et al., 2015). Epipsammic diatoms dissipate the excess of energy from light mostly through the Non-Photochemical Quenching of chlorophyll fluorescence (NPQ), which corresponds to de-epoxidation of xanthophyll pigments in the xanthophyll cycle (XC; Lavaud and Goss, 2014). Free motile epipelic diatoms dominate MPB assemblages in muddy sediments (Underwood, 2001). Light is strongly attenuated in muddy sediments (photic layer of 600 µm) and limits the growth of epipelic diatoms (Cartaxana et al., 2011). Consequently, they migrate at the sediment surface to meet optimal light conditions during daytime low tides. In addition, epipelic diatoms can achieve "micro-migrations" within the sediment topmost layer (~ 250 µm) *i.e.* a negative phototaxic short-term change of position (Kromkamp et al., 1998; Perkins et al., 2001; Cartaxana et al., 2011). In epipelic growth forms, NPQ physiological photoprotection is minimised and compensated by vertical migration (Serôdio et al., 2001, 2012; Raven, 2011).

The MPB photoinhibition is therefore the result of the outbalance between photoprotection efficiency and light conditions. Osmond (1994) and Osmond and Grace (1995) define dynamic photoinhibition as a short-term reversible, regulatory process for the dissipation of excessive light energy, and chronic photoinhibition as a slowly reversible process that may occur under prolonged and harmful light conditions. Photoinhibition of MPB photosynthesis was successfully measured in laboratory experiments (Serôdio et al., 2012). However, in regard to the physiological and behavioural adaptations, photoinhibition was rarely observed in the field. Serôdio et al. (2008) reported *in situ* photoinhibition of MPB assemblage on an intertidal mudflat in Portugal due to an incomplete recovery of the photosynthetic apparatus damaged from a previous light stress.

With regard to the photoprotective mechanisms of MPB, investigating photoinhibition and its consequences is highly of interest to accurately estimate MPB PP at the mudflat scale. The goal of this study is to quantify and map the potential impact of photoinhibition on MPB PP over the mudflat scale. For this purpose, the current study quantifies the impact of photoinhibition on MPB PP using a coupled physical-biological tri-dimensional (3D) model. The model

simulates the MPB dynamics (biomass and production) and grazing by gastropod deposit-feeder *Peringia ulvae* in order to estimate the potential effect of photoinhibition on MPB PP at the seasonal scale over the Brouage intertidal mudflat (NW France). In the paper, we describe first the physical-biological coupled 3D model. Second, we map the light, temperature and tidal conditions over the mudflat and we estimate the potential impact of photoinhibition on MPB PP at the mudflat scale. Finally, we discuss the spatial and temporal variability of photoinhibition of MPB PP.

MATERIAL AND METHODS

Study site

The study area is the Pertuis Charentais Sea and the study site is the Brouage mudflat (Fig. 45). It is a shallow semi-enclosed sea located on the French Atlantic coast. The semi-diurnal and macrotidal regime ranges up to ~ 6 m during spring tides. The study site is the 42-km^2 intertidal Brouage mudflat located in the South-Eastern part of the study area (Fig. 45) made of fine cohesive sediments (median grain size 17 µm and 85 % of grains with a diameter < 63 µm; Bocher et al., 2007) and characterised by a gentle slope (~ 1/1000; Le Hir et al., 2000) dominated by free motile epipelic diatoms.

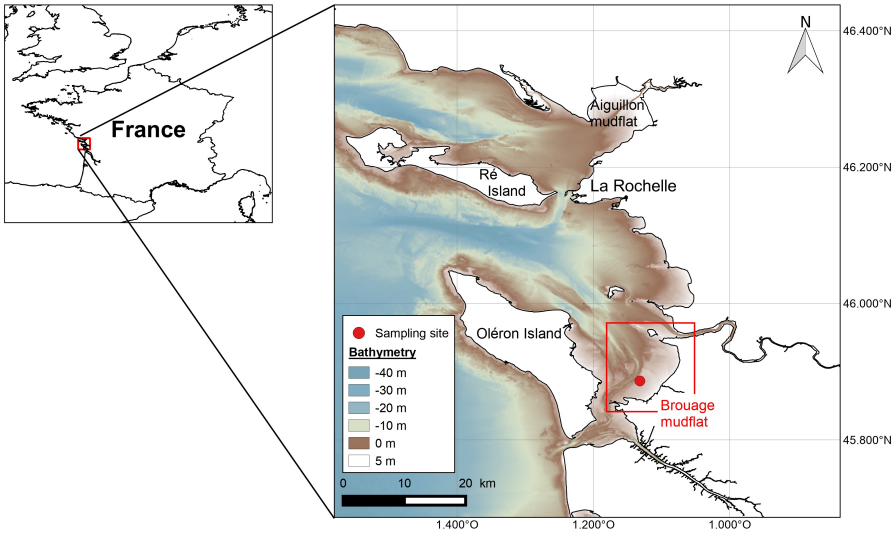

Figure 38: Bathymetry of the model domain covering the Pertuis Charentais Sea (source: SHOM) and location of the main intertidal mudflats. The site of MST and PAR measurements is represented by a red full point.

Observations

Two field campaigns were planed during spring low tides, on 5-6 May 2015, 2-3 July 2015. Incident photosynthetically active radiation (400 to 700 nm; PAR, µmol photons m^{-2} s^{-1}) and mud surface temperature (MST, °C) were measured with a 30-sec frequency at the "Merignac" site (45°53'20.87"N; 1°7'54.37"W; Fig. 45). In addition, we used the Production-Irradiance (P-I) data measured by Pniewski et al. (2015) on the upper part of the Aiguillon mudflat (46°15'N, 1°10'W) located north the Brouage mudflat and composed of fine cohesive sediment (< 63 µm; Haubois et al., 2005, Fig. 45). Pniewski et al. (2015) conducted field campaigns in March (spring), June-July (summer) and November-December (autumn) 2007 during which they sampled epipelic diatoms 3 to 5 times. The light curves were determined in a micro-respirometer according the method developed by Zurzycki and Starzecki (1971). More details on samplings and measurements are given in Pniewski et al. (2015).

The coupled physical-biological 3D model

The MARS-3D modelling system

The MARS-3D tri-dimensional model (3D hydrodynamical Model for Applications at Regional Scale) was used to simulate the physical environment (tides, PAR, MST) over the whole mudflat. This finite-difference model solves the Navier-Stokes primitive equations under assumptions of Boussinesq approximation, hydrostatic equilibrium and incompressibility (Blumberg and Mellor, 1987; Lazure and Dumas, 2008). The model was discretised into 100 m by 100 m horizontal grid cells and 20 σ vertical coordinates. The model was run over the same domain used by Polsenaere et al. (Fig. 45; 2017). The MARS-3D model is fully detailed in Lazure and Dumas (2008). Atmospheric forcings (wind speed in m s^{-1}, air temperature in °C, atmospheric pressure at sea level in Pa, nebulosity fraction, relative humidity and solar fluxes in W m^{-2}) were provided by Meteo France AROME model (https://donneespubliques.meteofrance.fr). MARS-3D simulates current velocity, seawater temperature and salinity for the whole domain. Along its open boundaries, the circulation model was forced with amplitudes and phases of 115 harmonic constituents from the cstFRANCE tidal model developed by French marine service for hydrography and oceanography (SHOM; Simon and Gonella, 2007). Initial and boundary conditions of seawater temperature, salinity, current velocity and sea surface height came out from the MANGA 2500 Ifremer model (Lazure et al., 2009).

The mud surface temperature model

The mud temperature model developed by Savelli et al. (2018) was coupled with MARS-3D. Thermodynamic equations detailed in Savelli et al. (2018) simulated

heat fluxes in a 1-cm deep sediment layer. No horizontal fluxes were considered. During low tides, the simulated MST resulted from heat exchanges between the Sun, the atmosphere, the sediment surface, from the heat conduction between mud and air, and from mud evaporation. During high tides, the simulated MST was set to the temperature of the overlying seawater simulated by MARS-3D. In their study, Savelli et al. (2018) successfully compared the simulated MST with 1-min MST data measured *in situ* on the Brouage mudflat. The differential equation of heat energy balance was solved by MARS-3D numerical scheme. The MST model is fully detailed in Savelli et al. (2018).

The MPB model

The MPB model developed by Savelli et al. (2018) was also coupled with MARS-3D. The MPB model simulated the MPB biomass concentration in the surface biofilm (S, mg Chl *a* m^{-2}), in the sediment first centimetre (F, mg Chl *a* m^{-2}) and the *Peringia ulvae* biomass (Z, mg C m^{-2}) at the sediment surface. The MPB model accounted for vertical MPB migration driven by diurnal and tidal cycles through exchanges of MPB biomass between S and F (Guarini et al., 2000). The MPB cells migrated upward from the sediment to the sediment surface to form a productive biofilm during daytime low tides. The MPB PP rate was regulated by PAR and mud temperature at the sediment surface. At nightfall or at the flood beginning, MPB migrated downward from S to F until the complete disappearance of biomass in the biofilm. The *P. ulvae* growth was sustained by grazing on MPB biofilm controlled by MST and MPB biomass in the biofilm. The MPB model and differential equations are fully detailed in Savelli et al. (2018).

Photoinhibition of MPB

The model of Platt and Jassby (1976) originally used in Savelli et al. (2018) was substituted by the model of Platt et al. (1980), which accounts for photoinhibition to determine the photosynthetic rate P^b (mg C mg Chl a^{-1} h^{-1}) as a function of light (I, µmol photons m^{-2} s^{-1}):

$$P^b = P_s^b \times \left[1 - exp\left(-\frac{\alpha I}{P_s^b}\right)\right] \times exp\left(-\frac{\beta I}{P_s^b}\right), \tag{43}$$

where P_s^b is the maximum potential light-saturated photosynthetic rate (mg C mg Chl a^{-1} h^{-1}). Considering that P-I data were measured in optimal temperature conditions, P_s^b was assimilated to P_{MAX}^b in the Production-Temperature relationship developed by Blanchard et al. (1996). Temperature-related parameters for MPB photosynthesis were adjusted in Savelli et al. (2018). α and β are the photosynthetic efficiency (mg C mg Chl a^{-1} h^{-1} (µmol photons m^{-2} s^{-1})$^{-1}$) and the photoinhibition parameter (mg C mg Chl a^{-1} h^{-1} (µmol photons m^{-2} s^{-1})$^{-1}$), respectively.

The differential evolution algorithm (DE) implemented in the R package "DEoptim" (Ardia et al., 2016) was used to minimise the differences between the predicted and observed photosynthetic rate in order to obtain α and β from fitting the 33 P-I datasets from Pniewski et al. (2015). The DE algorithm does not require arbitrary initial parameter values which can result into errors in optimisation of light-response models (Chen et al., 2016). The seasonal values of α and β correspond to the mean values extracted from the P-I data fit. Seasonal α and β in spring, summer and fall were then spline-interpolated at a daily time step over the year.

Two scenarios were investigated *i.e.* with and without photoinhibition (Fig. 39). In the scenario without photoinhibition (NoPhoto), β was set to zero. In the scenario with photoinhibition (Photo), α and β were set at values given in Table 16. P_s^b corresponds to the photosynthetic rate in absence of photoinhibition *i.e.* the asymptotic maximal light-saturated photosynthetic rate in the NoPhoto run (mg C mg Chl a^{-1} h^{-1}; Fig. 39). P_{max}^b is the maximal photosynthetic rate accounting for photoinhibition in the Photo run (mg C mg Chl a^{-1} h^{-1}; Fig. 39). In both scenarios, I_k is the light saturation parameter ($\frac{P_{max}^b}{\alpha}$; µmol photons m^{-2} s^{-1}). It represents the intersection between the photosynthetic efficiency α with the asymptotic P_s^b in the NoPhoto run or P_{max}^b in the Photo run. I_{opt} is the optimal light intensity (µmol photons m^{-2} s^{-1})$^{-1}$) at which the photosynthetic rate is maximal (= P_{max}^b in the Photo run or P_s^b in the NoPhoto run; Fig. 39). According the Platt et al. (1980) P-I model, it is obtained by:

$$I_{opt} = \frac{P_s^b}{\alpha} \times \ln\left(\frac{\alpha+\beta}{\beta}\right). \tag{44}$$

Beyond I_{opt}, the photosynthetic rate is photoinhibited and decreases.

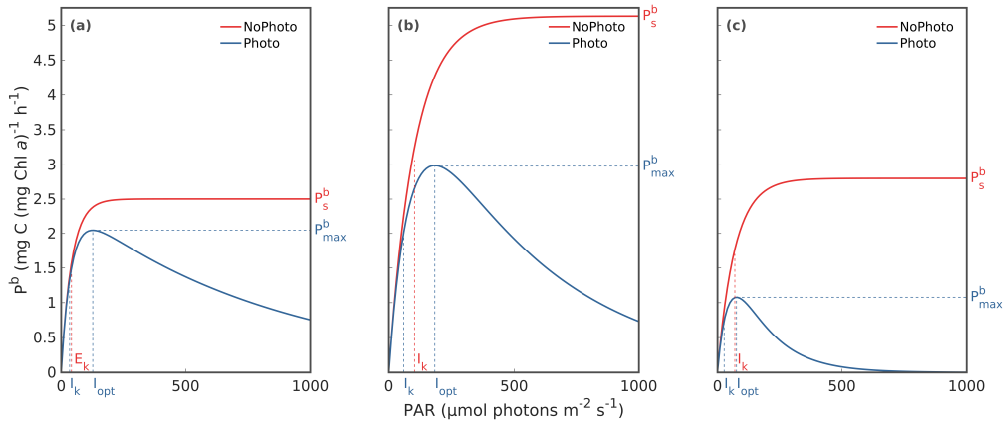

Figure 39: P-I characteristics **(a)** in spring, **(b)** in summer, and **(c)** in fall. In the NoPhoto run, I_k differs from Table 16 as it was computed with $\beta = 0$.

Table 16: Seasonally-averaged fitted parameters of the Platt et al. (1980) P-I model on the 33 P-I datasets from Pniewski et al. (2015). r^2 is the determination coefficient and RSD is the residual standard deviation.

Parameter	Spring	Summer	Fall
P_s^b (mg C mg Chl a^{-1} h^{-1})	2.5 ± 0.83	5.13 ± 2.5	2.8 ± 1.7
P_{max}^b (mg C mg Chl a^{-1} h^{-1})	2.02 ± 0.67	3.75 ± 1.7	1.5 ± 0.8
α (mg C mg Chl a^{-1} h^{-1} (µmol photons m^{-2} $s^{-1})^{-1}$)	0.06 ± 0.03	0.05 ± 0.01	0.04 ± 0.04
β (mg C mg Chl a^{-1} h^{-1} (µmol photons m^{-2} $s^{-1})^{-1}$)	0.003 ± 0.002	0.01 ± 0.02	0.02 ± 0.03
I_k (µmol photons m^{-2} s^{-1})	35 ± 7.93	76.85 ± 33.2	37.82 ± 23.47
I_{opt} (µmol photons m^{-2} s^{-1})	130.12 ± 25.81	300.8 ± 170.7	115.12 ± 65.47
r^2	0.91 ± 0.04	0.95 ± 0.1	0.84 ± 0.3
RSD (mg C mg Chl a^{-1} h^{-1})	0.24 ± 0.11	0.24 ± 0.14	0.14 ± 0.07

Modelling set-up and output

The physical-biological coupled model was initialised with a spin-up starting from 12 September 2014 00:00:00 UTC to 1 January 2015 00:00:00 UTC. F, S and Z were initially set to 100 mg Chl *a* m^{-2}, 0 mg Chl *a* m^{-2} and 1000 mg C m^{-2}, respectively. The physical-biological coupled model was then run from 1 January 2015 00:00:00 UTC to 1 January 2016 00:00:00 UTC.

Conditions at the sediment surface over the whole mudflat were seasonally-averaged (emersion duration and episodes, MST) and integrated (PP, PAR) during daytime emersions in winter (January to March), spring (April to June), summer (July to September) and fall (October to December). I_{opt} and the photoinhibition span, which corresponds to the cumulated duration of photoinhibition (when $I > I_{opt}$) relatively to the cumulated duration of daytime emersion periods were seasonally-averaged and integrated. In addition, we computed spatial analysis by spatially-averaging and integrating the outputs over the whole mudflat and on three tidal levels. Three equal areas of 11.93 km^2 were defined according to the mean time of emersion in 2015 (Fig. 40). Such partitioning distinguished the upper shore as it emerged more than 5.15 h from the middle shore emerging between 5.15 and 2.9 h and the lower shore emerging less than 2.9 h.

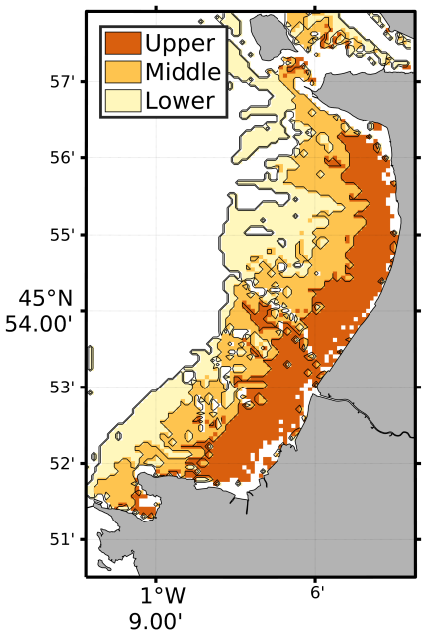

Figure 40: Partitions of the mudflat according to the tidal level.

RESULTS

Physical conditions on the mudflat

The simulated MST and PAR during daytime emersion periods reasonably compared to the 30-sec frequency measurements made in May and July 2015 at the study site (Fig. 41). Over the daytime emersion periods of 5-6 May 2015, the simulated PAR (1404.9 ± 101.3 µmol photons m^{-2} s^{-1}) showed a lower dispersion and underestimated observations (1514.7 ± 532.4 µmol photons m^{-2} s^{-1}) (Mann Whitney test: *p-value* < 0.01). The simulated mean PAR during daytime emersion periods in 2-3 July 2015 (1195.1 ± 304.9 µmol photons m^{-2} s^{-1}) significantly compared to the measured PAR (1229.9 ± 305.9 µmol photons m^{-2} s^{-1}) (Mann Whitney test: *p-value* > 0.01). In 5-6 May 2015, the simulated MST over daytime emersion periods was in average 20.7 ± 0.6 °C and was significantly higher than the observed mean MST on the same periods (19.5 ± 1.8 °C) (Mann Whitney test: *p-value* < 0.01). The simulated MST (31.2 ± 5 °C) was not significantly different than the measured MST during daytime low tides in 2-3 July 2015 (31.4 ± 3.4 °C) (Mann Whitney test: *p-value* > 0.01).

The simulated integrated PAR was not spatially uniform over the mudflat (Fig. 42b and Table 17). The total simulated PAR at the surface of the mud decreased seaward on the mudflat (Fig. 42b and Table 17). Annually, the total simulated PAR at the surface of the upper shore was 6.1×10^{10} mol photons, which was two- and three-fold higher than the middle and lower shores, re-

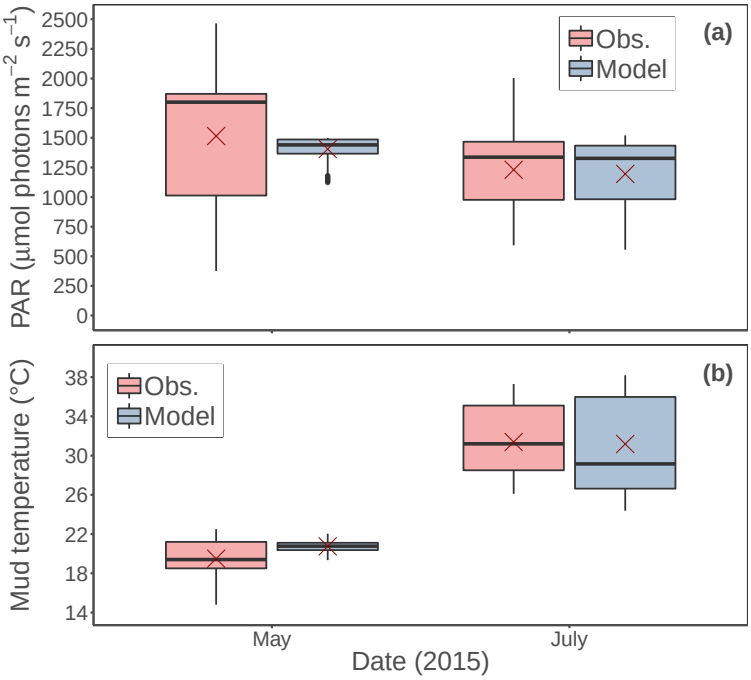

Figure 41: Simulated and observed **(a)** PAR and, **(b)** mud surface temperature during *in situ* measurements in 2015. Red crosses correspond the mean value of PAR and MST for the corresponding period.

spectively (Table 17). The integrated PAR was the highest during spring and summer and the lowest during fall over the whole mudflat (Table 17). In spring and summer, the seasonal total PAR available for MPB represented 70 % of the annual total PAR (Table 17). Moreover, the spring-summer total PAR on the upper and middle shores was almost one order of magnitude higher than on the lower shore (Table 17).

The simulated MST was spatially homogeneous over the whole mudflat scale during daytime emersion periods (Fig. 42a and Table 17). In winter, the simulated MST was 11 $\pm$ 4.4 °C in average on the mudflat (Table 17). In spring, the simulated MST increased to reach 19.9 $\pm$ 6 °C in average on the three tidal levels (Table 17). The simulated MST on the mudflat reached its seasonal maximum in summer with 22.8 $\pm$ 6.5 °C and decreased in fall to 15 $\pm$ 4.1 °C (Table 17).

The simulated daytime emersion period decreased seaward (Fig. 42c and Table 17). The upper shore emerged 6.8 $\pm$ 2.6 h in average, which was two- to five-fold longer than the emersion duration on the middle and lower shores, respectively (4 $\pm$ 1.7 and 1.3 $\pm$ 1.4 h, respectively; Table 17). The entire mudflat emerged longer in spring-summer compared to the other seasons (Table 17 and Fig. 42c).

The number of daytime emersion episodes decreased seaward (Fig. 42d). The upper shore emerged 1.4 $\pm$ 0.6 times per day in average (Table 17). The lower

shore rarely exceeded 1 daytime emersion period per day with an annual mean of 0.7 ± 0.6 times per day (Table 17). The number of daytime emersion per day slightly increased during spring and summer over the whole mudflat (Fig. 42d and Table 17).

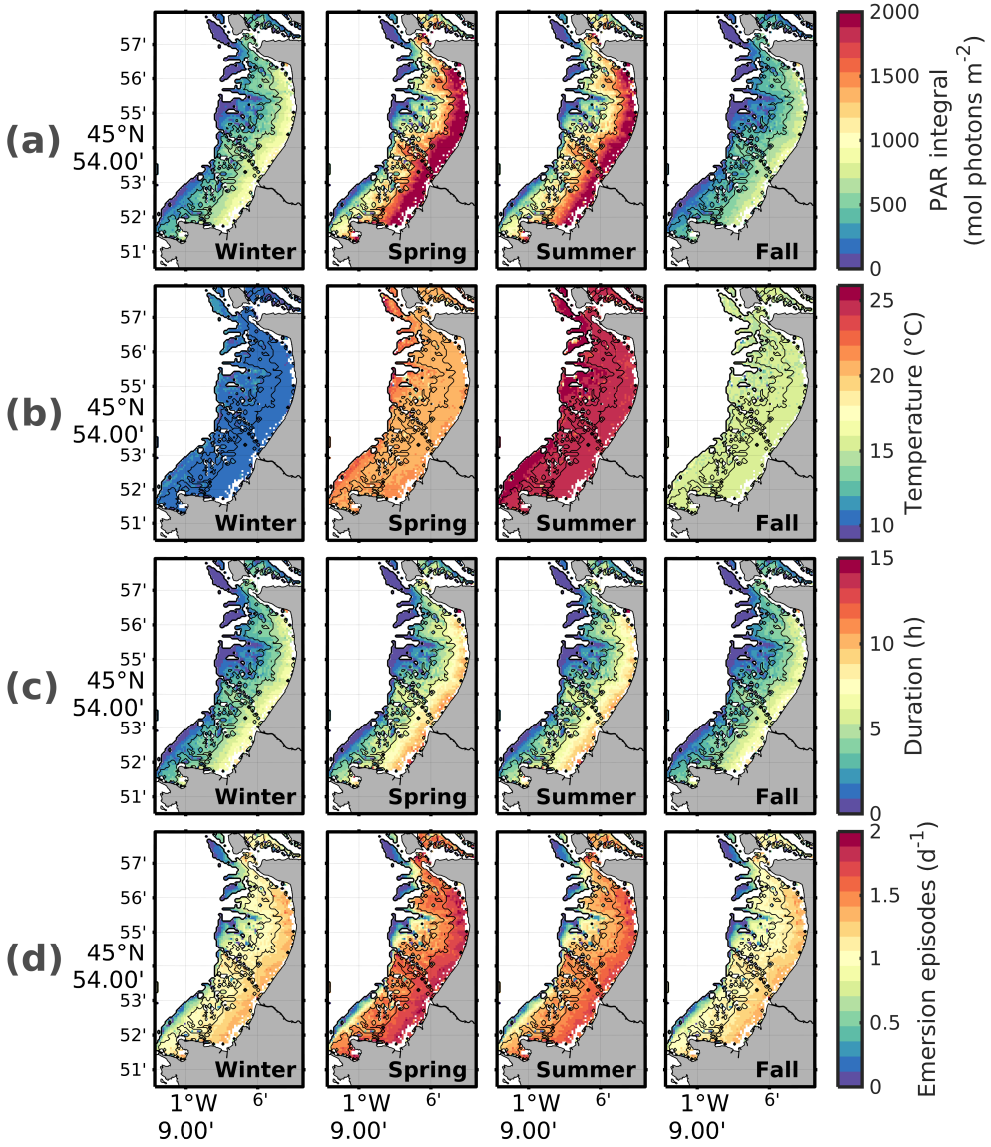

Figure 42: Map of seasonal diurnal emersion conditions of **(a)** mud surface temperature (°C), **(b)** total PAR (mol photons m^{-2}), **(c)** daytime emersion duration (h) and, **(d)** daytime emersion episodes (d^{-1}). The black contour lines indicate the three tidal levels.

Table 17: Seasonal mean (± standard deviation) of MST (° C), total integrated PAR (10^{10} mol photons), emersion duration (h) and daytime emersion episodes (d^{-1}) during daytime emersions according to the level of the mudflat in 2015.

	Season	Upper	Middle	Lower	Mudflat
PAR integral (10^{10} mol photons)	Winter	0.92	0.57	0.21	1.7
	Spring	2.28	1.35	0.44	4.07
	Summer	2.07	1.27	0.44	3.78
	Fall	0.76	0.47	0.17	1.42
	Annual	6.03	3.7	1.27	11
MST (°C)	Winter	10.5 ± 4.6	10.6 ± 4.5	10.6 ± 4.6	11 ± 4.4
	Spring	20.9 ± 6	20.7 ± 5.7	20.9 ± 5.8	19.9 ± 6
	Summer	24.1 ± 5.9	24.3 ± 5.9	24.9 ± 5.8	22.8 ± 6.5
	Fall	15.2 ± 4.4	15.2 ± 4.3	15.1 ± 4.4	15 ± 4.1
	Annual	18.4 ± 7.5	18.4 ± 7.4	18.4 ± 7.5	17.8 ± 7
Duration (h)	Winter	5.7 ± 1.9	3.3 ± 1.4	1.1 ± 1.2	1.3 ± 2.3
	Spring	8.1 ± 2.9	4.8 ± 1.8	1.4 ± 1.5	1.8 ± 3.2
	Summer	7.7 ± 2.4	4.5 ± 1.5	1.4 ± 1.4	1.7 ± 3
	Fall	5.7 ± 1.7	3.5 ± 1.3	1.2 ± 1.2	1.3 ± 2.3
	Annual	6.8 ± 2.6	4 ± 1.7	1.3 ± 1.4	1.5 ± 2.7
Emersion (d^{-1})	Winter	1.2 ± 0.5	1 ± 0.3	0.6 ± 0.5	0.4 ± 0.6
	Spring	1.7 ± 0.6	1.5 ± 0.6	0.8 ± 0.7	0.5 ± 0.8
	Summer	1.6 ± 0.5	1.4 ± 0.5	0.8 ± 0.7	0.5 ± 0.7
	Fall	1.2 ± 0.4	1 ± 0.3	0.6 ± 0.5	0.4 ± 0.6
	Annual	1.4 ± 0.6	1.2 ± 0.5	0.7 ± 0.6	0.4 ± 0.7

MPB biomass

In the NoPhoto run, the simulated MPB biomass was higher than in the Photo run in all seasons and levels of the mudflat (Table 18). In both runs, the MPB biomass was higher on the upper and middle shores than on the lower shore (Table 18). In the Photo run, the highest decrease of MPB biomass was on the lower shore where it decreased by 41 % compared to the NoPhoto run (Table 18). Even if the simulated seasonal cycle of MPB biomass was characterised by a maximum in winter and a minimum in summer, the mean simulated MPB biomass did not differ significantly over seasons as the variability of MPB biomass was high (Table 18).

Table 18: Mean simulated (± standard deviation) MPB biomass concentration in the sediment first cm (mg Chl *a* m^{-2}) in 2015.

Simulation	Season	Upper	Middle	Lower	Mudflat
NoPhoto	Winter	225.6 ± 133.4	190.9 ± 63.1	60.3 ± 68.1	70.4 ± 110.3
	Spring	65.1 ± 38	80.9 ± 26.2	36.6 ± 38.9	26.9 ± 39.6
	Summer	54.9 ± 32.5	67.5 ± 21.6	24.5 ± 30	21.7 ± 33.3
	Fall	96.5 ± 61.9	114.7 ± 38.9	43.1 ± 52.8	37.5 ± 58.3
	Annual	110.1 ± 102.5	113.1 ± 62.6	41 ± 51.3	38.9 ± 68
Photo	Winter	189.4 ± 109.3	148.4 ± 48.5	38.1 ± 52.5	55.5 ± 92.1
	Spring	57.8 ± 35.9	69.5 ± 26.1	22.2 ± 30.3	22.1 ± 35.1
	Summer	48.1 ± 29.8	54.3 ± 20.1	12.3 ± 20	16.9 ± 27.4
	Fall	88.3 ± 57.3	102.1 ± 35.9	24 ± 42.2	31.7 ± 52
	Annual	95.5 ± 86	93.3 ± 49.7	24.1 ± 32.2	31.4 ± 56.2

The effect of photoinhibition on MPB primary production

In both the NoPhoto and the Photo runs, the mean simulated annual PP was higher on the upper (195.6 ± 88.2 and 126.1 ± 48.5 g C m^{-2} in the NoPhoto and the Photo runs, respectively) and middle shores (172.2 ± 38 and 102.5 ± 22.3 g C m^{-2} in the NoPhoto and the Photo runs, respectively) than on the lower shore (47.8 ± 57.2 and 21.9 ± 33.2 g C m^{-2} in the NoPhoto and the Photo runs, respectively) (Table. 19 and Fig. 43ab).

Table 19: Mean annual PP (± standard deviation) (g C m^{-2}) in 2015.

Simulation	Upper	Middle	Lower	Mudflat
NoPhoto	195.6 ± 88.2	172.2 ± 38	47.8 ± 57.2	133.6 ± 93.5
Photo	126.1 ± 48.5	102.5 ± 22.3	21.9 ± 33.2	79.1 ± 58.6

In the Photo run, the simulated PP was lower than in the NoPhoto run in all seasons and levels of the mudflat (Fig. 43 and Table 20). As in the NoPhoto run, PP decreased seaward in the Photo run. The highest annual integrated PP was simulated on the upper shore in both the NoPhoto (2.33 Gg C) and Photo runs (1.43 Gg C) (Table 20). The upper and middle shores accounted for ~ 90 % of the annual PP in both runs (Table 20). When photoinhibition was introduced in the model, the decrease of PP on the upper shore (-0.9 Gg C, annually) was higher than the decrease on the middle and lower shores (-0.83 and -0.31 Gg C, annually; Table 20). Nevertheless, relatively to the initial PP simulated in the NoPhoto run, the highest decrease occurred on the lower shore (-54 %) compared to the upper and middle shores (-39 and -40 %, annually; Table 20).

In the Photo run, the highest PP was simulated in winter and fall, while it was simulated in spring in the NoPhoto run (Fig. 43a). In both runs, the simulated PP was the lowest in summer (Fig. 43ab and Table 20). In the NoPhoto run, the highest integrated PP was simulated in spring (Fig. 43a and Table 20). The annual PP in the Photo run was the highest in fall over the whole mudflat (0.85 Gg C annually; Fig. 43b and Table 20). When photoinhibition was introduced in the model, the highest and the lowest decreases of PP over the whole mudflat occurred in spring (-0.69 Gg C) and fall (-0.38 Gg C), respectively (Table 20). Relatively to the initial PP simulated in the NoPhoto run, the decrease of PP at the whole mudflat scale was the highest in spring and summer (-49 %) and the lowest in fall (-31 %; Table 20).

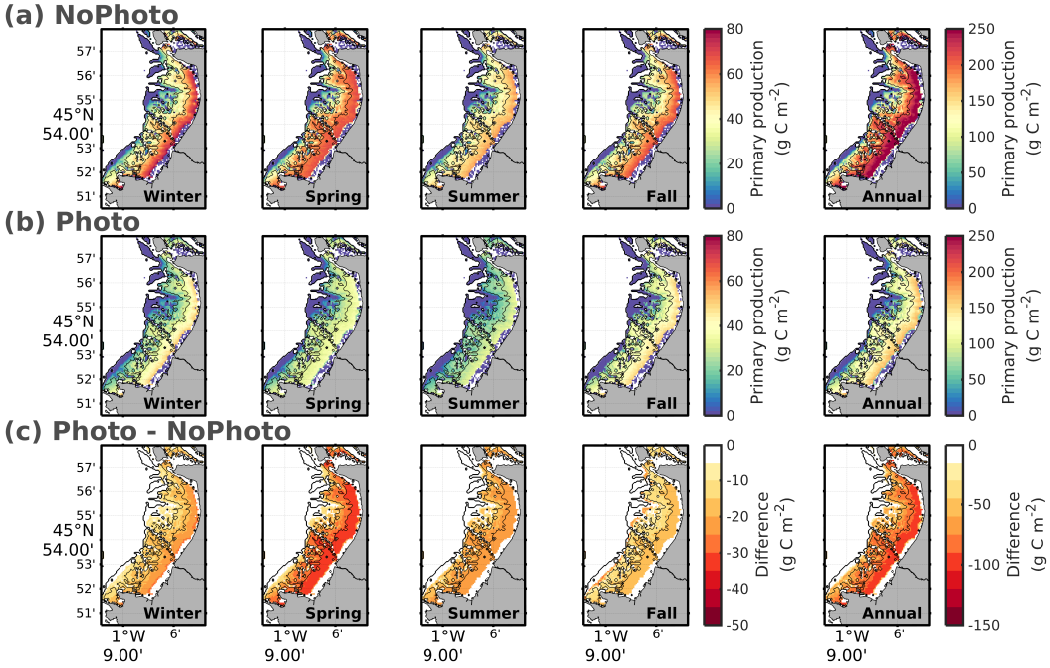

Figure 43: Map of annual and seasonal MPB PP (mg C m^{-2}) **(a)** without photoinhibition (NoPhoto), **(b)** with photoinhibition (Photo) and, **(c)** the difference between the Photo and the NoPhoto simulations. The black contour lines indicate the three tidal levels.

I_{opt} in the P-I model of Platt et al. (1980) set the irradiance threshold beyond which MPB photosynthesis is photoinhibited. The simulated I_{opt} was spatially homogeneous over the mudflat (Fig. 44a and Table 21). It decreased from winter (385.7 ± 189.2 µmol photons m^{-2} s^{-1}) to fall (134.1 ± 24.1 µmol photons m^{-2} s^{-1}), when it reached its seasonal minimum (Table 21). The photoinhibition span *i.e.* the duration of photoinhibition ($I > I_{opt}$) relative to the daytime emersion duration increased from the upper (71.2 % annually) to the lower shore (78.2 %; Fig. 44b and Table 21). The photoinhibition span was the lowest in winter (55.2 %) and the highest in summer (85.2 %) over the whole

Table 20: Spatially and seasonally-integrated PP (Gg C) according to the tidal levels in the Photo and the NoPhoto simulations in 2015.

Simulation	Season	Upper	Middle	Lower	Mudflat
NoPhoto	Winter	0.63	0.47	0.15	1.25
	Spring	0.64	0.61	0.16	1.41
	Summer	0.49	0.46	0.12	1.07
	Fall	0.57	0.51	0.14	1.23
	Annual	2.33	2.05	0.57	4.96
Photo	Winter	0.41	0.30	0.08	0.79
	Spring	0.33	0.31	0.07	0.72
	Summer	0.27	0.24	0.04	0.55
	Fall	0.41	0.37	0.07	0.85
	Annual	1.43	1.22	0.26	2.91
Difference (Gg C)	Winter	-0.22	-0.17	-0.07	-0.46
	Spring	-0.31	-0.3	-0.09	-0.69
	Summer	-0.22	-0.22	-0.08	-0.52
	Fall	-0.16	-0.14	-0.07	-0.38
	Annual	-0.9	-0.83	-0.31	-2.05
Difference (%)	Winter	-34	-36	-47	-37
	Spring	-48	-49	-56	-49
	Summer	-45	-48	-67	-49
	Fall	-28	-27	-50	-31
	Annual	-39	-40	-54	-41

mudflat (Table 21). Annually, the mudflat MPB PP was photoinhibited 72.3 % of the daytime emersion periods (Fig. 44b and Table 21).

DISCUSSION

Spatio-temporal variability of MPB primary production

The MPB PP is the highest on the upper and middle shores in the NoPhoto and Photo runs due to more frequent, longer emersion periods and higher MPB biomass than on the lower shore. On the upper and middle shores, the MPB PP varies from 125 to 250 g C m^{-2} yr^{-1} and from 80 to 150 g C m^{-2} yr^{-1} in the NoPhoto and the Photo runs, respectively and represents 90 % of the simulated annual MPB PP over the whole the mudflat. Annual MPB PP

Table 21: Seasonal mean (± standard deviation) of I_{opt} (µmol photons m^{-2} s^{-1}) and photoinhibition span (%) during daytime emersion periods according to the level of the mudflat in 2015.

	Season	Upper	Middle	Lower	Mudflat
I_{opt} (µmol photons m^{-2} s^{-1})	Winter	380.4 ± 186.7	378.7 ± 186.7	375.6 ± 192.3	385.7 ± 189.2
	Spring	353.4 ± 158.5	359.2 ± 159.1	366.3 ± 163.8	362.8 ± 157
	Summer	145.4 ± 49.4	144.3 ± 49.4	139.4 ± 49.3	149.7 ± 47.9
	Fall	134.3 ± 24.1	133.9 ± 24.7	132.3 ± 24.8	134.1 ± 24.1
	Annual	256.4 ± 169.6	256.8 ± 170.5	255.2 ± 174.7	261.2 ± 171.3
Photoinhibition span (%)	Winter	53.3	58.1	67.1	55.2
	Spring	67.1	66.5	69.8	67.2
	Summer	84	85.7	89.9	85.2
	Fall	77.5	79.3	84.3	78.7
	Annual	71.2	73	78.2	72.3

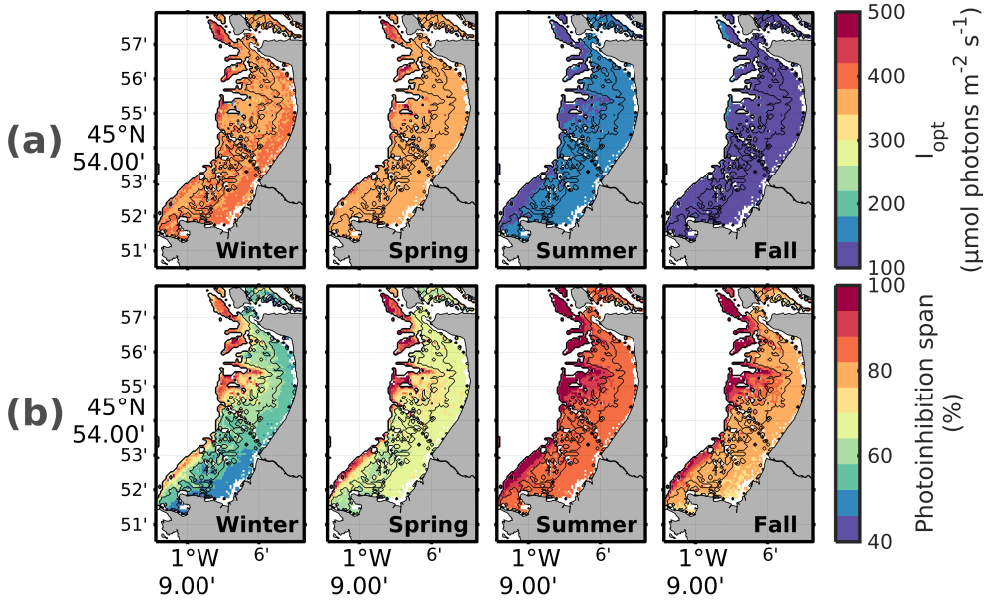

Figure 44: Seasonal **(a)** mean I_{opt} (µmol photons m^{-2} s^{-1}) and, **(b)** photoinhibition span (when PAR > I_{opt} during daytime emersion periods; % of the cumulated duration of emersion periods). The black contour lines indicate the three tidal levels.

simulated in both runs compares to simulations run for the same mudflat in 2008 (45°54'50"N, 01° 05'25"W; 127.3 g C m^{-2} yr^{-1}; Savelli et al., 2018) and 2012 (151.2 and 140.5 g C m^{-2} yr^{-1}; see Chapter 4). The simulated annual MPB PP in the present study is also in the range of MPB PP measurements made across other European mudflats listed by Underwood and Kromkamp (142 ± 82 g C m^{-2} yr^{-1}; 1999).

On a sandflat of the Bay of Paranaguá in Brazil, Fonseca et al. (2008) also measured with benthic chambers higher PP rates in the upper and middle shores (1.9 - 2.1 g C m^{-2} d^{-1} and 1.3 - 2.2 g C m^{-2} d^{-1}, respectively) compared to the lower shore (0.24 - 0.27 g C m^{-2} d^{-1}). Cook et al. (2004) measured CO_2 fluxes at the air-sediment interface of two tidal levels of a mudflat located in Tasmania. The uptake of inorganic carbon (total CO_2) at the benthic interface was greater in the upper shore (up to 15 000 µmol m^{-2} h^1) than in the lower shore (up to 6 000 µmol m^{-2} h^1), suggesting a higher benthic PP on the upper zone.

In the NoPhoto run, MPB PP reaches a seasonal peak in spring with a total of 1.41 Gg C (~ 30 % of the annual mudflat PP) and was low during summer (1.07 Gg C). Such a seasonality characterised by a spring bloom and a summer depression is consistent with the reported seasonal cycle of MPB PP at the study site (Cariou-Le Gall and Blanchard, 1995; Savelli et al., 2018). MST close

to the optimum for MPB growth and increasing solar irradiance trigger high rates of MPB PP and thus, accumulation of MPB biomass in the sediment in spring (Savelli et al., 2018). According to the authors, thermoinhibition of MPB PP due to high MST combined with a moderate but sustained grazing pressure is responsible to the low MPB PP and biomass in summer.

The simulated PAR and MST compare reasonably to time-coincident observations made on the same mudflat (45°53'20.87"N; 1°7'54.37"O). The model-data discrepancies result from the comparison of 30-sec frequency PAR and MST measurements with simulated PAR and MST constrained by 1-hour frequency meteorological forcings. Second, single-point measurements were compared to model outputs extracted at the corresponding horizontal 100 m × 100 m grid cell. The coarse horizontal resolution (2.5 km) of the meteorological model contributes also to simulation inaccuracies. Nevertheless, at the seasonal scale, the impact of such inaccuracies may be limited as the model succeeds to capture the mean MST and PAR conditions in 2015. The relative agreement of simulated MST and PAR with *in situ* measurements along with the consistent simulated annual PP compared to literature suggests that the model can resolve with confidence the spatio-temporal variability of MPB PP.

Spatial variability of photoinhibition

Until now, the MPB photoinhibition was only detected from *in situ* or laboratory single-point measurements (*e.g.* Serôdio et al., 2008; Serôdio et al., 2012). The present modelling study draws the first map and estimate of potential MPB photoinhibition over the whole mudflat. The mudflat can be divided into two systems: the upper and middle shores together (high light, high production, high biomass) and the lower shore (low light, low production, low biomass). Light has been previously identified as the key driver in MPB PP differences on a transversal transect on mudflats (Underwood and Kromkamp, 1999). The upper and middle shores are more exposed to light as they emerge longer and more frequently. Consequently, the upper and middle shores are more productive than the lower shore whose PP is limited to shorter periods of emersion. High tidal heights exhibit favourable light conditions in terms of photo-period (Underwood and Kromkamp, 1999). In the model, the photoinhibition span is relatively low when compared to the cumulated emersion duration on the upper shore. In contrast, the emersion time on the lower shore is shorter and less frequent as it emerges only during spring tides, at noon when the daily amplitude of solar irradiance is maximal. Consequently, in response to the exposure at high light levels, photoinhibition occurs during a large part of the emersion periods on the lower shore (78.2 % of the emersion periods, annually). Nevertheless, the high frequency of relatively short periods of photoinhibition on the upper shore drives the highest decrease of MPB PP when photoinhibition is introduced in the model (-0.9 Gg C, annually). On the lower shore, with

photoinhibition, the MPB PP decreases by 0.31 Gg C. Relatively to the initial low PP without photoinhibition on the lower shore, such a decline represents a decrease by 54 % of MPB PP on the lower shore. Our results suggest therefore that the effect of photoinhibition on MPB PP is higher on the upper shore than on the lower shore. However, the lower shore might be more sensitive to photoinhibition due to its low MPB biomass, PP and its emersion periods restricted to high light levels. In the field, this pattern may be tempered or enhanced by the capacity of cells to cope with high light levels (photoacclimation, photoprotective adaptations).

The MPB photoinhibition was only detected from *in situ* or laboratory single-point measurements (*e.g.* Serôdio et al., 2008; Serôdio et al., 2012). The present modelling study draws the first map of potential MPB photoinhibition over the whole mudflat. Similarly to our results, macroalgae studies investigating the spatial variability of photoinhibition also reported the higher effect of photoinhibition on the highly illuminated upper shore compared to the lower shore (Stengel and Dring, 1998; Gómez et al., 2004). However, macroalgae individuals from the upper shore can exhibit a higher recovery capacity than individuals from the lower shore, which tempers the photoinhibitory effect on photosynthesis (Hanelt et al., 1993). In the model, the MPB recovery after light stress is not accounted for and MPB is always fully operational as soon as light reaches non-inhibitory levels. In addition, the photoacclimation state might change in space over the mudflat with individuals on the upper shore more able to cope with high light levels as suggested for macroalgae (Hanelt et al., 1993). In the present study, MPB photoacclimation is assumed spatially homogeneous over the mudflat but high light acclimated MPB cells on the upper shore could have tempered the effect of photoinhibition. In addition, the spatial change in the MPB assemblage and thus in the capacity of tidal level-autochthonous species to cope with high light levels at different tidal height was not considered in the model. In the Severn Estuary (UK), non-motile epipsammon, which is more physiologically adapted to high light levels is more distributed on the lower shore than motile epipelic species, which are dominant on the upper and middle shores (Underwood, 1994). Finally, in the model, the use of photosynthetic parameters (α and β) estimated on MPB cells sampled on the upper shore of the Aiguillon mudflat might translate into a good estimation of photoacclimation and photoinhibition on the upper shore but requires to remain cautious when applied on the middle and lower shores.

Temporal variability of photoinhibition

The simulated effect of photoinhibition is the highest during spring-summer over the whole mudflat. Light levels are low during winter-fall and increase during spring until they reach their maximal amplitude in summer. In addition, spring tides in the study area drive longer exposure duration and coin-

cide with the maximal daily amplitude of solar irradiance at noon, promoting MPB photoinhibition over the whole mudflat. The lower shore is particularly exposed as it emerges only during spring tides. During neap tides, two low tides with a small tidal range occur early and late in the day when light levels are too low to induce photoinhibition. Nevertheless, low light levels during neap tides emersion periods limit also the MPB growth as showed previously by Savelli et al. (2018). This is in agreement with measurements made by Kwon et al. (2014) on the Hwaseong mudflat in South Korea. The authors observed lower MPB PP at low light levels during neap tides compared to spring tides. Consequently, spring tides conditions at our study site are more optimal for MPB growth than neap tides conditions even if photoinhibitory light levels are more frequently reached during spring tides.

The photosynthetic parameters were fitted on P-I data of Pniewski et al. (2015) measured on MPB cells sampled on the Aiguillon mudflat, north the Bay of Marennes-Oléron. The light saturation parameter (I_k) indicates the irradiance at which photosynthesis switches from light reactions (light absorption and photochemical energy conversion) to dark reactions (reductant utilisation) (Sakshaug et al., 1997). It was reported to vary seasonally for MPB (Blanchard and Cariou-Le Gall, 1994; Barranguet et al., 1998; Light and Beardall, 2001; Pniewski et al., 2015; Barnett et al., 2015). The light saturation parameter increases under high light levels in summer and decreases at low or moderate irradiance in winter, spring and fall (Sakshaug et al., 1997). The model parametrisation with a low light saturation parameter in spring and fall suggests low light acclimated MPB cells at these seasons. In summer, with a high light saturation parameter in the model, the MPB cells are high light acclimated and can cope with relatively high light levels. In addition, the photoacclimation status of MPB cells determines their light preferendum and their phototaxis (Ezequiel et al., 2015). Therefore, low light acclimated cells avoid photoinhibitory high light levels. Considering such behavioural mechanisms could have limit the high photoinhibition effect on the spring low light acclimated cells in the model.

In addition, during winter, the cells increase their Chl *a* content and reduce their C:Chl *a* ratio in order to make the most of low light levels (MacIntyre et al., 2002; Brunet et al., 2011). On the contrary, in summer, the increasing irradiance and day length lead to a decrease of the cell Chl *a* content and thus to a higher C:Chl *a* ratio (MacIntyre et al., 2002; Brunet et al., 2011). Consequently, high light acclimated cells have a lower carbon-specific rates of photosynthesis ($P_s^b \times Chla : C$) at sub-saturating irradiance compared to low light acclimated cells (MacIntyre et al., 2002). Therefore, the consideration in the model of a variable C:Chl *a* ratio as a function of light (see formulation in Savelli et al., 2018) can moderate photoinhibition of the carbon-specific rates of photosynthesis of low light acclimated cells at saturating irradiance.

The effect of mud surface temperature on photoinhibition

The introduction of photoinhibition detrimental effects adds to the already in play thermoinhibition of MPB PP in the model (Savelli et al., 2018). With high MST and desiccation driven by high solar irradiance and long exposure, photo- and thermoinhibition combine particularly on the upper shore and in spring-summer (Underwood, 1994; Guarini et al., 1997). In addition, temperature higher than the optimal temperature for MPB growth leads to a decrease of the photosynthetic capacity of microalgae (Salleh and McMinn, 2011; Defew et al., 2004) due to the de-activation of the carbon fixation enzymes such as RUBISCO (MacIntyre et al., 1997). Furthermore, the photoprotective NPQ physiological mechanism was shown to vary with temperature and some benthic diatoms species have a greater capacity to cope with high light levels via NPQ at high temperature (Salleh and McMinn, 2011). Damages to PSII photosynthetic apparatus and its structuring D1 protein can be caused by high light levels. The rate of D1 reparation process is temperature dependant and decreases with high temperature (Campbell et al., 2006). The exposure of MPB cells to high temperature could therefore alter the D1 reparation process and thus the subsequent recovery of the PSII system (Jensen and Knutsen, 1993; Long et al., 1994). Finally, behavioural photoprotective mechanisms of MPB cells can be altered by MST. High MST (> 35 °C) reduce the motility of MPB cells and thus their negative phototaxic capacity under high irradiance to avoid photoinhibition (Cohn et al., 2003; Laviale et al., 2015). The detrimental effect of high MST on cells motility is not accounted for in the model and could be implicitly represented through temperature-related migration capacity of cells.

CONCLUSIONS

This study is a first attempt to simulate the potential effect of the MPB photoinhibition on PP and its spatial and temporal variability at the scale of a whole mudflat. We numerically induce photoinhibition of MPB over the whole mudflat during one year. In the model, behavioural and physiological photoprotective mechanisms are not considered and MPB cells can therefore not avoid or dissipate harmful light levels. The model maps MPB PP under the potential effect of photoinhibition at the mudflat scale. Even if the simulated photoinhibition effect on MPB PP might be overestimated in regards to the absence of photoprotective mechanisms, the 3D physical-biological coupled model provides key findings about the spatial and temporal variability of MPB PP and its potential response to photoinhibition:

- The total of light reaching the mud surface is higher on the upper shore (two to three -fold higher than the middle and lower shores, respectively) as it emerges more frequently (almost twice every day) and longer (6.8 h in average) than the lower shore. The seasonal maximal amplitude of

irradiance drives high amount of light at the surface of the whole mudflat during spring-summer (70 % of the total annual irradiance reaching the mud surface).

- With or without photoinhibition, the annual MPB PP is higher on the upper shore (195.6 ± 88.2 g C m^{-2} and 126.1 ± 48.5 g C m^{-2} with and without photoinhibition, respectively) than on the lower shore (47.8 ± 57.2 g C m^{-2} and 21.9 ± 33.2 g C m^{-2} with and without photoinhibition, respectively).

- The quantitative difference of MPB PP under the effect of photoinhibition is higher on the upper shore (- 0.9 Gg C yr^{-1}) than on the lower shore (- 0.3 Gg C yr^{-1}). However, the lower shore might be more sensitive to photoinhibition due to its low MPB biomass, PP and its emersion periods restricted to high light levels.

- Without photoinhibition, MPB PP reaches its seasonal maximum and minimum during spring and summer, respectively. The simulated seasonality of MPB PP without photoinhibition compares to the reported seasonal cycle at the study site. The introduction of photoinhibition fades this consistent seasonality as the decrease by 50 % of MPB primary production in spring and summer results in a maximum of PP now reached in fall.

As MPB photoinhibition has been rarely observed *in situ*, the subsequent detrimental effect was not always considered in the P-I models used in MPB PP predictive models (*e.g.* Barranguet et al., 1998; Uthicke and Klumpp, 1998; Dizon and Yap, 1999; Serôdio and Catarino, 2000; Guarini et al., 2000; Migné et al., 2004; Denis et al., 2012; Kwon et al., 2014, 2018; Rakotomalala et al., 2019). The MPB photoprotective mechanisms are generally considered sufficient to exclude photoinhibition. The definition of a MPB PP model that takes into account such fine physiological processes and their regulation by temperature could lead to more realistic predictions of MPB PP. In the light of the model developed by Rakotomalala et al. (2019), in which MPB cells migrate vertically according to their C/N cell quota, a vertical migration scheme that take into account the light dose of MPB cells could be used to track the light history of the cells and modulate their recovery from stressful irradiance. The present work also highlights the need of a spatial investigation of photoinhibition to better understand the dynamics of MPB PP and biomass on intertidal mudflats. The estimation of the photosynthetic parameters on a transversal transect would allow us to detect spatial variations of potential photoinhibition according to tidal levels and to better parametrise physical-biological coupled models.

CHAPTER VI

COUPLING SPACE REMOTE SENSING AND COUPLED PHYSICAL-BIOLOGICAL MODELLING FOR MAPPING MICROPHYTOBENTHOS PRIMARY PRODUCTION

As suggested in the previous chapter, the tri-dimensional physical-biological coupled model is a relevant tool to infer at the appropriate spatial and temporal scale on MPB dynamics. In Chapter 6, we develop a MPB primary production algorithm that combines laboratory measurements, satellite data and time-coincident light, mud surface temperature and tidal height data simulated by the high-resolution physical-biological coupled 3D model set up in Chapter 5. PP predicted by the algorithm are consistent with PP measured *in situ* in the same periods. The algorithm presents interesting skills to predict PP on intertidal mudflats mostly composed by fine cohesive sediments dominated by epipelic diatoms and could be applied for other similar environments. The accurate assessment of MPB PP in a highly variable environment is a challenge in a perspective of quantifying MPB primary production over large mudflats from a synoptic to inter-annual time scale.

6

COUPLING SPACE REMOTE SENSING AND COUPLED PHYSICAL-BIOLOGICAL MODELLING FOR MAPPING MICROPHYTOBENTHOS GROSS PRIMARY PRODUCTION (GPP)

ABSTRACT

Microphytobenthos (MPB) at the sediment surface of intertidal mudflats are known to show a high spatial and temporal variability in response to the biotic and abiotic conditions prevailing at the mud surface. It makes monitoring of MPB primary production (PP) difficult over the long term and at large spatial scale. In the previous Chapters, we showed that coupled physical-biological modelling is relevant for predicting MPB PP and biomass at the mudflat scale on a seasonal basis. We also highlighted the benefit of using remote sensing for monitoring MPB from space. However, the remote sensing of MPB PP is only at its beginning at the scale of a whole mudflat.

Compared to the PP simulated by the regional physical-biological model presented in Chapter 5, the PP derived from the remote sensing algorithm is more consistent with measured PP estimates. Introducing photoinhibition in the model or parametrising the photosynthetic rate to get close to the observed biomass-specific PP leads to a better agreement between the simulated PP rates and measured estimates. Setting the photosynthetic capacity in both the numerical model and remote sensing algorithm might be a challenge in a perspective of mapping MPB PP over large mudflats from a synoptic to inter-annual time scale.

This chapter will be submitted as two articles. The first article on the GPP-algorithm will be submitted in the journal Frontiers (Méléder et al., in prep) and the second article on the accurate setting of the MPB photosynthetic capacity in predictive MPB PP models will be submitted in a journal which has not yet been determined.

Acronyms:
GPP: *Gross Primary Production*
MPB: *Microphytobenthos*
MST: *Mud Surface Temperature*
NDVI: *Normalised Difference Vegetation Index*
PAR: *Photosynthetically Active Radiation*
P-I: *Production-Irradiance*
PP: *Primary Production*

INTRODUCTION

Benthic microalgae or microphytobenthos (MPB) inhabiting the sediment surface sustain a high biological production in intertidal mudflats (MacIntyre et al., 1996; Underwood and Kromkamp, 1999). The MPB assemblage is mainly dominated by diatoms that form a dense biofilm at the sediment surface during daytime low tides (MacIntyre et al., 1996; Underwood and Kromkamp, 1999). As the main primary producer on intertidal mudflats, MPB are of key importance for higher trophic levels from benthic fauna to birds (Herman et al., 2000; Kang et al., 2006; Jardine et al., 2015) and for pelagic organisms when MPB are resuspended by tides and waves (Perissinotto et al., 2003; Krumme et al., 2008). With a global annual primary production estimated to ~ 500 million tons of carbon (Cahoon, 1999), MPB also participate to the Blue Carbon (Otani and

Endo, 2019). However, their contribution to the global carbon budget remains unknown, but is likely to be high.

The MPB spatial and temporal distribution is highly variable on mudflats as it is driven by highly variable physical (light, mud surface temperature (MST), tides, waves, current) and biological (grazing, biostabilisation, bioturbation) factors. Such a variability impedes an accurate and robust assessment of the role of MPB at the scale of the whole mudflat ecosystem and of its contribution to the global carbon cycle. MPB PP and biomass measurements are usually limited to single-point sampling (*e.g.* Orvain et al., 2014a; Pniewski et al., 2015; Cartaxana et al., 2015; Vieira et al., 2013). This approach succeeds in capturing the MPB temporal dynamics but is rapidly limited when dealing with spatial and temporal variations of MPB PP and biomass at the scale of the entire mudflat. Only a few studies resolved this MPB variability, as time and important logistical resources are required to meet this goal (*e.g.* Guarini et al., 1998; Ubertini et al., 2012).

Jobson et al. (1980) initiated the use of remote sensing to assess the MPB biomass from a tower-mounted sensor designed to scan a mudflat of South Carolina (USA). Since then, airborne and space remote sensing methods were increasingly developed and more widely used in MPB studies (*e.g.* Méléder et al., 2003a; Brito et al., 2013; Benyoucef et al., 2014; Daggers et al., 2018). Remote sensing data can cover large spatial scales (~ from one to a few hundred meters) and multispectral broadband sensors promise high quality data to map MPB biomass and PP over the whole mudflats. Some efforts would hence be required to upscale *in situ* measurements of MPB PP to the remote sensing scales. Daggers et al. (2018) were the first study to couple *in situ* measurements, satellite remote sensing data and tidal heights to map MPB spring PP at the scale of the Oosterschelde and Westerschelde estuaries (The Netherlands). However, the authors used air temperature to compute the MPB photosynthetic capacity and not MST that directly constrains the MPB growth. The methods they used to convert chlorophyll fluorometry data into MPB PP expressed in carbon first and then Normalised Difference Vegetation Index (NDVI) into chlorophyll *a* concentration can also be a source of uncertainty.

In order to minimise the uncertainty, we associate in a GPP-algorithm laboratory measurements with 3 NDVI scenes derived from remotely-sensed data and with time coincident light, temperature and tidal height data simulated by a tri-dimensional (3D) high resolution physical-biological coupled model. The seasonal adjustment of photosynthetic parameters used in the GPP-algorithm is obtained from fitting Production-Irradiance (P-I) curves on laboratory measurements expressed in NDVI-specific PP rates. In the paper, we first compare data of the physical environment (light, temperature) prevailing at the date of the *in situ* measurements and satellite sensor acquisition. Second, we compare the fitted data obtained using five P-I models widely used in the literature with the laboratory measurements. Finally, we map the MPB PP in winter, spring

and summer using the P-I models of Platt et al. (1980) and Eilers and Peeters (1988). The ability of the GPP-algorithm to map MPB PP at a mudflat scale and to provide new insights on the role played by MPB in the coastal carbon cycle is discussed.

MATERIAL AND METHODS

Study site

The study site is located in the Pertuis Charentais Sea, which is a shallow semi-enclosed sea located on the French Atlantic coast (Fig. 45). The tidal regime is semi-diurnal and macrotidal. The tidal range reaches up to ~ 6 m during spring tides. We focused on the Brouage mudflat, which extends over 42 km^2 in the Southeastern part of the area. The mudflat sediment is composed of very fine and cohesive grains (median grain size 17 µm and 85 % of grains with a diameter < 63 µm; Bocher et al., 2007) distributed on a gentle slope (~ 1/1000; Le Hir et al., 2000). The station for field campaign and sediment sampling was located at the "Merignac" site (Fig. 45, 45°53'20.87"N; 1°7'54.37"W).

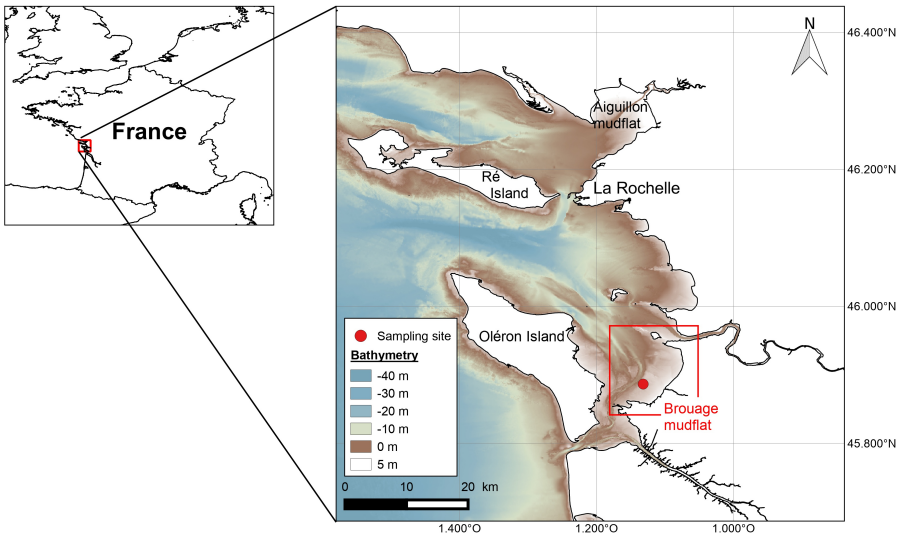

Figure 45: Bathymetry of the model domain covering the Pertuis Charentais Sea (source: SHOM) and location of the main intertidal mudflats. The study site is represented by a red full point.

Observations

In situ data

Three periods were selected for field campaigns and sediment sampling: March, with the highest value of MPB biomass, May, corresponding to medium value of MPB biomass and July, with the lowest value (Savelli et al., 2018; Méléder et al., in prep). Field campaigns were planed during spring tides and daytime low tides, on 5-6 May 2015, 2-3 July 2015 and 5 March 2018 for *in situ* measurements and sediment sampling for laboratory experiments. Carbon fluxes for estimation of the PP at the air-sediment interface were measured using benthic chambers. The CO_2 concentration was measured in the chambers continuously, over a period of 20 to 30 min using an infrared gas analyser (IRGA). A translucent chamber was used to measure net flow (= net primary production, NPP), including the flow due to photosynthesis and that due to respiration. A dark chamber was used to measure only the flow due to respiration (= Resp). Light and dark incubations were performed successively. Due to the duration of the tidal cycle, only 4 incubations were done per day: 2 lights and 2 darks. The difference between these fluxes gives the gross primary production (GPP) expressed in mg C m^{-2} h^{-1} (Eq. 45, Migné et al., 2002):

$$GPP = NPP + Resp \tag{45}$$

where Resp is negative.

In the aim to link GPP to the MPB biomass, reflectance (ρ) was measured near to the benthic chambers using a JAZ (OceanOptics®) spectroradiometer (200-1100 nm, sampling: 0.3 nm, spectral resolution: 0.3-10 nm full width at half maximum) to calculated the MPB-specific NDVI index (Eq. 46). Because the spectral resolution of this detector was higher than a multispectral one onboard a satellite, the red reflectance, ρ(R) was considered as the averaged value of data at 675 nm ± 3 nm and the NIR reflectance, ρ(NIR), as the average at 750 nm ± 3 nm (Méléder et al., 2003a, 2010). MPB-specific NDVI measured during the same period of NPP (*e.g.* during light incubations) were used to standardised GPP values to be expressed in mg C $(NDVI)^{-1}$ m^{-2} h^{-1} .

$$NDVI = \frac{\rho(NIR) - \rho(R)}{\rho(NIR) + \rho(R)} \tag{46}$$

Synchronously, incident photosynthetically active radiation (400 to 700 nm; PAR, µmol photons m^{-2} s^{-1}) and temperature (°C) were measured near to the chambers at the sediment surface with a 30-sec frequency.

In parallel to the NDVI measurements during the whole low tide, biomass and physiological status were surveyed. The biomass was estimated continuously by Chl *a* content in the first 250 µm of sediment by the "crème brulée" methodology sampling (Laviale et al., 2015). After freeze-drying of the sediment discs, pigments were extracted in a cold mixture (4°C) of 90 % methanol/0.2M

ammonium acetate (90/10 vol/vol) and 10 % ethyl acetate. Injection, High-Performance Liquid Chromatography (HPLC) device (Hitachi Lachrom Elite, Tokyo, Japan), pigment identification and quantification is detailed in Barnett et al. (2015) and Roy et al. (2011). Chl *a* amount was normalised to the sampled surface (1.5 cm^2) to be expressed in mg Chl *a* m^{-2}.

Laboratory experiments: P-I curves

During the three field campaigns, the upper-layer (~ the top first cm) of sediment was collected to be brought back to the laboratory. There, the mud was cleaned of the fauna by sieving through a 500 µm mesh. The sediment was homogenised by thoroughly mixing and was spread as plane layer in nine plastic trays of 4 cm-deep (Serôdio et al., 2012). A water layer was added for the night and sediment was left undisturbed overnight. The next morning, the water layer was manually removed by a syringe 3 hours before low tide and trays were kept in shadow at ~ 22 °C. Experimentation started two hours before low tide, when biofilm dark coloured the sediment surface. It consisted to light one of the nine trays with LEDs panel (LED Light SL 3500-E, Photo System Instrument, Czech Republic) during 30 min at controlled temperature (22 °C). During the 30 min, C flux was estimated by translucent benthic chambers. Light intensities used for the three periods varied from 5 to 2 200 µmol photons m^{-2} s^{-1}. For each intensity, a new tray of sediment was used. After the 30 min of lightening, respiration flux was measured using dark benthic chamber. GPP for each intensity was calculated using the flux from dark (= Resp) and translucent (NPP) chambers as done *in situ* (Eq. 45) and expressed by NDVI (mg C $(NDVI)^{-1}$ m^{-2} h^{-1}).

For the three periods, laboratory measurements of photosynthetic rate (P^b, mg C $(NDVI)^{-1}$ m^{-2} h^{-1}) were fitted using several P-I models: Platt et al. (1980), Eilers and Peeters (1988), Steele (1962), Platt and Jassby (1976) and modified Platt and Jassby (1976). The modified Platt and Jassby (1976) P-I model is as follow:

$$P^b = P^b_{max} \times \tanh\left(\frac{\alpha I}{P^b_{max}}\right) \times \left[1 - \tanh\left(\frac{\beta I}{P^b_{max}}\right)\right], \tag{47}$$

where P^b_{max} is the photosynthetic capacity (mg C $(NDVI)^{-1}$ m^{-2} h^{-1}), I is the PAR (µmol photons m^{-2} s^{-1}), α is the initial slope (mg C $(NDVI)^{-1}$ m^{-2} h^{-1} (µmol photons m^{-2} s^{-1})$^{-1}$) and β is the photoinhibition parameter (mg C $(NDVI)^{-1}$ m^{-2} h^{-1} (µmol photons m^{-2} s^{-1})$^{-1}$).

The differential evolution algorithm (DE) implemented in the R package "DEoptim" (Ardia et al., 2016) was used to minimise the difference between the predicted and observed photosynthetic rate to obtain the photosynthetic parameters of the five P-I models. The DE algorithm does not require arbitrary initial parameter values which can result in errors in optimisation of light-response models (Chen et al., 2016). Moreover, the parameters values were explored

within a range of values given in Table 23 based on graphical features of P-I data (Fig. 50).

Remote sensing data

Multispectral images for GPP mapping were selected from SPOT, Landsat and Pleiades archives following three acquisition criteria: 1) acquisition day the closest to the field campaign day; 2) acquisition time the closest to spring low tide, when mudflats were the most exposed; 3) acquisition under cloud-free conditions ($< 10\%$) with an almost zenithal sun. These criteria allowed to select three images from SPOT and Pleiades satellites: one per field campaign (Table 22). Images were atmospherically corrected and converted into surface reflectance with FLAASH correction (Fast Line of sight Atmospheric Analysis of Spectral Hypercubes), using ENVI software and MODTRAN4 transfer codes for the atmospheric corrections method (Matthews et al., 2000). For coherence within the images, the same FLAASH parameters were applied: US atmospheric model, 40 km initial visibility and maritime aerosol model. The images were registered in the WGS 84 UTM 30N coordinate system. Finally, the MPB-specific NDVI was then calculated from surface reflectance following Eq. (46) to estimate the horizontal distribution of the MPB biomass (*e.g.* Méléder et al., 2003a; Benyoucef et al., 2014; Echappé et al., 2018). These maps are used as an input in the GPP-algorithm (Fig. 46).

The lower horizontal resolution of the SPOT 6 image diluted the MPB biomass into larger pixels and resulted to lower MPB-specific NDVI compared to Pleaides images. Consequently, when the MPB-specific NDVI was compared between SPOT 6 and Pleaides images, it was normalised by the respective MPB-specific NDVI maximum (0.3 and 0.4 for SPOT 6 and Pleaides, respectively).

MARS-3D modelling system

The tidal height and photosynthetic available irradiance (PAR) were simulated over the mudflat by the 3D hydrodynamical Model for Applications at Regional Scale (MARS-3D). The bathymetry was extracted from the model numerical grid. The Navier-Stokes primitive equations were solved under assumptions of Boussinesq approximation, hydrostatic equilibrium and incompressibility (Blumberg and Mellor, 1987; Lazure and Dumas, 2008). The numerical domain of the Pertuis Charentais Sea consisted of 100 m $\times$ 100 m grid cells discretised over 20 sigma-levels (Fig. 45). The MARS-3D model is fully detailed in Lazure and Dumas (2008). The meteorological forcings (*i.e.* 10-m wind speed, 2-m air temperature and relative humidity, atmospheric pressure at sea level, nebulosity and solar fluxes) used to constrain MARS-3D were extracted from the Meteo France AROME model (https://donneespubliques.meteofrance.fr). The tidal model cstFRANCE developed by the SHOM (Simon and Gonella, 2007)

Table 22: Satellite image characteristics used to map the horizontal distribution of the MPB biomass, expressed in NDVI.

Satellite	Spatial resolution (m)	Blue band (nm)	Green band (nm)	Red band (nm)	NIR band (nm)	Acquisition day	Acquisition time (UTC)	Low tide (UTC)	Water height (m)
SPOT 6	6	455-525	530-590	625-695	760-890	18/05/2015	10:54	09:36	0.80
Pleiades	2	430-550	490-610	600-720	750-950	17/07/2015	11:11	10:30	1.30
Pleiades	-	-	-	-	-	03/03/2018	11:25	10:46	0.44

forced MARS-3D at the domain boundaries. The tidal model solved the amplitude and phase of 115 harmonic constituents. Initial and boundary conditions of seawater temperature, salinity, current velocity and sea surface height were extracted from the MANGA 2500 Ifremer model of 2.5 km lateral resolution (Lazure et al., 2009).

Mud surface temperature model

The simulated MST was obtained from the coupling of the MST model of Savelli et al. (2018) with MARS-3D. The simulated heat fluxes in a 1-cm deep sediment layer were solved by thermodynamic equations detailed in Savelli et al. (2018). The horizontal fluxes of heat were neglected. During exposure periods, the simulated MST resulted from heat exchanges between the sun, the atmosphere, the sediment surface, from the conduction between mud and air and from evaporation. The simulated MST of immersed mud was set to the temperature of the overlying seawater simulated by MARS-3D. The simulated MST data were successfully compared with time-coincident *in situ* 1-min data measured on the Brouage mudflat in 2008 (Savelli et al., 2018). The MST differential equation was solved by the MARS-3D numerical scheme. The MST model is fully detailed in Savelli et al. (2018).

MPB GPP-algorithm

To estimate MPB GPP, the algorithm (Fig. 46) coupled NDVI maps from SPOT and Pleiades scenes with forcings by hydrodynamical MARS-3D. Whereas the NDVI estimates the horizontal distribution of MPB biomass, the MARS-3D model simulates the emersion time over the whole mudflat using the bathymetry and the tidal height. Coupled with the MPB biomass, the emersion time determined the photosynthetically active biomass at the mud surface. We assumed that the MPB biomass detected by satellite corresponded to the fully-established biofilm during the daytime low tide (total photosynthetically active biomass). The migration behaviour of MPB biomass was introduced in the model through a progressive establishment of the total photosynthetically active biomass at the sediment surface taking place during 20 min (Herlory et al., 2004). The photosynthetically active biomass started to migrate at the sediment surface just after water removal to reach 50 % of the total amount (= NDVI/2) after 10 minutes of emersion of respective grid cells. After 20 minutes, the MPB biofilm at the sediment surface was fully-formed. 20 minutes before the immersion, downward migration started to leave only the half of the total photosynthetically active biomass at the surface after 10 minutes and no biomass when water overlaid the sediment.

We used the PAR and MST simulated by MARS-3D to constrain the algorithm. The relationship of Blanchard et al. (1996) was used to compute the

photosynthetic capacity (mg C (NDVI)$^{-1}$ m^{-2} h^{-1}) according to the simulated temperature. The Platt et al. (1980) and Eilers and Peeters (1988) P-I models and their respective parameters values fitted on the laboratory measurements were used to compute the MPB photosynthetic rates (mg C (NDVI)$^{-1}$ m^{-2} h^{-1}) according to the simulated light conditions. Assuming that temperature was optimal during light curves acquisition in the laboratory, the maximal photosynthetic capacity (P^b_{MAX}) in the model of Blanchard et al. (1996) was set to the value of P^b_s which represents the photosynthetic rate without photoinhibition in the model of Platt et al. (1980). Combined with the horizontal distribution of the MPB biomass of the NDVI scenes, the photosynthetic capacity was further used to simulate the MPB GPP (mg C m^{-2} h^{-1}).

The current configuration of the GPP-algorithm was consistent only for intertidal mudflats as the studied mudflat is mostly composed by very fine cohesive grains (Bocher et al., 2007) and for epipelic diatoms as they dominate MPB assemblages in muddy sediments (Underwood, 2001). Consequently, we used a MST model developed and validated for the mud (Savelli et al., 2018). Then, laboratory measurements were conducted on mud collected at the very surface of the sediment in order to sample mostly epipelic diatoms mixed with sediment.

With the GPP-algorithm, we computed maps of daily-integrated GPP (mg C m^{-2} d^{-1}) and hourly GPP (mg C m^{-2} h^{-1}) averaged over the emersion duration of the respective pixel. In addition, for each satellite scene, we integrated the daily GPP over the entire mudflat. The comparison of the GPP obtained with the GPP-algorithm with *in situ* GPP rates was made difficult due to the error introduced by different physical conditions and NDVI during satellite acquisition and field campaigns. Therefore, in order to evaluate the skill of the GPP-algorithm without the effect of the environment, we computed the GPP with the production-temperature relationship of Blanchard et al. (1996) and the Platt et al. (1980) and Eilers and Peeters (1988) P-I models constrained by the same temperature, light and NDVI conditions than during the field campaigns. In addition, the GPP values obtained with the GPP-algorithm extracted from the pixel corresponding to the study site were still compared with GPP rates measured *in situ* during the same period.

Comparison with GPP simulated by MARS-3D

We compared the remotely-sensed MPB GPP with the MPB GPP simulated by MARS-3D (see Chapter 5). In the 3D model, the photosynthetic capacity depended on MST and PAR according to the relationship of Blanchard et al. (1996) and Platt et al. (1980), respectively. Consequently, we compared the PP simulated by MARS-3D with that derived from the algorithm parametrised with the Platt et al. (1980) P-I model only. MARS-3D was run with and without photoinhibition (see Chapter 5).The Photo and the NoPhoto runs were simulations of

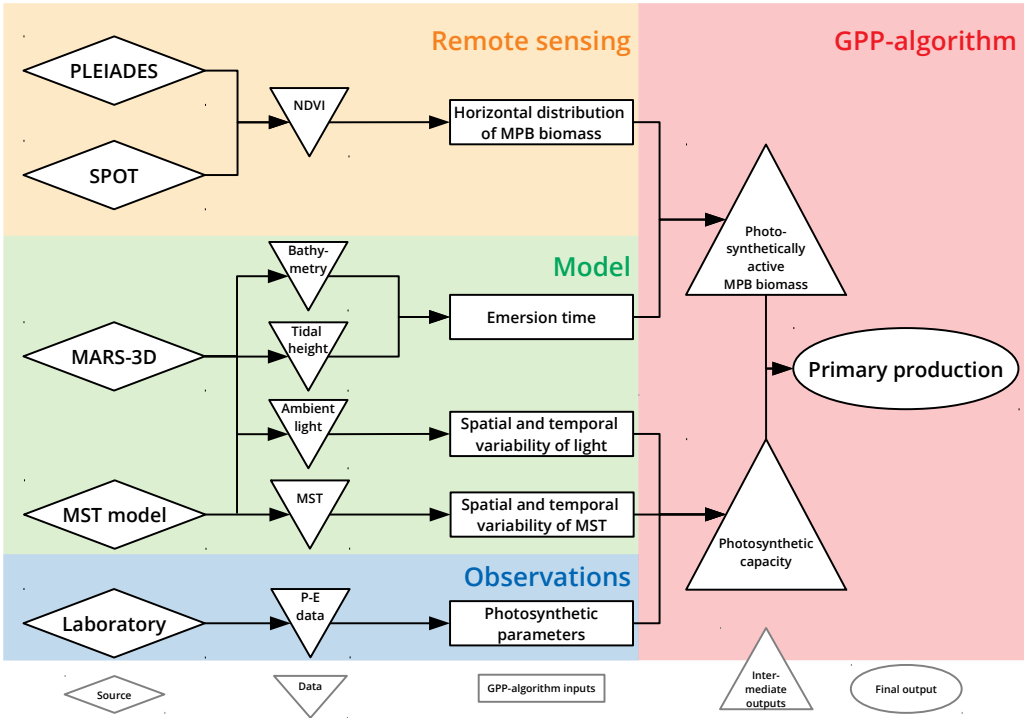

Figure 46: Conceptual scheme of the MPB GPP-algorithm.

MPB PP with (β set to 0.003 mg C mg Chl a^{-1} h^{-1} (µmol photons m^{-2} s^{-1})$^{-1}$ in spring, 0.01 mg C mg Chl a^{-1} h^{-1} (µmol photons m^{-2} s^{-1})$^{-1}$ in summer and 0.02 mg C mg Chl a^{-1} h^{-1} (µmol photons m^{-2} s^{-1})$^{-1}$ in fall) and without photoinhibition (β permanently set to zero), respectively. A third run (P^b_{fix} run) was used, parametrised as the NoPhoto run but with a photosynthetic rate (P^b) (mg C (mg Chl a)$^{-1}$ h^{-1}) whose value during the day of *in situ* measurements (May and July 2015) was constrained by the mean value of the biomass-specific production rate (mg C (mg Chl a)$^{-1}$ h^{-1}) measured during the field campaigns. This biomass-specific production rate was obtained by dividing the GPP measured *in situ* (mg C m^{-2} h^{-1}) by the mean *in situ* MPB biomass in mg Chl a m^{-2} averaged over the time of each GPP measurement (20 min). Therefore, the simulated production rate in the P^b_{fix} run did not account for light and temperature conditions any more and was set to 0.28 mg C (mg Chl a)$^{-1}$ h^{-1} during 5-6 May 2015 and 0.32 mg C (mg Chl a)$^{-1}$ h^{-1} during 02-03 July 2015.

RESULTS

Physical environment

The simulated MST and PAR on matching days with *in situ* measurements reasonably compared to the 30-sec frequency PAR and MST measured in May-July

2015 and March 2018 at the study site (Fig. 47). In March, the simulated PAR (710 ± 125.5 µmol photons m^{-2} s^{-1}) was significantly higher than the measured PAR (630.4 ± 139.4 µmol photons m^{-2} s^{-1}; Mann Whitney test: *p-value* < 0.01). In May, the model underestimated PAR (1404.9 ± 101.3 µmol photons m^{-2} s^{-1}) compared to more scattered observations (1514.7 ± 532.4 µmol photons m^{-2} s^{-1}; Mann Whitney test: *p-value* < 0.01). In July, the simulated PAR (1195.1 ± 304.9 µmol photons m^{-2} s^{-1}) was not significantly different from the measured PAR (1229.9 ± 305.9 µmol photons m^{-2} s^{-1}; Mann Whitney test: *p-value* > 0.01). With respect to MST, in March, the simulated MST (16.4 ± 0.9 °C) was not significantly different from the measured MST (15.7 ± 2.1 °C; Mann Whitney test: *p-value* > 0.01). The simulated MST in May was in average 20.7 ± 0.6 °C and was significantly different from the MST measurements (19.5 ± 1.8 °C; Mann Whitney test: *p-value* < 0.01). In July, the simulated MST (31.2 ± 5 °C) was not significantly different from the measured MST (31.4 ± 3.4 °C; Mann Whitney test: *p-value* > 0.01).

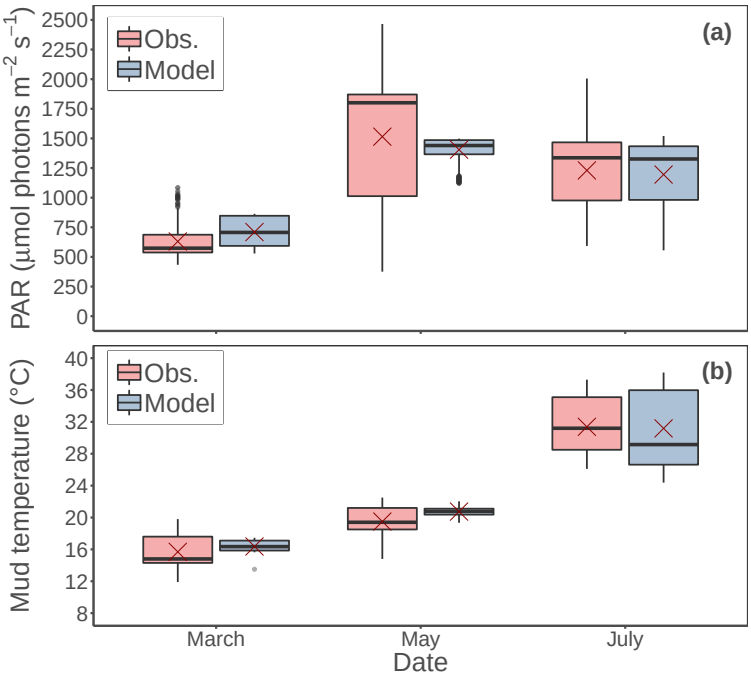

Figure 47: **(a)** PAR measured *in situ* and, simulated by MARS-3D on matching days with *in situ* measurements at the study site and, **(b)** MST measured *in situ* and, simulated by MARS-3D on matching days with *in situ* measurements at the study site. Red crosses correspond the mean value of PAR and MST for the corresponding period.

Overall, the PAR and temperature conditions simulated by MARS-3D on satellite data matching days were not significantly different from the *in situ* data (Fig. 48). In March, the simulated PAR matching the satellite scene acquisition (941.8 ± 33.7 µmol photons m^{-2} s^{-1}) was significantly higher than

the measured PAR (630.4 ± 139.4 µmol photons m^{-2} s^{-1}; Mann Whitney test: *p-value* < 0.01). In May, the simulated PAR was in average 1110.9 ± 125.8 µmol photons m^{-2} s^{-1}, which compared to the PAR data measured *in situ* (1514.7 ± 532.4 µmol photons m^{-2} s^{-1}; Mann Whitney test: *p-value* = 0.01). In July, the simulated PAR (1319.7 ± 133.7 µmol photons m^{-2} s^{-1}) was not significantly different from the observed PAR measured *in situ* (1229.9 ± 305.9 µmol photons m^{-2} s^{-1}; Mann Whitney test: *p-value* > 0.01). With respect to MST, in March, the model simulated a mean MST of 15.7 ± 0.7 °C that was not significantly different from the *in situ* MST (15.7 ± 2.1 °C; Mann Whitney test: *p-value* > 0.01). In May, the mean simulated MST (18.5 ± 4.8 °C) was not significantly different from the observed MST measured *in situ* (19.5 ± 1.8 °C; Mann Whitney test: *p-value* > 0.01). In July, the model simulated a mean MST of 30.3 ± 3.4 °C that was not significantly different from the *in situ* MST (31.4 ± 3.4 °C; Mann Whitney test: *p-value* > 0.01). The comparison between simulations and *in situ* data showed the robustness of the prediction of the MST and PAR models.

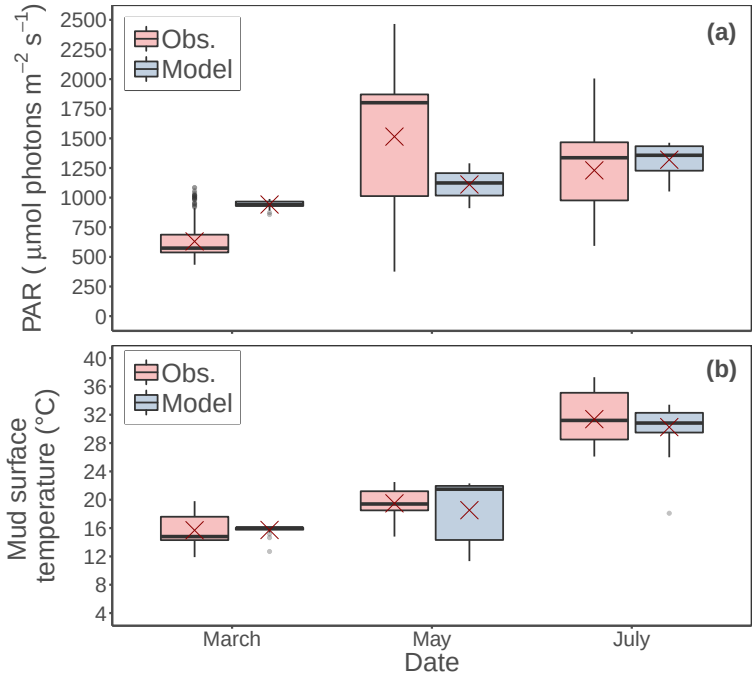

Figure 48: **(a)** PAR measured *in situ* and, simulated by MARS-3D on satellite data matching days at the study site and, **(b)** MST measured *in situ* and, simulated by MARS-3D on satellite data matching days at the study site. Red crosses correspond the mean value of PAR and MST for the corresponding period.

To ensure that the delay (respectively 13, 14 and 2 days in May 2015, July 2015 and March 2018) between field campaigns used to calibrate P-I models, and images acquisition used to map GPP, was not an issue, simulated physical conditions were analysed (Fig. 49). The main risk was a change in acclimation

status of MPB cells due to a change in light and temperature conditions during this delay (Fig. 49). For this purpose, simulated physical conditions were averaged during daytime emersion periods two weeks before *in situ* measurements and satellite scenes to be compared (Fig. 49). In March 2018, the PAR averaged over daytime emersion periods simulated two weeks before the *in situ* measurements (456.9 ± 280.7 µmol photons m^{-2} s^{-1}) was not significantly different from the PAR averaged over daytime emersion periods simulated two weeks before the satellite scene acquisition (412.3 ± 236.7 µmol photons m^{-2} s^{-1}; Student test: *p-value* > 0.01). In May 2015, the PAR averaged over daytime emersion periods simulated two weeks before the *in situ* measurements (646.3 ± 445 µmol photons m^{-2} s^{-1}) was not significantly different from the PAR averaged over daytime emersion periods simulated two weeks before the satellite scene acquisition (844.2 ± 387.4 µmol photons m^{-2} s^{-1}; Student test: *p-value* > 0.01). Two weeks before the measurements gathered in July 2015, the PAR averaged over daytime emersion periods simulated by MARS-3D was 765.6 ± 370 µmol photons m^{-2} s^{-1}, which was not significantly different from the PAR averaged over daytime emersion periods simulated two weeks before the satellite scene acquisition (853.7 ± 414.3 µmol photons m^{-2} s^{-1}; Student test: *p-value* > 0.01).

Similarly, the MST conditions simulated two weeks before *in situ* measurements and satellite scene were not significantly different. In March 2018, the MST averaged over daytime emersion periods simulated two weeks before the *in situ* measurements was 4.9 ± 8 °C. It was not significantly different from the MST averaged over daytime emersion periods simulated two weeks before the satellite scene acquisition (6.3 ± 7.1 °C; Student test: *p-value* > 0.01). In May 2015, the MST averaged over daytime emersion periods simulated two weeks before the *in situ* measurements (19.5 ± 5.3 °C) compared to the MST averaged over daytime emersion periods simulated two weeks before the satellite scene acquisition (21.3 ± 3.7 °C; Student test: *p-value* > 0.01). In July 2015, the MST averaged over daytime emersion periods simulated two weeks before the *in situ* measurements (25.4 ± 3.2 °C) was not significantly different from the MST averaged over daytime emersion periods simulated two weeks before the satellite scene acquisition (26.6 ± 4.9 °C; Student test: *p-value* > 0.01). These results mean that MPB cells were in the same acclimation status and satellite images can be used to estimate GPP, even if the data to calibrate P-I models were not obtained the same day.

Evaluating P-I models

The shape of the relationship between the NDVI-specific photosynthetic rate (P^b) and the irradiance measured in laboratory varied with seasons (Fig. 50) and so the fitted photosynthetic parameters P-I models (Table 23). In all P-I models, the highest value for the photosynthetic capacity (P_s^b in the Platt

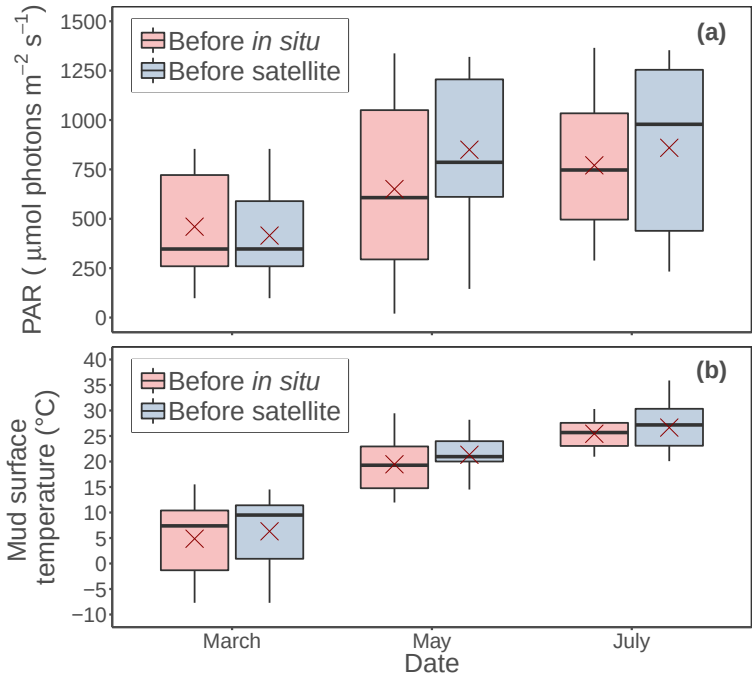

Figure 49: **(a)** PAR and, **(b)** MST simulated by MARS-3D two weeks before the *in situ* measurements and the satellite scene acquisition and averaged over daytime emersion periods. Red crosses correspond the mean value of PAR and MST for the corresponding period.

et al. (1980) model or P^b_{max} otherwise) occurred in May 2015 (Fig. 50 and Table 23). In May 2015, the photoinhibition was also the strongest (Fig. 50) as showed by the highest β values reported in the Platt et al. (1980) and modified Platt and Jassby (1976) models. In March 2018, the best fit on the laboratory measurements was obtained with the Platt et al. (1980) and Eilers and Peeters (1988) models, which exhibited a higher determination coefficient (r^2) and a lower Residual Standard Deviation (RSD)(0.88 and ~ 8.4 mg C (NDVI)$^{-1}$ m^{-2} h^{-1}, respectively; Fig. 50 and Table 24). In May 2015, the models of Eilers and Peeters (1988), Steele (1962) and modified Platt and Jassby (1976) best fitted the laboratory measurements (r^2 = 0.96 and RSD < 12 mg C (NDVI)$^{-1}$ m^{-2} h^{-1}; Fig. 50 and Table 24). In July 2015, the best fit on laboratory measurements was obtained with the Platt et al. (1980), Eilers and Peeters (1988) models (r^2 = 0.96 and RSD < 7 mg C (NDVI)$^{-1}$ m^{-2} h^{-1}; Fig. 50 and Table 24). Overall, the highest r^2 and lowest RSD suggested that the Platt et al. (1980), Eilers and Peeters (1988) and modified Platt and Jassby (1976) models best fitted the laboratory measurements. As the Platt et al. (1980) and Eilers and Peeters (1988) models are well-referenced and widely used, we applied both of them in our MPB GPP-algorithm.

Under similar light and temperature conditions prevailing during the GPP measurements, the GPP rates estimated with the models of Eilers and Peeters

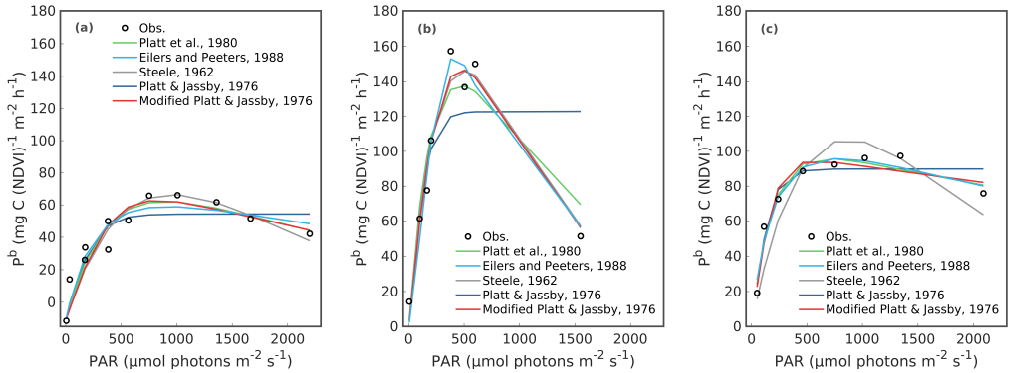

Figure 50: Measured and predicted NDVI-specific photosynthetic rate according to the evaluated P-I models in **(a)** March 2018, **(b)** May 2015 and, **(c)** July 2015.

(1988) and Platt et al. (1980) were in the same order of magnitude than the observed rates except in March 2018 when the predicted rates were 5- to 10-fold higher than the measured GPP rates. This predicted GPP in March was much higher than the measured GPP as it was constrained by the high MPB-specific NDVI measured *in situ* in March 2018 compared to May and July 2015 (Fig. 53). The predicted and measured GPP in March was therefore excluded from the following skill assessment of the GPP-algorithm. The models of Eilers and Peeters (1988) in May and July 2015, showed the best agreement with the measured PP compared to Platt et al. (1980) (Fig. 51). The model of Eilers and Peeters (1988) exhibited a slope close to 1 and an intercept close to 0 mg C m^{-2} h^{-1} (Fig. 51). The model showed a better fit than that of Platt et al. (1980) characterised by a slope of 0.4 and an intercept of 4.4 mg C m^{-2} h^{-1} (Fig. 51). Moreover, the Eilers and Peeters (1988) model has a higher r^2 (0.34) than the model of Platt et al. (0.06; 1980).

The remote sensing of the MPB GPP

Over the mudflat, the MPB-specific NDVI varied from 0 to 0.4 on the Pleiade image in March 2018 (Fig. 52). In May 2015, the MPB-specific NDVI varied from 0 to 0.3 on the SPOT 6 image (Fig. 52). In July 2015, the MPB-specific NDVI derived from the Pleiade image varied from 0 to 0.3 (Fig. 52).

Over the mudflat, the normalised MPB-specific NDVI was the highest in March 2018 (0.51 ± 0.21; Fig. 52) and the lowest in July 2015 (0.35 ± 0.13; Fig. 52). In May 2015, the normalised MPB-specific NDVI was 0.47 ± 0.17 (Fig. 52). The MPB-specific NDVI was higher on the middle and lower shores than on the upper shore, especially in March and May (Fig. 52).

The MPB-specific NDVI measured *in situ* was always higher than the remotely-sensed MPB-specific NDVI at the study site. In March 2018, the MPB-specific NDVI measured *in situ* (0.61 ± 0.03) was almost 5-fold higher than the remotely-

Table 23: Parameters of the P-I models fitted with the differential evolution method in **(a)** March 2018, **(b)** May 2015 and, **(c)** July 2015. The interval gives the lower and upper bound of the explored values, respectively.

Model	March		May		July	
	Interval	Value	Interval	Value	Interval	Value
Platt et al. (1980)						
P_s^b	[0; 150]	108.2	[0; 250]	250	[0; 200]	108.67
α	[0; 10]	0.27	[0; 10]	0.9	[0; 10]	0.57
β	[0; 50]	0.03	[0; 50]	0.21	[0; 50]	0.02
Eilers and Peeters (1988)						
P_{max}^b	[0; 150]	70.41	[0; 250]	154.2	[0; 200]	95.82
α	[0; 10]	0.34	[0; 10]	0.43	[0; 10]	0.64
I_{opt}	[0; 1000]	922.3	[0; 1000]	415.75	[0; 1000]	784.68
Steele (1962)						
P_{max}^b	[0; 150]	77.89	[0; 250]	145.93	[0; 200]	106.68
α	[0; 10]	0.08	[0; 10]	0.29	[0; 10]	0.12
Platt and Jassby (1976)						
P_{max}^b	[0; 150]	65.77	[0; 250]	122.83	[0; 200]	89.87
α	[0; 10]	0.24	[0; 10]	0.71	[0; 10]	0.5
Modified Platt and Jassby (1976)						
P_{max}^b	[0; 150]	92.73	[0; 250]	250	[0; 200]	100.43
α	[0; 10]	0.21	[0; 10]	0.66	[0; 10]	0.46
β	[0; 50]	0.02	[0; 50]	0.17	[0; 50]	0.01

sensed MPB-specific NDVI at the study site (0.14; Fig. 53). The MPB-specific NDVI measured *in situ* in May 2015 (0.14 $\pm$ 0.02) was 1.5-fold higher than the remotely-sensed MPB-specific NDVI at the study site (0.09; Fig. 53). In July 2015, the MPB-specific NDVI measured *in situ* (0.18 $\pm$ 0.09) was almost 1.8-fold higher than the remotely-sensed MPB-specific NDVI at the study site (0.1; Fig. 53).

The hourly MPB GPP averaged over 24 h was the highest in March 2018 and the lowest in July 2015 with both P-I models (Fig. 54). At the three dates, the amplitude of the hourly GPP was same with the Platt et al. (1980) and Eilers and Peeters (1988) models. In March 2018, the hourly PP was high on the middle and lower shores with values up to 2.4 mg C m^{-2} h^{-1} (Fig. 54). The upper shore was less productive with an hourly GPP of $\sim$ 1.25 mg C m^{-2} h^{-1} (Fig. 54). In May 2015, the upper shore was almost as much productive as in March 2018 ($\sim$ 1 mg C m^{-2} h^{-1}) but the middle and lower shores were less productive than in March 2018 ($\sim$ 1.25 mg C m^{-2} h^{-1}; Fig. 54). The hourly PP exhibited no spatial pattern in July 2015, because GPP was low over the entire mudflat ($\sim$ 0.3 mg C m^{-2} h^{-1}; Fig. 54).

Table 24: Scores of the P-I models fitted with the differential evolution method in **(a)** March 2018, **(b)** May 2015 and, **(c)** July 2015. r^2 is the determination coefficient and RSD is the residual standard deviation.

Model	March		May		July	
	r^2	RSD	r^2	RSD	r^2	RSD
Platt et al. (1980)	0.88	8.4	0.92	16.26	0.95	6.37
Eilers and Peeters (1988)	0.88	8.33	0.96	10.71	0.96	5.86
Steele (1962)	0.86	8.94	0.96	11.54	0.77	13.81
Platt and Jassby (1976)	0.82	10.25	0.58	36.11	0.92	8.27
Modified Platt and Jassby (1976)	0.85	9.36	0.96	10.67	0.94	7.19

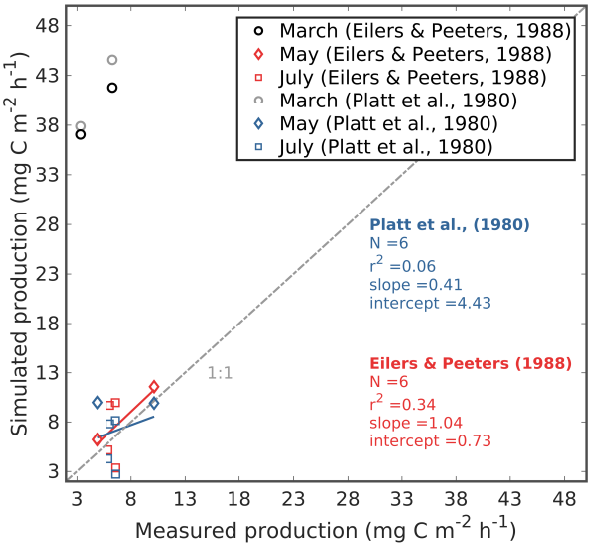

Figure 51: Measured GPP and GPP predicted by the GPP-algorithm constrained by the same light, temperature and NDVI conditions concomitant to the GPP *in situ* measurements. Predicted GPP rates in March 2018 were considered as outliers and were not considered in the metrics.

The seasonal amplitude of the daily-integrated GPP was similar in the Platt et al. (1980) and Eilers and Peeters (1988) models (Fig. 55). In March 2018, both models simulated the highest daily-integrated GPP (Fig. 55). Integrated over the mudflat, GPP in March 2018 was 2.15 and 2.06 t C with the Platt et al. (1980) and Eilers and Peeters (1988) models, respectively (Table 25). The daily-integrated PP was particularly high on the middle and lower shores with values as high as 100 mg C m^{-2} in both P-I models (Fig. 55). In May 2015, the daily-integrated PP was lower in March 2018, especially on the middle and lower shores (~ 40 mg C m^{-2}; Fig. 55). Integrated over the mudflat, GPP reached 1.44 and 1.42 t C in May 2015 with the Platt et al. (1980) and Eilers and Peeters

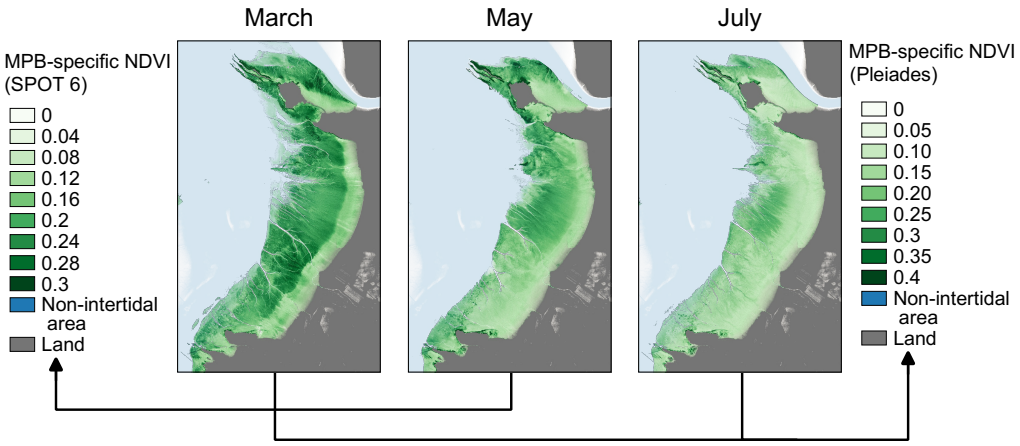

Figure 52: MPB-specific NDVI from Pleaides in March 2018 and July 2015 and, from SPOT 6 in May 2015.

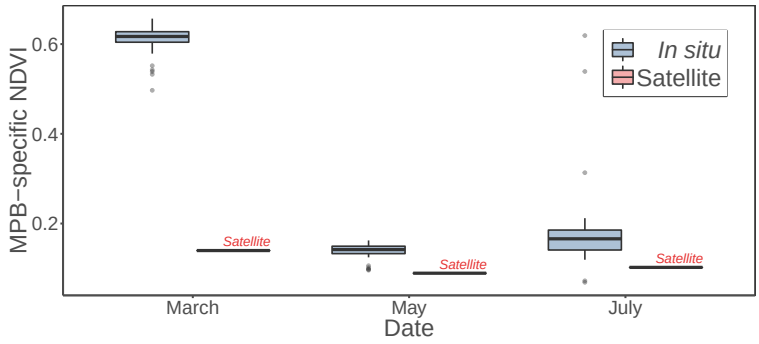

Figure 53: MPB-specific NDVI measured *in situ* and remotely-sensed at the study site in March 2015 (Pleiades), May 2015 (SPOT 6) and July 2015 (Pleiades).

(1988) models, respectively, which was lower than in July 2015 (Table 25). The daily-integrated GPP was the lowest in July 2015 when GPP rarely exceeded 20 mg C m^{-2} on the upper shore (Fig. 55). In July 2015, the GPP integrated over the entire mudflat was 0.63 and 0.8 t C with the Platt et al. (1980) and Eilers and Peeters (1988) models, respectively (Table 25).

In March 2018, the measured GPP (4.8 $\pm$ 2.08 mg C m^{-2} h^{-1}) was lower than the GPP remotely-sensed at the corresponding grid cell with the Platt et al. (1980) and Eilers and Peeters (1988) models (8.1 $\pm$ 3.2 and 7.8 $\pm$ 3.1 mg C m^{-2} h^{-1}, respectively; Fig. 56). In May 2015, the remotely-sensed GPP with the Platt et al. (4.2 $\pm$ 2.4 mg C m^{-2} h^{-1}; 1980) and Eilers and Peeters (4.1 $\pm$ 2.2 mg C m^{-2} h^{-1}; 1988) compared to GPP measured at the study site (5.7 $\pm$ 3.2 mg C m^{-2} h^{-1}; Fig. 56). The remotely-sensed GPP in July 2015 (1.4 $\pm$ 1.2 and 2.2 $\pm$ 1.4 mg C m^{-2} h^{-1} with the Platt et al. (1980) and Eilers and Peeters (1988) models, respectively) was lower than the GPP measured at the study site (6.3 $\pm$ 0.3 mg C m^{-2} h^{-1}; Fig. 56).

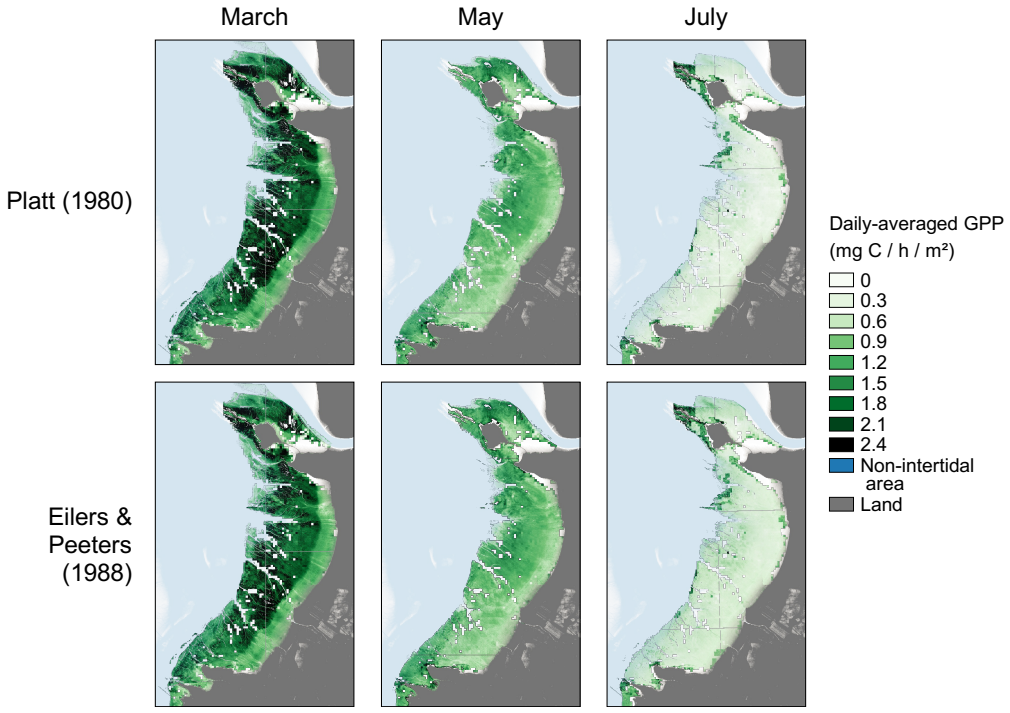

Figure 54: Daily-averaged GPP (mg C m^{-2} h^{-1}) remotely-sensed with the GPP-algorithm in March 2018, May 2015 and July 2015.

Table 25: Integrated-GPP (t C) in March 2018, May 2015 and July 2015 according to the GPP-algorithm.

	March	May	July
Platt et al. (1980)	2.15	1.44	0.63
Eilers and Peeters (1988)	2.06	1.42	0.8

Comparison of the MARS-3D simulated, measured and remotely-sensed GPP

In this section, we compare GPP rates simulated by the MARS-3D model, remotely-sensed using the GPP-algorithm with the Platt et al. (1980) P-I model and measured *in situ*. In the NoPhoto run, the simulated GPP was higher than the remotely-sensed GPP in May and July 2015 (Fig. 57). In the Photo run, the simulated PP was higher than the remotely-sensed GPP only in May 2015 (Fig. 57). In the Photo run, there was no difference in the GPP in July 2015, except on the upper mudflat where the remotely-sensed GPP remained lower than the simulated PP (Fig. 58).

In May 2015, in the NoPhoto run, the simulated biomass-specific GPP averaged over the daytime emersion (3.7 $\pm$ 1.7 mg C (mg Chl *a*)$^{-1}$ m^{-2} h^{-1}) was higher than the measured biomass-specific GPP (0.28 $\pm$ 0.1 mg C (mg Chl *a*)$^{-1}$

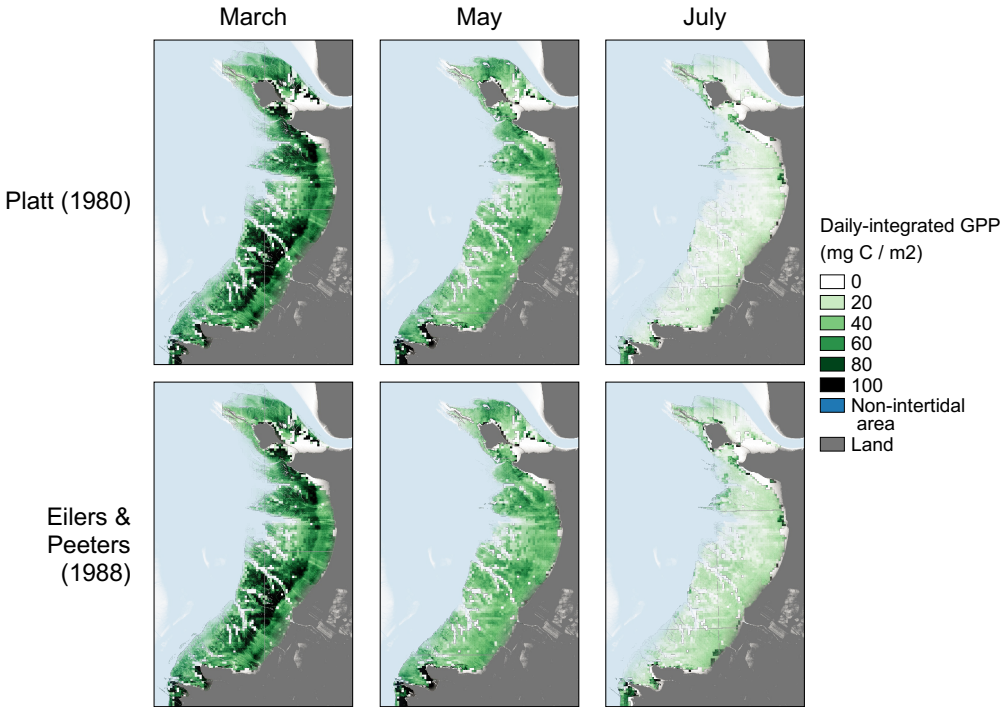

Figure 55: Daily-integrated GPP (mg C m^{-2}) remotely-sensed with the GPP-algorithm in March 2018, May 2015 and July 2015.

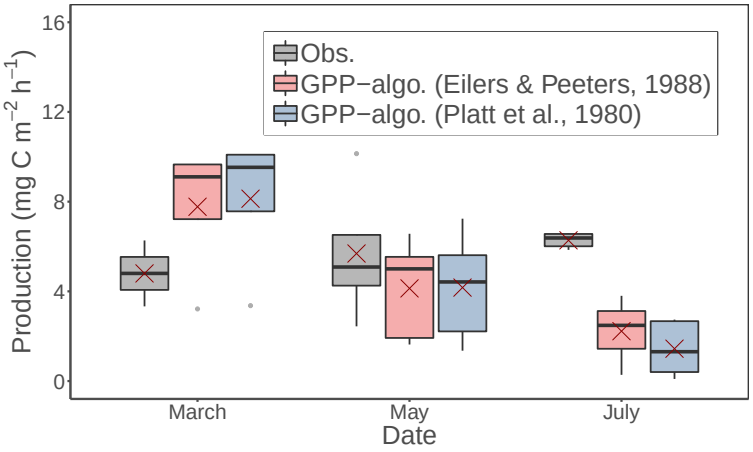

Figure 56: Measured GPP during *in situ* measurements and GPP remotely-sensed at the study site with the GPP-algorithm during satellite scene acquisition in March 2018, May 2015 and July 2015. Red crosses correspond the mean value of PAR and MST for the corresponding period.

m^{-2} h^{-1}; Fig. 59a). In the NoPhoto run, the GPP simulated in May 2015 (93 ± 42.6 mg C m^{-2} h^{-1}) was 17-fold higher than the measured GPP (5.7 ± 3.2 mg C m^{-2} h^{-1}) Fig. 59b). In July 2015, the biomass-specific GPP simulated in the

NoPhoto run was 1.4 ± 1.2 mg C (mg Chl *a*)$^{-1}$ m^{-2} h^{-1}, which was higher than the measured biomass-specific GPP (0.32 ± 0.12 mg C (mg Chl *a*)$^{-1}$ m^{-2} h^{-1}; Fig. 59a). In July 2015, the GPP simulated in the NoPhoto run (35.1 ± 30.4 mg C m^{-2} h^{-1}) was 6-fold higher than the measured PP (6.3 ± 0.3 mg C m^{-2} h^{-1}; Fig. 59b). The hourly rates of GPP simulated in the NoPhoto run on 5-6 May 2015 and 2-3 July 2015 never compared to the measured GPP. In addition, the amplitude of GPP simulated in the NoPhoto run from 28 April to 12 May 2015 rarely compared to the measured GPP on 5-6 May 2015 and 2-3 July 2015 (Fig. 60).

With an average over the daytime emersion of 0.47 ± 0.2 mg C (mg Chl *a*)$^{-1}$ m^{-2} h^{-1}, the biomass-specific GPP simulated in the Photo run better compared with the biomass-specific GPP measured in May 2015 (Fig. 59a). In contrast, the biomass-specific GPP simulated in the Photo run (0.11 ± 0.19 mg C (mg Chl *a*)$^{-1}$ m^{-2} h^{-1}) was comparable with the measurements (Fig. 59a). In the Photo run, the simulated GPP in May 2015 (11.7 ± 5.1 mg C m^{-2} h^{-1}) and July 2015 (3 ± 4.7 mg C m^{-2} h^{-1}) was 8-fold to 11-fold lower than the GPP simulated in the NoPhoto run (Fig. 59b). Such a result suggests that a better model/*in situ* data comparison with the Photo run than with the NoPhoto run in May and July 2015 59b). The GPP simulated in the Photo run on 5-6 May 2015 and 2-3 July 2015 compared with measurements. Moreover, the GPP simulated in the Photo run often reached values similar to those measured during the simulated two weeks period (Fig. 60).

In MARS-3D, the MPB biomass simulated in the biofilm quickly saturated at 25 mg Chl *a* m^{-2} at daytime for each low tide (Fig. 61). Such a model behaviour agreed with the biomass at the sediment surface averaged during *in situ* measurements in May 2015 (20.6 ± 6.9 mg Chl *a* m^{-2}) and July 2015 (22.6 ± 10.8 mg Chl *a* m^{-2}; Fig. 61). In May and July 2015, the NDVI data suggested that the MPB biomass was distributed more on the middle shore than on the upper shore (Fig. 62). Both in the NoPhoto and Photo runs, the MPB biomass simulated in the biofilm during the satellite scene acquisition saturated at 25 mg Chl *a* m^{-2} on a major part of the mudflat. The simulated MPB biomass was particularly high on the upper shore (Fig. 62).

In the P^{b}_{fix} run, in which we set a photosynthetic rate similar to the measured biomass-specific GPP (0.28 ± 0.11 and 0.32 ± 0.13 mg C (mg Chl *a*)$^{-1}$ h^{-1} in May and July, respectively), the simulated GPP compared with the measured GPP (Fig. 63). In May and July 2015, the simulated biomass-specific GPP was 0.2 ± 0.1 mg C (mg Chl *a*)$^{-1}$ m^{-2} h^{-1} in average in both the NoPhoto and the Photo runs (Fig. 63a). Consequently, the simulated GPP with the constrained photosynthetic rate in the 3D model was lower than with the photosynthetic rate as a function of PAR and MST (Fig. 63b). In the P^{b}_{fix} run, the simulated GPP matching the *in situ* measurements was 4.89 ± 2.2 mg C m^{-2} h^{-1} in May 2015 and 5.1 ± 2.6 mg C m^{-2} h^{-1} in July 2015 and compared the GPP measured *in situ* (Fig. 63b).

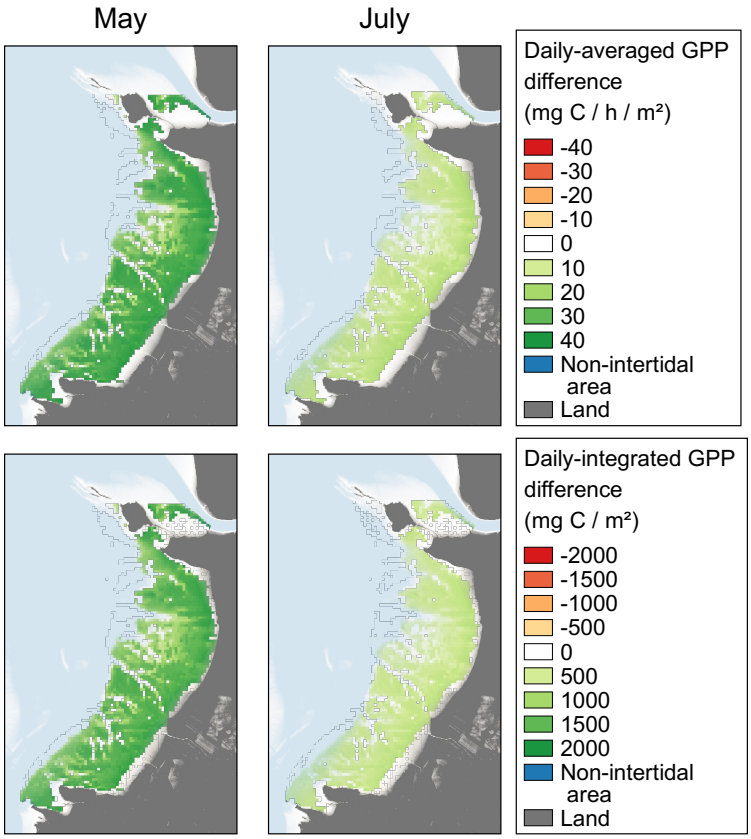

Figure 57: Daily-averaged (mg C m^{-2} h^{-1}) and daily-integrated GPP (mg C m^{-2}) difference between the GPP simulated with MARS-3D in the NoPhoto run and the GPP remotely-sensed with the GPP-algorithm.

DISCUSSION

Remotely-sensed NDVI variability

The GPP-algorithm is based on NDVI data remotely-sensed by the satellite sensor. MPB-specific NDVI data obtained from Pleiades and SPOT 6 reach maximal values of 0.4 and 0.3, respectively. Such values are in the range of the MPB-specific NDVI derived from satellite data over temperate mudflats (*e.g.* van der Wal et al., 2010; Brito et al., 2013; Benyoucef et al., 2014; Echappé et al., 2018). In our study, the NDVI data suggest a seasonal cycle characterised by a seasonal maximum and minimum of MPB biomass in spring and summer, respectively. No satellite scenes nor field campaigns were conducted in fall. Nevertheless, the NDVI seasonality observed in the Brouage mudflat is consistent with the seasonal pattern reported for the same mudflat in previous studies (Cariou-Le Gall and Blanchard, 1995; Savelli et al., 2018) and for other northern European mudflats (*i.e.* van der Wal et al., 2010; Echappé et al., 2018).

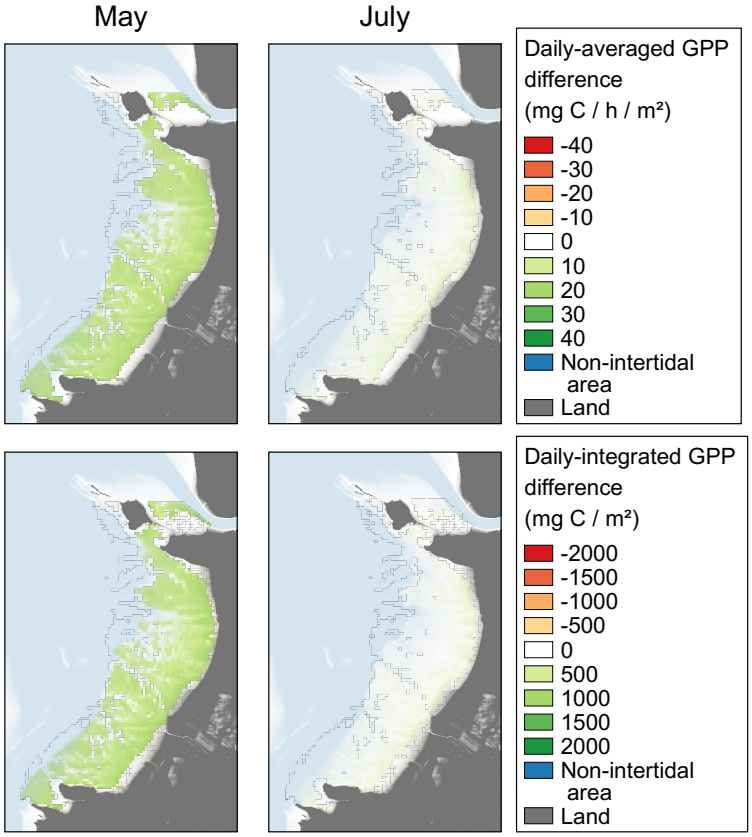

Figure 58: Daily-averaged (mg C m^{-2} h^{-1}) and daily-integrated GPP (mg C m^{-2}) difference between the GPP simulated with MARS-3D in the Photo run and the GPP remotely-sensed with the GPP-algorithm.

The NDVI is a proxy of Chl *a* absorption and thus, of MPB biomass at the mud surface. As the biomass-specific photosynthetic capacity is expressed in terms of Chl *a* (mg C (mg Chl *a*)$^{-1}$ h^{-1}), the higher the Chl *a* in the sediment photic layer, the higher the PP. Given that the NDVI-Chl *a* relationship is non-linear, especially at high values (Méléder et al., 2003a; Méléder et al., 2003b; Serôdio et al., 2009), and that the C:Chl *a* ratio of MPB varies according to seasons and species (Gould and Gallagher, 1990; de Jonge et al., 2012), the Chl *a* photosynthetic rate obtained from the NDVI-Chl *a* relationship is hazardous. The model developed by Daggers et al. (2018) required the conversion of the NDVI into Chl *a*, which introduces uncertainties. The GPP-algorithm we developed in this study is the first to be NDVI-calibrated rather than Chl *a*-calibrated. NDVI-specific photosynthetic parameters estimated during laboratory experiments combined with *in situ* radiometry reduces the uncertainty due to a NDVI-Chl *a* relationship.

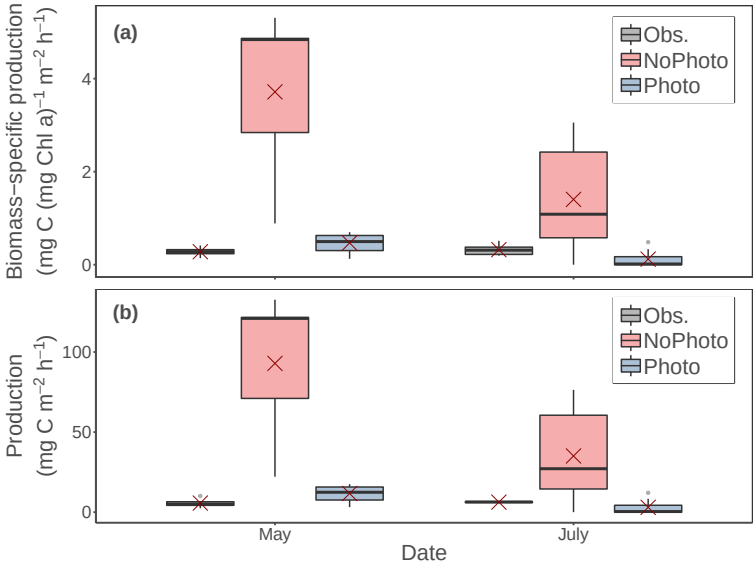

Figure 59: **(a)** Measured biomass-specific GPP and biomass-specific GPP (mg C (mg Chl *a*)$^{-1}$ m^{-2} h^{-1}) simulated with MARS-3D on matching days with *in situ* measurements and, **(b)** measured hourly GPP and hourly GPP (mg C m^{-2} h^{-1}) simulated with MARS-3D on matching days with *in situ* measurements. Red crosses correspond the mean value for the corresponding period.

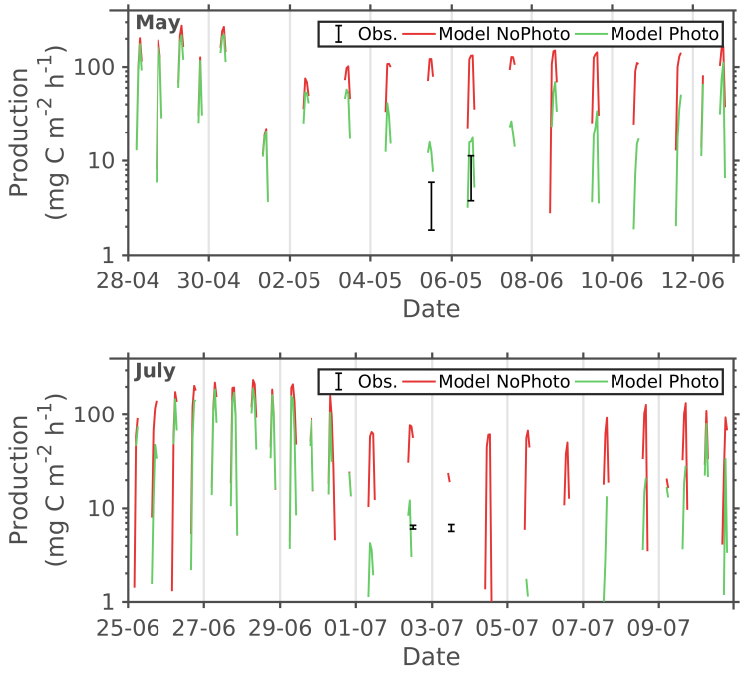

Figure 60: Measured hourly GPP and hourly GPP (mg C m^{-2} h^{-1}) simulated with MARS-3D one week before and after *in situ* measurements.

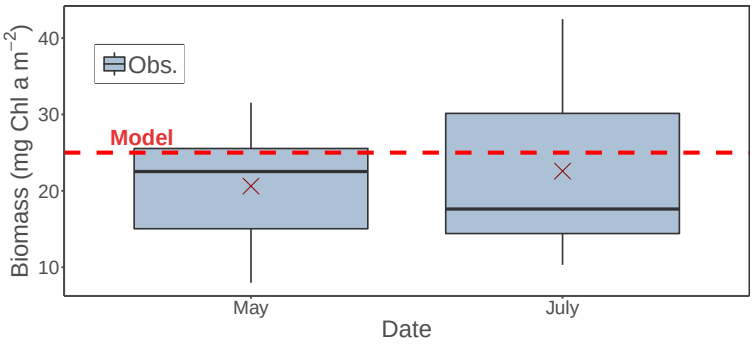

Figure 61: Measured and simulated MPB biomass in the biofilm during *in situ* measurements). Red crosses correspond the mean value for the corresponding period.

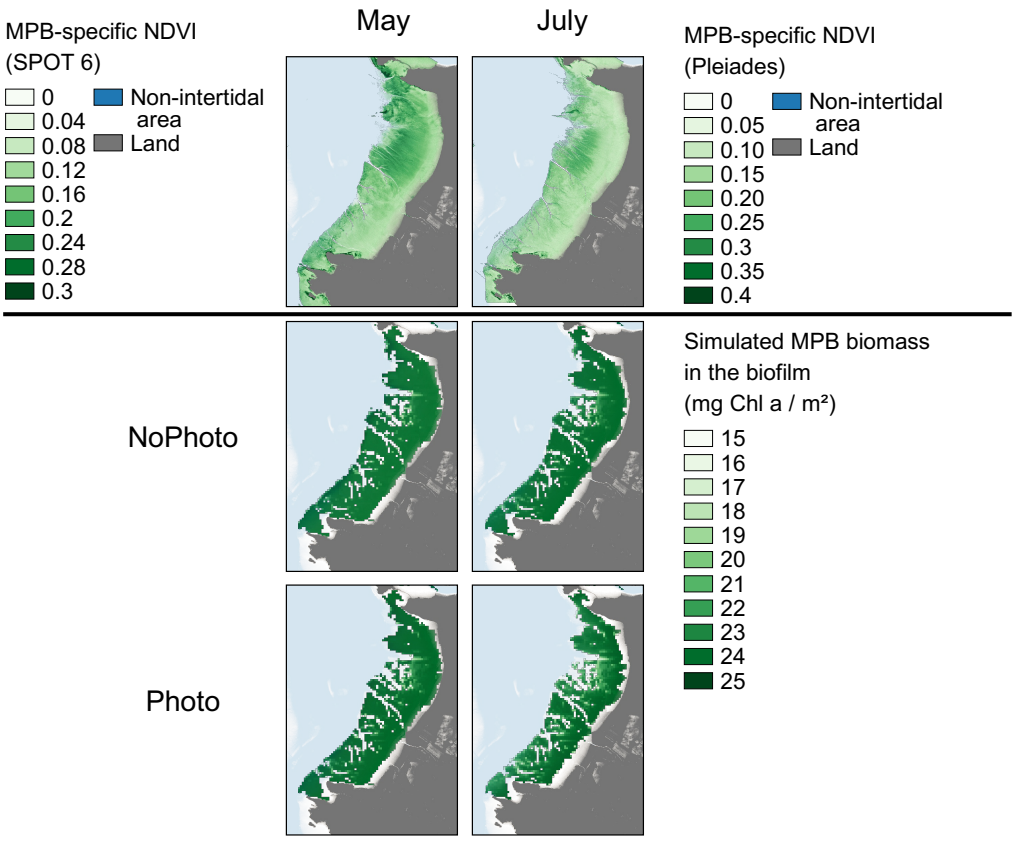

Figure 62: MPB-specific NDVI and simulated MPB biomass with MARS-3D in May and July 2015.

Inherent skills of the GPP-algorithm

In order to minimise errors due to discrepancies between *in situ* and satellite-derived NDVI data, the predictive capacity of the GPP-algorithm was first

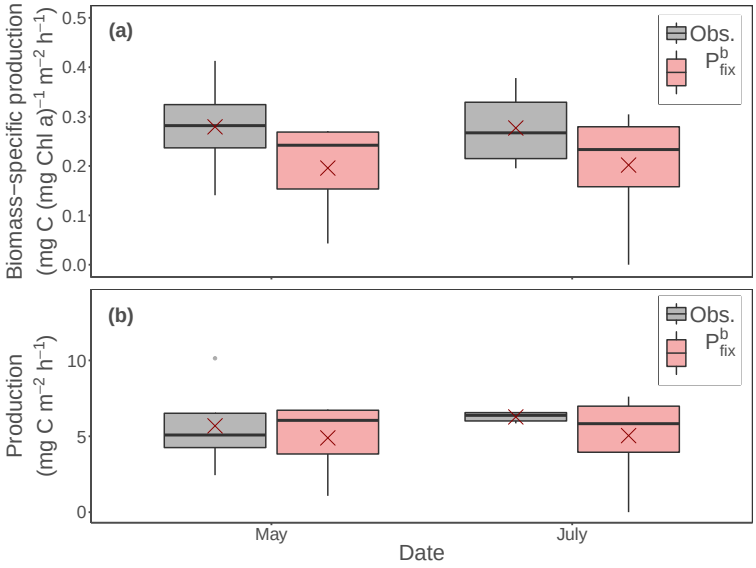

Figure 63: **(a)** Measured biomass-specific production and biomass-specific production simulated with MARS-3D (mg C (mg Chl *a*)$^{-1}$ m^{-2} h^{-1}) and, **(b)** measured hourly GPP and hourly GPP simulated with MARS-3D (mg C m^{-2} h^{-1}) during *in situ* measurements. Simulation was run with a constant photosynthetic capacity set to the average biomass-specific production during *in situ* measurements. Red crosses correspond the mean value for the corresponding period.

tested by constraining the algorithm with environmental data (light, MST) and NDVI data (radiometry) measured *in situ* during the 2015 and 2018 field campaigns. With rates ranging from 3 to 11 mg C m^{-2} h^{-1}, the predicted GPP lies in the range of the observed rates reported in other European mudflats (Barranguet et al., 1998; Underwood and Kromkamp, 1999; Hubas et al., 2006). However, the predicted GPP departs from the GPP measured in the field, particularly in March 2018. Such discrepancies can be due to differences in the photosynthetic properties of the MPB cells and NDVI measured *in situ*. The measured *in situ* NDVI is particularly high in March 2018 compared to May and July 2015. The high NDVI value in March may be driven by the spring bloom of MPB biomass reported on the study site (Savelli et al., 2018). Such a difference with *in situ* measured NDVI in May and July is responsible of the high predicted GPP compared to the measured GPP in March 2018. Benthic chambers deployed in the field might have measured GPP of a less dense MPB biofilm at the sediment surface few meters away from NDVI measurements due to the high MPB patchiness.

The calibration of the GPP-algorithm relies on photosynthetic parameters resulting from the fitting of the Platt et al. (1980) and Eilers and Peeters (1988) P-I models on the light curves we measured in laboratory. Only one light curve was measured per season, which may not be representative of the photosyn-

thetic properties of the *in situ* MPB community. Moreover, the fit of different P-I models reveals that the scores of the adjustment is sensible to the quality of the data measured as the score of a model can vary with seasons. We suggest that more P-I measurements would be required to better estimate the photosynthetic properties of the MPB community and so the GPP by the algorithm.

Ability of the GPP-algorithm to map the current state of the mudflat

When constrained by the light and MST conditions simulated by the MARS-3D model during the satellite sensor acquisitions, the GPP predicted with the GPP-algorithm compares with the GPP measured *in situ* during the same time periods. The reported algorithm-*in situ* data discrepancies can be related to differences between the *in situ* and remotely-sensed NDVI data. The NDVI measured *in situ* at the sediment surface can depart from the remotely-sensed NDVI due to variations of the environmental conditions. In addition, the GPP-algorithm uses a vertical migration scheme of MPB biomass within the upper layer of sediment that is represented through the modulation of the total photosynthetically active biomass detected from the remotely-sensed NDVI. Such a migration scheme in the GPP-algorithm was set according to the observation of the progressive sediment covering by MPB during low tides (Herlory et al., 2004). This simplification of the process may miss the short-term variations of the MPB biomass at the sediment surface in response to light conditions during the low tide (Kromkamp et al., 1998; Perkins et al., 2001; Cartaxana et al., 2011). Moreover, the representativeness of the *in situ* NDVI data is questionable as it is inferred from highly synoptic and localised reflectance measurements. NDVI data derived from reflectances remotely-sensed by the satellite sensors dilute the *in situ* patchiness of MPB biomass in large pixels, which is likely to be more reliable to get an overview of the studied system. Consequently, and in contrast with the GPP measured *in situ*, the seasonality of the remotely-sensed GPP at the study site characterised with a spring bloom and a summer depression is consistent with previous studies (Cariou-Le Gall and Blanchard, 1995; Savelli et al., 2018). However, the differences between the GPP measured *in situ* and the remotely-sensed GPP are not fully explained by differences between the NDVI measured *in situ* and the remotely-sensed NDVI. Indeed, an *in situ*-measured NDVI higher than a remotely-sensed NDVI do not systematically corresponds to a GPP measured *in situ* higher than the remotely-sensed GPP.

The photoacclimation status of MPB cells during the sampling periods can impact the photosynthetic response of MPB cells to the light conditions prevailing during the satellite sensor acquisitions. The high photoinhibition of MPB photosynthesis at a moderate irradiance in May 2015 suggests that MPB cells were low light acclimated. Photoinhibition hence constrains the GPP predicted by the algorithm that depend on the light environment during the satellite scenes acquisitions. However, comparable light and MST conditions simulated

by the MARS-3D model two weeks before *in situ* measurements and two weeks before the satellite scenes for the three periods suggest that the light and temperature acclimation status of MPB cells during the *in situ* measurements and satellite sensor acquisition may be similar. Consequently, differences in the thermo- and photoacclimation status of MPB cells is likely to translate into limited algorithm-measurements GPP discrepancies only.

GPP-algorithm physical setting

The GPP-algorithm is well adapted for intertidal mudflat composed of fine cohesive sediments and dominated by epipelic diatoms. NDVI data are derived from spectroradiometry measurements that correspond to a proportion of the solar energy returned back to the sensor (satellite or *in situ*) after interacting with the upper sediment layer. The optical depth varies with the MPB biomass at the sediment surface, the sediment texture, the organic and water content and the wavelengths of the incident light. The length of the path of the reflected light corresponds to the photic zone, where the biomass is photosynthetically active. In muddy sediments, the photic zone rarely exceeds 500 µm (Cartaxana et al., 2011). In the present study, the NDVI data reflect the MPB biomass in the biofilm constituted by epipelic diatoms as the mud surface (Kazemipour et al., 2012). In the model of Daggers et al. (2018), the vertical distribution of the MPB biomass in the sediment is set by the formulation of Jesus et al. (2006). In their study, the sediment is sandier than our study site. As a result, light penetrates deeper in the sediment (Cartaxana et al., 2011) and the MPB biomass remotely-sensed at the sediment surface is not representative of the photosynthetically active biomass and needs to be extended in depth.

The MST and light conditions simulated by the MARS-3D model compare to the conditions observed in the field. The model-*in situ* data comparison suggests that the 3D model can resolve with confidence the physical environment experienced by MPB at the sediment surface. In regards to the frequency of the atmospheric AROME model (1 h), the simulated light conditions vary less than the observations. The 3D model cannot reproduce the observed synoptic variations of light at the sub-hourly scale that can induce a substantial variability in the MPB GPP over a low tide. In addition, the horizontal resolution of the 3D model (100 m $\times$ 100 m) may also translate into model-data discrepancies. Indeed, in regards to the MPB patchiness observed in the field, a 100 m lateral resolution implies that we compared GPP extracted from a relatively coarse grid cell with very localised *in situ* GPP measurements. Such a comparison is also made difficult as the corresponding 100 m $\times$ 100 m grid cell of the 3D model emerged $\sim$ 30 min later than the study site due to the inaccuracy in the bathymetric level. Nevertheless, as the physical conditions simulated by the model are reasonably close to the *in situ* conditions prevailing during the 2015

and 2018 field campaigns, we are confident on the ability of the GPP-algorithm to predict GPP values representative of the productive state of the mudflat.

Differences between measurements, MARS-3D and GPP-algorithm

The GPP simulated by the MARS-3D model without accounting for photoinhibition is much higher than the GPP measured *in situ*. Accounting for the photoinhibition process decreases the simulated GPP that, in turn, better compares to measurements. As the simulated MPB biomass in the biofilm lies in the range of the observations, the model-*in situ* discrepancies in the GPP can be attributed to differences in the MPB photosynthetic rate in the model and on the field. When set up with a photosynthetic rate (P^b) comparable to the observed values , GPP simulated by the 3D model better compared to *in situ* GPP measurements. As the simulated physical conditions are consistent with those prevailing during the field campaigns, they may not fully explain the reported differences in the MPB photosynthetic capacity between the 3D model and the measurements. We hence suggest that the 3D model is sensitive to the parametrisation of the MPB photosynthetic capacity when compared to highly synoptic measurements.

In the 3D model, the MPB photosynthetic parameters (α and β) are set from fitting the Platt et al. (1980) P-I model on the P-I data from Pniewski et al. (2015) at three seasons (spring, summer and fall). The relationship between the photosynthetic capacity and the MST is ruled by the model of Blanchard et al. (1996) that is parametrised for the four seasons (see Chapter 2, section 2.4.2). With this parametrisation, the purpose of the 3D model is limited to a seasonal scale and it can not reproduce precisely the hourly to daily temporal scale, contrary to the GPP-algorithm that was fitted on highly synoptic data. The GPP-algorithm predicts GPP rates consistent with measurements as it is parametrised using photosynthetic parameters (α, β, P_s^b, P_{max}^b and I_{opt}) estimated on the basis of time-coincident field campaigns. Interestingly, the 3D model-*in situ* GPP data comparison suggests a potential impact of photoinhibition, especially in July 2015. This result echoes to the Chapter 5 conclusions which suggest the potential importance of MPB photoinhibition in summer on the Brouage mudflat.

CONCLUSIONS

We developed a GPP-algorithm that combines data from satellite remote sensing scenes with data derived from laboratory measurements and a 3D physical model. The algorithm is constrained by realistic simulated two-dimensional (2D) fields of tidal heights, MST and PAR. It is parametrised by NDVI-specific photosynthetic parameters estimated from laboratory measurements and expressed in carbon fixation rates hence limiting possible bias due to unit conversions. This study shows that:

- The NDVI data retrieved from the SPOT 6 and Pleaides sensors are consistent with the seasonality of the MPB biomass reported for the study site and their range are comparable to NDVI data from other mudflats;
- The GPP-algorithm succeeds in reproducing MPB GPP rates in the range of *in situ* GPP measurements and the seasonal variability of GPP;
- The GPP-algorithm is well adapted to intertidal mudflats mostly composed by fine cohesive sediments dominated by epipelic diatoms and could be applied for similar environments.

The horizontal resolution of the MARS-3D model (100 m) is lower than the SPOT 6 and Pleiades sensors resolution (6 m and 2 m, respectively). A finer horizontal mesh of the bathymetry and of the simulated water height might improve the simulated emersion-immersion cycles, MST and light fields and thus, GPP. While the GPP-algorithm might prove useful to monitor MPB GPP at the scale of an entire mudflat, it will be limited by the still too low spectral resolution of the multispectral (3-10 bands) satellite sensors. Airborne hyperspectral (hundreds of bands) data could complement such satellite remote sensing data in a era of remote sensing drone aircraft democratisation (Launeau et al., 2018). A first hyperspectral index, the MPB_{LUE} was recently developed to estimate a GPP proxy (= Electron Transfer Rate or ETR) using laboratory experiments (Méléder et al., 2018). Such an index can be promising, but it must also be validated with *in situ* measurements before to be applied to hyperspectral data. The GPP comparison with the 3D physical-biological coupled model underlines the caution to set a realistic photosynthetic capacity in both the numerical model and remote sensing algorithm. The accurate estimation of the photosynthetic response of MPB to its highly variable environment is a challenge in a perspective of quantifying MPB PP over large mudflats from a synoptic to inter-annual time scale.

CHAPTER VII

CONCLUSIONS

7

CONCLUSIONS

Acronyms:
MPB: *Microphytobenthos*
PP: *Primary Production*

We developed a physical-biological coupled model in close association with observational data to infer on the spatial and temporal dynamics of MPB in the Brouage intertidal mudflat. Gastropod *Peringia ulvae* was for the first time represented explicitly as a state variable in a mass flux model. The model simulated consistent MPB biomass levels and primary production (PP) rates. It also simulated a realistic seasonal dynamics of MPB and *P. ulvae*. Part of the novelty of the thesis relies on the approach that combines physical-biological modelling, remote sensing, and *in situ* data analysis. Such an approach allowed us to answer the objective of the thesis and to bring new insights on MPB dynamics in intertidal mudflats at temperate latitudes:

- The combination of light and temperature are intrinsically responsible of the seasonal cycle of MPB on the intertidal mudflat. Light is the main limiting driver, especially in fall and winter. When light levels increase along with mud surface temperature in spring, it drives the MPB spring bloom in terms of biomass and PP. In summer, high mud surface temperature drives the thermoinhibition of MPB PP. At saturating light levels, photoinhibition of MPB PP can potentially superimpose on thermoinhibition in spring and summer. With more frequent and longer emersion periods, the upper shore of the mudflat receives higher amount of light and might experience stronger photoinhibition than the lower shore. However, the lower shore might be more sensitive to photoinhibition due to its low MPB biomass, PP and its emersion periods restricted to high light levels. Grazing and resuspension of MPB biomass add to the intrinsic MPB seasonal cycle. Both processes shape the dynamics of the photosynthetically active and competent biomass. Grazing pressure by *P. ulvae* increases in late-spring with increasing MPB biomass and combines with the already low thermoinhibited MPB PP in summer. Grazing and temperature are responsible of a seasonal depletion of the MPB biomass. In addition, bioturbation resulting from the *P. ulvae* activity lead to a substantial chronic export of MPB biomass from the sediment to the water column in spring and summer. Waves significantly contribute to the MPB resuspension through massive resuspension events in winter, spring and fall. At the tidal scale, MPB resuspension occurs mostly at the flood beginning and at the end of ebb, and is enhanced during spring tides.

- The annual export of MPB biomass from the sediment to the water column accounts for almost 50 % of the MPB annual PP. The export is high

in spring with the effect of both chronic and massive MPB resuspension events. Furthermore, the occurrence of the spring bloom of MPB biomass in the sediment results into a high biostabilisation of the sediment and thus to an accumulation of MPB biomass in the sediment. This positive feedback enhances the export of MPB biomass once the sediment is eroded. The export of MPB from the sediment to the water column is the highest in winter and spring and represents one third of the MPB annual PP.

- Combining for the first time remote sensing data with outputs of the physical-biological coupled model into a single algorithm led us to provide the first estimates of the MPB PP at the whole Brouage mudflat scale. We produced maps of MPB PP that showed a good agreement with *in situ* measurements. The comparison with PP simulated by the tri-dimensional (3D) physical-biological coupled model was less satisfactory but it underlines future ways of improving MPB predictions at the mudflat scale along with the future development of remote sensing.

CHAPTER VIII

PERSPECTIVES

8

PERSPECTIVES

Acronyms:
MPB: *Microphytobenthos*
PP: *Primary Production*

The developments made during the thesis pave the way for a better understanding and assessment of the export flux of biogenic matter from the land-ocean interface to the coastal ocean. In addition to bring new insights on the MPB dynamics, this work proposes new numerical tools to monitor and predict MPB primary production (PP) and its fate in coastal waters in a context of climate change.

THE FATE OF MPB-DERIVED ORGANIC CARBON

In the water column, MPB can be subject to grazing, senescence, deposition and advective-diffusive transport (MacIntyre et al., 1996; Miller et al., 1996; Guizien et al., 2014). Once resuspended, MPB can grow and contribute to the PP of coastal waters by producing fresh carbon through photosynthesis in the water column under favourable light and nutrients conditions (Guarini et al., 2008b; Polsenaere et al., 2012). In the thesis, processes such as advection-diffusion, grazing or growth were not considered in the one-dimensional (1D) model (Chapter 3 and 4). In the tri-dimensional (3D) model, the absence of wave forcings excluded any representation of the lateral and vertical export of resuspended MPB biomass. A next step would be the coupling of the MPB model including the resuspension processes into ocean-biogeochemical coupled 3D models that resolve the 3D fields of advection and diffusion in the water column, the two-dimensional (2D) fields of wave parameters and the planktonic ecosystem. Such an approach would allow an assessment of benthopelagic MPB fluxes driven by the action of waves and tidal currents and of the lateral and vertical flux of resuspended MPB biomass within the water column.

In addition, such an approach would allow to quantify the contribution of resuspended MPB to the pelagic PP. In the field, this contribution can be assessed by combining atmospheric and aquatic eddy covariance measurements. The atmospheric eddy covariance measures at high frequency CO_2 fluxes at the air-water and air-sediment interfaces during high and low tides, respectively (Baldocchi et al., 1988; Aubinet et al., 1999; Zemmelink et al., 2009; Polsenaere et al., 2012). The aquatic eddy covariance measures benthic O_2 fluxes at the sediment-water interface (Berg et al., 2003). Consequently, the measurement of metabolic fluxes (production, respiration) both in the water and in the atmosphere during high and low tides would allow us to detect changes in CO_2 fluxes at air-water interface, a marker of MPB resuspension. Tracking the fate of MPB organic carbon in coastal waters would open the door to an accurate

estimation of the contribution of productive intertidal biofilms to the coastal carbon cycle.

MPB IN A CONTEXT OF CLIMATE CHANGE

In 2019 and for the first time in Human history (3 billions years ago), the CO_2 atmospheric concentration reached 415 ppm (NOAA, 2019). By the end of the century, it could increase by 200 % in the worst IPCC climate change scenario (RCP 8.5; IPCC, 2014). Under such a scenario, the global mean surface temperature would rise by 4.3 °C by 2081-2100 compared to 1850-1900 (IPCC, 2019). In addition, the global mean sea level will rise by 0.84 m in 2100 with respect to 1986-2005 (IPCC, 2019).

The consequences of climate change on the MPB PP are uncertain. The response of MPB to increasing temperature is uncertain as seasonal response of primary production can compensate. The predicted increase in frequency of high temperature events (IPCC, 2013) might induce longer and stronger periods of MPB thermoinhibition in summer. With regard to benthic MPB grazers, a temperature increase could promote their metabolism. Consequently, the top-down control on MPB might increase and induce a depletion of MPB biomass. This hypothesis relies on the metabolic theory of ecology, which states that chemical reactions are generally stimulated by temperature and that feeding, growth and reproduction by heterotroph are more strongly stimulated than photosynthesis of autotrophs (Brown et al., 2004; López-Urrutia et al., 2006). In the model developed in the thesis, the ingestion of MPB by *P. ulvae* is asymptotic at high temperature, which limits the increase of grazing with increasing temperature. Nevertheless, further work is needed to assess the effect of increasing temperature on both MPB and benthic grazers.

By 2100, ~ 48 % of the global coastline could experience change in its wave regime due to modifications of off-shore wave parameters (significant wave height, wave period, wave direction) under the most pessimistic IPCC climate change scenario (RCP 8.5; Morim et al., 2019). Combined with sea-level rise, it might result in a decrease of intertidal areas (Pethick and Crooks, 2000; Fujii, 2012). Murray et al. (2019) already detected a global decrease by 3 % of tidal flats since 1999. In addition, the existence of coastal defences might imped the landward migration of tidal flats and salt marshes, resulting in the narrowing of those areas (Carpenter and Pye, 1996; Fujii, 2012).

To conclude, the pressure on the MPB PP is high and the MPB responses might be multiple. MPB are not accounted for in global ocean biogeochemical model as their horizontal resolution is too coarse to account for coastal processes such as benthic PP. However, it would be interesting to implement MPB processes into high resolution regional coastal models that resolve benthic habitats. They could be further constrained by downscaled global climate models forced by the IPCC scenarios of climate change in order to identify the drivers

of the future response of MPB dynamics and to quantify the global variability of MPB PP in a changing climate.

COMBINING MODELLING AND REMOTE SENSING: A PROMISING TOOL TO MONITOR MPB

With the improvement of satellites and on board sensors (*i.e.* bands, horizontal resolution, revisit time), remote sensing is a very relevant tool to cover large spatial scales. The use of remote sensing data in the thesis provides additional support to modelling and enlarges the spatial extent of *in situ* observations. The many earth-observation satellites and the different on board sensors open the door to a diversity of applications rather than just synoptic maps of MPB biomass. The deployment of hyperspectral broadband sensors is promising as more MPB biofilms properties such as MPB PP can be inferred from high spectral resolution images (Méléder et al., 2018). Time series of remote sensing data is already and could be an even more powerful tool to monitor the MPB biomass and PP at the mudflat scale.

We expect the thesis could be seen as an example of how physical-biological models could be helpful to bring new insights on the underlying processes of observations. However, it is important to note that we were confronted to a limited set of data for the validation of the model because too few observations repeated in time and space were available. In the future, we could expect the implementation of fixed monitoring stations allowing high-frequency measurements, such as benthic and in-water fluorometry and gases exchanges sensors (eddy covariance) for PP estimation. Nevertheless, the model developed during the thesis could be a relevant tool that might be used to monitor and predict the MPB dynamics on intertidal mudflats at the seasonal, annual and inter-annual scales and ultimately to improve our knowledge on the fate of MPB carbon in the coastal ocean or the response of MPB to climate change.

9

BIBLIOGRAPHY

BIBLIOGRAPHY

Admiraal, W.: Salinity tolerance of benthic estuarine diatoms as tested with a rapid polarographic measurement of photosynthesis, Marine Biology, 39, 11–18, 1976.

Admiraal, W.: Tolerance of estuarine benthic diatoms to high concentrations of ammonia, nitrite ion, nitrate ion and orthophosphate, Marine Biology, 43, 307–315, 1977.

Admiraal, W.: The ecology of estuarine sediment inhabiting diatoms, Progress in Phycological Research, 3, 269–314, 1984.

Admiraal, W. and Peletier, H.: Distribution of diatom species on an estuarine mud flat and experimental analysis of the selective effect of stress, Journal of Experimental Marine Biology and Ecology, 46, 157 – 175, 1980.

Admiraal, W., Bouwman, L. A., Hoekstra, L., and Romeyn, K.: Qualitative and quantitative interactions between microphytobenthos and herbivorous meiofauna on a brackish intertidal mudflat, International Review of Hydrobiology, 68, 175–191, 1983.

Andersen, T., Fredsoe, J., and Pejrup, M.: In situ estimation of erosion and deposition thresholds by Acoustic Doppler Velocimeter (ADV), Estuarine, Coastal and Shelf Science, 75, 327–336, 2007.

Andersen, T. J.: Seasonal variation in erodibility of two temperate, microtidal mudflats, Estuarine, Coastal and Shelf Science, 53, 1–12, 2001.

Androuin, T., Polerecky, L., Decottignies, P., Dubois, S., Dupuy, C., Hubas, C., Jesus, B., Le Gall, E., Marzloff, M., and Carlier, A.: Subtidal microphytobenthos: a secret garden stimulated by the engineer species Crepidula fornicata, Frontiers in Marine Science, 5, 475, 2018.

Ardia, D., Mullen, K., Peterson, B., Ulrich, J., Boudt, K., and Mullen, M. K.: Package 'DEoptim', 2016.

Ariathurai, R. and Krone, R. B.: Finite element model for cohesive sediment transport, Journal of the Hydraulics Division, 102, 323–338, 1976.

Arkema, K. K., Guannel, G., Verutes, G., Wood, S. A., Guerry, A., Ruckelshaus, M., Kareiva, P., Lacayo, M., and Silver, J. M.: Coastal habitats shield people and property from sea-level rise and storms, Nature Climate Change, 3, 913, 2013.

Armonies, W. and Hartke, D.: Floating of mud snails Hydrobia ulvae in tidal waters of the Wadden Sea, and its implications in distribution patterns, Helgoländer Meeresuntersuchungen, 49, 529, 1995.

Asmus, H.: Benthic grazers and suspension feeders: Which one assumes the energetic dominance in Königshafen?, Helgoländer Meeresuntersuchungen, 48, 217, 1994.

Asmus, H. and Asmus, R.: The importance of grazing food chain for energy flow and production in three intertidal sand bottom communities of the northern Wadden Sea, Helgoländer Meeresuntersuchungen, 39, 273, 1985.

Aubinet, M., Grelle, A., Ibrom, A., Rannik, Ü., Moncrieff, J., Foken, T., Kowalski, A. S., Martin, P., Berbigier, P., Bernhofer, C., et al.: Estimates of the annual net carbon and water exchange of forests: the EUROFLUX methodology, in: Advances in ecological research, 113–175 vol. 30, Elsevier, 1999.

Austen, I., Andersen, T. J., and Edelvang, K.: The influence of benthic diatoms and invertebrates on the erodibility of an intertidal mudflat, the Danish Wadden Sea, Estuarine, Coastal and Shelf Science, 49, 99–111, 1999.

Baillie, P. W. and Welsh, B. L.: The effect of tidal resuspension on the distribution of intertidal epipelic algae in an estuary, Estuarine and Coastal Marine Science, 10, 165–180, 1980.

Baldocchi, D. D., Hincks, B. B., and Meyers, T. P.: Measuring biosphere-atmosphere exchanges of biologically related gases with micrometeorological methods, Ecology, 69, 1331–1340, 1988.

Bannister, T. T.: Quantitative description of steady state, nutrient-saturated algal growth, including adaptation, Limnology and Oceanography, 24, 76–96, 1979.

Baretta, J., Ebenhöh, W., and Ruardij, P.: The European regional seas ecosystem model, a complex marine ecosystem model, Netherlands Journal of Sea Research, 33, 233–246, 1995.

Barnett, A., Méléder, V., Blommaert, L., Lepetit, B., Gaudin, P., Vyverman, W., Sabbe, K., Dupuy, C., and Lavaud, J.: Growth form defines physiological photoprotective capacity in intertidal benthic diatoms, The ISME journal, 9, 32, 2015.

Barranguet, C., Kromkamp, J. C., and Peene, J.: Factors controlling primary production and photosynthetic characteristics of intertidal microphytobenthos, Marine Ecology Progress Series, 173, 117–126, 1998.

Bassoullet, P., Le Hir, P., Gouleau, D., and Robert, S.: Sediment transport over an intertidal mudflat: field investigations and estimation of fluxes within

the "Baie de Marennes-Oléron"(France), Continental shelf research, 20, 1635–1653, 2000.

Battjes, J. A. and Janssen, J.: Energy loss and set-up due to breaking of random waves, Coastal Engineering Proceedings, 1, 1978.

Belin, C. and Raffin, B.: REPHY (Réseau de suivi du phytoplancton) : Inventaire cartographique des points de prélèvements (1990), Technical document, France, 1990.

Benyoucef, I., Blandin, E., Lerouxel, A., Jesus, B., Rosa, P., Méléder, V., Launeau, P., and Barillé, L.: Microphytobenthos interannual variations in a north-European estuary (Loire estuary, France) detected by visible-infrared multispectral remote sensing, Estuarine, Coastal and Shelf Science, 136, 43–52, 2014.

Berg, P., Røy, H., Janssen, F., Meyer, V., Jørgensen, B. B., Huettel, M., and de Beer, D.: Oxygen uptake by aquatic sediments measured with a novel non-invasive eddy-correlation technique, Marine Ecology Progress Series, 261, 75–83, 2003.

Bertin, X., Chaumillon, E., Sottolichio, A., and Pedreros, R.: Tidal inlet response to sediment infilling of the associated bay and possible implications of human activities: the Marennes-Oléron Bay and the Maumusson Inlet, France, Continental Shelf Research, 25, 1115–1131, 2005.

Bertin, X., Bruneau, N., Breilh, J.-F., Fortunato, A. B., and Karpytchev, M.: Importance of wave age and resonance in storm surges: The case Xynthia, Bay of Biscay, Ocean Modelling, 42, 16–30, 2012.

Bidlot, J.-R., Janssen, P., and Abdalla, S.: A revised formulation of ocean wave dissipation and its model impact, ECMWF Tech. Memo., 509, 2007.

Blackford, J.: The influence of microphytobenthos on the Northern Adriatic ecosystem: a modelling study, Estuarine, Coastal and Shelf Science, 55, 109–123, 2002.

Blanchard, G. F.: Measurement of meiofauna grazing rates on microphytobenthos: is primary production a limiting factor?, Journal of Experimental Marine Biology and Ecology, 147, 37–46, 1991.

Blanchard, G. F. and Cariou-Le Gall, V.: Photo synthetic characteristics of microphytobenthos in Marennes-Oléron Bay, France: Preliminary results, Journal of experimental marine biology and ecology, 182, 1–14, 1994.

Blanchard, G. F., Guarini, J.-M., Richard, P., Gros, P., and Mornet, F.: Quantifying the short-term temperature effect on light- saturated photosynthesis of intertidal microphytobenthos, Marine Ecology Progress Series, 134, 309–313, 1996.

Blanchard, G. F., Guarini, J.-M., Gros, P., and Richard, P.: Seasonal effect on the relationship between the photosynthetic capacity of intertidal microphytobenthos and temperature, Journal of Phycology, 33, 723–728, 1997a.

Blanchard, G. F., Sauriau, P.-G., Cariou-Le Gall, V., Gouleau, D., Garet, M., and Olivier, F.: Kinetics of tidal resuspension of microbiota:testing the effects of sediment cohesiveness and bioturbation using flume experiments, Marine Ecology Progress Series, 151, 17–25, 1997b.

Blanchard, G. F., Guarini, J.-M., Provot, L., Richard, P., and Sauriau, P.-G.: Measurement of ingestion rate of Hydrobia ulvae (Pennant) on intertidal epipelic microalgae: the effect of mud snail density, Journal of Experimental Marine Biology and Ecology, 255, 247–260, 2000a.

Blanchard, G. F., Paterson, D. M., Stal, L., Richard, P., Galois, R., Huet, V., Kelly, J., Honeywill, C., de Brouwer, J., Dyer, K., Christie, M., and Seguignes, M.: The effect of geomorphological structures on potential biostabilisation by microphytobenthos on intertidal mudflats, Continental Shelf Research, 20, 1243 – 1256, 2000b.

Blanchard, G. F., Guarini, J.-M., Dang, C., and Richard, P.: Characterizing and quantifying photoinhibition in intertidal microphytobenthos, Journal of phycology, 40, 692–696, 2004.

Blanchard, G. F., Agion, T., Guarini, J.-M., Herlory, O., and Richard, P.: Analysis of the short-term dynamics of microphytobenthos biomass on intertidal mudflats, Verhandelingen van de Koninklijke Nederlandse Akademie van Wetenschappen-Natuurkunde-Ser 2, 103, 85–98, 2006.

Blanchard, G. F., Simon-Bouhet, B., and Guarini, J.-M.: Properties of the dynamics of intertidal microphytobenthic biomass, Journal of the Marine Biological Association of the United Kingdom, 82, 1027–1028, 2002.

Blum, M. D. and Roberts, H. H.: Drowning of the Mississippi Delta due to insufficient sediment supply and global sea-level rise, Nature Geoscience, 2, 488, 2009.

Blumberg, A. F. and Mellor, G. L.: A description of a three-dimensional coastal ocean circulation model, Three-dimensional coastal ocean models, 4, 1–16, 1987.

Bocher, P., Piersma, T., Dekinga, A., Kraan, C., Yates, M. G., Guyot, T., Folmer, E. O., and Radenac, G.: Site-and species-specific distribution patterns of molluscs at five intertidal soft-sediment areas in northwest Europe during a single winter, Marine Biology, 151, 577–594, 2007.

Bondoc, K. G. V., Heuschele, J., Gillard, J., Vyverman, W., and Pohnert, G.: Selective silicate-directed motility in diatoms, Nature Communications, 7, 10 540, 2016.

Bondoc, K. G. V., Lembke, C., Lang, S. N., Germerodt, S., Schuster, S., Vyverman, W., and Pohnert, G.: Decision-making of the benthic diatom Seminavis robusta searching for inorganic nutrients and pheromones, The ISME journal, 13, 537, 2019a.

Bondoc, V. K. G., Lembke, C., Vyverman, W., and Pohnert, G.: Selective chemoattraction of the benthic diatom Seminavis robusta to phosphate but not to inorganic nitrogen sources contributes to biofilm structuring, MicrobiologyOpen, 8, e00 694, 2019b.

Brito, A., Newton, A., Fernandes, T., and Tett, P.: The role of microphytobenthos on shallow coastal lagoons: A modelling approach, Biogeochemistry, 106, 207–228, 2011.

Brito, A. C., Newton, A., Tett, P., Icely, J., and Fernandes, T. F.: The yield of microphytobenthic chlorophyll from nutrients: enriched experiments in microcosms, Journal of Experimental Marine Biology and Ecology, 384, 30–43, 2010.

Brito, A. C., Benyoucef, I., Jesus, B., Brotas, V., Gernez, P., Mendes, C. R., Launeau, P., Dias, M. P., and Barillé, L.: Seasonality of microphytobenthos revealed by remote-sensing in a South European estuary, Continental Shelf Research, 66, 83–91, 2013.

Britton, C. and Dodd, J.: Relationships of photosynthetically active radiation and shortwave irradiance, Agricultural Meteorology, 17, 1–7, 1976.

Brock, T. D.: Calculating solar radiation for ecological studies, Ecological Modelling, 14, 1–19, 1981.

Brotas, V. and Serôdio, J.: A mathematical model for the vertical distribution of chlorophyll A in estuarine intertidal sediments, Netherlands Journal of Aquatic Ecology, 29, 315–321, 1995.

Brown, J. H., Gillooly, J. F., Allen, A. P., Savage, V. M., and West, G. B.: Toward a metabolic theory of ecology, Ecology, 85, 1771–1789, 2004.

Brunet, C., Johnsen, G., Lavaud, J., and Roy, S.: Pigments and photoacclimation processes, 2011.

Cadée, G. and Hegeman, J.: Primary production of the benthic microflora living on tidal flats in the dutch wadden sea, Netherlands Journal of Sea Research, 8, 260–291, 1974.

Cadée, G. and Hegeman, J.: Distribution of primary production of the benthic microflora and accumulation of organic matter on a tidal flat area, Balgzand, Dutch Wadden Sea, Netherlands Journal of Sea Research, 11, 24–41, 1977.

Cahoon, L.: The role of benthic microalgae in neritic ecosystems, Oceanogr. Mar. Biol., 37, 47–86, 1999.

Campbell, S. J., McKenzie, L. J., and Kerville, S. P.: Photosynthetic responses of seven tropical seagrasses to elevated seawater temperature, Journal of Experimental Marine Biology and Ecology, 330, 455–468, 2006.

Cariou-Le Gall, V. and Blanchard, G. F.: Monthly HPLC measurements of pigment concentration from an intertidal muddy sediment of Marennes-Oleron Bay, France, Marine Ecology Progress Series, 121, 171–180, 1995.

Carling, P., Williams, J., Croudace, I., and Amos, C.: Formation of mud ridge and runnels in the intertidal zone of the Severn Estuary, UK, Continental Shelf Research, 29, 1913–1926, 2009.

Carlton, J. T. and Hodder, J.: Maritime mammals: terrestrial mammals as consumers in marine intertidal communities, Marine Ecology Progress Series, 256, 271–286, 2003.

Carpenter, K. and Pye, K.: Saltmarsh change in England and Wales: Its history and causes, Environment Agency, 1996.

Cartaxana, P., Ruivo, M., Hubas, C., Davidson, I., Serôdio, J., and Jesus, B.: Physiological versus behavioral photoprotection in intertidal epipelic and epipsammic benthic diatom communities, Journal of experimental marine biology and ecology, 405, 120–127, 2011.

Cartaxana, P., Domingues, N., Cruz, S., Jesus, B., Laviale, M., Serôdio, J., and da Silva, J. M.: Photoinhibition in benthic diatom assemblages under light stress, Aquatic Microbial Ecology, 70, 87–92, 2013.

Cartaxana, P., Vieira, S., Ribeiro, L., Rocha, R. J., Cruz, S., Calado, R., and da Silva, J. M.: Effects of elevated temperature and CO 2 on intertidal microphytobenthos, BMC ecology, 15, 10, 2015.

Cartaxana, P., Ribeiro, L., Goessling, J., Cruz, S., and Kühl, M.: Light and O2 microenvironments in two contrasting diatom-dominated coastal sediments, Marine Ecology Progress Series, 545, 2016.

Chalker, B.: Simulating light-saturation curves for photosynthesis and calcification by reef-building corals, Marine Biology, 63, 135–141, 1981.

Chen, L., Li, Z.-B., Hui, C., Cheng, X., Li, B.-L., and Shi, P.-J.: A general method for parameter estimation in light-response models, Scientific reports, 6, 27 905, 2016.

Chen, X., Zhang, C., Zhou, Z., Gong, Z., Zhou, J., Tao, J., Paterson, D. M., and Feng, Q.: Stabilizing effects of bacterial biofilms: EPS penetration and redistribution of bed stability down the sediment profile, Journal of Geophysical Research: Biogeosciences, 122, 3113–3125, 2017.

Chennu, A., Volkenborn, N., De Beer, D., Wethey, D. S., Woodin, S. A., and Polerecky, L.: Effects of bioadvection by Arenicola marina on microphytobenthos in permeable sediments, PloS one, 10, e0134 236, 2015.

Christie, M., Dyer, K., and Turner, P.: Sediment flux and bed level measurements from a macrotidal mudflat, Estuarine, Coastal and Shelf Science, 49, 667–688, 1999.

Cibic, T., Blasutto, O., Burba, N., and Umani, S. F.: Microphytobenthic primary production as 14C uptake in sublittoral sediments of the Gulf of Trieste (northern Adriatic Sea): methodological aspects and data analyses, Estuarine, Coastal and Shelf Science, 77, 113–122, 2008.

Cloern, J. E.: Turbidity as a control on phytoplankton biomass and productivity in estuaries, 1367–1381 Continental shelf research, 1987.

Cloern, J. E.: Our evolving conceptual model of the coastal eutrophication problem, Marine ecology progress series, 210, 223–253, 2001.

Cloern, J. E., Grenz, C., and Vidergar-Lucas, L.: An empirical model of the phytoplankton chlorophyll: carbon ratio-the conversion factor between productivity and growth rate, Limnology and Oceanography, 40, 1313–1321, 1995.

Coelho, H., Vieira, S., and Serôdio, J.: Effects of desiccation on the photosynthetic activity of intertidal microphytobenthos biofilms as studied by optical methods, Journal of Experimental Marine Biology and Ecology, 381, 98–104, 2009.

Coelho, H., Cartaxana, P., Brotas, V., Queiroga, H., and Serôdio, J.: Pheophorbide a in Hydrobia ulvae faecal pellets as a measure of microphytobenthos ingestion: Variation over season and period of day, Aquatic Biology, 13, 119–126, 2011.

Coelho, J., Flindt, M., Jensen, H. S., Lillebø, A., and Pardal, M.: Phosphorus speciation and availability in intertidal sediments of a temperate estuary: relation to eutrophication and annual P-fluxes, Estuarine, Coastal and Shelf Science, 61, 583–590, 2004.

Cohn, S. A., Farrell, J. F., Munro, J. D., Ragland, R. L., Weitzell Jr, R. E., and Wibisono, B. L.: The effect of temperature and mixed species composition on diatom motility and adhesion, Diatom Research, 18, 225–243, 2003.

Como, S., Lefrancois, C., Maggi, E., Antognarelli, F., and Dupuy, C.: Behavioral responses of juvenile golden gray mullet Liza aurata to changes in coastal temperatures and consequences for benthic food resources, Journal of sea research, 92, 66–73, 2014.

Consalvey, M., Paterson, D. M., and Underwood, G. J. C.: The ups and downs of life in a benthic biofilm: migration of benthic diatoms, Diatom Research, 19, 181–202, 2004.

Cook, P. L., Butler, E. C., and Eyre, B. D.: Carbon and nitrogen cycling on intertidal mudflats of a temperate Australian estuary. I. Benthic metabolism, Marine Ecology Progress Series, 280, 25–38, 2004.

Daehnick, A., Sullivan, M., and Moncreiff, C.: Primary production of the sand microflora in seagrass beds of Mississippi Sound, Botanica Marina, 35, 131–140, 1992.

Daggers, T. D., Kromkamp, J. C., Herman, P. M., and Van Der Wal, D.: A model to assess microphytobenthic primary production in tidal systems using satellite remote sensing, Remote sensing of environment, 211, 129–145, 2018.

Davis, W. R.: The role of bioturbation in sediment resuspension and its interaction with physical shearing, Journal of Experimental Marine Biology and Ecology, 171, 187–200, 1993.

de Jong, D. J. and de Jonge, V. N.: Dynamics and distribution of microphytobenthic chlorophyll-a in the Western Scheldt estuary (SW Netherlands), Hydrobiologia, 311, 21–30, 1995.

de Jong, S., Hofman, P., and Sandee, A.: Construction and calibration of a rapidly responding pH mini-electrode: Application to intertidal sediments., Marine ecology progress series. Oldendorf, 45, 187–192, 1988.

de Jonge, V. N.: Fluctuations in the organic carbon to chlorophyll a ratios for estuarine benthic diatom populations, 345–353 Marine Ecology Progress Series, 1980.

de Jonge, V. N. and van Beusekom, J. E. E.: Contribution of resuspended microphytobenthos to total phytoplankton in the EMS estuary and its possible role for grazers, Netherlands Journal of Sea Research, 30, 91–105, 1992.

de Jonge, V. N. and van Beusekom, J. E. E.: Wind and tide-induced resuspension of sediment and microphytobenthos from tidal flats in the Ems estuary, Limnology and Oceanography, 40, 776–778, 1995.

de Jonge, V. N., de Boer, W. F., de Jong, D. J., and Brauer, V. S.: Long-term mean annual microphytobenthos chlorophyll a variation correlates with air temperature, Marine Ecology Progress Series, 468, 43–56, 2012.

Deborde, J., Anschutz, P., Auby, I., Glé, C., Commarieu, M.-V., Maurer, D., Lecroart, P., and Abril, G.: Role of tidal pumping on nutrient cycling in a temperate lagoon (Arcachon Bay, France), Marine Chemistry, 109, 98–114, 2008.

Decho, A. W.: Microbial exopolymer secretions in ocean environments: their role (s) in food webs and marine processes, Oceanogr Mar Biol, 28, 9–16, 1990.

Decho, A. W.: Microbial biofilms in intertidal systems: an overview, Continental shelf research, 20, 1257–1273, 2000.

Defew, E., Perkins, R., and Paterson, D. M.: The influence of light and temperature interactions on a natural estuarine microphytobenthic assemblage, Biofilms, 1, 21–30, 2004.

Demers, S., Therriault, J.-C., Bourget, E., and Bah, A.: Resuspension in the shallow sublittoral zone of a macrotidal estuarine environment: Wind influence, Limnology and Oceanography, 32, 327–339, 1987.

Denis, L., Gevaert, F., and Spilmont, N.: Microphytobenthic production estimated by in situ oxygen microprofiling: Short-term dynamics and carbon budget implications, Journal of Soils and Sediments, 12, 1517–1529, 2012.

Deppe, F.: Intertidal mudflats worldwide, Common Wadden Sea Secretariat (CWSS), Wilhelmshaven, 100, 2000.

Dizon, R. and Yap, H.: Short-term responses of coral reef microphytobenthic communities to inorganic nutrient loading, Limnology and Oceanography, 44, 1259–1267, 1999.

Dodds, W., Biggs, B., and Lowe, R.: Photosynthesis-irradiance patterns in benthic microalgae: Variations as a function of assemblage thickness and community structure, Journal of Phycology, 35, 42–53, 1999.

Duarte, C. M., Middelburg, J. J., and Caraco, N.: Major role of marine vegetation on the oceanic carbon cycle, Biogeosciences discussions, 1, 659–679, 2004.

Dupuy, C., Mallet, C., Guizien, K., Montanié, H., Bréret, M., Mornet, F., Fontaine, C., Nérot, C., and Orvain, F.: Sequential resuspension of biofilm components (viruses, prokaryotes and protists) as measured by erodimetry experiments in the Brouage mudflat (French Atlantic coast), Journal of sea research, 92, 56–65, 2014.

Duraiappah, A. K., Naeem, S., Agardy, T., Ash, N. J., Cooper, H. D., Diaz, S., Faith, D. P., Mace, G., McNeely, J. A., Mooney, H. A., et al.: Ecosystems and human well-being: synthesis; a report of the Millennium Ecosystem Assessment, Island, Washington, DC, 2005.

Echappé, C., Gernez, P., Méléder, V., Jesus, B., Cognie, B., Decottignies, P., Sabbe, K., and Barillé, L.: Satellite remote sensing reveals a positive impact of living oyster reefs on microalgal biofilm development, Biogeosciences, 15, 905–918, 2018.

Edgar, L. A. and Pickett-Heaps, J. D.: The mechanism of diatom locomotion. I. An ultrastructural study of the motility apparatus, Proceedings of the Royal Society of London. Series B. Biological Sciences, 218, 331–343, 1983.

Eilers, P. and Peeters, J.: A model for the relationship between light intensity and the rate of photosynthesis in phytoplankton, Ecological Modelling, 42, 199 – 215, 1988.

Engel, F. G., Alegria, J., Andriana, R., Donadi, S., Gusmao, J. B., van Leeuwe, M. A., Matthiessen, B., and Eriksson, B. K.: Mussel beds are biological power stations on intertidal flats, Estuarine, Coastal and Shelf Science, 191, 21–27, 2017.

Ezequiel, J., Laviale, M., Frankenbach, S., Cartaxana, P., and Serôdio, J.: Photoacclimation state determines the photobehaviour of motile microalgae: the case of a benthic diatom, Journal of Experimental Marine Biology and Ecology, 468, 11–20, 2015.

Fagherazzi, S. and Mariotti, G.: Mudflat runnels: Evidence and importance of very shallow flows in intertidal morphodynamics, Geophysical Research Letters, 39, 2012.

Feuillet-Girard, M., Gouleau, D., Blanchard, G. F., and Joassard, L.: Nutrient fluxes on an intertidal mudflat in Marennes-Oléron Bay, and influence of the emersion period, Aquatic Living Resources, 10, 49–58, 1997.

Fleming, R. H.: The control of diatom populations by grazing, ICES Journal of Marine Science, 14, 210–227, 1939.

Fonseca, A., Brandini, N., da Costa Machado, E., and Brandini, F. P.: Variação espacial e sazonal da produção primária microfitobêntica em uma planície entremarés subtropical, Baía de Paranaguá, Paraná-Brasil, INSULA Revista de Botânica, 37, 19, 2008.

French, J. R., Burningham, H., and Benson, T.: Tidal and Meteorological Forcing of Suspended Sediment Flux in a Muddy Mesotidal Estuary, Estuaries and Coasts, 31, 843, 2008.

French Observation and Monitoring program for Phytoplankton and Hydrology in coastal waters: REPHY dataset - French Observation and Monitoring program for Phytoplankton and Hydrology in coastal waters. 1987-2016 Metropolitan data, 2017.

Fujii, T.: Climate change, sea-level rise and implications for coastal and estuarine shoreline management with particular reference to the ecology of intertidal benthic macrofauna in NW Europe, Biology, 1, 597–616, 2012.

Galván, K., Fleeger, J. W., and Fry, B.: Stable isotope addition reveals dietary importance of phytoplankton and microphytobenthos to saltmarsh infauna, Marine Ecology Progress Series, 359, 37–49, 2008.

García-Robledo, E., Corzo, A., Papaspyrou, S., Jiménez-Arias, J. L., and Villahermosa, D.: Freeze-lysable inorganic nutrients in intertidal sediments: Dependence on microphytobenthos abundance, Marine Ecology Progress Series, 403, 155–163, 2010.

Garcia-Robledo, E., Bohorquez, J., Corzo, A., Jimenez-Arias, J. L., and Papaspyrou, S.: Dynamics of inorganic nutrients in intertidal sediments: Porewater, exchangeable, and intracellular pools, Frontiers in Microbiology, 7, 2016.

Geider, R. J., Maclntyre, H. L., and Kana, T. M.: A dynamic regulatory model of phytoplanktonic acclimation to light, nutrients, and temperature, Limnology and oceanography, 43, 679–694, 1998.

Gernez, P., Doxaran, D., and Barillé, L.: Shellfish aquaculture from space: potential of Sentinel2 to monitor tide-driven changes in turbidity, chlorophyll concentration and oyster physiological response at the scale of an oyster farm, Frontiers in Marine Science, 4, 137, 2017.

Glibert, P. M., Wilkerson, F. P., Dugdale, R. C., Raven, J. A., Dupont, C. L., Leavitt, P. R., Parker, A. E., Burkholder, J. M., and Kana, T. M.: Pluses and minuses of ammonium and nitrate uptake and assimilation by phytoplankton and implications for productivity and community composition, with emphasis on nitrogen-enriched conditions, Limnology and Oceanography, 61, 165–197, 2016.

Gómez, I., López-Figueroa, F., Ulloa, N., Morales, V., Lovengreen, C., Huovinen, P., and Hess, S.: Patterns of photosynthesis in 18 species of intertidal macroalgae from southern Chile, Marine Ecology Progress Series, 270, 103–116, 2004.

Gons, H. J.: Optical teledetection of chlorophyll a in turbid inland waters, 1127–1132 Environmental Science & Technology, 1999.

Gons, H. J., Rijkeboer, M., and Ruddick, K. G.: Effect of a waveband shift on chlorophyll retrieval from MERIS imagery of inland and coastal waters, Journal of Plankton research, 27, 125–127, 2005.

Goto, N., Mitamura, O., and Terai, H.: Seasonal variation in primary production of microphytobenthos at the Isshiki intertidal flat in Mikawa Bay, Limnology, 1, 133–138, 2000.

Gould, D. M. and Gallagher, E. D.: Field measurement of specific growth rate, biomass, and primary production of benthic diatoms of Savin Hill Cove, Boston, Limnology and Oceanography, 35, 1757–1770, 1990.

Gouleau, D., Jouanneau, J., Weber, O., and Sauriau, P.-G.: Short-and long-term sedimentation on Montportail–Brouage intertidal mudflat, Marennes–Oleron Bay (France), Continental Shelf Research, 20, 1513–1530, 2000.

Goulletquer, P.: Shellfish culture in France : present status and new approaches to optimise production, 1998.

Graunt, J.: 1662. Natural and political observations mentioned in a following index, and made upon the bills of mortality, London. Republished as an introduction by B. Benjamin in the Journal of the Institute of Actuaries, 90, 1–61, 1662.

Green, M. O. and Coco, G.: Review of wave-driven sediment resuspension and transport in estuaries, Reviews of Geophysics, 52, 77–117, 2014.

Guarini, J.-M.: Modélisation de la dynamique du microphytobenthos des vasières intertidales du bassin de Marennes-Oléron. Effets des synchroniseurs physiques sur la régulation de la production, Ph.D. thesis, Paris 6, 1998.

Guarini, J.-M., Blanchard, G. F., Gros, P., and Harrison, S. J.: Modelling the mud surface temperature on intertidal flats to investigate the spatio-temporal dynamics of the benthic microalgal photosynthetic capacity, Marine Ecology Progress Series, 153, 25–36, 1997.

Guarini, J.-M., Blanchard, G. F., Bacher, C., Gros, P., Riera, P., Richard, P., Gouleau, D., Galois, R., Prou, J., and Sauriau, P.-G.: Dynamics of spatial patterns of microphytobenthic biomass: inferences from a geostatistical analysis of two comprehensive surveys in Marennes-Oléron Bay (France), 131–141 Marine Ecology Progress Series, 1998.

Guarini, J.-M., Blanchard, G. F., Gros, P., Gouleau, D., and Bacher, C.: Dynamic model of the short-term variability of microphytobenthic biomass on temperate intertidal mudflats, 291–303 Marine Ecology Progress Series, 2000.

Guarini, J.-M., Gros, P., Blanchard, G. F., Richard, P., and Fillon, A.: Benthic contribution to pelagic microalgal communities in two semi-enclosed, European-type littoral ecosystems (Marennes-Oléron Bay and Aiguillon Bay, France), Journal of Sea Research, 52, 241–258, 2004.

Guarini, J.-M., Blanchard, G. F., Gros, P., and Richard, P.: Modelling the dynamics of the microphytobenthic biomass and primary production in European

intertidal mudflats , 187–226 in: Functioning of microphytobenthos in estuaries. Amsterdam, Royal Netherlands Academy of Arts and Sciences, Royal Netherlands Academy of Arts and Sciences, 2006.

Guarini, J.-M., Sari, N., and Moritz, C.: Modelling the dynamics of the microalgal biomass in semi-enclosed shallow-water ecosystems, Ecological Modelling, 211, 267–278, 2008a.

Guarini, J.-M., Chauvaud, L., and Coston-Guarini, J.: Can the intertidal benthic microalgal primary production account for the" Missing Carbon Sink"?, Journal of Oceanography, Research and data, 1, 2008b.

Guizien, K., Dupuy, C., Ory, P., Montanié, H., Hartmann, H., Chatelain, M., and Karpytchev, M.: Microorganism dynamics during a rising tide: disentangling effects of resuspension and mixing with offshore waters above an intertidal mudflat, Journal of Marine Systems, 129, 178–188, 2014.

Hammersley, J. and Handscomb, D.: Monte Carlo Methods, London: Methuen & Co. Ltd, 1964.

Hanelt, D., Huppertz, K., and Nultsch, W.: Daily course of photosynthesis and photoinhibition in marine macroalgae investigated in the laboratory and field, Marine ecology progress series. Oldendorf, 97, 31–37, 1993.

Harrison, S. J.: Heat exchanges in muddy intertidal sediments: Chichester Harbour, West Sussex, England, Estuarine, Coastal and Shelf Science, 20, 477–490, 1985.

Harrison, S. J. and Phizacklea, A. P.: Seasonal changes in heat flux and heat storage forth estuary, scotland in the intertidal mudflats of the forth estuary, scotland, Journal of Climatology, 5, 473–485, 1985.

Harrison, S. J. and Phizacklea, A. P.: Vertical temperature gradients in muddy intertidal sediments in the Forth estuary, Scotland, Limnology and Oceanography, 32, 954–963, 1987.

Hasselmann, K., Barnett, T., Bouws, E., Carlson, H., Cartwright, D., Enke, K., Ewing, J., Gienapp, H., Hasselmann, D., Kruseman, P., et al.: Measurements of wind-wave growth and swell decay during the Joint North Sea Wave Project (JONSWAP), Ergänzungsheft 8-12, 1973.

Hasselmann, S., Hasselmann, K., Allender, J., and Barnett, T.: Computations and parameterizations of the nonlinear energy transfer in a gravity-wave spectrum. Part II: parameterizations of the nonlinear energy transfer for application in wave models., Journal of Physical Oceanography, 15, 1378–1391, 1985.

Haubois, A.-G., Guarini, J.-M., Richard, P., Blanchard, G. F., and Sauriau, P.-G.: Spatio–temporal differentiation in the population structure of Hydrobia ulvae on an intertidal mudflat (Marennes-Oléron Bay, France), Journal of the Marine Biological Association of the United Kingdom, 82, 605–614, 2002.

Haubois, A.-G., Guarini, J.-M., Richard, P., Fichet, D., Radenac, G., and Blanchard, G. F.: Ingestion rate of the deposit-feeder Hydrobia ulvae (Gastropoda) on epipelic diatoms: effect of cell size and algal biomass, Journal of Experimental Marine Biology and Ecology, 317, 1–12, 2005.

Healy, T., Wang, Y., and Healy, J.-A.: Muddy coasts of the world: processes, deposits and function, vol. 4, Elsevier, 2002.

Heilskov, A. C., Alperin, M., and Holmer, M.: Benthic fauna bio-irrigation effects on nutrient regeneration in fish farm sediments, Journal of Experimental Marine Biology and Ecology, 339, 204–225, 2006.

Herlory, O., Guarini, J.-M., Richard, P., and Blanchard, G. F.: Microstructure of microphytobenthic biofilm and its spatio-temporal dynamics in an intertidal mudflat (Aiguillon Bay, France), Marine Ecology Progress Series, 282, 33–44, 2004.

Herlory, O., Richard, P., and Blanchard, G. F.: Methodology of light response curves: Application of chlorophyll fluorescence to microphytobenthic biofilms, Marine Biology, 153, 91–101, 2007.

Herman, P. M. J., Middelburg, J. J., Widdows, J., Lucas, C. H., and Heip, C. H. R.: Stable isotopes as trophic tracers: Combining field sampling and manipulative labelling of food resources for macrobenthos, Marine Ecology Progress Series, 204, 79–92, 2000.

Hernández Fariñas, T., Ribeiro, L., Soudant, D., Belin, C., Bacher, C., Lampert, L., and Barillé, L.: Contribution of benthic microalgae to the temporal variation in phytoplankton assemblages in a macrotidal system, Journal of phycology, 53, 1020–1034, 2017.

Hicks, N., Bulling, M. T., Solan, M., Raffaelli, D., White, P. C., and Paterson, D. M.: Impact of biodiversity-climate futures on primary production and metabolism in a model benthic estuarine system, BMC ecology, 11, 7, 2011.

Hochard, S., Pinazo, C., Grenz, C., Evans, J., and Pringault, O.: Impact of microphytobenthos on the sediment biogeochemical cycles: A modeling approach, Ecological Modelling, 221, 1687–1701, 2010.

Hochard, S., Pinazo, C., Rochelle-Newall, E., and Pringault, O.: Benthic pelagic coupling in a shallow oligotrophic ecosystem: Importance of microphytobenthos and physical forcing, Ecological modelling, 247, 307–318, 2012.

Hopkinson, C. and Smith, E. M.: Estuarine respiration: an overview of benthic, pelagic, and whole system respiration, 122–146 Respiration in aquatic ecosystems, 2005.

Hubas, C., Davoult, D., Cariou, T., and Artigas, L. F.: Factors controlling benthic metabolism during low tide along a granulometric gradient in an intertidal bay (Roscoff Aber Bay, France), Marine Ecology Progress Series, 316, 53–68, 2006.

Jahnke, R., Alexander, C., and Kostka, J.: Advective pore water input of nutrients to the Satilla River Estuary, Georgia, USA, Estuarine, Coastal and Shelf Science, 56, 641–653, 2003.

Jansson, B.-O. and Wulff, F.: Ecosystem analysis of a shallow sound in the northern Baltic: a joint study by the Askö group, University of Stockholm, Sweden, 1977.

Jardine, C. B., Bond, A. L., Davidson, P. J., Butler, R. W., and Kuwae, T.: Biofilm consumption and variable diet composition of Western Sandpipers (Calidris mauri) during migratory stopover, PloS one, 10, e0124 164, 2015.

Jensen, S. and Knutsen, G.: Influence of light and temperature on photoinhibition of photosynthesis inspirulina platensis, Journal of applied phycology, 5, 495–504, 1993.

Jesus, B., Mendes, C., Brotas, V., and Paterson, D. M.: Effect of sediment type on microphytobenthos vertical distribution: Modelling the productive biomass and improving ground truth measurements, Journal of Experimental Marine Biology and Ecology, 332, 60 – 74, 2006.

Jesus, B., Brotas, V., Ribeiro, L., Mendes, C., Cartaxana, P., and Paterson, D. M.: Adaptations of microphytobenthos assemblages to sediment type and tidal position, Continental Shelf Research, 29, 1624–1634, 2009.

Jobson, D. J., Zingmark, R. G., and Katzberg, S. J.: Remote sensing of benthic microalgal biomass with a tower-mounted multispectral scanner, Remote Sensing of Environment, 9, 351–362, 1980.

Joint, I.: Microbial production of an estuarine mudflat, Estuarine and Coastal Marine Science, 7, 185–195, 1978.

Juneau, P., Barnett, A., Méléder, V., Dupuy, C., and Lavaud, J.: Combined effect of high light and high salinity on the regulation of photosynthesis in three diatom species belonging to the main growth forms of intertidal flat inhabiting microphytobenthos, Journal of experimental marine biology and ecology, 463, 95–104, 2015.

Kang, C., Lee, Y., Eun, J. C., Shin, J., Seo, I., and Hong, J.: Microphytobenthos seasonality determines growth and reproduction in intertidal bivalves, Marine Ecology Progress Series, 315, 113–127, 2006.

Kazemipour, F., Launeau, P., and Méléder, V.: Microphytobenthos biomass mapping using the optical model of diatom biofilms: Application to hyperspectral images of Bourgneuf Bay, Remote sensing of environment, 127, 1–13, 2012.

Ke, X., Collins, M., and Poulos, S.: Velocity structure and sea bed roughness associated with intertidal (sand and mud) flats and saltmarshes of the Wash, UK, Journal of Coastal Research, 10, 1994.

Kervella, S.: Dynamique des sédiments fins et mixtes des zones intertidales de la baie de Marennes-Oléron: caractérisation des sédiments, processus hydro-sédimentaires et modélisation appliquée, Ph.D. thesis, La Rochelle, 2009.

Kingston, M. B.: Effect of subsurface nutrient supplies on the vertical migration of Euglena proxima (Euglenophyta), Journal of Phycology, 38, 872–880, 2002.

Kocum, E., Underwood, G. J. C., and Nedwell, D. B.: Simultaneous measurement of phytoplanktonic primary production, nutrient and light availability along a turbid, eutrophic UK east coast estuary (the Colne Estuary), Marine ecology progress series, 231, 1–12, 2002.

Kofoed, L. H.: The feeding biology of Hydrobia ventrosa (Montagu). II. Allocation of the components of the carbon-budget and the significance of the secretion of dissolved organic material, Journal of Experimental Marine Biology and Ecology, 19, 243–256, 1975.

Koh, C.-H., Khim, J. S., Araki, H., Yamanishi, H., Mogi, H., and Koga, K.: Tidal resuspension of microphytobenthic chlorophyll a in a Nanaura mudflat, Saga, Ariake Sea, Japan: flood–ebb and spring–neap variations, Marine Ecology Progress Series, 312, 85–100, 2006.

Koh, C.-H., Khim, J. S., Araki, H., Yamanishi, H., and Koga, K.: Within-day and seasonal patterns of microphytobenthos biomass determined by co-measurement of sediment and water column chlorophylls in the intertidal mudflat of Nanaura, Saga, Ariake Sea, Japan, Estuarine, coastal and shelf science, 72, 42–52, 2007.

Komen, G. J., Cavaleri, L., Donelan, M., Hasselmann, K., Hasselmann, S., and Janssen, P.: Dynamics and modelling of ocean waves, Cambridge university press, 1996.

Kristensen, E.: Organic matter diagenesis at the oxic/anoxic interface in coastal marine sediments, with emphasis on the role of burrowing animals, 1–24 in: Life at interfaces and under extreme conditions, Springer, 2000.

Kromkamp, J. C., Barranguet, C., and Peene, J.: Determination of microphytobenthos PSII quantum efficiency and photosynthetic activity by means of variable chlorophyll fluorescence, Marine Ecology Progress Series, 162, 45–55, 1998.

Krumme, U., Keuthen, H., Barletta, M., Saint-Paul, U., and Villwock, W.: Resuspended intertidal microphytobenthos as major diet component of planktivorous Atlantic anchoveta Cetengraulis edentulus (Engraulidae) from equatorial mangrove creeks, Ecotropica, 14, 121–128, 2008.

Kühl, M. and Jørgensen, B. B.: Spectral light measurements in microbenthic phototrophic communities with a fiber-optic microprobe coupled to a sensitive diode array detector, Limnology and Oceanography, 37, 1813–1823, 1992.

Kwon, B.-O., Koh, C.-H., Khim, J. S., Park, J., Kang, S.-G., and Hwang, J. H.: The relationship between primary production of microphytobenthos and tidal cycle on the Hwaseong mudflat, west coast of Korea, Journal of Coastal Research, 30, 1188–1196, 2014.

Kwon, B.-O., Kim, H.-C., Koh, C.-H., Ryu, J., Son, S., Kim, Y., and Khim, J.: Development of temperature-based algorithms for the estimation of microphytobenthic primary production in a tidal flat: A case study in Daebu mudflat, Korea, Environmental Pollution, 241, 115–123, 2018.

Kühl, M., Lassen, C., and Jørgensen, B. B.: Light penetration and light intensity in sandy marine sediments measured with irradiance and scalar irradiance fiber-optic microprobes, Marine Ecology Progress Series, 106, 140–148, 1995.

Larson, F. and Sundbäck, K.: Role of microphytobenthos in recovery of functions in a shallow-water sediment system after hypoxic events, Marine Ecology Progress Series, 357, 1–16, 2008.

Launeau, P., Méléder, V., Verpoorter, C., Barillé, L., Kazemipour-Ricci, F., Giraud, M., Jesus, B., and Le Menn, E.: Microphytobenthos Biomass and Diversity Mapping at Different Spatial Scales with a Hyperspectral Optical Model, Remote Sensing, 10, 2018.

Lavaud, J. and Goss, R.: 421–443 The Peculiar Features of Non–Photochemical Fluorescence Quenching in Diatoms and Brown Algae, Springer Netherlands, Dordrecht, 2014.

Lavergne, C., Agogué, H., Leynaert, A., Raimonet, M., De Wit, R., Pineau, P., Bréret, M., Lachaussée, N., and Dupuy, C.: Factors influencing prokaryotes in an intertidal mudflat and the resulting depth gradients, Estuarine, Coastal and Shelf Science, 189, 74–83, 2017.

Laverock, B., Gilbert, J. A., Tait, K., Osborn, A. M., and Widdicombe, S.: Bioturbation: impact on the marine nitrogen cycle, 2011.

Laviale, M., Barnett, A., Ezequiel, J., Lepetit, B., Frankenbach, S., Méléder, V., Serôdio, J., and Lavaud, J.: Response of intertidal benthic microalgal biofilms to a coupled light–temperature stress: evidence for latitudinal adaptation along the Atlantic coast of Southern Europe, Environmental microbiology, 17, 3662–3677, 2015.

Lazure, P. and Dumas, F.: An external–internal mode coupling for a 3D hydrodynamical model for applications at regional scale (MARS), Advances in water resources, 31, 233–250, 2008.

Lazure, P., Garnier, V., Dumas, F., Herry, C., and Chifflet, M.: Development of a hydrodynamic model of the Bay of Biscay. Validation of hydrology, Continental Shelf Research, 29, 985–997, 2009.

Le Fouest, V., Zakardjian, B., Xie, H., Raimbault, P., Joux, F., and Babin, M.: Modeling plankton ecosystem functioning and nitrogen fluxes in the oligotrophic waters of the Beaufort Sea, Arctic Ocean: a focus on light-driven processes, Biogeosciences, 10, 4785–4800, 2013.

Le Hir, P., Roberts, W., Cazaillet, O., Christie, M., Bassoullet, P., and Bacher, C.: Characterization of intertidal flat hydrodynamics, Continental shelf research, 20, 1433–1459, 2000.

Le Hir, P., Monbet, Y., and Orvain, F.: Sediment erodability in sediment transport modelling: can we account for biota effects?, Continental Shelf Research, 27, 1116–1142, 2007.

Leach, J.: Epibenthic algal production in an intertidal mudflat, Limnology and Oceanography, 15, 514–521, 1970.

Lebreton, B., Richard, P., Radenac, G., Bordes, M., Bréret, M., Arnaud, C., Mornet, F., and Blanchard, G. F.: Are epiphytes a significant component of intertidal Zostera noltii beds?, Aquatic Botany, 91, 82–90, 2009.

Lebreton, B., Richard, P., Galois, R., Radenac, G., Brahmia, A., Colli, G., Grouazel, M., André, C., Guillou, G., and Blanchard, G. F.: Food sources used by sediment meiofauna in an intertidal Zostera noltii seagrass bed: a seasonal stable isotope study, Marine Biology, 159, 1537–1550, 2012.

Lebreton, B., Rivaud, A., Picot, L., Prévost, B., Barillé, L., Sauzeau, T., Pollack, J. B., and Lavaud, J.: From ecological relevance of the ecosystem services concept to its socio-political use. The case study of intertidal bare mudflats in the Marennes-Oléron Bay, France, Ocean & Coastal Management, 172, 41–54, 2019.

Leguerrier, D., Niquil, N., Boileau, N., Rzeznik, J., Sauriau, P.-G., Le Moine, O., and Bacher, C.: Numerical analysis of the food web of an intertidal mudflat

ecosystem on the Atlantic coast of France, Marine ecology progress series, 246, 17–37, 2003.

Leroux, S.: Phytoplancton et contenus stomacaux d'huîtres portugaises (Gryphea angulata Lmk) dans le bassin d'Arcachon, Rev Trav Inst Pêches Marit, 20, 163–170, 1956.

Li, X., Leonardi, N., and Plater, A. J.: Wave-driven sediment resuspension and salt marsh frontal erosion alter the export of sediments from macro-tidal estuaries, Geomorphology, 325, 17–28, 2019.

Light, B. R. and Beardall, J.: Photosynthetic characteristics of sub-tidal benthic microalgal populations from a temperate, shallow water marine ecosystem, Aquatic Botany, 70, 9–27, 2001.

Long, S. P., Humphries, S., and Falkowski, P. G.: Photoinhibition of photosynthesis in nature, Annual review of plant biology, 45, 633–662, 1994.

Longuet-Higgins, M. S. and Stewart, R.: Radiation stresses in water waves; a physical discussion, with applications, in: Deep Sea Research and Oceanographic Abstracts, 529–562 vol. 11, Elsevier, 1964.

López-Urrutia, Á., San Martin, E., Harris, R. P., and Irigoien, X.: Scaling the metabolic balance of the oceans, Proceedings of the National Academy of Sciences, 103, 8739–8744, 2006.

Lotka, A.: Elements of physical biology. Williams and Wilkins, Baltimore, Md, 1925.

Lovelock, C. E., Feller, I. C., Reef, R., Hickey, S., and Ball, M. C.: Mangrove dieback during fluctuating sea levels, Scientific Reports, 7, 1680, 2017.

Lucas, C. H., Banham, C., and Holligan, P. M.: Benthic-pelagic exchange of microalgae at a tidal flat. 2. Taxonomic analysis, Marine Ecology Progress Series, 212, 39–52, 2001.

Luna-Acosta, A., Budzinski, H., Le Menach, K., Thomas-Guyon, H., and Bustamante, P.: Persistent organic pollutants in a marine bivalve on the Marennes-Oléron Bay and the Gironde Estuary (French Atlantic Coast)—part 1: bioaccumulation, Science of The Total Environment, 514, 500–510, 2015.

MacIntyre, H. L. and Cullen, J.: Fine-scale vertical resolution of chlorophyll and photosynthetic parameters in shallow-water benthos, Marine Ecology Progress Series, 122, 227–237, 1995.

MacIntyre, H. L., Geider, R. J., and Miller, D. C.: Microphytobenthos: the ecological role of the "secret garden" of unvegetated, shallow-water marine habitats. I. Distribution, abundance and primary production, Estuaries, 19, 186–201, 1996.

MacIntyre, H. L., Sharkey, T. D., and Geider, R. J.: Activation and deactivation of ribulose-1, 5-bisphosphate carboxylase/oxygenase (Rubisco) in three marine microalgae, Photosynthesis Research, 51, 93–106, 1997.

MacIntyre, H. L., Kana, T. M., Anning, T., and Geider, R. J.: Photoacclimation of photosynthesis irradiance response curves and photosynthetic pigments in microalgae and cyanobacteria, Journal of phycology, 38, 17–38, 2002.

Mackin, J. E. and Aller, R. C.: Ammonium adsorption in marine sediments 1, Limnology and Oceanography, 29, 250–257, 1984.

Madsen, K. N., Nilsson, P., and Sundbäck, K.: The influence of benthic microalgae on the stability of a subtidal sediment, Journal of experimental marine biology and ecology, 170, 159–177, 1993.

Malthus, T. R.: An essay on the principle of population, as it affects the future improvement of society. With remarks on the speculations of mr. Godwin, m. Condorcet, and other writers. By TR Malthus, 1798.

Mann, K.: The Ecology of coastal waters—A systems approach, Blackwell, Oxford, 1982.

Marani, M., D'Alpaos, A., Lanzoni, S., Carniello, L., and Rinaldo, A.: The importance of being coupled: Stable states and catastrophic shifts in tidal biomorphodynamics, Journal of Geophysical Research: Earth Surface, 115, 2010.

Mariotti, G. and Fagherazzi, S.: Modeling the effect of tides and waves on benthic biofilms, Journal of Geophysical Research: Biogeosciences, 117, 2012.

Mariotti, G. and Fagherazzi, S.: Wind waves on a mudflat: The influence of fetch and depth on bed shear stresses, Continental Shelf Research, 60, S99–S110, 2013.

Marshall, N., Oviatt, C. A., and Skauen, D. M.: Productivity of the benthic microflora of shoal estuarine environments in southern New England, Internationale Revue der gesamten Hydrobiologie und Hydrographie, 56, 947–955, 1971.

Martin, S., Thouzeau, G., Chauvaud, L., Jean, F., Guérin, L., and Clavier, J.: Respiration, calcification, and excretion of the invasive slipper limpet, Crepidula fornicata L.: implications for carbon, carbonate, and nitrogen fluxes in affected areas, Limnology and Oceanography, 51, 1996–2007, 2006.

Martin-Jézéquel, V., Hildebrand, M., and Brzezinski, M. A.: Silicon metabolism in diatoms: implications for growth, Journal of phycology, 36, 821–840, 2000.

Matthews, O., Dittus, H., Wiegand, M., Rath, H., Schmidtke, G., Wienhold, F., and Neske, E.: BREM-STAR and TIGER-STAR: A small satellite concept for thermospheric-ionospheric 3D monitoring, Physics and Chemistry of the Earth, Part C: Solar, Terrestrial and Planetary Science, 25, 477–482, 2000.

Mcleod, E., Chmura, G. L., Bouillon, S., Salm, R., Björk, M., Duarte, C. M., Lovelock, C. E., Schlesinger, W. H., and Silliman, B. R.: A blueprint for blue carbon: toward an improved understanding of the role of vegetated coastal habitats in sequestering CO2, Frontiers in Ecology and the Environment, 9, 552–560, 2011.

Mehta, A. J., Hayter, E. J., Parker, W. R., Krone, R. B., and Teeter, A. M.: Cohesive sediment transport. I: Process description, Journal of Hydraulic Engineering, 115, 1076–1093, 1989.

Méléder, V., Launeau, P., Barillé, L., and Rincé, Y.: Cartographie des peuplements du microphytobenthos par télédétection spatiale visible-infrarouge dans un écosystème conchylicole, Comptes Rendus Biologies, 326, 377–389, 2003a.

Méléder, V., Launeau, P., Barillé, L., Combe, J., Carrère, V., Jésus, B., and Verpoorter, C.: Hyperspectral imaging for mapping microphytobenthos in coastal areas, 2010.

Méléder, V., Jesus, B., Barnett, A., Barillé, L., and Lavaud, J.: Microphytobenthos primary production estimated by hyperspectral reflectance, PloS one, p. e0197093, 2018.

Méléder, V., Savelli, R., Barnett, A., Polseneare, P., Le Fouest, V., and Lavaud, J.: Coupling multispectral remote sensing and modelling to map intertidal microphytobenthos Gross Primary Production, Frontiers in Marine Sciences, in prep.

Mengual, B., Hir, P., Cayocca, F., and Garlan, T.: Modelling fine sediment dynamics: Towards a common erosion law for fine sand, mud and mixtures, Water, 9, 564, 2017.

Mermillod-Blondin, F. and Rosenberg, R.: Ecosystem engineering: the impact of bioturbation on biogeochemical processes in marine and freshwater benthic habitats, Aquatic Sciences, 68, 434–442, 2006.

Migné, A., Davoult, D., Spilmont, N., Menu, D., Boucher, G., Gattuso, J.-P., and Rybarczyk, H.: A closed-chamber CO 2-flux method for estimating intertidal primary production and respiration under emersed conditions, Marine Biology, 140, 865–869, 2002.

Migné, A., Spilmont, N., and Davoult, D.: In situ measurements of benthic primary production during emersion: Seasonal variations and annual production in the Bay of Somme (eastern English Channel, France), Continental Shelf Research, 24, 1437–1449, 2004.

Miller, D. C., Geider, R. J., and MacIntyre, H. L.: Microphytobenthos: the ecological role of the "secret garden" of unvegetated, shallow-water marine habitats. II. Role in sediment stability and shallow-water food webs, Estuaries, 19, 202–212, 1996.

Moncreiff, C. A. and Sullivan, M. J.: Trophic importance of epiphytic algae in subtropical seagrass beds: evidence from multiple stable isotope analyses, Marine Ecology Progress Series, 215, 93–106, 2001.

Moncreiff, C. A., Sullivan, M. J., and Daehnick, A. E.: Primary production dynamics in seagrass beds of Mississippi Sound: the contributions of seagrass, epiphytic algae, sand microflora, and phytoplankton, Marine Ecology-Progress Series, 87, 161–161, 1992.

Montagna, P. A., Blanchard, G. F., and Dinet, A.: Effect of production and biomass of intertidal microphytobenthos on meiofaunal grazing rates, Journal of Experimental Marine Biology and Ecology, 185, 149–165, 1995.

Morim, J., Hemer, M., Wang, X. L., Cartwright, N., Trenham, C., Semedo, A., Young, I., Bricheno, L., Camus, P., Casas-Prat, M., et al.: Robustness and uncertainties in global multivariate wind-wave climate projections, Nature Climate Change, 9, 711–718, 2019.

Morris, E. P. and Kromkamp, J. C.: Influence of temperature on the relationship between oxygen-and fluorescence-based estimates of photosynthetic parameters in a marine benthic diatom (Cylindrotheca closterium), European Journal of Phycology, 38, 133–142, 2003.

Morrisey, D. J.: Differences in effects of grazing by deposit-feeders Hydrobia ulvae (Pennant) (Gastropoda : Prosobranchia) and Corophium arenarium Crawford (Amphipoda) on sediment microalgal populations. II. Quantitative effects, Journal of Experimental Marine Biology and Ecology, 118, 43 – 53, 1988.

Murray, A. and Parslow, J.: Port Phillip Bay integrated model: final report, Port Phillip Bay Environment Study Technical Report, 1997.

Murray, N. J., Phinn, S. R., DeWitt, M., Ferrari, R., Johnston, R., Lyons, M. B., Clinton, N., Thau, D., and Fuller, R. A.: The global distribution and trajectory of tidal flats, Nature, 565, 222, 2019.

Méléder, V., Barillé, L., Launeau, P., Carrère, V., and Rincé, Y.: Spectrometric constraint in analysis of benthic diatom biomass using monospecific cultures, Remote Sensing of Environment, 88, 386 – 400, 2003b.

Neumeier, U., Lucas, C. H., and Collins, M.: Erodibility and erosion patterns of mudflat sediments investigated using an annular flume, Aquatic Ecology, 40, 543–554, 2006.

Newell, C., Shumway, S., Cucci, T., and Selvin, R.: The effects of natural seston particle size and type on feeding rates, feeding selectivity and food resource availability for the mussel Mytilus edulis Linnaeus, 1758 at bottom culture sites in Maine, J. Shellfish Res, 8, 187–196, 1989.

Nicholls, R. and Wong, P.: Climate Change 2007: Impacts, Adaptation, and Vulnerability, vol. 4, Cambridge University Press, 2007.

Nils, R.-P.: Coupled nitrification-denitrification in autotrophic and heterotrophic estuarine sediments: On the influence of benthic microalgae, Limnology and Oceanography, 48, 93–105, 2003.

Nishiyama, Y., Allakhverdiev, S. I., and Murata, N.: A new paradigm for the action of reactive oxygen species in the photoinhibition of photosystem II, Biochimica et Biophysica Acta (BBA)-Bioenergetics, 1757, 742–749, 2006.

NOAA: https://www.esrl.noaa.gov/gmd/ccgg/trends/, accessed: 2019-10-12, 2019.

Ogilvie, B., Nedwell, D., Harrison, R., Robinson, A., and Sage, A.: High nitrate, muddy estuaries as nitrogen sinks: the nitrogen budget of the River Colne estuary (United Kingdom), Marine Ecology Progress Series, 150, 217–228, 1997.

Orvain, F., Le Hir, P., and Sauriau, P.-G.: A model of fluff layer erosion and subsequent bed erosion in the presence of the bioturbator, Hydrobia ulvae, Journal of Marine Research, 61, 821–849, 2003.

Orvain, F., Sauriau, P.-G., Sygut, A., Joassard, L., and Le Hir, P.: Interacting effects of Hydrobia ulvae bioturbation and microphytobenthos on the erodibility of mudflat sediments, Marine ecology progress series, 278, 205–223, 2004.

Orvain, F., Sauriau, P.-G., Le Hir, P., Guillou, G., Cann, P., and Paillard, M.: Spatio-temporal variations in intertidal mudflat erodability: Marennes-Oléron Bay, western France, Continental Shelf Research, 27, 1153–1173, 2007.

Orvain, F., De Crignis, M., Guizien, K., Lefebvre, S., Mallet, C., Takahashi, E., and Dupuy, C.: Tidal and seasonal effects on the short-term temporal patterns of bacteria, microphytobenthos and exopolymers in natural intertidal biofilms (Brouage, France), Journal of Sea Research, 92, 6–18, 2014a.

Orvain, F., Guizien, K., Lefebvre, S., Bréret, M., and Dupuy, C.: Relevance of macrozoobenthic grazers to understand the dynamic behaviour of sediment erodibility and microphytobenthos resuspension in sunny summer conditions, Journal of Sea Research, 92, 46–55, 2014b.

Osmond, C.: What is photoinhibition? Some insights from comparisons of shade and sun plants, 1–24 Photoinhibition of photosynthesis–from molecular mechanisms to the field, 1994.

Osmond, C. and Grace, S.: Perspectives on photoinhibition and photorespiration in the field: quintessential inefficiencies of the light and dark reactions of photosynthesis?, Journal of Experimental Botany, 46, 1351–1362, 1995.

Otani, S. and Endo, T.: CO 2 flux in tidal flats and salt marshes, 223–250 in: Blue Carbon in Shallow Coastal Ecosystems, Springer, 2019.

Pachauri, R. K., Allen, M. R., Barros, V. R., Broome, J., Cramer, W., Christ, R., Church, J. A., Clarke, L., Dahe, Q., Dasgupta, P., et al.: Climate change 2014: synthesis report. Contribution of Working Groups I, II and III to the fifth assessment report of the Intergovernmental Panel on Climate Change, IPCC, 2014.

Pan, J., Cuadrado, D. G., and Bournod, C. N.: Diatom-driven recolonization of microbial mat-dominated siliciclastic tidal flat sediments, FEMS microbiology ecology, 93, 2017.

Partheniades, E.: A study of erosion and deposition of cohesive soils in salt water, University of California, Berkeley, 1962.

Pascal, P.-Y., Dupuy, C., Richard, P., Haubois, A.-G., and Niquil, N.: Influence of environment factors on bacterial ingestion rate of the deposit-feeder Hydrobia ulvae and comparison with meiofauna, Journal of Sea Research, 60, 151–156, 2008.

Pascal, P.-Y., Dupuy, C., Richard, P., Mallet, C., Niquilb, N., et al.: Seasonal variation in consumption of benthic bacteria by meio-and macrofauna in an intertidal mudflat, Limnology and Oceanography, 54, 1048–1059, 2009.

Pascual, E. and Drake, P.: Physiological and behavioral responses of the mud snails Hydrobia glyca and Hydrobia ulvae to extreme water temperatures and salinities: implications for their spatial distribution within a system of temperate lagoons, Physiological and Biochemical Zoology, 81, 594–604, 2008.

Passarelli, C., Olivier, F., Paterson, D. M., Meziane, T., and Hubas, C.: Organisms as cooperative ecosystem engineers in intertidal flats, Journal of Sea Research, 92, 92–101, 2014.

Passeri, D. L., Hagen, S. C., Medeiros, S. C., Bilskie, M. V., Alizad, K., and Wang, D.: The dynamic effects of sea level rise on low-gradient coastal landscapes: A review, Earth's Future, 3, 159–181, 2015.

Paterson, D. M.: Short-term changes in the erodibility of intertidal cohesive sediments related to the migratory behavior of epipelic diatoms, Limnology and Oceanography, 34, 223–234, 1989.

Paterson, D. M. and Hagerthey, S.: Microphytobenthos in constrasting coastal ecosystems: biology and dynamics, 105–125 in: Ecological comparisons of sedimentary shores, Springer, 2001.

Paulmier, G.: Seston, phytoplancton et microphytobenthos en rivière d'Auray: leur rôle dans le cycle biologique des huitres Ostrea edulis L, Ph.D. thesis, 1972.

Peer, N., Miranda, N. A., and Perissinotto, R.: Impact of fiddler crab activity on microphytobenthic communities in a South African mangrove forest, Estuarine, Coastal and Shelf Science, p. 106332, 2019.

Perissinotto, R., Nozais, C., Kibirige, I., and Anandraj, A.: Planktonic food webs and benthic-pelagic coupling in three South African temporarily-open estuaries, Acta Oecologica, 24, S307–S316, proceedings of the Plankton Symposium, Espinho, Portugal, 2003.

Perkins, R. G., Underwood, G. J. C., Brotas, V., Snow, G. C., Jesus, B., and Ribeiro, L.: Responses of microphytobenthos to light: Primary production and carbohydrate allocation over an emersion period, Marine Ecology Progress Series, 223, 101–112, 2001.

Perkins, R. G., Lavaud, J., Serôdio, J., Mouget, J.-L., Cartaxana, P., Rosa, P., Barillé, L., Brotas, V., and Jesus, B.: Vertical cell movement is a primary response of intertidal benthic biofilms to increasing light dose, Marine Ecology Progress Series, 416, 93–103, 2010.

Pethick, J. S. and Crooks, S.: Development of a coastal vulnerability index: a geomorphological perspective, Environmental Conservation, 27, 359–367, 2000.

Piccolo, M., Perillo, G., and Daborn, G.: Soil temperature variations on a tidal flat in Minas Basin, Bay of Fundy, Canada, Estuarine, Coastal and Shelf Science, 36, 345–357, 1993.

Pierre, G., Graber, M., Orvain, F., Dupuy, C., and Maugard, T.: Biochemical characterization of extracellular polymeric substances extracted from an intertidal mudflat using a cation exchange resin, Biochemical Systematics and Ecology, 38, 917–923, 2010.

Pierre, G., Graber, M., Rafiliposon, B. A., Dupuy, C., Orvain, F., De Crignis, M., and Maugard, T.: Biochemical composition and changes of Extracellular Polysaccharides (ECPS) produced during microphytobenthic biofilm development (Marennes-Oléron, France), Microbial Ecology, 63, 157–169, 2012.

Pinckney, J. and Zingmark, R.: Modeling the annual production of intertidal benthic microalgae in estuarine ecosystems, Journal of Phycology, 29, 396–407, 1993.

Pinckney, J. L. and Zingmark, R.: Effects of tidal stage and sun angles on intertidal benthic microalgal productivity, Marine Ecology Progress Series, 76, 81, 1991.

Pinckney, J. L., Carman, K. R., Lumsden, S. E., and Hymel, S. N.: Microalgal-meiofaunal trophic relationships in muddy intertidal estuarine sediments, Aquatic Microbial Ecology, 31, 99–108, 2003.

Pivato, M., Carniello, L., Moro, I., and D'Odorico, P.: On the feedback between water turbidity and microphytobenthos growth in shallow tidal environments, Earth Surface Processes and Landforms, 44, 1192–1206, 2019.

Platt, T. and Jassby, A. D.: The relationship between photosynthesis and light for natural assemblages of coastal marine phytoplankton, Journal of Phycology, 12, 421–430, 1976.

Platt, T., Gallegos, C. L., and Harrison, W. G.: Photoinhibition of photosynthesis in natural assemblages of marine phytoplankton, Journal of Marine Research, 38, 687–701, 1980.

Pniewski, F. F., Biskup, P., Bubak, I., Richard, P., Latała, A., and Blanchard, G. F.: Photo-regulation in microphytobenthos from intertidal mudflats and non-tidal coastal shallows, Estuarine, Coastal and Shelf Science, 152, 2015.

Polsenaere, P., Lamaud, E., Lafon, V., Bonnefond, J.-M., Bretel, P., Delille, B., Deborde, J., Loustau, D., and Abril, G.: Spatial and temporal CO2 exchanges measured by Eddy Covariance over a temperate intertidal flat and their relationships to net ecosystem production, 249–268 Biogeosciences, 2012.

Polsenaere, P., Soletchnik, P., Le Moine, O., Gohin, F., Robert, S., Pépin, J.-F., Stanisière, J.-Y., Dumas, F., Béchemin, C., and Goulletquer, P.: Potential environmental drivers of a regional blue mussel mass mortality event (winter of 2014, Breton Sound, France), Journal of sea research, 123, 39–50, 2017.

Pomeroy, L. R.: Algal Productivity in Salt Marshes of Georgia 1, Limnology and Oceanography, 4, 386–397, 1959.

Pörtner, H. O., Roberts, D., Masson-Delmotte, V., Zhai, P., Tignor, M., Poloczanska, E., Mintenbeck, K., Nicolai, M., Okem, A., Petzold, J., Rama, B., and

Weyer, N.: IPCC, 2019: Summary for Policymakers, in: IPCC Special Report on the Ocean and Cryosphere in a Changing Climate, IPCC, 2019.

Prins, T. C., Smaal, A. C., and Dame, R. F.: A review of the feedbacks between bivalve grazing and ecosystem processes, Aquatic Ecology, 31, 349–359, 1997.

Rakotomalala, C., Guizien, K., Grangeré, K., Lefebvre, S., Dupuy, C., and Orvain, F.: Modelling the functioning of a coupled microphytobenthic-EPS-bacterial system in intertidal mudflats, Marine Environmental Research, 150, 104 754, 2019.

Rast, M., Bezy, J., and Bruzzi, S.: The ESA Medium Resolution Imaging Spectrometer MERIS a review of the instrument and its mission, International Journal of Remote Sensing, 20, 1681–1702, 1999.

Raven, J. A.: Inorganic carbon acquisition by marine autotrophs, in: Advances in botanical research, 85–209 vol. 27, Elsevier, 1997.

Raven, J. A.: The cost of photoinhibition, Physiologia Plantarum, 142, 87–104, 2011.

Remmert, H.: Ökologie: ein Lehrbuch, Springer-Verlag, 2013.

Revsbech, N. P. and Jørgensen, B. B.: Microelectrodes: their use in microbial ecology, 293–352 in: Advances in microbial ecology, Springer, 1986.

Riera, P. and Richard, P.: Isotopic Determination of Food Sources ofCrassostrea gigasAlong a Trophic Gradient in the Estuarine Bay of Marennes-Ol éron, Estuarine, Coastal and Shelf Science, 42, 347–360, 1996.

Rijstenbil, J.: Effects of UVB radiation and salt stress on growth, pigments and antioxidative defence of the marine diatom Cylindrotheca closterium, Marine Ecology Progress Series, 254, 37–47, 2003.

Riley, G. A.: Factors controlling phytoplankton populations on Georges Bank, J. mar. Res, 6, 54–73, 1946.

Riley, G. A.: A theoretical analysis of the zooplankton population of Georges Bank., J. mar. Res., 6, 104–113, 1947.

Riley, G. A.: Quantitative ecology of the plankton of the western North Atlantic, Bull. Bingham Oceanogr. Collection, 12, 1–169, 1949.

Risgaard-Petersen, N., Nicolaisen, M., Revsbech, N., and Lomstein, B.: Competition between Ammonia-Oxidizing Bacteria and Benthic Microalgae, Applied and environmental microbiology, 70, 5528–37, 2004.

Riznyk, R. Z., Edens, J. I., and Libby, R. C.: Production of epibenthic diatoms in a Southern California impounded estuary, Journal of Phycology, 14, 273–279, 1978.

Roland, A., Zhang, Y. J., Wang, H. V., Meng, Y., Teng, Y.-C., Maderich, V., Brovchenko, I., Dutour-Sikiric, M., and Zanke, U.: A fully coupled 3D wave-current interaction model on unstructured grids, Journal of Geophysical Research: Oceans, 117, 2012.

Roncarati, F., Rijstenbil, J., and Pistocchi, R.: Photosynthetic performance, oxidative damage and antioxidants in Cylindrotheca closterium in response to high irradiance, UVB radiation and salinity, Marine biology, 153, 965–973, 2008.

Round, F.: Benthic marine diatoms, Oceanogr. Mar. Biol. Ann. Rev., 9, 83–139, 1971.

Roy, S., Llewellyn, C. A., Egeland, E. S., and Johnsen, G.: Phytoplankton pigments: characterization, chemotaxonomy and applications in oceanography, Cambridge University Press, 2011.

Rysgaard, S., Christensen, P. B., and Nielsen, L. P.: Seasonal variation in nitrification and denitrification in estuarine sediment colonized by benthic microalgae and bioturbating infauna, Marine Ecology Progress Series, 126, 111–121, 1995.

Rzeznik-Orignac, J., Fichet, D., and Boucher, G.: Spatio-temporal structure of the nematode assemblages of the Brouage mudflat (Marennes Oléron, France), Estuarine, Coastal and Shelf Science, 58, 77–88, 2003.

Saburova, M. A. and Polikarpov, I. G.: Diatom activity within soft sediments: behavioural and physiological processes, Marine Ecology Progress Series, 251, 115–126, 2003.

Sahan, E., Sabbe, K., Creach, V., Hernandez-Raquet, G., Vyverman, W., Stal, L. J., and Muyzer, G.: Community structure and seasonal dynamics of diatom biofilms and associated grazers in intertidal mudflats, Aquatic Microbial Ecology, 47, 253–266, 2007.

Saint-Béat, B., Dupuy, C., Bocher, P., Chalumeau, J., De Crignis, M., Fontaine, C., Guizien, K., Lavaud, J., Lefebvre, S., Montanié, H., et al.: Key features of intertidal food webs that support migratory shorebirds, Plos One, 8, e76 739, 2013.

Saint-Béat, B., Dupuy, C., Agogué, H., Carpentier, A., Chalumeau, J., Como, S., David, V., De Crignis, M., Duchêne, J.-C., Fontaine, C., et al.: How does the resuspension of the biofilm alter the functioning of the benthos–pelagos coupled food web of a bare mudflat in Marennes-Oléron Bay (NE Atlantic)?, Journal of Sea Research, 92, 144–157, 2014.

Sakshaug, E., Bricaud, A., Dandonneau, Y., Falkowski, P. G., Kiefer, D. A., Legendre, L., Morel, A., Parslow, J., and Takahashi, M.: Parameters of photosynthesis: definitions, theory and interpretation of results, Journal of Plankton Research, 19, 1637–1670, 1997.

Salleh, S. and McMinn, A.: The effects of temperature on the photosynthetic parameters and recovery of two temperate benthic microalgae, Amphora CF. Coffaeformis and Cocconeis CF. Sublittoralis (Bacillariophycae)[1], Journal of phycology, 47, 1413–1424, 2011.

Santos, C. D., Granadeiro, J. P., and Palmeirim, J. M.: Feeding ecology of dunlin Calidris alpina in a southern European estuary, Ardeola, 52, 235–252, 2005.

Sanz-Luque, E., Chamizo-Ampudia, A., Llamas, A., Galvan, A., and Fernandez, E.: Understanding nitrate assimilation and its regulation in microalgae, Frontiers in plant science, 6, 899, 2015.

Sauriau, P.-G., Mouret, V., and Rince, J.-P.: Trophic system of wild soft-bottom molluscs in the Marennes-Oleron oyster-farming bay, Oceanologica Acta, 12, 193–204, 1989.

Savelli, R., Dupuy, C., Barillé, L., Lerouxel, A., Guizien, K., Philippe, A., Bocher, P., Polsenaere, P., and Le Fouest, V.: On biotic and abiotic drivers of the microphytobenthos seasonal cycle in a temperate intertidal mudflat: a modelling study, Biogeosciences, 15, 7243–7271, 2018.

Schlichting, H. and Gersten, K.: Boundary-layer theory, Springer, 2016.

Scholz, B. and Liebezeit, G.: Growth responses of 25 benthic marine Wadden Sea diatoms isolated from the Solthörn tidal flat (southern North Sea) in relation to varying culture conditions, Diatom Research, 27, 65–73, 2012.

Serodio, J. and Catarino, F.: Fortnightly light and temperature variability in estuarine intertidal sediments and implications for microphytobenthos primary productivity, 235–241 Aquatic Ecology, 1999.

Serôdio, J., da Silva, J. M., and Catarino, F.: Use of in vivo chlorophyll a fluorescence to quantify short-term variations in the productive biomass of intertidal microphytobenthos, Marine Ecology Progress Series, 218, 45–61, 2001.

Serôdio, J., Ezequiel, J., Barnett, A., Mouget, J.-L., Méléder, V., Laviale, M., and Lavaud, J.: Efficiency of photoprotection in microphytobenthos: role of vertical migration and the xanthophyll cycle against photoinhibition, Aquatic Microbial Ecology, 67, 161–175, 2012.

Serôdio, J. and Catarino, F.: Modelling the primary productivity of intertidal microphytobenthos: Time scales of variability and effects of migratory rhythms, Marine Ecology Progress Series, 192, 13–30, 2000.

Serôdio, J., Vieira, S., and Cruz, S.: Photosynthetic activity, photoprotection and photoinhibition in intertidal microphytobenthos as studied in situ using variable chlorophyll fluorescence, Continental Shelf Research, 28, 1363–1375, 2008.

Serôdio, J., Cartaxana, P., Coelho, H., and Vieira, S.: Effects of chlorophyll fluorescence on the estimation of microphytobenthos biomass using spectral reflectance indices, Remote Sensing of Environment, 113, 1760 – 1768, 2009.

Shaffer, G. P. and Onuf, C. P.: Reducing the error in estimating annual production of benthic microflora: hourly to monthly rates, patchiness in space and time, Mar. Ecol. Prog. Ser, 26, 221–231, 1985.

Sibert, V., Zakardjian, B., Saucier, F., Gosselin, M., Starr, M., and Senneville, S.: Spatial and temporal variability of ice algal production in a 3D ice–ocean model of the Hudson Bay, Hudson Strait and Foxe Basin system, Polar Research, 29, 353–378, 2010.

Sibert, V., Zakardjian, B., Gosselin, M., Starr, M., Senneville, S., and LeClainche, Y.: 3D bio-physical model of the sympagic and planktonic productions in the Hudson Bay System, Journal of Marine Systems, 88, 401–422, 2011.

Simon, B. and Gonella, J.: La marée océanique côtière, Institut océanographique, 2007.

Smaal, A. C. and Zurburg, W.: The uptake and release of suspended and dissolved material by oysters and mussels in Marennes-Oleron Bay, Aquatic Living Resources, 10, 23–30, 1997.

Soetaert, K., Herman, P. M., and Middelburg, J. J.: A model of early diagenetic processes from the shelf to abyssal depths, Geochimica et Cosmochimica Acta, 60, 1019–1040, 1996.

Soletchnik, P., Faury, N., Razet, D., and Goulletquer, P.: Hydrobiology of the Marennes-Oléron Bay. Seasonal indices and analysis of trends from 1978 to 1995, Hydrobiologia, 386, 131–146, 1998.

Soletchnik, P., Le Moine, O., and Polsenaere, P.: Evolution de l'environnement hydroclimatique du bassin de Marennes-Oléron dans le contexte du changement global, Scientific report, France, 2017.

Soletchnik, P., Polsenaere, P., and Le Moine, O.: Effet du changement global sur la biologie de l'huître creuse (C. gigas) dans le Bassin de Marennes-Oléron. Résultats, hypothèses et discussion, Scientific report, France, 2018.

Soulsby, R.: Dynamics of marine sands: a manual for practical applications, Thomas Telford, 1997.

Staats, N., Stal, L. J., and Mur, L. R.: Exopolysaccharide production by the epipelic diatom Cylindrotheca closterium: effects of nutrient conditions, Journal of Experimental Marine Biology and Ecology, 249, 13–27, 2000.

Stal, L. J.: Microphytobenthos as a biogeomorphological force in intertidal sediment stabilization, Ecological Engineering, 36, 236–245, 2010.

Steele, D. J., Franklin, D. J., and Underwood, G. J. C.: Protection of cells from salinity stress by extracellular polymeric substances in diatom biofilms, Biofouling, 30, 987–998, 2014.

Steele, J. H.: Plant production in the northern North Sea, HM Stationery Office, 1958.

Steele, J. H.: Environmental control of photosynthesis in the sea, Limnology and Oceanography, 7, 137–150, 1962.

Stengel, D. B. and Dring, M. J.: Seasonal variation in the pigment content and photosynthesis of different thallus regions of Ascophyllum nodosum (Fucales, Phaeophyta) in relation to position in the canopy, Phycologia, 37, 259–268, 1998.

Stocker, T. F., Qin, D., Plattner, G.-K., Tignor, M., Allen, S. K., Boschung, J., Nauels, A., Xia, Y., Bex, V., Midgley, P. M., et al.: Climate change 2013: The physical science basis, 2013.

Struski, C. and Bacher, C.: Preliminary estimate of primary production by phytoplankton in Marennes-Oléron Bay, France, 323–334 Estuarine, Coastal and Shelf Science, 2006.

Sundbäck, K., Miles, A., and Göransson, E.: Nitrogen fluxes, denitrification and the role of microphytobenthos in microtidal shallow-water sediments: an annual study, Marine Ecology Progress Series, 200, 59–76, 2000.

Swart, D. H.: Offshore sediment transport and equilibrium beach profiles, Ph.D. thesis, TU Delft, Delft University of Technology, 1974.

Syvitski, J. P., Vörösmarty, C. J., Kettner, A. J., and Green, P.: Impact of humans on the flux of terrestrial sediment to the global coastal ocean, science, 308, 376–380, 2005.

Talling, J.: The phytoplankton population as a compound photosynthetic system, New phytologist, 56, 133–149, 1957.

Thompson, R., Roberts, M., Norton, T., and Hawkins, S.: Feast or famine for intertidal grazing molluscs: a mis-match between seasonal variations in grazing intensity and the abundance of microbial resources, Hydrobiologia, 440, 357–367, 2000.

Thornton, D. C., Dong, L. F., Underwood, G. J. C., and Nedwell, D. B.: Factors affecting microphytobenthic biomass, species composition and production in the Colne Estuary (UK), Aquatic Microbial Ecology, 27, 285–300, 2002.

Torstensson, A., Chierici, M., and Wulff, A.: The influence of increased temperature and carbon dioxide levels on the benthic/sea ice diatom Navicula directa, Polar Biology, 35, 205–214, 2012.

Toublanc, F., Brenon, I., and Coulombier, T.: Formation and structure of the turbidity maximum in the macrotidal Charente estuary (France): Influence of fluvial and tidal forcing, Estuarine, Coastal and Shelf Science, 169, 1–14, 2016.

Tuchman, N. C., Schollett, M. A., Rier, S. T., and Geddes, P.: Differential heterotrophic utilization of organic compounds by diatoms and bacteria under light and dark conditions, 167–177 in: Advances in Algal Biology: A Commemoration of the Work of Rex Lowe, Springer, 2006.

Tucker, C. J.: Red and photographic infrared linear combinations for monitoring vegetation, Remote sensing of Environment, 8, 127–150, 1979.

Ubertini, M., Lefebvre, S., Gangnery, A., Grangeré, K., Le Gendre, R., and Orvain, F.: Spatial variability of benthic-pelagic coupling in an estuary ecosystem: consequences for microphytobenthos resuspension phenomenon, PloS one, 7, e44 155, 2012.

Underwood, G. J. C.: Seasonal and spatial variation in epipelic diatom assemblages in the severn estuary, Diatom Research, 9, 451–472, 1994.

Underwood, G. J. C.: Microphytobenthos, 1770–1777 in: Encyclopedia of Ocean Sciences, edited by Steele, J. H., Academic Press, Oxford, 2001.

Underwood, G. J. C. and Kromkamp, J. C.: Primary Production by Phytoplankton and Microphytobenthos in Estuaries, in: Estuaries, edited by Nedwell, D. and Raffaelli, D., 93–153 vol. 29 of *Advances in Ecological Research*, Academic Press, 1999.

Underwood, G. J. C. and Paterson, D. M.: Seasonal changes in diatom biomass, sediment stability and biogenic stabilization in the Severn Estuary, Journal of the Marine Biological Association of the United Kingdom, 73, 871–887, 1993.

Underwood, G. J. C. and Provot, L.: Determining the environmental preferences of four estuarine epipelic diatom taxa: growth across a range of salinity, nitrate and ammonium conditions, European Journal of Phycology, 35, 173–182, 2000.

Underwood, G. J. C. and Smith, D.: Predicting epipelic diatom exopolymer concentrations in intertidal sediments from sediment chlorophyll a, Microbial Ecology, 35, 116–125, 1998.

Uthicke, S. and Klumpp, D.: Microphytobenthos community production at a near-shore coral reef: Seasonal variation and response to ammonium recycled by holothurians, Marine Ecology Progress Series, 169, 1–11, 1998.

Valentine, K., Mariotti, G., and Fagherazzi, S.: Repeated erosion of cohesive sediments with biofilms, Advances in Geosciences, 39, 9–14, 2014.

van Bavel, C. and Hillel, D.: Calculating potential and actual evaporation from a bare soil surface by simulation of concurrent flow of water and heat, Agricultural Meteorology, 17, 453–476, 1976.

van Broekhoven, W., Jansen, H., Verdegem, M., Struyf, E., Troost, K., Lindeboom, H., and Smaal, A.: Nutrient regeneration from feces and pseudofeces of mussel Mytilus edulis spat, Marine Ecology Progress Series, 534, 107–120, 2015.

van de Koppel, J., Herman, P. M. J., Thoolen, P., and Heip, C. H. R.: Do alternate stable states occur in natural ecosystems? Evidence from a tidal flat, Ecology, 82, 3449–3461, 2001.

van der Heijden, L., Rzeznik-Orignac, J., Asmus, R., Fichet, D., Bréret, M., Kadel, P., Beaugeard, L., Asmus, H., and Lebreton, B.: How do food sources drive meiofauna community structure in soft-bottom coastal food webs?, Marine Biology, 165, 2018.

van der Heijden, L., Graeve, M., Asmus, R., Rzeznik-Orignac, J., Niquil, N., Bernier, Q., Guillou, G., Asmus, H., and Lebreton, B.: Trophic importance of microphytobenthos and bacteria to meiofauna in soft-bottom intertidal habitats: A combined trophic marker approach, Marine environmental research, 149, 50–66, 2019.

van der Wal, D., Wielemaker-van den Dool, A., and Herman, P. M. J.: Spatial synchrony in intertidal benthic algal biomass in temperate coastal and estuarine ecosystems, Ecosystems, 13, 338–351, 2010.

van Leeuwe, M. A., Brotas, V., Consalvey, M., Forster, R. M., Gillespie, D., Jesus, B., Roggeveld, J., and Gieskes, W. W. C.: Photoacclimation in microphytobenthos and the role of xanthophyll pigments, European Journal of Phycology, 43, 123–132, 2008.

Varela, M. and Penas, E.: Primary production of benthic microalgae in an intertidal sand flat of the Ria de Arosa, NW Spain, Marine Ecology Progress Series, 25, 111–119, 1985.

Verhulst, P.: La loi d'accroissement de la population, Nouv. Mem. Acad. Roy. Soc. Belle-lettr. Bruxelles, 18, 1845.

Verney, R., Brun-Cottan, J.-C., Lafite, R., Deloffre, J., and Taylor, J.: Tidally-induced shear stress variability above intertidal mudflats in the macrotidal Seine Estuary, Estuaries and coasts, 29, 653–664, 2006.

Veuger, B. and van Oevelen, D.: Long-term pigment dynamics and diatom survival in dark sediment, Limnology and Oceanography, 56, 1065–1074, 2011.

Vieira, S., Ribeiro, L., da Silva, J. M., and Cartaxana, P.: Effects of short-term changes in sediment temperature on the photosynthesis of two intertidal microphytobenthos communities, Estuarine, Coastal and Shelf Science, 119, 112–118, 2013.

Vieira, S., Cartaxana, P., Máguas, C., and Marques Da Silva, J.: Photosynthesis in estuarine intertidal microphytobenthos is limited by inorganic carbon availability, Photosynthesis Research, 128, 85–92, 2016.

Volterra, V.: Variazioni e fluttuazioni del numero d'individui in specie animali conviventi., Memorie della Regia Accademia Nazionale dei Lincei, Serie 6, 2, 31–113, 1926.

Vos, P. C. and De Wolf, H.: Diatoms as a tool for reconstructing sedimentary environments in coastal wetlands; methodological aspects, Hydrobiologia, 269, 285–296, 1993.

Webb, W., Newton, M., and Starr, D.: Carbon dioxide exchange of Alnus rubra - A mathematical model, Oecologia, 17, 281–291, 1974.

Weerman, E. J., Herman, P. M., and van de Koppel, J.: Top-down control inhibits spatial self-organization of a patterned landscape, Ecology, 92, 487–495, 2011.

Williams, R. B.: Division Rates of Salt Marsh Diatoms in Relation to Salinity and Cell Size, Ecology, 45, 877–880, 1964.

Willows, R. I., Widdows, J., and Wood, R.: Influence of an infaunal bivalve on the erosion of an intertidal cohesive sediment: a flume and modeling study, Limnology and Oceanography, 43, 1332–1343, 1998.

Wiltshire, K. H., Tolhurst, T., Paterson, D. M., Davidson, I., and Gust, G.: Pigment fingerprints as markers of erosion and changes in cohesive sediment surface properties in simulated and natural erosion events, Geological Society, London, Special Publications, 139, 99–114, 1998.

Yamaguchi, A., Umezawa, Y., Wada, M., and Sayama, M.: Potential contribution of microalgal intracellular phosphorus to phosphorus distribution in tidal flat sediments during winter, Plankton and Benthos Research, 10, 1–10, 2015.

Zabel, M., Dahmke, A., and Schulz, H.: Regional distribution of diffusive phosphate and silicate fluxes through the sediment–water interface: the eastern South Atlantic, Deep Sea Research Part I: Oceanographic Research Papers, 45, 277–300, 1998.

Zedler, J. B.: Algal mat productivity: comparisons in a salt marsh, Estuaries, 3, 122–131, 1980.

Zedler, J. B., Winfield, T., and Mauriello, D.: Primary productivity in a southern California estuary, in: Coastal Zone, vol. 78, 1978.

Zemmelink, H., Slagter, H., Van Slooten, C., Snoek, J., Heusinkveld, B., Elbers, J., Bink, N., Klaassen, W., Philippart, C., and De Baar, H.: Primary production and eddy correlation measurements of CO2 exchange over an intertidal estuary, Geophysical research letters, 2009.

Zetsche, E., Paterson, D. M., Lumsdon, D., and Witte, U.: Temporal variation in the sediment permeability of an intertidal sandflat, Marine Ecology Progress Series, 441, 49–63, 2011.

Zhang, Y. J., Ye, F., Stanev, E. V., and Grashorn, S.: Seamless cross-scale modeling with SCHISM, Ocean Modelling, 102, 64–81, 2016.

Zhu, Q., van Prooijen, B., Maan, D., Wang, Z., Yao, P., Daggers, T., and Yang, S.: The heterogeneity of mudflat erodibility, Geomorphology, 345, 2019.

Zingmark, R.: Feasibility of remote sensing benthic microalgae. Final report., 1979.

Zurzycki, J. and Starzecki, W.: Volumetric methods, 257–270 Plant Photosynthetic Production: Manual of Methods, Dr W. Junk NV Publ., The Hague, 1971.

Étude de la dynamique du microphytobenthos des vasières intertidales aux latitudes tempérées

Résumé :
La production primaire (PP) élevée des vasières intertidales aux latitudes tempérées est principalement assurée par le microphytobenthos (MPB), qui soutient les réseaux trophiques benthiques et pélagiques. Dans cette thèse, nous utilisons un modèle couplé physique-biologie pour étudier la variabilité spatio-temporelle de la dynamique du MPB sur une vasière intertidale de la côte Atlantique française. Le modèle simule explicitement la biomasse du MPB et du brouteur *Peringia ulvae*. Les résultats fournissent des conclusions clées sur la dynamique du MPB. À l'hiver et au printemps, une lumière et une température de surface de la vase (TSV) optimales pour la croissance du MPB donnent lieu à une efflorescence printanière du MPB. La lumière est le facteur le plus limitant annuellement. Cependant, la TSV limite la croissance du MPB 40 % du temps en été. La photoinhibition pourrait se superposer à la thermoinhibition au printemps et en été. Le broutage et la remise en suspension (RES) du MPB façonnent également la dynamique du MPB. La bioturbation par *P. ulvae* contribue à une RES chronique du MPB du sédiment vers la colonne d'eau au printemps et en été. Les vagues contribuent à la RES du MPB par le biais d'événements de RES massive en hiver, au printemps et en automne. 50 % de la PP annuelle du MPB est exporté vers la colonne d'eau par le biais de RES chroniques et massives. Nous avons également développé une méthode qui combine les données de télédétection et les résultats du modèle couplé physique-biologique en un algorithme capable de prédire la PP à partir de données satellitales. En plus d'apporter de nouvelles perspectives sur la dynamique du MPB, ce travail propose de nouveaux outils numériques pour surveiller et prédire la PP du MPB et son devenir dans les eaux côtières dans un contexte de changement climatique.
Mots clés : microphytobenthos, vasière intertidale, production primaire, modélisation physique-biologie, télédétection

Study of microphytobenthos dynamics in temperate intertidal mudflats

Summary :
The high primary production (PP) of intertidal mudflats at temperate latitudes is mostly supported by microphytobenthos (MPB), which support both benthic and pelagic food webs. In the present thesis, we use a physical-biological coupled model to investigate the spatial and temporal variability of MPB dynamics on a large temperate intertidal mudflat of the French Atlantic coast. The model explicitly simulates the MPB biomass and the grazer (*Peringia ulvae*) biomass and density. The outputs provide key findings on MPB dynamics. In winter-spring, optimal light and mud surface temperature (MST) conditions for MPB growth lead to a MPB spring bloom. Light is the most limiting driver over the year. However, a high MST limits the MPB growth 40 % of the time during summer. The photoinhibition of MPB photosynthesis can potentially superimpose on thermoinhibition in spring-summer. Grazing and resuspension of MPB biomass also shape the dynamics of the MPB biomass. Bioturbation by *P. ulvae* contributes to a chronic export of MPB biomass from the sediment to the water column in spring-summer. Waves contribute to the MPB resuspension through massive resuspension events in winter, spring and fall. 50 % of the annual MPB PP is exported to the water column through chronic and massive resuspension events. We also developed a new method that combine remote sensing data with outputs of the physical-biological coupled model into a single algorithm that can predict PP from satellite data. In addition to bring new insights on the MPB dynamics, this work proposes new numerical tools to monitor and predict MPB PP and its fate in coastal waters in a context of climate change.
Keywords : microphytobenthos, intertidal mudflat, primary production, physical-biological modelling, remote sensing

LIENSs (LIttoral ENvironnement et Sociétés)

2 rue Olympe de Gouges

17000 LA ROCHELLE